ABSTRACT

Title of Dissertation : PIEZOELECTRIC HYDRAULIC HYBRID ACTUATOR FOR A POTENTIAL SMART ROTOR APPLICATION

Jayant Sirohi, Doctor of Philosophy, 2002

Dissertation directed by: Professor Inderjit Chopra
Department of Aerospace Engineering

A piezoelectric hydraulic hybrid actuator is proposed as a potential actuator for a trailing edge flap on a smart rotor. Piezoceramics are very attractive for the smart rotor concept due to their high energy density and electro-mechanical coupling. To optimally design systems based on piezoceramic actuators and sensors, accurate prediction of their response and power consumption is necessary. However, at present, experimental data as well as analytical tools in this regard are limited. Additionally, actuation capabilities of conventional piezoceramic actuators are often limited by their small stroke.

In order to address this issue, detailed experiments were conducted on PZT-5H piezoceramic sheet elements to identify their actuation, sensing and power consumption characteristics. The response of PZT-5H sheet actuators was measured under a variety of mechanical loadings and electrical conditions. Using this experimental data, a simple empirical model predicting the hysteretic free strain behavior of a PZT-5H sheet was developed. Calibration of piezoelectric strain sensors was performed along

with the theoretical derivation and experimental validation of shear lag and transverse sensitivity correction factors. Power consumption of piezoceramic actuators was modeled and experimentally validated. Empirical correction factors to account for the nonlinear variation of material properties with applied electric field were identified. Additionally, the possibility of reducing the magnitude of current drawn by the actuator was investigated in conjunction with the novel use of a pseudo-inductor.

In order to obtain higher output stroke levels than that of conventional piezoceramic actuators, a hybrid device combining piezoceramic actuation and hydraulic power transmission was investigated. A prototype was designed to meet the requirements of a trailing edge flap on a section of a full scale MD900 rotor blade. The prototype was fabricated and tested, specifically concentrating on high pumping frequency operation. The device was actuated by two P-804.10 piezostacks in series, which had a total length of 36 mm and cross-sectional area 10 mm^2. The device was tested up to a pumping frequency of 1 kHz, and achieved its maximum flow rate at a frequency of 300 Hz. Under uni-directional actuation, a blocked force of 33 lbs and a no-load velocity of 1.2 in/sec was measured. Under bi-directional actuation, at a frequency of 5 Hz, the amplitude of the output displacement was measured to be 32 mils under no external load, dropping to 15 mils under an external spring load of 180 lbs/in. The no-load output displacement amplitude drops to 12 mils at a frequency of 10 Hz.

It can be concluded that while the present prototype meets the requirements for a trailing edge flap actuator in terms of blocked force and quasi-static stroke, it does not have adequate bandwidth. In order to satisfy the bandwidth requirements, the flow rate at high pumping frequencies needs to be improved.

PIEZOELECTRIC HYDRAULIC HYBRID ACTUATOR FOR A POTENTIAL SMART ROTOR APPLICATION

by

Jayant Sirohi

Dissertation submitted to the Faculty of the Graduate School of the
University of Maryland, College Park in partial fulfillment
of the requirements for the degree of
Doctor of Philosophy
2002

Advisory Committee:

Professor Inderjit Chopra, Chair/Advisor
Associate Professor Darryll J. Pines
Associate Professor Norman M. Wereley
Assistant Professor Chris Cadou
Professor Amr M. Baz, Dean's Representative

© Copyright by

Jayant Sirohi

2002

DEDICATION

This work is dedicated to Lord Ganapathi, and to my Grandparents, who could not wait to see it complete

ACKNOWLEDGEMENTS

I would like to express my gratitude to my advisor, Professor Inderjit Chopra for his patient and inspiring guidance over the course of my graduate study. While giving me enormous freedom to conduct my research, he also never hesitated to point out the correct way to do things, and to provide important inputs when I did not see my way clearly. It is to this combination of freedom and direction that I attribute the large amount of knowledge I have gained over the past few years.

I am also greatly indebted to the other members of my thesis committee: Dr. Darryll Pines, Dr. Norman Wereley, Dr. Amr Baz and Dr. Chris Cadou for their time and effort, and for providing valuable insights into my research. Special thanks are due to Dr. Pines and Dr. Wereley for the encouragement they have given me over the past few years.

I am very thankful for the existence of my 'family away from home': Anand, Kashyap, Nagarajan, Nitin, Prakash and Lakshmi for their companionship and for everything else; some of them have been with me ever since I started graduate school.

I have also benefitted greatly from the excellent companionship of my colleagues at the Alfred Gessow Rotorcraft Center. Many thanks to the old-timer Paul and not-quite-as-old-timers Ashish and Harsha for all our enlightening technical discussions, as well as the good times spent together both inside and outside the Patterson building. Jinhyeong Yoo, Taeoh Lee, Andy Bernhard and Nikhil Koratkar were invaluable sources of information, help and support, and I learnt a lot from them. Many thanks are also due to Bernie LaFrance and Mr. Lee of the Machine Shop for all their help and enthusiasm.

I would also like to add that I can never really acknowledge my parents adequately, especially in such a short space. Suffice to say that they are really the reason for the existence of this work, and also for what I am today. Without them, I would have probably been in an entirely different profession.

TABLE OF CONTENTS

List of Tables 10

List of Figures 11

Chapter 1 Introduction 1

1.1 Background and problem statement 1

1.2 Helicopter vibration and noise 3

1.2.1 Passive isolation 5

1.2.2 Active vibration control schemes 5

1.2.3 Active vibration control: Control surfaces 8

1.2.4 Primary flight controls: Swashplateless rotor 10

1.3 Smart rotor concept 11

1.3.1 Role of smart structures and active materials in the smart rotor 13

1.3.2 Active material actuators and sensors 13

1.4 Smart actuators used in active rotors 17

1.4.1 Model scale active rotors 17

1.4.2 Full scale active rotors 21

1.5 Motivation of the present research 23

1.6 Objectives of the present research 28

1.7 Outline of the dissertation 29

1.8 Contributions of the present work 31

Chapter 2 Piezoceramic Sheet Actuators 41

2.1 Basic actuation mechanism 42

2.2 Piezoelectric constitutive relations 44

2.3 Experimental sample preparation and cycling 47

2.4 Behavior under static excitation fields 49

2.4.1 Static free strain 49

2.4.2 Effect of external stresses 50

2.4.3 Drift 53

2.5 Behavior under dynamic excitation fields 55

2.5.1 Strain hysteresis 55

2.5.2 Dynamic strain response 57

2.5.3 Effect of DC bias 59

2.6 Depoling behavior and dielectric breakdown 60

2.7 Summary and conclusions 62

Chapter 3 Piezoelectric Sensors 77

3.1 Introduction 77

3.2 Basic sensing mechanism 79

3.2.1 PZT sensors 81

3.2.2 PVDF sensors 81

3.3 Sensor Calibration 82

3.3.1 Experimental setup 82

3.3.2 Conversion of voltage output to strain 83

3.3.3 Signal conditioning 84

3.4 Correction factors 87

3.4.1 Poisson's ratio effect · · · · · 87
3.4.2 Shear lag effect · · · · · 88
3.5 Experimental results · · · · · 91
3.6 General operating considerations · · · · · 93
3.6.1 Effect of sensor transverse length · · · · · 93
3.6.2 Effect of temperature on sensor characteristics · · · · · 94
3.7 Summary and conclusions · · · · · 95

Chapter 4 Power Consumption of Piezoelectric Actuators 105
4.1 Electro-mechanical impedance approach · · · · · 106
4.1.1 Electrical impedance of a free actuator · · · · · 106
4.1.2 Electro-mechanical impedance of the actuator · · · · · 108
4.1.3 Mechanical impedance of the structure · · · · · 109
4.1.4 Electro-mechanical impedance of the actuator-structure combination · · · · · 110
4.2 Theory of L-C oscillator circuits · · · · · 113
4.3 Development of non-ideal circuit behavior · · · · · 115
4.3.1 Case (I): $R_l = R_c$ · · · · · 117
4.3.2 Case (II): $R_l = 0$, $R_c \neq 0$ · · · · · 119
4.3.3 Case (III): $R_c \neq R_l \neq 0$ · · · · · 119
4.4 Implementation of the current reduction circuit · · · · · 120
4.5 Implementation of a pseudo-inductor · · · · · 122
4.6 Experimental results · · · · · 125
4.7 Summary and conclusions · · · · · 128

Chapter 5 Piezoelectric Hydraulic Hybrid Actuator: Design and Development 144
5.1 Piezoelectric hydraulic actuation concept · · · · · 146

5.2 Current state of the art 150
5.3 Basic working principle 152
5.4 Prototype design and construction 153
5.5 Preliminary sizing considerations 155
5.5.1 Quasi-static pumping assumption 155
5.5.2 Work output per cycle: load-line analysis 156
5.5.3 Simplified system model 157
5.5.4 Pump body 159
5.5.5 Piezostack internal stiffness 159
5.5.6 Piston and diaphragm 159
5.5.7 Fluid and tubing 160
5.5.8 Accumulators 160
5.5.9 Work done per cycle: calculation of operating points 161
5.5.10 Stiffness of the fluid in the pumping chamber 162
5.5.11 Maximum output work 163
5.6 Pumping head and check valves 167
5.6.1 Type I valves 168
5.6.2 Type II valves 168
5.7 Delivery of electrical power 169
5.7.1 Piezostack driver 170
5.8 Experimental setup 172
5.8.1 Performance evaluation of the piezoelectric pump 173
5.8.2 Output power of the device 174

Chapter 6 Theoretical Modeling 192
6.1 Modeling of the pumping chamber and check valves 193

6.1.1 Derivation of governing equation using a control volume approach · · · · · 193
6.1.2 Modeling of the check valves · · · · · 195
6.1.3 Numerical solution · · · · · 197
6.2 Modeling of the overall device performance · · · · · 199
6.2.1 Lumped parameter - state space method · · · · · 199
6.2.2 States of the device · · · · · 200
6.2.3 Setting up the state-space equations · · · · · 201
6.2.4 Fluid impedance · · · · · 202
6.2.5 Assembly of the state-space matrices · · · · · 206
6.2.6 Numerical solution · · · · · 208
6.3 Modeling of piezostack self-heating · · · · · 209

Chapter 7 Experimental Results and Discussion 219
7.1 Performance of the piezoelectric pump · · · · · 220
7.1.1 Effect of system bias pressure · · · · · 221
7.1.2 Effect of piezostack actuation method · · · · · 222
7.2 Output power of the device · · · · · 223
7.2.1 Effect of system bias pressure · · · · · 224
7.2.2 Effect of check valves · · · · · 225
7.2.3 Effect of pumping frequency and piezostack driving method · · 227
7.2.4 Effect of diaphragm stiffness and bonding · · · · · 230
7.2.5 Effect of fluid viscosity · · · · · 233
7.2.6 Bidirectional actuation · · · · · 234
7.3 Conclusions · · · · · 237
7.4 Recommendations for future work · · · · · 241

Appendix A Piezoelectric Pump: Technical Drawings 259

Appendix B State-Space Analysis of the Device 268

Bibliography 274

LIST OF TABLES

2.1 Small signal PZT-5H characteristics 48

3.1 Typical properties at 25 °C 82

5.1 Prototype device parameters 166

6.1 Values of various parameters used in the state-space model 210

LIST OF FIGURES

1.1 Sources of helicopter vibration · · · · · 33

1.2 IBC hydraulic pitch link [36] · · · · · 33

1.3 Main rotor hub of Dauphin AS365 N2, from Eurocopter · · · · · 34

1.4 Swashplateless hub, UM-Raven [56] · · · · · 34

1.5 Smart rotor concept · · · · · 34

1.6 Types of piezoceramic actuators · · · · · 35

1.7 Comparison of output characteristics of piezoceramic based actuators [69] 36

1.8 Comparison of the ouput characteristics of typical actuators · · · · · 37

1.9 Active twist rotor using piezoceramic sheet actuators [80] · · · · · 38

1.10 Mach scaled active rotor blade with trailing edge flap actuated by piezo-bender elements [98] · · · · · 38

1.11 Mach scaled rotor blade with Smart Active Blade Tip (SABT) [9] · · · · · 39

1.12 X-frame piezostack amplifier [112] · · · · · 39

1.13 Full scale BK117 rotor blade with trailing edge flaps and piezoactuators [128] · · · · · 40

1.14 L-L Amplification actuator [131] · · · · · 40

2.1 Typical PZT unit cell · · · · · 64

2.2 Piezoceramic sheet · · · · · 64

2.3 Strain during DC cycling · · · · · 65

2.4 Static free strain behavior of PZT-5H · · · · · 66
2.5 Tensile testing fixture · · · · · 67
2.6 Variation of static free strain with transverse tensile stress · · · · · 67
2.7 Static strain drift behavior · · · · · 68
2.8 Drift under combined excitation · · · · · 69
2.9 Quasi-static hysteresis curve, uncycled PZT · · · · · 69
2.10 Quasi-static hysteresis curves, after AC cycling · · · · · 70
2.11 Variation of strain hysteresis with field and frequency for a free actuator · 71
2.12 Response of a free PZT actuator · · · · · 72
2.13 Effective stiffness and damping variation, PZT-5H · · · · · 73
2.14 Model validation at three different frequencies and two excitation voltages of 80 V_{peak} and 120 V_{peak} · · · · · 74
2.15 Effect of a DC bias field · · · · · 75
2.16 Variation of depoling field with excitation frequency · · · · · 75
2.17 Depoling behavior · · · · · 76

3.1 Calibration setup · · · · · 97
3.2 Charge amplifier circuit · · · · · 97
3.3 Circuit characteristics · · · · · 98
3.4 Forces and moments acting on the sensor · · · · · 99
3.5 Shear lag effects along sensor length · · · · · 100
3.6 Foil strain gage and PZT sensor impulse response in the time domain · · · 101
3.7 Foil strain gage and PZT sensor impulse response in the frequency domain 102
3.8 Correlation of PZT sensor and foil strain gage with correction factor · · · 102
3.9 Correlation of PZT sensor and foil strain gage for response at low strain levels · · · · · 103

3.10 Correlation of PVDF sensor and foil strain gage response · · · · · · · · · · 103
3.11 Correlation of foil strain gage and PZT sensors of different sizes, keeping gage length constant · 104
3.12 PZT sensor output variation with temperature · · · · · · · · · · · · · · · · · 104

4.1 Experimentally measured current and $\tan\delta$ for a free piezoelectric sheet · 130
4.2 Variation in piezoelectric material constants with applied electric field · · 131
4.3 Current consumption predictions for a free actuator, $3.0\text{kV}_{\text{rms}}/\text{cm}$ · · · · · 132
4.4 Current consumption predictions for a pair of actuators bonded onto a beam, $3.0\text{kV}_{\text{rms}}/\text{cm}$ · 133
4.5 Ideal series and parallel configurations · 134
4.6 Variation of R_c for $\tan\delta$=0.035, relative permittivity of 3400 · · · · · · · · · 134
4.7 Variation of Z_c for $\tan\delta$=0.035, relative permittivity of 3400 · · · · · · · · · 135
4.8 Non-ideal L-C circuit · 135
4.9 Inductance requirement, $R_c = R_l$ · 136
4.10 Required inductance and Z_p/Z_c for $f = 10Hz$ · · · · · · · · · · · · · · · · · 136
4.11 Required inductance and Z_p/Z_c for $f = 100Hz$ · · · · · · · · · · · · · · · · · 137
4.12 Variation of Z_p/Z_c with frequency for a 7μF actuator, in parallel with a 1H inductor · 137
4.13 Z_p/Z_c achievable by continuous tuning, 7μF actuator, $R_l = 50\Omega$ · · · · · · 138
4.14 Pseudo-inductor circuit-1 · 138
4.15 Pseudo-inductor circuit-2 · 139
4.16 Comparison of choke coil and pseudo-inductor performance · · · · · · · · · 139
4.17 Pseudo-inductor circuit performance · 140
4.18 Variation of current drawn with frequency · · · · · · · · · · · · · · · · · · · 141
4.19 Time variation of voltage, current and strain at 30 Hz · · · · · · · · · · · · · 142

4.20 Pseudo-inductor circuit performance with adaptive tuning · · · · · · · · · · 143
4.21 Pseudo-inductor power consumption · 143

5.1 Schematic of piezoelectric hydraulic hybrid actuator · · · · · · · · · · · · · · 177
5.2 Nominal output design goals · 177
5.3 Pumping cycle for an ideal incompressible working fluid · · · · · · · · · · · 178
5.4 Pumping cycle for a real working fluid · 178
5.5 Schematic of the piezoelectric pump · 179
5.6 Exploded view of the piezoelectric pump assembly · · · · · · · · · · · · · · · 179
5.7 First prototype of the piezoelectric pump · 180
5.8 Load-line analysis · 181
5.9 Simplified system model, outlet valve open · · · · · · · · · · · · · · · · · · 181
5.10 Simplified system model, pumping chamber · · · · · · · · · · · · · · · · · · 182
5.11 Correlation between theoretical and measured diaphragm stiffness · · · · · 182
5.12 Fluid line between pumping chamber and output actuator · · · · · · · · · · 183
5.13 Equivalent spring stiffness of fluid in the pumping chamber · · · · · · · · · 183
5.14 Dependence of work output per cycle on pumping chamber geometry, $\Delta_{gap} = 0.05''$ · 184
5.15 Type I: Ball type check valves · 185
5.16 Type II: Reed valves · 186
5.17 Schematic of the piezostack switched driver circuit · · · · · · · · · · · · · · 187
5.18 Comparison of sinusoidal waveform and switch driver waveform · · · · · · 188
5.19 Experimental setup for the evaluation of device performance · · · · · · · · 189
5.20 Experimental setup · 190
5.21 Parts of the experimental setup · 191

6.1 Control volume in the pumping chamber · 214

6.2 Check valve flow factor · · · · · 214
6.3 Correlation of measured differential pressure rise with theory, 50 psi bias pressure · · · · · 215
6.4 Schematic of the device · · · · · 215
6.5 Correlation of theoretical device output performance with experimentally measured values · · · · · 216
6.6 Temperature rise in the piezostacks at 50 psi bias and 150 psi bias pressure, 250 Hz excitation · · · · · 217
6.7 Heat transfer from the piezostack · · · · · 217
6.8 Correlation of measured piezostack temperature rise with theory · · · · · 218

7.1 Effect of system bias pressure on differential pressure rise in the accumulators · · · · · 243
7.2 Comparison of differential pressure rise with two piezostack excitation methods; switched driver and sinusoidal excitation · · · · · 244
7.3 Effect of system bias pressure on device output with 0.01” steel diaphragm, Type I valves · · · · · 245
7.4 Comparison of output performance with Type I and Type II valves · · · · · 246
7.5 Measured pumping chamber force-displacement curves, for 50 Hz pumping frequency, and 50 psi bias pressure, Type I valves · · · · · 246
7.6 Pumping chamber force-displacement curves, Type I valves, 50 psi bias pressure · · · · · 247
7.7 Pumping chamber force-displacement curves, Type II valves, 50 psi bias pressure · · · · · 248
7.8 High frequency excitation · · · · · 249
7.9 Test specimen for measuring passive cooling effectiveness · · · · · 249

7.10 Steady state piezostack temperatures, passive cooling · · · · · · · · · · · · · 250
7.11 TEM cooling test setup · 250
7.12 Effect of TEM on temperature rise of piezostacks · · · · · · · · · · · · · · · 251
7.13 Output force-velocity curves with 0.002” spring steel diaphragm, Type II valves, 50 psi bias pressure · 251
7.14 Degradation in device performance with pumping cycles · · · · · · · · · · · 252
7.15 Output cylinder velocity as a function of load and pumping frequency, 50 psi bias pressure · 253
7.16 No-load cylinder velocity with pumping frequency, Type II valves and using switched driver · 254
7.17 Effect of fluid viscosity on performance, with Type II valves · · · · · · · · · 254
7.18 Output cylinder no-load velocity, with the 4 way valve and 2cst oil · · · · 255
7.19 Output no-load cylinder displacement at 5 Hz, with a pumping frequency of 100 Hz, and with 50 psi bias pressure · 256
7.20 Output cylinder stroke as a function of output frequency, at various pumping frequencies, no external load · 256
7.21 Output cylinder stroke as a function of output frequency, with external spring load, at 300 Hz pumping frequency · 257
7.22 Correlation of measured no-load output displacement with theory at 300 Hz pumping frequency · 258

A.1 Sealing ring · 260
A.2 Pumping head: Type I check valves · 261
A.3 Pumping head: Type II check valves · 262
A.4 Pumping piston · 263
A.5 Piezostack assembly spherical end cap · 264

A.6 Piezostack assembly base 265
A.7 Preload base fixture 266
A.8 Pump body 267

Chapter 1

Introduction

1.1 Background and problem statement

Helicopters have the unique ability to both hover efficiently as well as cruise in forward flight. This is achieved by means of a large diameter main rotor with a low disk loading. However, the main rotor of a helicopter is also the source of a variety of problems.

Helicopters are characteristically susceptible to high vibratory loads, and noise levels. The high vibration levels limit helicopter performance [1] and reduce the structural life of components [2], which leads to increased maintenance and operating costs. In addition, the high vibration and noise levels lead to pilot fatigue and passenger discomfort, and have been recognized as major barriers to public acceptance of rotorcraft for the short haul commuter transport role [3]. Even in military applications, high vibration levels are undesirable from the point of view of crew fatigue and errors in target tracking and firing systems. Decreasing noise levels has also become a priority in modern rotorcraft. The civilian rotorcraft sector has seen the introduction of increasingly stringent noise requirements for rotorcraft flying in and around airports and residential areas. Military rotorcraft would like to generate as little noise as possible in order to increase stealth and improve battlefield survivability.

A large amount of research is presently directed towards realizing the goal of jet-smooth-and-quiet rotary-wing flight [4], to improve the cost effectiveness and to achieve wider community acceptance of rotorcraft. Extensive research has been focused on active and passive methods of vibration control. Passive methods suffer from several inherent disadvantages like a large weight penalty and poor off design performance. Active control strategies show much more promise for controlling vibration levels over a wide range of flight conditions. Recent advances in active materials and smart structures technology have introduced the possibility of designing compact, lightweight actuators that can be integrated in the blade structure in order to deflect a control surface or change the blade geometry. In this manner, the airloads on the rotor blade could be affected in an active control scheme.

A large number of such actuation mechanisms have been proposed, both in the model scale and the full scale. Most of these mechanisms are based on piezoceramic actuators, that provide the benefits of high energy density and high bandwidth. Additionally, the coupled electro-mechanical behavior of piezoceramics enables the use of these materials as sensors as well as actuators. This property creates a large number of possibilities, for example, self-sensing actuators for collocated control and high sensitivity embedded sensors to sense strain in the rotor blade. The on-blade actuators and sensors, together with real time control algorithms, comprise a smart rotor system.

Recent interest has also been focused on the concept of a swashplateless rotor, where the bulky and mechanically complex swashplate of the main rotor would be replaced by much more compact fly-by-wire type control systems. Primary control of the vehicle would be achieved by means of on-blade actuators that deflect control surfaces or create shape changes in the rotor blades. These actuators would operate off electrical power that would be transmitted from the fixed frame to the rotating frame through an electrical

slip ring unit. Because the basic hardware requirements are the same, a smart rotor could be designed to achieve the objectives of both active vibration control and primary flight control.

In order to design an optimum smart rotor, precise analytical modeling of the various elements of the system is required. Currently, design tools as well as experimental data to predict the behavior of these actuators and sensors over a wide range of operating conditions is not available. For example, in order to get useful deflections out of the active materials, they are often operated at high excitation fields, where non-linearities are dominant. However, most of the existing material data and theoretical models only take into account low excitation fields, with operation purely in the linear region of the material. In addition, current actuation systems are often mechanically complex and have a poor weight efficiency. A large part of the benefit of using active materials is lost as a result of mechanisms designed to amplify the small stroke of these materials.

The research presented in this dissertation is aimed at characterizing the behavior of piezoceramic sheet actuators and sensors over a wide range of mechanical and electrical operating conditions, in the context of their application to smart rotor systems. Additionally, the development of a new type of actuation mechanism to meet the requirements of a trailing edge flap actuator on a full scale smart rotor is described in detail. This actuation mechanism is based on the frequency rectification concept, and combines the advantages of piezoceramic actuation and hydraulic power transmission.

1.2 Helicopter vibration and noise

Most of the vibration and noise originates from the main rotor of the helicopter. The aerodynamic environment on the main rotor is unsymmetric and three-dimensional. In forward flight, the rotor blades encounter a 1/rev variation in angle of attack. They also

encounter effects such as blade stall on the retreating side, and compressibility effects including transonic shocks on the advancing side. The retreating side of the rotor disk always has a circular region of reversed flow of a diameter equal to the advance ratio.

The vibration is most pronounced in transition flight (advance ratio around 0.1) and in high speed flight conditions. The complex aerodynamic environment and the dynamic response of the elastic rotor blades result in large vibratory forces that are transmitted through the hub to the fuselage [5,6]. In addition to the dominant main rotor vibratory forces at discrete harmonics, the helicopter is subject to vibrations originating from the transmission, power-train, and rotor/fuselage and rotor/tail-rotor interactional aerodynamics. The wake from the main rotor interacts in a complicated manner with the fuselage and tail rotor, for example, each rotor blade encounters a periodic 1/rev forcing as it passes over the tail structure of the helicopter. Blade dissimilarities generate strong 1/rev loads. Typically, for a helicopter with N_b blades, the $N_b - 1$/rev, N_b/rev, and $N_b + 1$/rev vibratory loads on the blades are transferred through the hub to the fuselage as N_b/rev forces and moments [7,8]. However, this is true only for a perfectly tracked rotor with identical blades. In reality, as the blades are never perfectly identical, vibratory forces containing all harmonics are transmitted to the fuselage. The major sources of helicopter vibration are shown in Figure 1.1.

Additionally, the powerplant/gearbox assembly that is mounted directly on top of the passenger compartment generates a high frequency vibration signal. Secondary sources such as this significantly broaden the spectrum of the fuselage vibration spectrum. In practice, the fuselage vibration spectrum is dominated by the N_b/rev signature which is the primary target of vibration reduction.

Rotor noise can be broadly classified into two categories: high speed impulsive noise and low speed implusive or Blade Vortex Interaction (BVI) noise. Blade vortex interaction noise is generated mainly from unsteady pressure fluctuations on a blade due

to interactions with tip vortices shed from preceeding blades. BVI noise has a strong radiation directivity pattern, mostly forward and under the rotor plane.

For a detailed discussion of the sources of helicopter vibration and noise, and active methods of vibration cancellation, the reader is directed to Reference [9].

1.2.1 Passive isolation

Passive isolators and absorbers have been routinely used to isolate or to diffuse the fuselage vibration using dampers or tuned masses [10, 11, 12]. However they incur a large weight penalty (up to 3% of gross weight) and rapidly degrade in performance away from the tuned flight condition. Cabin mounted vibration suppressors do not require a detailed knowledge of the sources of excitation, and can be installed whenever required. However, they incur a large weight penalty and are effective only in a narrow band of excitation frequencies. Hub mounted absorbers are self tuning, however they create an increase in parasite drag. Acoustic treatments are often used inside the cabin for attenuating noise levels. The main disadvantage of this is again the large weight penalty.

1.2.2 Active vibration control schemes

Active vibration control schemes are more attractive than passive schemes because they can be used to suppress vibrations over a wide range of operating conditions. The incurred weight penalty is also expected to be lower in the case of active schemes.

Active vibration control schemes can be grouped under two broad categories: fixed frame based schemes and rotating frame based schemes.

Fixed frame active vibration control: ACSR

Fixed frame active control involves installation of high authority actuators at critical load points on the fuselage, for example at the gearbox struts. This method is also known as Active Control of Structural Response (ACSR). By applying control forces at these points, vibration transmitted to the cabin interior can be suppressed. This method requires a detailed and accurate coupled rotor-fuselage dynamic model in order to determine the optimal placement of actuators. Such systems have been implemented on the production EH101 [13, 14], and have been tested on the Sikorsky S-76 [15] and more recently on a Kawasaki Industries BK 117-C [16]. The Sikorsky S-92 also features a fixed frame active vibration system, wherein the cabin is fitted with a set of distributed active inertial force generators [17], based on successful flight test trials in a UH-60 Blackhawk. The force generators are adapted from passive tuned absorbers and incorporate hydraulic actuators, permitting variable frequency tuning, which enable them to operate over a wide range of flight conditions.

Rotating frame active vibration control: HHC and IBC

The goal of rotating frame active vibration control schemes is to suppress the vibrations right at their source, which is the main rotor. By changing the geometry of the rotor blade, or by deflecting on-blade control surfaces, the airloads on the blade can be influenced. If these airloads are correctly phased, they can be used to cancel the unsteady airloads that are the primary cause of the vibratory forces transmitted to the fuselage. There are two main methods for implementing this concept: Higher Harmonic Control (HHC) and Individual Blade Control (IBC).

In the HHC system, the blades are excited by exciting the swashplate at higher harmonics of the rotational speed. This in turn causes a variation in blade root

pitch, which results in new unsteady airloads on the blades. The swashplate inputs are superimposed on the collective setting and the primary flight control inputs. Typical pitch input requirements are on the order of 2° . The effectiveness of HHC in reducing vibration levels has been shown analytically [18, 19, 20, 21, 22], and experimentally [23, 24, 25, 26, 27]. However, the HHC system has a considerable weight penalty and it is limited to N_b/rev excitations of the swashplate. The power requirement of servo-actuators needed to drive the swashplate becomes substantial at extreme flight conditions. Also, HHC has been shown to promote blade stall at extreme flight conditions [20].

Another approach is IBC, in which the actuators are incorporated in the rotating frame, located between the swashplate and rotor blades [28, 29, 30, 31, 32]. This concept appeared to expand the capabilities of HHC systems because it allows the blade excitation over a wide range of frequencies that do not need to be a multiple of blade harmonics. The results of flight tests and wind tunnel tests showed that improvement in vibration as well as noise were possible with IBC [33, 34, 35]. An IBC system using hydraulic pitch links (Figure 1.2) in conjunction with a hydraulic slip ring has recently been tested in the wind tunnel [36]. Another similar hydraulic IBC system underwent flight tests on a Sikorsky CH-53G. However, a major drawback of the conventional IBC system is the complexity and weight penalty due to hydraulic slipring unit. Also, the required actuation power could be up to 2% of the installed maximum sea level power at maximum cruise speed [29].

IBC research also has been focussed on applications another than vibration reduction; for example: lag damping augmentation [31], gust alleviation [37], stall flutter suppression [38] and flight test of BVI noise reduction [39]. Müller et. al. [40] present an overview of experimental activity in field of HHC and IBC active rotors. For a detailed literature survey on HHC and IBC the reader is directed to the introduction

of Reference [41].

1.2.3 Active vibration control: Control surfaces

In both HHC and IBC, changes in airloads are achieved by means of changing the blade root pitch. As the inboard section of the blade is in a region of relatively low dynamic pressure, it does not have a major effect on the airloads. Therefore, changing the pitch of the entire rotor blade is not a very efficient means of modifying the airloads. One solution to this problem is to achieve changes in the airloads by means of control surfaces installed on the rotor blade itself. Using on-blade all moving aerodynamic control surfaces like trailing-edge flaps can significantly reduce actuation power requirements for IBC and provide performance benefits [42, 43]. Another approach is to use active blade twist to modify the airloads. Millott and Friedman [43] present a brief overview of active helicopter vibration reduction approaches including fixed frame active control of structural response, HHC/IBC and active trailing edge/servo flaps.

On-blade control surfaces have been used by several designers in the past. For example, Kaman uses on-blade servoflaps for primary flight control on their helicopters. An active flap will alter the local lift and pitching moment distribution on the rotor blade. Depending on the blade dynamics, the flap either operates as a dominant direct lift flap or a moment flap. Flaps whose dominant effect is the creation of a moment that twists the blade are termed servoflaps, as in the case of the Kaman main rotor control systems, and flaps whose dominant effect is the increase in local lift on the blade section are termed plain flaps.

One of the first investigations on the use of flaps for active vibration control was conducted by Kaman in their Multicyclic Controllable Twist Rotor (MCTR) HHC research. This concept utilized servoflaps on the rotor blade driven by push-pull rods attached to the swashplate. Higher harmonic servoflap inputs were superimposed on

the primary flight control inputs. A flap deflection of approximately $\pm 6^\circ$ was achieved at frequencies of upto 4/rev. Experimental results showed significant reductions in vibratory hub loads and control loads [44, 45, 46, 47].

Another important proof-of-concept investigation of the plain flap was conducted by McDonnell Douglas Helicopter Systems with their Active Flap Rotor (AFR) model [48, 49, 50]. This rotor was a 12 foot diameter model, with plain flaps on the rotor blade that were driven by a cam and cable linkage. The goal of these experiments were to investigate the effectiveness of a plain flap in terms of vibration control, BVI noise reduction and power requirements. Tests were performed with open loop multicyclic flap control inputs, whose phasing could be adjusted by means of a mechanical arrangement.

More recently, trailing edge flaps driven by on-blade hydraulic actuators have been tested on a Mach scaled model as part of an Active Rotor Control (ARC) test by Sikorsky [51]. The hydraulic fluid is supplied to the rotating frame through a hydraulic slip ring. State of the art 4 way spool valves and custom electronics enable operation of the hydraulic actuators at frequencies of upto 50 Hz. The Sikorsky research effort on active rotors is part of the Variable Geometry Rotor Technology (VGART) program, with the goal of developing next generation rotors with improved vibration and noise characteristics and enhanced performance.

Extensive analytical studies on active flaps can be found in the literature. Analytical studies of vibration reduction using actively controlled servo flaps were conducted by Millott and Friedmann [52,43,53]. Milgram and Chopra [41,54] conducted a parametric study for a plain trailing edge flap. The results indicate the feasibility of significant vibration reduction with flap sizes ranging from 10-20% span, 25% chord and flap deflections of the order $\pm 5^\circ$. A further important conclusion was that the optimum location of the flap midspan was related to the blade dynamics and is near the 75% span

station.

1.2.4 Primary flight controls: Swashplateless rotor

Developments in active rotor technology have recently spawned considerable interest in the swashplateless rotor concept. The goal of this concept is to utilize the on-blade active control surfaces, or active blade twist in order to achieve primary control of the helicopter. This would result in elimination of the swashplate assembly from the main rotor of the helicopter, with two major benefits.

Firstly, the elimination of the swashplate will result in a much simpler hub design. Modern helicopter hubs have a large number of components and need periodic maintenance and overhaul. They are also very complex mechanical assemblies, that are expensive to produce and maintain. The emergence of hingless and bearingless hubs have resulted in large simplifications in hub design as compared to articulated hubs. However, the swashplate still remains a common feature of all the rotor hubs, as a means of achieving primary flight control.

Secondly, the main rotor hub, with the swashplate and pitch links exposed to the free stream, is a significant source of parasite drag. A swashplateless design would lead to a cleaner fuselage and hub, with improved aerodynamic performance.

The actuation requirements for primary control are more severe than the requirements for vibration control. Recent studies indicate that on-blade elevon type control surfaces have the potential to provide sufficient collective and cyclic pitch authority to satisfy general requirements of primary flight control [55]. An elevon type control surface, that is completely buried inside the blade structure, is favored due to the lower parasite drag penalty as compared to an exposed servo-flap type configuration. The torsional frequency of the rotor blade is reduced to between 1.5/rev-2.5/rev and the rotor blade works at freestream velocities well above the elevon reversal speed.

An overview of many possible concepts to achieve a swashplateless rotor design can be found in a recent design study by Tarascio et. al. [56]. The search and rescue helicopter designed in this study, called the UM-Raven, had a Maximum Take-Off Weight (MTOW) of 8680 lbs, and featured a 5 bladed swashplateless rotor. Out of various concepts, the final methodology downselected for the swashplateless main rotor of the UM-Raven was a system of on-blade trailing edge flaps actuated by means of a novel Magnetic Shape Memory Alloy actuator. Control inputs for noise and vibration cancellation are superimposed on primary flight control inputs.

The main rotor hub of a Dauphin AS365 N2 helicopter is shown in Figure 1.3. Most of the pitch links and swashplate mechanism is covered by fairings from the fuselage. This hub is a modern hingless hub, known as the Starflex hub. However, it can be seen that the swashplate-pitch link mechanism is still quite complex, and a large frontal area is presented by this assembly. For comparison, the main rotor hub design of the UM-Raven, which has the same rotor diameter as the Dauphin AS365 N2, and is in the same MTOW range, is shown in Figure. 1.4. The advantages of the swashplateless design in terms of reduced mechanical complexity and decreased wetted surface area can be easily seen from the figure.

1.3 Smart rotor concept

Actuation of on-blade control surfaces by means of mechanical linkages originating from the fixed frame, as in the case of the MCTR and AFR, are too mechanically complicated to be incorporated into real helicopters and would have an unacceptably high weight penalty. On-blade actuators are necessary in order to integrate active control techniques on the rotor systems of production helicopters.

However, due to the severe volumetric constraints in a rotor blade, and the stringent

limitations on allowable weight penalty, it is very difficult to integrate conventional actuators in the smart rotor concept. In addition, conventional actuators typically have a large number of moving parts and are not designed to operate under the high centrifugal force fields that are encountered on helicopter rotor blades.

Recent advances in active materials and smart structures technology open the door to a wide range of possibilities for on-blade actuators [4, 57, 58]. Active materials, with coupled electro-mechanical behavior create the possibility of combining the functions of sensors and actuators, resulting in opportunities for the application of collocated control algorithms that are known to have superior performance. This leads to the concept of a smart rotor, that has blades with embedded actuators and sensors, with a signal conditioning/controller unit on the fixed frame (Figure 1.5). The signal conditioning/controller unit sends control inputs to the on-blade actuators in response to parameters sensed by the embedded sensors, or other sensors on board the aircraft. The integration of actuators, sensors and control electronics into the rotor make it a smart rotor, as opposed to an active rotor concept, which would only include actuators [59, 60, 4].

In addition to achieving the primary goals of vibration and noise reduction, the smart rotor has potential benefits in other areas like handling qualities and performance enhancement, stall alleviation, aeromechanical stability augementation, minimization of dynamic stresses on rotor components and rotor health monitoring. For example, recent research has been conducted into the application of the trailing edge flaps on an active rotor as a means of interrogating the rotor, for the purposes of detecting helicopter rotor faults [61]. The blade response is measured using the on-blade embedded sensors. It was shown that even a small amount of sensor noise adversely affects the damage detection methodology. High signal to noise ratio piezoelectric sensors could concievably provide large benefits in such applications.

1.3.1 Role of smart structures and active materials in the smart rotor

Recently there has been a growing interest in the application of smart structures technology to helicopter rotor systems [62, 4]. A comprehensive review of the current state of the art in smart structures technology applied to rotorcraft systems can be found in Reference [4].

Active materials such as piezoceramics and magnetostrictives are very attractive for the smart rotor concept because they are compact, light-weight, provide a high bandwidth, possess high energy densities and can provide actuation with a minimum of moving parts. Blade active systems using smart materials, such as rotors with trailing-edge flaps or controllable twist blades, offer the advantage of IBC, require lower actuation power, and eliminate the need for a hydraulic slip ring. All control inputs and sensor signals are transmitted between the fixed and rotating frame through an electrical slip ring, which is a very mature and reliable technology. Additionally, materials like piezoceramics, that exhibit electro-mechanical coupling, can be used both as sensors and actuators, leading to the possibility of collocated control techniques.

Numerous active control systems have been proposed and to some extent developed and tested, both in the model scale and for potential full scale rotors. At this stage a brief review of current active materials and their characteristics is warranted.

1.3.2 Active material actuators and sensors

Piezoelectric materials are one of the most popular candidates for smart actuators. These materials exhibit an electro-mechanical coupling. They undergo mechanical deformation in response to an electric field and generate an electric field in response to a mechanical strain field. Conventional piezoelectric actuators are typically based on piezoceramics. This allows the manufacture of a variety of actuators in a large number

of shapes, for example, sheets, tubes, rods and stacks. Most of these actuators utilize the d_{31} mode of actuation, or in the case of piezostacks, the d_{33} mode of actuation. However, some actuators are designed to utilize the d_{15} mode, or shear mode, which exhibits the largest electro-mechanical coupling. Piezoceramic actuators are typically as stiff as aluminum, and have a very high bandwidth, on the order of tens of kHz. Typical strain levels are on the order of 1000$\mu\varepsilon$ (for piezostacks) with stiffnesses on the order of 70 GPa. Depending on the configuration of the actuator, they can require excitation voltages on the order of 100 V, or even 1-2 kV. Due to their high energy density, high bandwidth, ease of embeddability and ease of integration into structures, they are extremely attractive for smart rotor systems. As a result of their electro-mechanical coupling, they can also be used as sensors.

Piezoceramic material is available in the form of sheets, rods and tubes, as well as in several other shapes. The base piezoceramic material can be fashioned into solid state actuators, using either specific electrode configurations, or geometrical arrangements. The basic types of such solid state piezoceramic actuators are shown in Figure 1.6. Figure 1.6(a) shows piezoceramic sheets and stacks, that consist of piezoceramic sheets with uniform electrodes on the 1-2 plane. These actuators use the d_{31} and d_{33} effect respectively. Figure 1.6(b) [63, 64] shows a piezoceramic sheet, and a composite with piezoceramic fibers, both with interdigitated electrodes. The special electrode pattern enables these actuators to operate in the d_{33} mode. Figure 1.6(c) [65] shows a bimorph and a C-block actuator, that achieve amplified output displacements as a result of their geometry. Several other actuators based on the same concept exist, such as the RAINBOW [66] and the THUNDER [67, 68] actuators. An overview of currently available piezoceramic materials and actuator geometries is presented by Near [69], from which Figure 1.7 is reproduced. It can be seen that piezoceramic stack actuators (MLAs) provide the highest energy density without mechanical amplification.

A detailed discussion of piezoceramics and actuators based on piezoceramics can be found in References [70] and [71].

Electrostrictive materials are similar to piezoelectric material, with slightly improved strain capability and lower hysteresis effect, but are highly temperature sensitive. In addition, the response of these materials to field is highly non-linear and depends only on the magnitude of the applied field, resulting in only uni-directional strains. Magnetostrictive materials (Terfenol-D) on the other hand respond to magnetic fields generated by coils located on or near the structure. These actuators generate low strain with high force over a large range of activation frequencies. The primary drawback of actuators based on magnetostrictive materials are that they are complex and very bulky due to the size of the magnetic coils required to create the magnetic fields.

Shape Memory Alloys (SMAs) are alloys of Nickel and Titanium that undergo phase changes depending on the their temperature. As a result, actuation can be achieved by means of heating and cooling the material. Their unique capacity to develop very large plastic strains (of the order of 5%) that is recoverable upon heating makes them attractive materials for use in low-frequency (less than 1Hz) actuators. For smart rotor applications, they are not very useful for vibration and primary flight control requirements as a result of their low bandwidth, but are excellent solutions for low bandwidth applications. As a result of their high stroke and high force capability, mechanical power transmission mechanisms are not required. SMA actuators have been used in trailing edge tab actuators [72, 73] and more recently, in active twist of tiltrotor blades [74]. SMA torsional actuators have also been investigated to actuate a control surface on a fixed wing aircraft, in conjunction with the Smart Wing program [75, 76].

A new active material has recently been developed, called a Magnetic Shape Memory Alloy (MSMA). This material has the potential for large output strokes (5%

strain) at moderate force levels, as well as a high bandwidth on the order of 100 Hz [77]. An actuator based on this material has been designed to meet the requirements of a primary flight control system employing trailing edge flaps on a full scale helicopter rotor [56].

A comparison of various actuators based on their specific stress and strain output is shown in Figure 1.8(a). On the Y-axis, the quantity plotted is the stress of the actuator divided by its density, and on the X-axis is plotted the strain of the actuator. The product of the two gives a measure of the specific work output of the actuator, per unit mass. It should be noted that in a smart rotor application, in addition to the severe volumetric constraint, there is also a weight penalty limitation. Hence, an actuator has to be judged not only on the basis of its specific work output per unit mass, but also by its specific work output per unit volume. It can be seen that hydraulic actuators and shape memory alloy actuators have the highest specific energy density, however, the main drawback of hydraulic actuators is their complexity and large number of moving parts. This is one of the issues addressed by the present research on a piezoelectric hydraulic hybrid actuator, that focuses on the development of a hydraulic pump which is very compact and has a small number of moving parts. Shape memory alloys are limited by their low bandwidth. This can be seen from Figure 1.8(b), which compares various actuators on the basis of their stress-strain product, which is a measure of their output energy capability, and their frequency response. From these two comparsions, it can be seen that piezoelectric actuators offer the best combination of high energy density and high bandwidth.

1.4 Smart actuators used in active rotors

While some smart rotor concepts involve SMA actuators and electromagnetic actuators, a majority are based on piezoceramics. The following discussion reviews some of the recent developments in on-blade actuators driving a control surface or twisting the rotor blade.

1.4.1 Model scale active rotors

The first active twist rotor, using direct twist actuation was developed by Chen and Chopra [78, 79, 80]. The rotor blade incorporated dual-layer monolithic piezo patch elements embedded at +45° under the upper skin and -45° under the lower skin of the rotor blade, see Figure 1.9. The piezo elements extended from approximately 17.5% to 70% chord and the ratio of the piezo to fiberglass skin thickness was of the order of 4:1. With both the upper and lower piezo elements excited in phase a net shear strain is induced in the skin, and blade twists. A 1.83 m (6ft) diameter Froude scale active twist rotor was tested in hover and in the wind tunnel. The tip Mach number of the reduced speed rotor was 0.28. Blade tip twist amplitudes of $\pm 0.25°$ were achieved (excitation field -560 to 1110 V/mm, excitation frequency below the torsional resonance frequency of 4.75/rev). The open loop wind tunnel tests demonstrated that despite the low blade tip twist amplitudes it was possible to appreciably alter the rotor hub loads.

Another active twist concept involves the integration of active piezo-fiber plies into the composite blade structure. Interdigitated electrodes are deposited on the active plies in order to utilize the larger d_{33} effect of the piezoelectric material. Active piezoceramic fibers replace the conventional graphite or glass fibers in a resin matrix, creating an active composite ply. When cured in a +45/-45 orientation on the blade, actuation of these active layers results in a linear twist along the blade section.

The piezo fiber concept was originally developed by Hagood et. al. [81, 82, 83, 84] and has subsequently been commercialized [85]. A two bladed 1/6th Mach scale model of the CH-47 rotor with active piezofibers was tested by Rodgers et. al. [84]. A tip twist of $\pm 0.4^\circ$ was measured at full rotor speed and 8° collective, with a mass penalty of 16%.

Cesnik et. al. [86, 87, 88] have developed an analytic model for active twist blades featuring active fiber composites. In parallel to this computational effort, a 1/6 Mach scale active fiber rotor blade was also designed and fabricated [87]. This rotor was hover tested in a heavy gas medium (Mach-scale) at the NASA Langley transonic wind tunnel. During the open loop hover test, oscillatory tip twist amplitudes of ± 1 deg were achieved in the 3-5/rev frequency range. A team from Boeing/MIT has recently built and tested an advanced geometry active rotor model with piezo-fiber composites actuating the blade in torsion [89].

Extensive research has been conducted on Froude and Mach scaled rotor models with trailing edge flaps actuated by piezo-bender elements. Early research efforts encountered problems with friction in the mechanical components as well as clamping problems in the actuator [90, 91]. These problems limited the flap deflection to less than $\pm 2^\circ$ at full speed. Improvements made in the actuator mechanism by Koratkar and Chopra [92, 93, 94, 95, 96, 97, 98] enabled testing of Froude scaled and Mach scaled model rotors on the hover stand and subsequent testing of a Mach scaled model in the wind tunnel (Figure 1.10). In the wind tunnel, the rotor was tested at rotational speeds of upto 1800 RPM and an advance ratio of 0.3 and a collective pitch setting of 6° . The piezo-bender actuators were excited at 90 Vrms with a 3:1 bias, upto frequencies of 5/rev and generated a deflection on the order of $\pm 4^\circ$.

Fulton and Ormiston successfully tested an improved bimorph flap on a reduced speed rotor (tip Mach 0.27, diameter 2.23 m). The 12% span, 10% chord flap was

centered at 75% radius and was driven by two 38.1 mm wide piezo bimorphs. The test program included a hover test [99], a wind tunnel test [100] and validation of the analytic model [101]. At full speed, open loop flap deflections of $\pm 7.5^{\circ}$ were achieved at an excitation of ± 610 V/mm. The test program clearly demonstrated the ability of the trailing edge flap to alter the blade torsion and flap bending loads.

A scaled up version of the piezo-bender concept was also designed for a full scale MD900 rotor [98]. Flap deflections on the order of $\pm 5^{\circ}$ were predicted with voltage inputs of 800 V. The weight of the full scale piezo-bender was predicted to be 3.4 lbs and along with the mounting fixtures, 5.6 lbs. This actuation scheme appears suitable only for scaled rotor models.

Bernhard and Chopra have developed a novel actuation mechanism consisting of a bending-torsion coupled composite beam with piezoceramic sheet actuators bonded on its surface [9,102,103,104](Figure 1.11). When the piezoceramic actuators are actuated in a bending configuration, the total bending in the beam cancels out and the total twist adds up. The resulting tip twist has been used to actuate trailing edge flaps as well as an all moving, 10% span blade tip (Smart Active Blade Tip, SABT). Froude and Mach scaled tests have been conducted on active rotors with this actuation mechanism. For the Froude scaled rotor, flap deflection amplitudes of $\pm 2^{\circ}$ were achieved at 900 RPM in hover in the 1-5/rev frequency range. In Mach scaled hover tests, at 2000 RPM, at 2° collective, and for an actuation voltage of 125 Vrms, the measured tip deflection at the first four rotor harmonics is between $\pm 1.7^{\circ}$ to $\pm 2.8^{\circ}$, increasing to $\pm 5.3^{\circ}$ at 5/rev due to resonance amplification. The tip activation resulted in over 50% variation in the steady rotor thrust levels at 8° collective.

The Mach scale SABT rotor was also used as a testbed for a time domain neural network control algorithm, developed by Spencer et. al. [105, 106, 107]. The same control algorithm was used to actively control vibrations on the Mach scaled active

rotor with trailing edge flaps actuated by piezo-bimorphs described above, by Koratkar et. al. [98]. The control algorithm and the active rotor system hardware were validated both in hover as well as in forward flight by means of wind tunnel experiments [97, 108]

Bothwell et. al. [109] researched the concept of actuating trailing edge flaps by means of an extension-torsion coupled composite tube, with an internal piezostack or magnetostrictive actuator. As a result of the composite coupling the tube extends and twists in response to extension of the actuator. Based on experimental success, it was proposed to stack multiple tubes in series to generate sufficient twist to deflect a trailing edge flap.

Modifications of the conventional straight bender have also been proposed, such as the C-block actuator [65, 110, 111]. The C-block has a greater stroke capability than a conventional straight bender at the cost of reduced force output. A blade section incorporating a 10% chord trailing edge flap, with a 50% pivot overhang for aerodynamic balancing was windtunnel tested. With a driving voltage of 55% (of the maximum level), flap deflections of $\pm 5^\circ$ to 9° were measured, however the dynamic pressure was less than 3% of full scale dynamic pressure.

The X-frame actuator concept was pioneered by Prechtl and Hall [112, 113, 114, 115, 116]. The X-frame is a piezo-stack amplification mechanism that uses stroke amplification via shallow angles. The actuator was integrated into a 1/6th Mach-scale Boeing CH-47 (Chinook) blade and tested in hover [114]. The flap is a slotted servo-flap with a 11.5% span, 20% chord and aerodynamic overhang 27.5% of flap chord. At the operating speed (tip mach number 0.63) and 8° collective, flap deflections of $\pm 3.9^\circ$ were achieved.

1.4.2 Full scale active rotors

The baseline theoretical and experimental work validated in the model scale is slowly transitioning into full scale applications. The development of the AFR rotor was accompanied by a detailed feasibility study and development program for the full scale active flap rotor program at McDonnel-Douglas/Boeing [117, 118, 119, 120, 121]. The application is for a MD900 Explorer helicopter, which is an 8-seat utility helicopter with a MTOW of 6250 lbs, with a 5 bladed, 34 foot diameter bearingless rotor. The final actuator design downselected consists of a 3 foot span trailing edge flap driven by a bidirectional version of the X-frame actuator described above. The actuator has been scaled up from the model scale in order to meet full scale requirements [121, 122]. Two X-frames are coupled together in order to obtain a positive force during both extension and retraction of the flap actuator push rod. The dual X-frame actuator is capable of a blocked force of 80 lbs and a free displacement of approximately 100 mils. A dual X-frame actuator undergoing benchtop testing is shown in Figure 1.12.

Early studies by Eurocopter for a full-scale active trailing edge flap used a piezo stack actuator with a shallow angle flextensional amplification mechanism [123, 124, 125, 126]. The same actuator has also been proposed for a leading edge droop concept, for delaying dynamic stall [127]. More recently, Eurocopter has investigated and selected two candidate technologies for vibration cancellation and BVI noise suppression by means of IBC using trailing edge flaps [128]. The first approach is using DWARF piezoceramic actuators driving a 15% chord flap integrated in modified BK117/ATR rotor blades (Figure 1.13). Ground and flight tests were planned for the year 2001. The second approach utilizes COCE electromagnetic actuators driving a 25% chord flap in a modified Dauphin blade section.

A bi-directional flap actuator driven by piezostacks, based on lever arm

amplification has been developed by Lee and Chopra [129, 130, 131] (Figure 1.14). This actuator was designed to meet the requirements of a trailing edge flap on the blade section of a full-scale MD900 Explorer helicopter. The actuator was driven by 5 piezoceramic stack elements driven at a peak to peak voltage of 120 V and achieved a blocked force of approximately 9 lbs with a free stroke of approximately 75 mils. This actuator was tested in a vacuum chamber spin test and in a wind tunnel, at frequencies of upto 5/rev. Spin testing results showed less than 10% degradation of actuator deflection at 710g's of centrifugal accelaration. In the wind tunnel, peak to peak flap deflections of upto 12° were measured at free stream velocities of 120 ft/sec and 12° collective. However, analytical predictions overpredicted the performance of the actuator as a result of the finite stiffness of the linkages. A bidirectional version of the same actuator has also been designed and is currently undergoing spin testing in vacuum.

While most full-scale smart rotor activities have centered around piezoelectric actuation systems, some electromagnetic actuation systems have also been proposed. The above mentioned COCE actuators used by Eurocopter are one example. Another example is the work of Fink et. al. [132,133]. In this study a proprietary electromagnetic actuator was used to drive a 11.3 % span, 46% chord flap centered at 91% blade radius of an OH-58 (Kiowa Warrior) rotor blade. The actuator was designed to replace blade tip balance weights to minimize the weight penalty. Flap deflection amplitudes of ± 6 deg were achieved at a tip Mach number of 0.48 (81% of design speed). Average flap power requirement was reported as 220 W, that represents less than 0.05% of the maximum installed power of an OH-58D.

A shear mode piezoelectric tube actuator has been developed to drive a trailing edge flap [134, 135]. This actuation mechanism utilizes the d_{15} effect of the base piezoelectric material, which is the largest piezoelectric coupling effect. Design studies were conducted for a Boeing MD 900 helicopter with a plain trailing edge flap. It was

estimated that flap deflections of $\pm 2.5^\circ$ can be achieved at full speed. This is based on a 6% span flap, with a 25% chord, driven by a tube with an outer and inner diameter of 17.8 and 11.4 mm, respectively, and a length of 203 mm (corresponding to 4% of rotor radius). Using a spring to simulate aerodynamics, $\pm 1.5^\circ$ were measured in a bench top test, at 75% of the maximum electrical field, on the order of 1kV.

A trailing edge flap actuator based on MSMA as the active material was recently designed to provide primary flight control authority on a search and rescue helicopter [56]. Two trailing edge flaps were used on each blade and flap deflections on the order of $\pm 5^\circ$ at hinge moments of approximately 3 lb-ft were required for trim. Two permanent magnets were used in conjunction with two magnetic coils that provided a differential magnetic field of ± 100 kA/m. The total actuator weight including the housing was 1.9 lbs, of which 0.798 lbs was the active MSMA material itself. The power requirement was 210 W, at a current of 4 A, which corresponds to approximately 0.2% of the total installed continuous power of the vehicle. This design study clearly demonstrates the feasibility and attractiveness of the swashplateless concept.

1.5 Motivation of the present research

From the discussion above, it can be seen that piezoceramic actuators are the most attractive in terms of application to on-blade actuation systems. The subsequent discussion will therefore imply piezoceramics whenever the term 'active material' is used.

In the application of active materials to the smart rotor concept, the major barrier is their small stroke [57]. As a result, in order to achieve the required control authority, the active materials are excited at high fields, far in excess of their linear region. This leads to considerable non-linear behavior, that is not modeled in conventional analyses. The

non-linearities have significant effect on material properties and power consumption of the actuators. In addition, the high electric field values expose the actuators to the danger of depoling the active material. In order to design efficient systems incorporating piezoelectric actuators, accurate analytical tools are required, to predict the response of the actuators coupled to a structure, their power consumption, depoling limits and the effect of material non-linearities. Current analyses often simplify the behavior of piezoelectric actuators to a linear working region, with constant material properties. They also do not include the effect of external stresses, that are encountered in smart rotor applications, where centrifugal accelerations of 700g's at the actuator location are typical. Larger excitation fields, and larger volumes of active material translate to increased levels of power consumption. The large currents drawn by on-blade actuators result in larger electrical slip ring units, with increased cross talk between power and signal channels. Addressing this issue demands a clear understanding of the power consumption of piezoelectric actuators.

In rotor blade health monitoring applications, high sensitivity embedded sensors are very important. The high signal to noise ratio of piezoelectric sensors make them very attractive for this application. However, the sensing mechanism needs to be accurately modeled and the effects of transverse stresses and shear lag factors need to be incorporated into the analysis. Many researchers have used piezoceramic sheet elements as sensors in controllable structural systems and also in health monitoring applications, however, limited attempt has been made to accurately calibrate the magnitude of the measured sensor voltage with actual structural strain.

In addition to operating the active materials at high excitation fields, various other methods need to be employed in order to increase the stroke of the active material. These methods, many of which have been described above, can be grouped into a few broad categories, based on their fundamental concept.

1. **Mechanical amplification:** An arrangement of levers or linkages is used in order to amplify the stroke of the piezostack. Examples of this method are the L-L actuator, X-frame actuator, and to some extent the flextensional actuator. These actuators trade off force capability for stroke, and therefore utilize high blocked force piezostacks as their base active material. However, in order to maximize the efficiency of transmitting power through the amplification device, the deformation of the mechanism itself has to be kept to a minimum. In order to achieve this, the levers and linkages have to be made extremely stiff, which increases the weight penalty of the device. Amplification mechanisms that rely on flexures have an inherently lower transmission efficiency as a result of the strain energy stored in the flexures. In practice, amplification ratios of more than 15-20 are difficult to achieve [131].

2. **Structural coupling:** The transmission of power from the active material to the output is by means of a passive structurally coupled element, that transforms one type of displacement to another type of displacement. Examples of this are the bending-torsion coupled beam of Bernhard and Chopra [9] and the extension-torsion coupled beam of Bothwell et. al. [109]. The major drawback of these concepts is that a large amount of the work output of the active material is utilized in deforming the structurally coupled material. This decreases the efficiency of the device. Although the bending-torsion coupled beam was very successful in the model scale, implementation on a full scale smart rotor system is challenging and would lead to unacceptably large weight penalties.

3. **Active material working as an active linkage:** In these devices, the active material itself forms part of the power transmission linkage. Examples of this are the piezo-bender devices [98] and the piezoelectric shear tube [134]. As a result

of the geometry of the active material, or the actuation method, amplification is achieved in the case of the piezo-bender, and rotary output motion is achieved in the case of the shear tube. These devices have the highest weight efficiency, as they have a minimum of passive strucutral components in the power transmission path. However, the scaling of the piezo-bender to full scale requirements is difficult, and would result in a large weight penalty [98]. The shear tube is very promising for flap actuation as it delivers a rotary output without any need for mechanical power transmission, however, its installation in a rotor blade could lead to a large weight penalty as a result of the mass balancing required.

4. **Distributed actuation:** Piezo-fibers are an example of a distributed actuator. The active material forms part of the overall structure and is distributed over a large part of its surface. The major drawback of this concept is the weight penalty in full scale applications. Stiffness issues as a result of the large fraction of piezoelectric fibers also need to be addressed. Additionally, this actuation method requires very large voltages, on the order of 1-2kV, to be supplied through an electrical slip ring to the rotor blades.

5. **Electromagnetic actuators:** Examples of electromagnetic actuators investigated for full scale requirements are the work of Fink et. al. [132] and investigations by Eurocopter [128, 136]. One of the major differences between electromagnetic actuators and piezoelectric actuators is their performance under loss of power. Piezoceramics actuators are inherently stiff, and under loss of power can maintain a zero deflection of the control surface. However, electromagnetic actuators have almost no stiffness without their control voltage, which would leave them free to flutter about their hinge line with potentially dangerous consequences. One solution could be to introduce a mechanical locking mechanism. Another issue

to be addressed regarding electromagnetic actuators is dissipation of the heat generated in the actuator.

Electromagnetic actuators typically feature higher energy densities compared to piezoelectric actuators. A measure of energy density is the area under the force-stroke curve of the actuator divided by the mass of the actuator. The COCE electromagnetic actuator has a typical energy density of 0.36 J/kg, while piezoceramic DWARF actuator has an energy density of 0.15 J/kg [128]. It is important to note that for a typical low voltage piezostack, the P-804.10 (Physik Instrumente [137]) with a blocked force of 5000 N and a free displacement of approximately 15 microns, the energy density is approximately 2.5 J/kg. The stroke amplification mechanism, support structure and load transfer members decrease the overall energy density of a typical piezoceramic actuator by almost an order of magnitude compared to the base active material.

In order to eliminate the drawbacks associated with the above mentioned actuation schemes, the present research work investigates the feasibility of a piezoelectric hydraulic hybrid actuator as a possible actuator for a control surface on a full scale smart rotor. This actuation concept is based on frequency rectification, that trades off the high frequency, low stroke displacement of the active material into a lower frequency, high stroke output displacement. Several other actuation concepts exist based on frequency rectification, like ultrasonic motors and inchworm motors [138, 139], and are discussed in more detail in Chapter 5. However, these concepts rely on friction between the moving and stationary parts of the actuator to achieve relative motion. As a result, they are subject to wear problems and have relatively short useful lifetimes. No attempts have been made upto the present to integrate these actuators in a rotor blade. However, ultrasonic motors have been integrated in a fixed wing application, as part of the Smart

Wing project [75, 76].

Although the piezoelectric hydraulic hybrid actuator is based on the frequency rectification principle, it is not friction based. It also combines the high bandwidth of piezostacks with the advantages of a hydraulic power transmission. Because the frequency rectification eliminates the need for large amplification ratios, higher transmission efficiencies are achievable using this concept as opposed to the concepts described above. The present research only focuses on the development of a benchtop experimental prototype, however, in the long term, piezoelectric hydraulic hybrid actuators are envisaged as compact, localized systems to actuate on-blade control surfaces.

1.6 Objectives of the present research

The goal of the present research work is twofold:

1. To systematically investigate and evaluate the various aspects of piezoceramic materials, used both as actuators and sensors, in conjunction with their application to a smart rotor blade concept.

2. Recognizing the capabilities and limitations of current actuators for smart rotors as described above, to evaluate the design and performance of a new actuator based on a piezoelectric-hydraulic hybrid concept, as a possible actuator for trailing edge flaps on a full scale smart rotor. The new actuation scheme will be designed keeping in mind the requirements of both vibration control and primary flight control.

1.7 Outline of the dissertation

The dissertation consists of seven chapters, divided roughly into two parts focusing on the goals described above. Chapters 2-4 will discuss the behavior and characterization of piezoceramic elements, used as both actuators and sensors, being part of an overall smart rotor blade concept, while Chapters 5-7 will specifically focus on the piezoelectric-hydraulic actuation concept.

A brief description of the chapters follows

1. **Chapter 1: Introduction.** A brief introduction to the problem of noise and vibrations on helicopters. The smart rotor concept is introduced, along with a brief review of the current state of the art, emphasizing current efforts in the direction of full scale applications.

2. **Chapter 2: Piezoceramic Sheet Actuators.** This chapter discusses in detail, the behavior and characterization of piezoceramic sheet actuators. A variety of loading conditions is discussed, both electrical and mechanical. Other phenomena of interest in a practical application, like static strain drift and depoling of the actuators is also addressed.

3. **Chapter 3: Piezoelectric Sensors.** This chapter discusses the use of piezoelectric sensors to sense structural deformations. In addition to piezoceramic sensors, polymer piezo-film is also discussed. Piezoelectric strain sensors are calibrated by means of a reference strain gage, and correction factors are derived to account for effects like piezoelectric transverse isotropy and shear lag. The superiority of piezoelectric strain sensors compared to conventional foil type resistive strain gages is demonstrated, which translates into important potential benefits of using piezoelectric sensors as sensing elements on a smart rotor blade.

4. **Chapter 4: Power Consumption of Piezoelectric Actuators.** The measurement and prediction of power consumed by piezoelectric actuators is discussed, with the main motivation being the requirements of the electrical slip ring unit on a smart rotor system. Empirical correction factors are introduced to account for non-linearities of the piezoelectric material at high excitation fields. Means of decreasing the current drawn by the piezoelectric actuators is discussed. A theoretical analysis of the limits of the decrease in current achievable by using L-C oscillator circuits is described, along with experimental results of a novel L-C oscillator circuit based on a pseudo-inductor.

5. **Chapter 5: Piezoelectric Hydraulic Hybrid Actuator: Design.** This chapter introduces the concept of frequency rectification of piezoelectric actuators. A review of the current state of the art in frequency rectification devices is presented, focusing on hydraulic frequency rectification. The preliminary design of a piezoelectric hydraulic hybrid actuator is discussed and the fabrication of a prototype is described. The experimental setup to measure the performance of the device is also discussed.

6. **Chapter 6: Piezoelectric Hydraulic Hybrid Actuator: Theoretical Modeling.** Theoretical models are developed to understand and predict the behavior of the device, as observed in the experiments described in Chapter 5. An analysis of self-heating of the piezostacks is also presented, as this is one of the key issues relating to the maximum achievable output power density.

7. **Chapter 7: Piezoelectric Hydraulic Hybrid Actuator: Experimental Results and Discussion.** This chapter presents some results from experiments performed on the device. Important conclusions are drawn from these results and recommendations are made for improvements of the design as well as future

research goals.

1.8 Contributions of the present work

Some specific contributions of the present research work are listed below

1. Testing and characterization of piezoceramic sheet actuators under a variety of mechanical and electrical loading. Identification of several strong non-linearities at the operating region of interest.

2. Development of a phenomenological model, taking into account the non-linearities, to predict the strain response and power consumption of piezoceramic sheet actuators. In the literature, although the existence of these non-linearities is known, most of the analyses assume linear, small signal properties that are significantly different from the properties observed at the operating region of interest for smart rotor applications.

3. Calibration of piezoelectric strain sensors, based on a reference conventional resistance based foil strain gage. Correction factors were analytically derived and experimentally validated to account for the specific characteristics of installing piezoelectric strain sensors.

4. Fabrication and testing of a simple signal conditioning circuit for piezoelectric sensors, with voltage output.

5. Derivation of theoretical limits to the achievable benefit by using an L-C oscillator circuit to reduce the current drawn by piezoelectric actuators. Fabrication and testing of a novel L-C oscillator circuit based on a pseduo-inductor.

6. Design, fabrication and testing of a compact piezoelectric hydraulic hybrid actuator capable of pumping frequencies upto 1kHz. The highest pumping frequency reported in the literature at present is 300 Hz.

7. Evaluation of the extent of validity of theoretical models at these high frequencies. Quantification of piezostack self-heating.

8. Investigation of active and passive methods of heat dissipation from the piezostacks. Experiments were performed on active cooling using Thermoelectric modules and passive heat dissipation.

9. Design, fabrication and testing of a compact piezostack driver capable of exciting the piezostacks at high frequencies. This method of driving the piezostack is shown to generate larger flow rates than the conventional sinusoidal excitation.

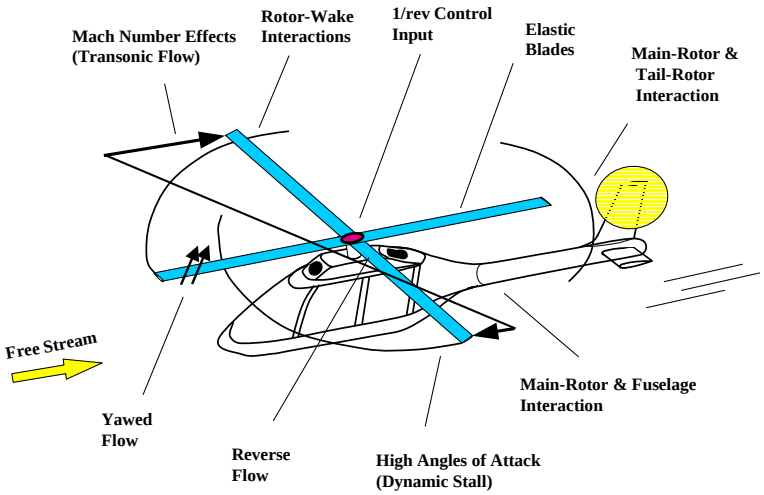

Figure 1.1 Sources of helicopter vibration

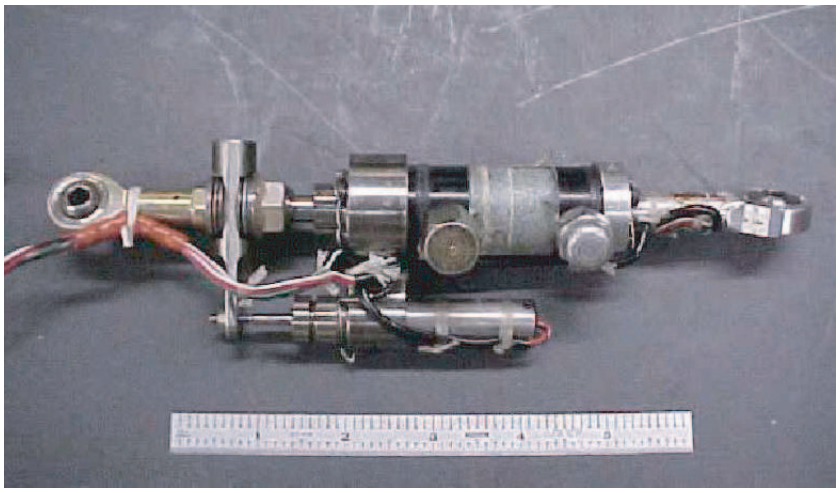

Figure 1.2 IBC hydraulic pitch link [36]

Figure 1.3 Main rotor hub of Dauphin AS365 N2, from Eurocopter

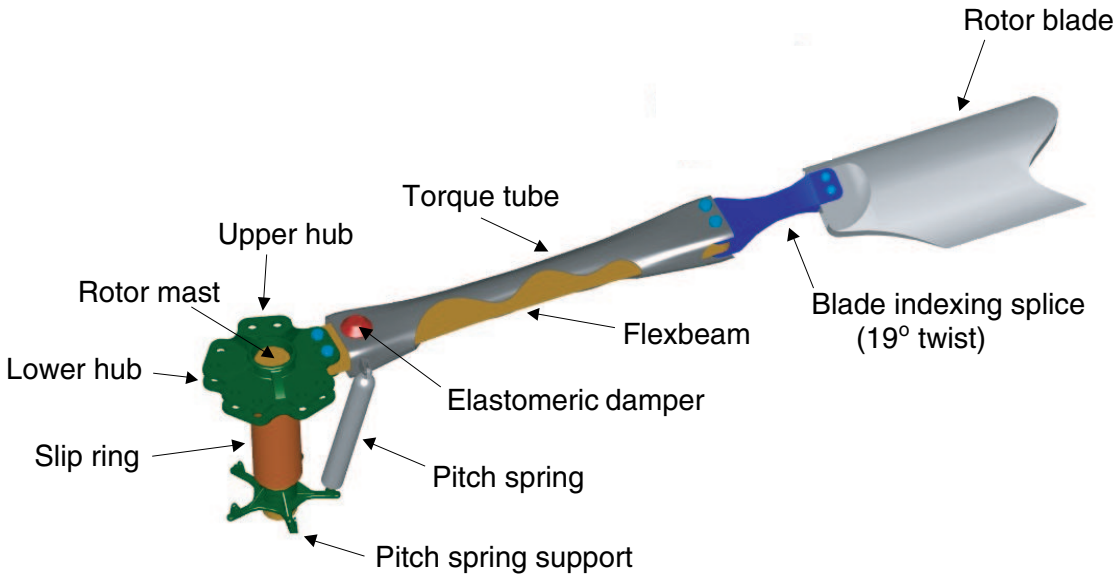

Figure 1.4 Swashplateless hub, UM-Raven [56]

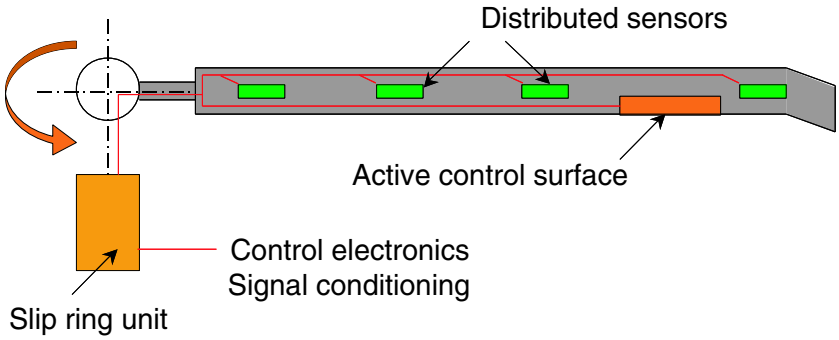

Figure 1.5 Smart rotor concept

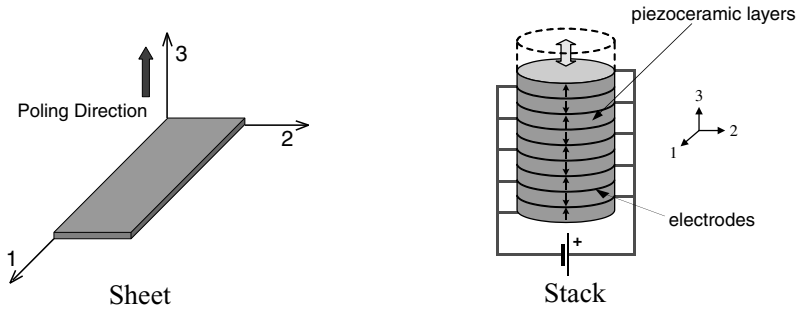

(a) Base material with 1-2 plane electroded

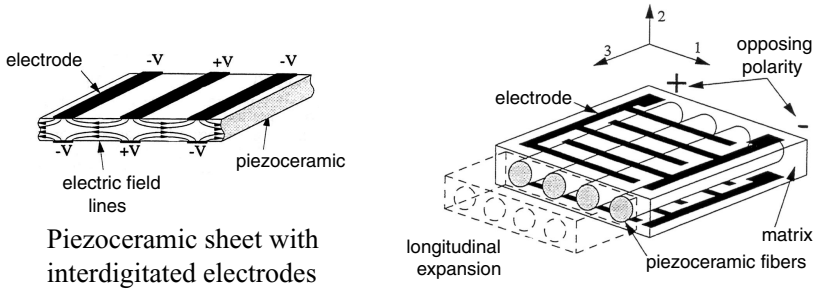

(b) Special electrode configuration

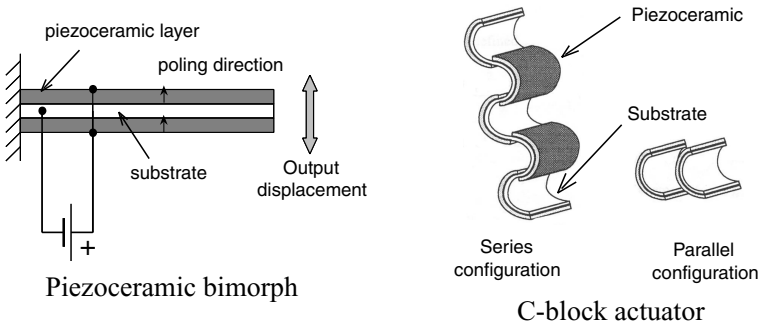

(c) Inherent geometrical amplification

Figure 1.6 Types of piezoceramic actuators

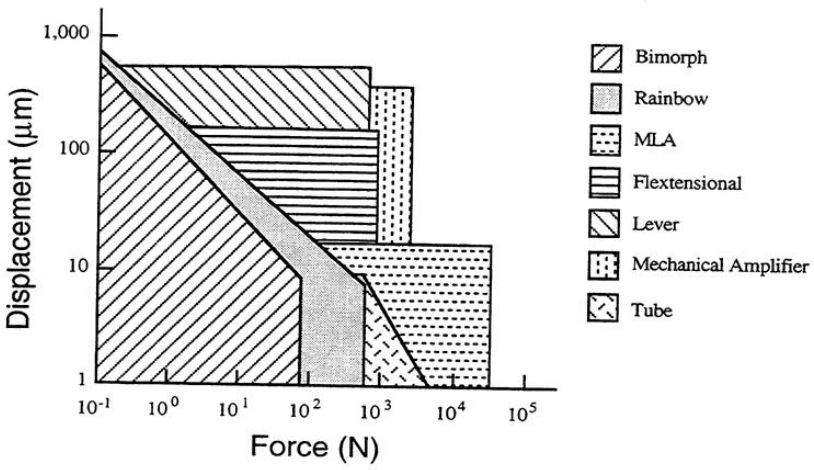

Figure 1.7 Comparison of output characteristics of piezoceramic based actuators [69]

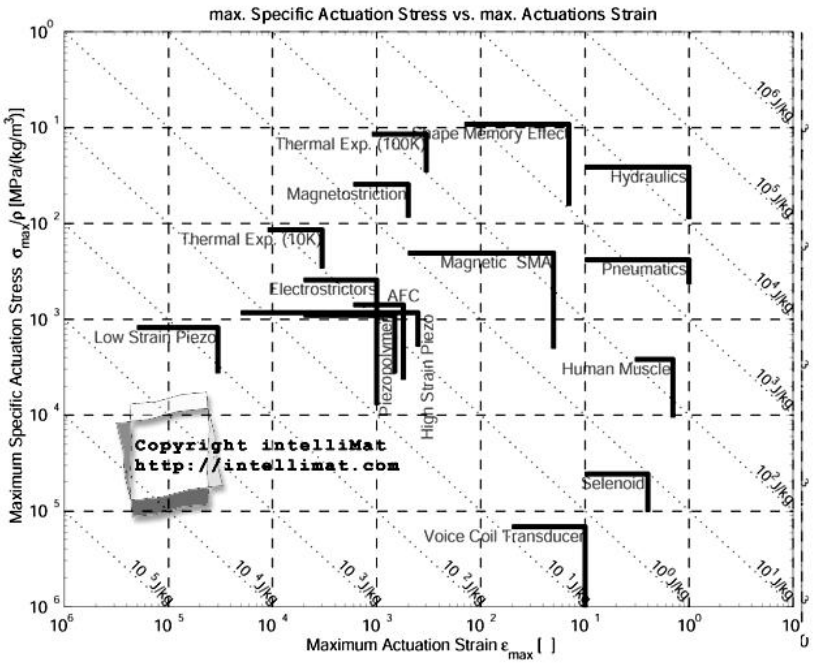

(**a**)Specific work output, per unit mass

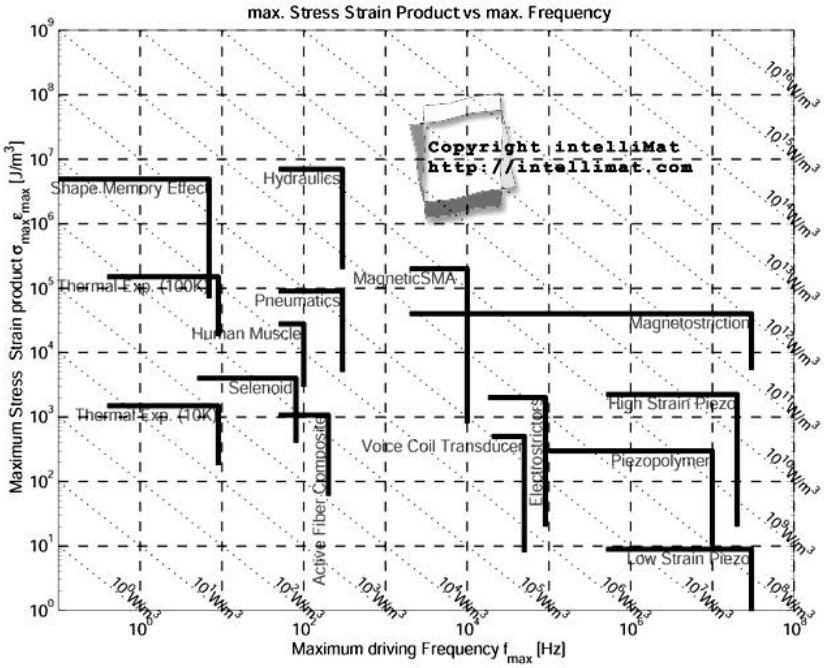

(**b**)Specific work output, with frequency response

Figure 1.8 Comparison of the ouput characteristics of typical actuators

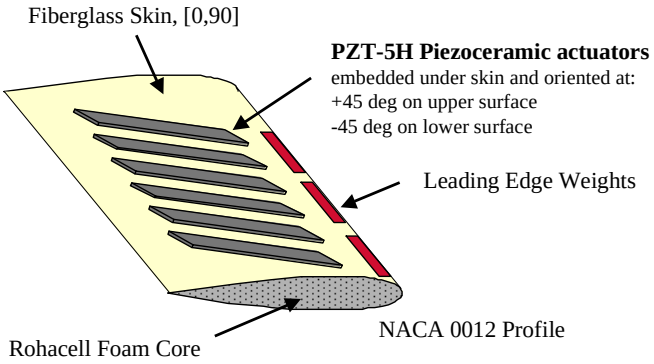

Figure 1.9 Active twist rotor using piezoceramic sheet actuators [80]

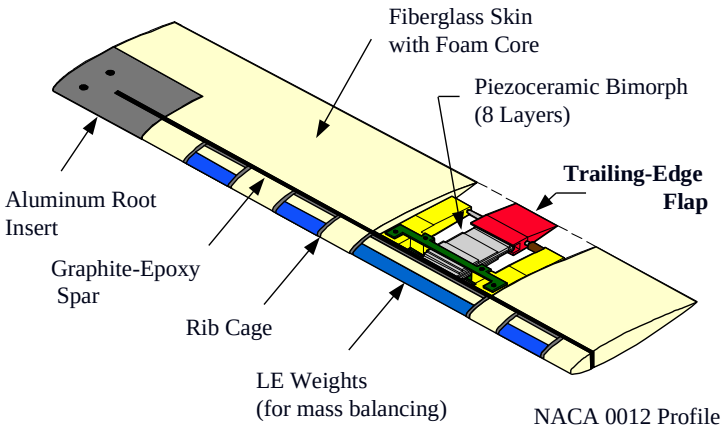

Figure 1.10 Mach scaled active rotor blade with trailing edge flap actuated by piezo-bender elements [98]

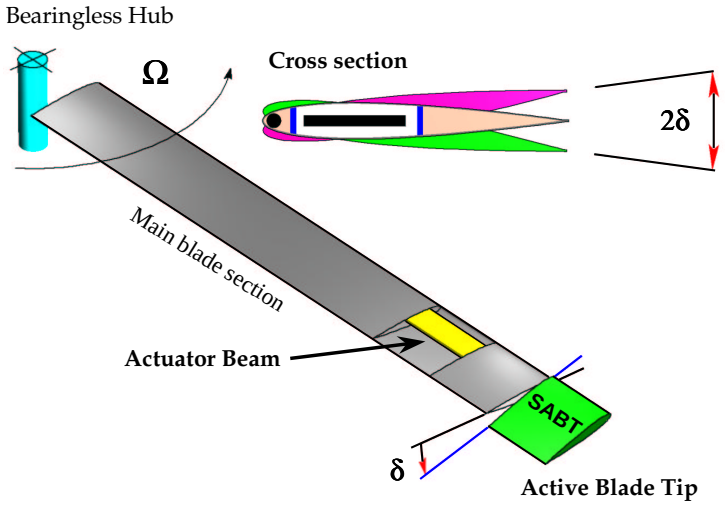

Figure 1.11 Mach scaled rotor blade with Smart Active Blade Tip (SABT) [9]

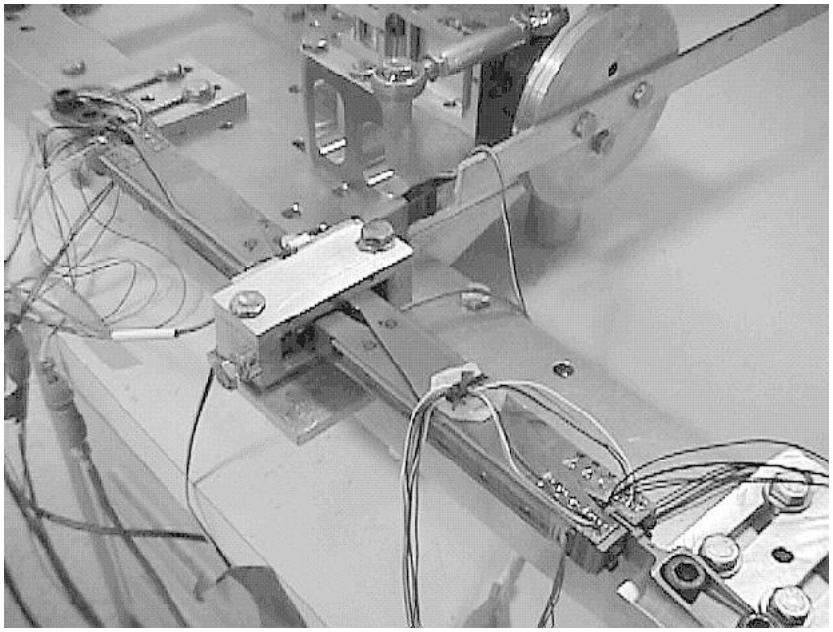

Figure 1.12 X-frame piezostack amplifier [112]

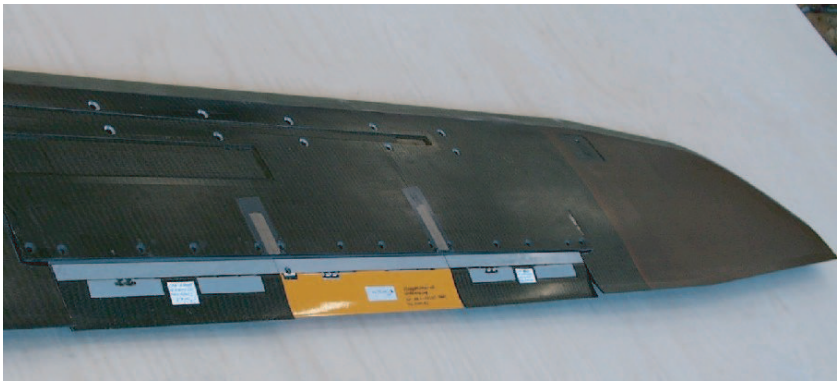

Figure 1.13 Full scale BK117 rotor blade with trailing edge flaps and piezoactuators [128]

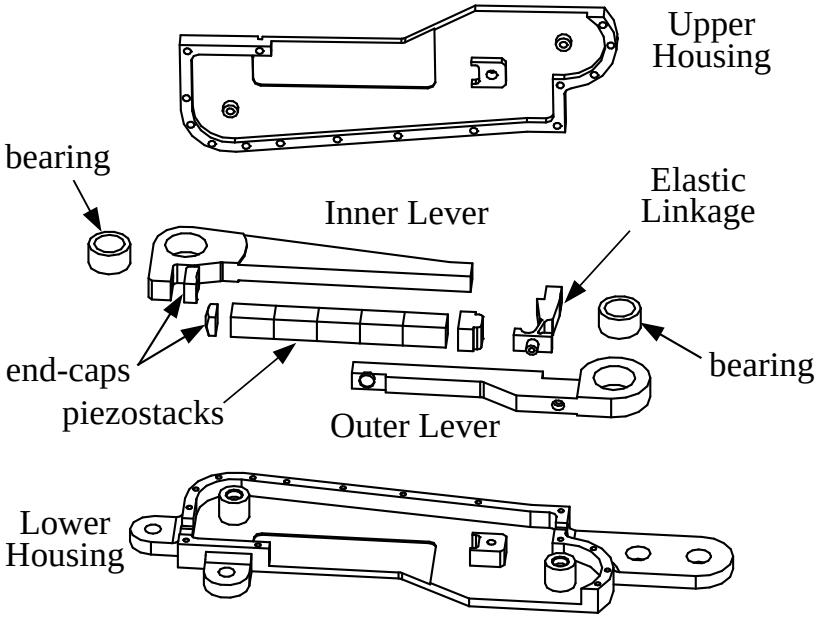

Figure 1.14 L-L Amplification actuator [131]

Chapter 2

Piezoceramic Sheet Actuators

Piezoceramics are potential actuators for a wide range of applications in aerospace, automotive, civil structures, machine tools and bio-medical systems to actively control vibration and noise, improve performance, and augment stability. One of the major barriers for various applications is the stroke of these actuators [57]. To increase induced strain, these actuators are often driven under high electric fields, and sometimes even to extreme limits. In addition to this, the operating condition of the system itself may cause high mechanical loads on the actuator. For example, in rotorcraft applications, actuators placed on rotor blades are exposed to high tensile stresses due to centrifugal forces [58]. Though the piezoelectric material is relatively well behaved and linear at low electric fields and low mechanical stress levels, it shows considerable nonlinearity at high values of electric field and mechanical stress. In order to develop an efficient structural system with piezoceramic actuators, it is necessary to accurately predict the response of the actuators, including magnitude and phase of induced strain, power consumption and integrity under different excitation and loading levels. Currently, mathematical tools to cover a wide range of operating conditions along with reliable test data to validate these tools are not available.

This chapter discusses the behavior of piezoceramic sheet actuators under different

types of excitation and mechanical loading. The testing is driven by the application of these actuators in smart rotor systems. The free strain response of the actuators under DC excitation is experimentally investigated along with the associated drift of the strain over time. The drift phenomenon is especially important in cases of static deflection of control surfaces or blade geometry. The effect of tensile stress on the free strain response is examined, in order to quantify the effect of the high centrifugal forces experienced by actuators mounted on rotor blades. The magnitude and phase of the free strain response of the actuator under different excitation fields and frequencies is measured, and a phenomenological model to predict this behavior is developed and validated experimentally. The power consumption of the actuators, which is very important for sizing the electrical slip ring units, is calculated by an electro-mechanical impedance method. This is then validated by measuring the power consumption of a free actuator and a pair of actuators surface bonded to a host structure. The performance of actuators in a practical application is constrained by depoling limits and dielectric breakdown of the actuator material. These aspects are also discussed in this chapter, along with the feasibility of recovering performance by repoling in the event of accidental depoling. The procedures outlined in this chapter can be applied to any generic actuator in order to obtain preliminary quantitative data about its performance and capabilities. These data would be very valuable for the initial design of a smart system.

2.1 Basic actuation mechanism

A detailed explanation of the piezoelectric effect, structure of a piezoelectric unit cell and other background information can be found in published references. A short description of the basic actuation mechanism is given here for completeness.

The most commonly used type of piezoceramics, Lead Zirconate Titanates (PZTs)

are solid solutions of lead zirconate and lead titanate, often doped with other elements to obtain specific properties. These ceramics are manufactured by mixing together proportional amounts of lead, zirconium and titanium oxide powders and heating the mixture to around 800-1000°C . They then react to form the perovskite PZT powder. This powder is mixed with a binder and sintered into the desired shape. During the cooling process, the material undergoes a paraelectric to ferroelectric phase transition and the cubic unit cell becomes tetragonal. As a result, the unit cell becomes elongated in one direction and has a permanent dipole moment oriented along its long axis (c-axis). A typical PZT unit cell is shown in Figure 2.1. A volume of the material in which the polar moments of the unit cell are all oriented in the same direction is called a domain. The unpoled ceramic consists of many randomly oriented domains and thus has no net polarization.

Application of a high electric field has the effect of aligning most of the domains in such a way that the polar axes of the unit cells are oriented as closely parallel to the applied field as allowed by the crystal structure. This process is called poling and it imparts a permanent net polarization to the ceramic. Since the polar axis (c-axis) of the unit cell is longer than the other two axes (a, b-axes), the reorientation of the domains also creates a permanent mechanical distortion. The polar axes can be reoriented in certain specific directions governed by the crystal symmetry in the presence of a high electric field or mechanical stress. This process is called switching. In the case of tetragonal PZTs, either 90° or 180° switching can occur. The 90° switching is always accompanied by mechanical distortion due to the longer length of the unit cell along the polar axes, while the 180° switching can occur without any distortion. It is also known that an electric field can cause both 180° and 90° domain switching but a mechanical stress can only cause 90° switching. Consequently, a mechanical stress can depole a piezoelectric ceramic but cannot repole it.

The poled ceramic exhibits the direct and converse piezoelectric effects. The converse effect is the deformation of the piezoceramic in response to an electric field and there are three main phenomena causing it. The first one is the piezoelectric effect of the aligned domains. This is the deformation of the unit cell caused by the electric field and is also called the intrinsic effect. The second one is as a result of deformations caused by non-180° domain wall motion and related phenomena. These effects are also called extrinsic effects. Studies in the past [140] have presented evidence to show that extrinsic effects are the major cause of non-linearity and losses in the piezoceramic. The intrinsic contribution to such losses is small. The third one is the electrostriction effect. The electrostrictive deformation is proportional to the square of the electric field and is independent of the direction of the field. The relation between the field and deformation is centrosymmetrical, in contrast to the piezoelectric effect, which is noncentrosymmetrical. The electrostrictive effects are usually much smaller than the other two effects.

The poled piezoceramic can be used as either a sensor or an actuator. As they can be manufactured in various shapes and with electrodes on any desired face, they can be tailored to suit the required application in terms of geometry and deformation behavior. However, all subsequent discussions will remain focussed on piezoceramic sheets, that are used both in sensor mode and actuator mode.

2.2 Piezoelectric constitutive relations

Under small field conditions, the constitutive relations for a piezoelectric ceramic can be written in the form [141]

$$D_i = e_{ij}^{\sigma} E_j + d_{im}^{d} \sigma_m \tag{2.1}$$

$$\varepsilon_k = d_{jk}^{c} E_j + s_{km}^{E} \sigma_m \tag{2.2}$$

where vector D_i of size (3x1) is the electric displacement, ε_k is the strain vector (6x1), E_j is the applied electric field vector (3x1) and σ_m is the stress vector (6x1). The piezoelectric constants are the dielectric permittivity e_{ij}^{σ} of size (3x3), the piezoelectric coefficients d_{im}^{d} (3x6) and d_{jk}^{c} (6x3), and the elastic compliance s_{km}^{E} of size (6x6). The superscripts c and d have been added to differentiate between the converse and direct piezoelectric effects, though in practice, these coefficients are numerically equal. Hence, d_{jk}^{c} is just the transpose of d_{jk}^{d}. The superscripts σ and E indicate that the quantity is measured at constant stress and constant electric field respectively. In the case of a piezoceramic sheet actuator, the poling direction, which is along the thickness, is denoted as the 3-axis. The 1-axis and 2-axis are in the plane of the piezoceramic sheet, and these faces are electroded (Figure 2.2). For such a configuration the d_{jk}^{c} matrix can then be expressed as

$$\mathbf{d} = \begin{bmatrix} 0 & 0 & d_{31} \\ 0 & 0 & d_{32} \\ 0 & 0 & d_{33} \\ 0 & d_{24} & 0 \\ d_{15} & 0 & 0 \\ 0 & 0 & 0 \end{bmatrix} \tag{2.3}$$

where d_{31} and d_{33} relate the normal strain in the 1 (or 2) and 3 directions respectively to a field along the poling direction, E_3, while d_{15} relates the shear strain in the 2-3 and 1-3 planes to the transverse fields, E_1 and E_2. Note that there is no shear in the 1-2 plane. For PZT-5H, $d_{31} = d_{32}$ and the material is considered transversely isotropic piezoelectrically and electricallly. Mechanically, the material is isotropic. On the other hand, a material like Polyvinylidene Flouride (PVDF) is piezoelectrically orthotropic ($d_{31} \neq d_{32}$ and $d_{24} \neq d_{15}$). From the piezoelectric coupling matrix, Equation 2.3, it can be seen that it is not possible to induce shear deformations in the 1-2 plane.

The compliance matrix is of the form

$$\mathbf{s} = \begin{bmatrix} S_{11} & S_{12} & S_{13} & 0 & 0 & 0 \\ S_{12} & S_{22} & S_{13} & 0 & 0 & 0 \\ S_{13} & S_{13} & S_{33} & 0 & 0 & 0 \\ 0 & 0 & 0 & S_{44} & 0 & 0 \\ 0 & 0 & 0 & 0 & S_{55} & 0 \\ 0 & 0 & 0 & 0 & 0 & S_{66} \end{bmatrix} \tag{2.4}$$

and the permittivity matrix is

$$\mathbf{e}^{\sigma} = \begin{bmatrix} e_{11}^{\sigma} & 0 & 0 \\ 0 & e_{22}^{\sigma} & 0 \\ 0 & 0 & e_{33}^{\sigma} \end{bmatrix} \tag{2.5}$$

Equation (2.1) can be considered as the sensor equation and Equation (2.2) as the actuator equation. Actuator applications are based on the converse piezoelectric effect. The actuator is bonded to a structure and an external electric field is applied to it, which results in an induced strain distribution. This chapter will focus on actuators, while sensor applications will be discussed in more detail in Chapter 3.

It should be noted that measurements of piezoelectric coefficients by the direct effect is usually more difficult and less accurate than measurements based on the converse effect. This is because application of a pure uniaxial stress is difficult and some of the charge generated by the application of stress can leak off before it is measured. On the other hand, while using the converse effect, it is much easier to apply a uniform electric field and assure a zero stress state within the sample. It is also difficult to control the electrical boundary conditions during static testing. However, static measurements may be made more accurate by superimposing a low frequency alternating electric field or mechanical stress.

2.3 Experimental sample preparation and cycling

The samples investigated in all the experiments described below were piezoceramic (PZT-5H) sheets of dimension 1” x 0.5” x 0.01” obtained from Morgan Matroc Inc. [142](Figure 2.2). Some of the manufacturer supplied characteristics of this material are shown in Table 2.1. Most of these data are valid only for small excitation fields. However, in using these materials as actuators, they frequently encounter high excitation fields, and as will be discussed in subsequent sections, the material properties can vary significantly from the tabulated small-signal values. All the samples were poled along their thickness. They were excited along the poling direction and strains were measured in a plane perpendicular to the poling direction. Each sample was instrumented with a strain gage with a gage length of 0.125” in a quarter bridge configuration. The excitation leads were soldered to the faces of the sheet and the sample was suspended by means of the excitation leads, so there were no structural boundary constraints. The experimental data shown below represents the average behavior of three randomly selected samples for each test. A careful averaging process was necessary as a variation of properties of upto 15% was found to be not uncommon in the experimental samples. Before the tests were carried out, the samples were cycled to erase the effect of previous excitations. The cycling can be of two types, depending on whether the properties to be observed are static or dynamic.

If the application involves a static excitation, a DC cycling is performed on the actuator. This involves exciting the actuator with its highest operating DC field, switching off the field, and then measuring the residual strain. This process is repeated several times until the residual strain after each cycle has stabilized. A schematic of the actuator strain during the DC cycling process is shown in Figure 2.3. After each cycle, the residual strain keeps decreasing until it becomes almost zero. The number of cycles

d_{31}	$-274\text{x}10^{-12}\text{m/V}$
d_{33}	$593\text{x}10^{-12}\text{m/V}$
d_{15}	$741\text{x}10^{-12}\text{m/V}$
s_{11}^{E}	$16.5\text{x}10^{-12}\text{m}^2/\text{N}$
s_{33}^{E}	$20.7\text{x}10^{-12}\text{m}^2/\text{N}$
s_{44}^{E}	$43.5\text{x}10^{-12}\text{m}^2/\text{N}$
s_{12}^{E}	$-4.78\text{x}10^{-12}\text{m}^2/\text{N}$
s_{13}^{E}	$-8.45\text{x}10^{-12}\text{m}^2/\text{N}$
ρ	$7500\ \text{kg/m}^3$
Curie point	193° C
K_{11}^{σ}	3130
K_{33}^{σ}	3400
Compressive strength	$>$75,000 psi
Static tensile strength	$\sim$11,000 psi
Poling field	$\sim$ 12 kV/cm
Dielectric breakdown	$\sim$ 20 kV/cm
Depoling field (DC)	$\sim$ 5.5 kV/cm

Table 2.1 Small signal PZT-5H characteristics

needed to stabilize the performance depends on the cycling field and normally increases with increasing cycling field. A cycled actuator has an inherent bias and will show almost zero residual strain on the application of an excitation field less than the cycling field. Note that the polarity of the field is important and that reversing the polarity, either during cycling or during operation of the acutator, will destroy the bias. This treatment is therefore suitable only for unipolar operations. If the actuator is exposed to the DC cycling field for a long period of time, it is observed that there is an additional effect of stabilizing the drift, as will be discussed later. Another type of cycling treatment is AC cycling which involves exciting the actuator for several cycles under an AC field. The effect of this treatment is that it removes all biases in the actuator.

2.4 Behavior under static excitation fields

2.4.1 Static free strain

A typical DC field (along the polarized direction) versus transverse free strain (in a plane normal to the polarized direction) plot for a PZT-5H actuator is shown in Figure 2.4. To obtain the static free strain plot, the following steps were taken. DC cycling was initially carried out on the sample to minimize its residual strains. A typical sample required on the order of 10 DC cycles to bring the residual strain to less than $3\mu\varepsilon$. Each point on the curve is then obtained by applying a DC field and measuring the resulting strain with a strain gage. After each reading, the excitation is switched off and the gage is reset. This effectively ignores the hysteresis and drift and generates a quasi-steady free strain curve. The curve is almost linear at low applied electric field levels and the linear piezoelectric coefficients can be used to satisfactorily predict this part of the curve. In this region, the slope of the curve is the coefficient d_{31} and the value quoted by the manufacturer [142] is -274x10^{-12} m/V. The strains predicted by this linear relation are

also plotted for comparision. The negative value of d_{31} means that a positive electric field in the polarization direction results in a compressive strain on the surface of the PZT sheet. At higher electric fields, nonlinear effects become apparent. These effects are attributed to effects like reversible domain wall motion. The reason that such effects are much smaller at lower values of electric field is that non-180° domain wall motion results in a permanent mechanical distortion of the material and consequently requires a larger energy, and hence, occurs at larger field strengths. At high field strengths, a larger change in induced strain per unit increase in field is expected, both for negative and positive fields. Also, strain values for the same positive and negative fields are not equal, which means the free strain curve is asymmetric. Such an asymmetry has also been observed in the inverse piezoelectric response of Rochelles salt [143] and is attributed to the permanent electric polarization in the crystal. The asymmetry present in piezoceramics is small for low values of field but becomes larger as the field is increased. In terms of actual voltage applied to the piezoceramic sheet, a voltage of a 100 Volts corresponds to a field of 3.937 kV/cm.

Figure 2.4(b) shows a free strain curve spanning a much higher field range. The maximum positive field is limited by the breakdown of the dielectric, which in this case is the ceramic itself, whereas the maximum negative field is limited by the piezoceramic depoling, which for PZT-5H, is approximately -5.5 kV/cm.

2.4.2 Effect of external stresses

In the literature, investigations have been carried out to examine the effect of external mechanical stresses on the behavior of piezoceramics. However, most of the existing works are focussed on the effect of compressive loads, since many early applications of piezoceramics were in underwater devices where the materials are exposed to high hydrostatic stresses [144, 145, 146, 147]. Compressive stresses tend to align the c-axes

of the domains perpendicular to the direction of stress. For example, if the compressive stress acts along the X-axis, say in the plane of the sheet, the c-axes of the domains are randomly reoriented parallel to the YZ plane, which is across the thickness. This destroys some of the initial polarization and thus reduces the net polarization. Hard ceramics like PZT-8 and PZT-4 experience large changes in piezoelectric coefficients but show good recovery upon removal of the stress [147]. But soft ceramics like PZT-5H show a permanent degradation in properties with stress cycles.

Limited work has been done to see the effect of tensile stress on the behavior of piezoceramics, which is very pertinent to their application in the development of a smart rotor [148]. Experiments were carried out to observe the effects of tensile loads perpendicular to the poling direction on the free strain. A test fixture was designed to apply tensile loads to a piezoceramic sample while allowing it to strain freely. The ceramic samples tested were 2”x1”x0.01” commercially available PZT-5H sheets. Loads were applied to the sample by means of weights suspended from a sliding bracket (Figure 2.5). The static free strain curves were obtained for different values of applied tensile load. The data obtained from 10 samples were averaged out to obtain the final free strain values. The results are shown in Figure 2.6. From the plot, it can be seen that there is a slight increase in free strain with an increase in applied tensile load. Though this is a very small increase, the averaging process makes it more likely that this is a phenomenological change rather than experimental scatter. It was not possible to apply stresses higher than 2500 psi because of stress concentration near the end supports and a small amount of bending in the sample due to misalignment. Data found in the literature [149, 142] indicate that the static tensile strength of a typical piezoceramic is around 13,000 psi, but samples invariably fracture at a lower average stress.

For PZT-5H under a compressive stress parallel to the poling axis (i.e. along the thickness), d_{31} remains constant or shows a slight increase at low values of stress and

then drops off at high values of stress [150]. Such a stress will tend to randomly reorient the c-axes of the unit cells in a plane perpendicular to the poling direction (i.e. in the plane of the sheet). A uniaxial tensile stress acting along the length of the sheet will also tend to align the dipoles along the plane of the sheet, with a preference along the direction of stress. Hence, it can be expected that these two stress states will produce similar changes in properties of the material. Consequently, the behavior seen in Figure 2.6, with tensile stress in the plane of the piezoceramic sheet is consistent with previously observed phenomena [150] with compressive stress along the poling direction.

A curve was fit to these data points in order to empirically predict the variation of free strain with applied external stresses. The curve fit was of the form

$$\varepsilon = a + bE + cE^2 + dE^3 \tag{2.6}$$

For simplicity, a linear variation of the coefficients *a*, *b*, *c* and *d* with applied tensile stress was fit to the data. This variation is given by

$$a = -1.9637 - 7.039 \times 10^{-4} P \tag{2.7}$$

$$b = -25.82 - 7.54 \times 10^{-4} P \tag{2.8}$$

$$c = -0.1535 + 3.86 \times 10^{-4} P \tag{2.9}$$

$$d = -0.298 - 1.244 \times 10^{-4} P \tag{2.10}$$

where ε is the strain in microstrains, E is the electric field strength in kV/cm and P is the applied tensile stress in psi. As expected, at zero external stress, the free strain curve reduces to that in Figure 2.4(a). The increase in free strain is of the order of 10% at 3.937 kV/cm under a tensile stress of 2500psi.

2.4.3 Drift

An effect often observed experimentally is the drift of the actuator strain in response to a DC excitation. The drift phenomenon is a slow increase of the free strain with time after the application of a DC field. An uncontrolled drift in the actuator position is obviously detrimental to the overall performance of systems wherein the actuator is meant to maintain a certain static deflection, for example the steady deflection of a trailing edge flap. The basic drift phenomenon is as follows: after the application of a DC field, the strain jumps to a certain value and then increases slowly with time. When the field is switched off, the strain falls back to some value and then slowly decreases until it stabilizes at some residual strain. The curves describing both the slow increase and the slow decrease are of a similar nature and are roughly logaritmic with time. One of the piezostack manufacturers [137] has given the following formula for drift of a piezostack actuator

$$\Delta\varepsilon = \Delta\varepsilon_o \left(1 + \gamma \ln \frac{t}{0.1}\right) \tag{2.11}$$

where t is the time in seconds, $\Delta\varepsilon_o$ is the strain 0.1 seconds after the application of the field and γ is a factor which depends on the system's characteristics, typically of the order of a few percent. Note that the percentage increase in strain after the application of the field is independent of the field strength. Experimental observations on a PZT sheet (Figure 2.7(a)) shows a family of drift curves for DC excitation fields from 0.4 kV/cm to 5.5 kV/cm. The experimental data show that the percentage drift is roughly the same regardless of excitation field. Figure 2.7(b) shows the percentage drift in response to a positive and a negative field of the same magnitude, 4 kV/cm. It can be concluded that the direction of applied field has negligible effect on the magnitude or the rate of strain drift.

Similar phenomena have been observed during investigations on Rochelle's

salt [143]. This gives reason to believe that the drift phenomenon is largely intrinsic in nature. The reason for the drift is probably due to a gradual change in the permanent polarization of the material. Such effects also depend on the state of the material as a result of previous mechanical or electrical treatment, referred to as the ”fatigue” effect [143].

In an attempt to stabilize the drift, an AC field of 5% of the steady DC field was superimposed at high as well as low frequencies. The following five different types of excitations were tried out:

(a) 3.937 kV/cm DC field

(b) 0.196 kV_{rms}/cm sinusoidal field at 10 Hz riding on a 3.937 kV/cm DC field

(c) 0.196 kV_{rms}/cm sinusoidal field at 500 Hz riding on a 3.937 kV/cm DC field

(d) 1.968 kV_{rms}/cm sinusoidal field at 500 Hz riding on a 3.937 kV/cm DC field

(e) 3.937 kV/cm DC field on an actuator which was previously exposed to a DC field of the same magnitude for three hours.

The effect of these excitations is shown in Figure 2.8. The percent drift from the instantaneous strain is plotted versus time. After half an hour, the strain signal had increased by approximately 10% to 18%. It can be seen that there is not much change in the drift due to a pure DC field in comparision to those with different superimposed AC fields. The only exception is case (e) where the percent drift is the smallest. The data plotted has been averaged out over three trials. There is some amount of scatter since the repeatability of such drift tests is very sensitive to the previous excitation of the sample. The kind of treatment given to the actuator in case (e) is similar to the fatigue effect, and it appears possible to stabilize drift by exposing the piezoceramic continuously to

a DC field for several hours before the actual excitation. It was also observed that the drift is similarly reduced for any excitation field of magnitude less than the stabilization field. This kind of DC stabilization introduces a bias in the piezoceramic and zeros out residual strains in response to an excitation in the same direction. The bias however, is destroyed on reversing the polarity of the field.

2.5 Behavior under dynamic excitation fields

2.5.1 Strain hysteresis

To observe the losses and the actual hysteretic behavior of the material, a quasi-steady free strain test was performed by changing the field successively from point to point. In contrast to the earlier static free strain curve, the excitation was not switched off and the gage was not zeroed after each reading. At each point, the strain was allowed to stabilize before taking a measurement. The experiments were carried out on several different samples and each point is the average of three measurements. The curve shown in Figure 2.9 was the response of a brand new sample (uncycled). The field was slowly changed in steps of 0.3937 kV/cm. The strain response seems to have some bias and takes around three cycles to stabilize. The same experiment was repeated after exciting the actuator with a moderately high $3.15 kV_{rms}/cm$, 5 Hz sinusoidal field. This is referred to as 'AC cycling' and is done in an attempt to train the actuator to a certain excitation, such that its residual strain and drift are minimized. The quasi-static strain response, shown in Figure 2.10(a) now seems to have less bias and stabilizes in the second cycle itself. The aspect ratio (lateral width to length ratio) of the hysteresis curves is around 15%. Figure 2.10(b) shows the quasi-steady hysteresis curve at a lower maximum field: the aspect ratio becomes smaller. It can be seen that the normalized area under the curve is larger when the maximum field is larger. Also, the curves

are asymmetric with respect to the zero strain axis, which is similar to the asymmetry observed in the static free strain curves and is due to the permanent electric polarization of the ceramic. Another interesting feature is that the curves in Figure 2.10(b) were obtained by starting with a negative excitation whereas the curves in Figure 2.10(a) were obtained by starting with a positive excitation. This difference is seen in the first quarter of the first cycle. The remainder of the curves show no dependence on the sequence of excitation. It can also be seen that the aspect ratio of the quasi-static hysteresis curves increases with peak applied field. This can be attributed to poling effects, that are the gradual change in polarization of the piezoelectric with time when exposed to an external field. This behavior is not seen in AC hysteresis loops, as the poling effect does not have enough time to affect the strain response.

The shape of the strain-field hysteresis loop changes with excitation frequency and field. Figure 2.11(a) shows the variation in the experimentally measured strain-field hysteresis loop at 5 Hz for a free actuator. It can be seen that with increasing field, the overall shape of the curve is not affected much, but the mean slope increases with increasing field. Also plotted for the sake of comparision is the DC free strain curve, which matches closely with the increasing positive excitation and increasing negative excitation segments of the hysteresis curves. This is to be expected, since the DC free strain curve is obtained from the low frequency strain-hysteresis response by ignoring the hysteresis. The dynamic hysteresis curves reduce to the static free strain curve as the frequency of excitation is decreased. The effect of frequency is seen in Figure 2.11(b). These hysteresis curves can be generated using the phenomenological model developed below, which also traces out the static free strain curve when the frequency goes to zero.

2.5.2 Dynamic strain response

To observe the magnitude and phase of the induced strain of a free actuator under AC excitation, the sample was excited by a sinusoidal field stepped from 0 to 200 Hz. This was carried out at different excitation fields to see the effect of excitation field as well as excitation frequency and these results are summarized in Figure 2.12. The dependence of crucial material properties such as e_{33}^{σ} and $\tan\delta$ on the magnitude and frequency of the excitation can be calculated from the magnitude and phase of the current drawn by the actuator. These parameters are very important for predicting the power consumption of actuators bonded to a structure. From Figure 2.12(a), it can be seen that the free strain, and hence, d_{31}, is relatively independent of the actuation frequency. The slight increase seen at higher frequencies is due to an electro-mechanical resonance around 1 kHz. The influence of the resonant dynamics can be seen more clearly in Figure 2.12(b), which is a plot of the phase of the free strain. These dynamics, though important for a free actuator, are of less interest while investigating the performance of actuators bonded to a structure, where the dynamics of the parent structure is dominant. At low frequencies, the free strain increases by approximately 10% due to poling effects. At higher frequencies and excitation fields, nonlinear effects cause the free strain to increase by as much as 15% compared to the free strain in the linear region.

This variation can be described in terms of the following relation

$$V = A\varepsilon + B\dot{\varepsilon} \tag{2.12}$$

where V is the excitation voltage in volts and ε is the free strain of the actuator in microstrain. By analogy with a mechanical spring-damper system, the coefficients A and B can be considered as an effective stiffness and damping respectively. The variation of this stiffness and damping with excitation voltage and field is calculated from the transfer function shown above and curves are fit through the data. The values of the

stiffness and damping are shown in Figure 2.13.

It can be seen that the stiffness depends to a large extent on excitation voltage, as expected, but the frequency dependence is small. A quadratic variation of stiffness with frequency is calculated and is given by

$$A = a f^2 + b f + c \tag{2.13}$$

where f is the frequency of excitation in Hertz, and the coefficients a, b and c are linear functions of the excitation voltage.

$$a = 15.1\text{x}10^{-9}E - 6.09\text{x}10^{-6} \tag{2.14}$$

$$b = -2.59\text{x}10^{-6}E + 1.4\text{x}10^{-3} \tag{2.15}$$

$$c = -2.44\text{x}10^{-3}E + 0.893 \tag{2.16}$$

The variation of damping with field is not significant, especially at higher values of frequency, so the damping is expressed as

$$B = \frac{1.5}{f} \tag{2.17}$$

This expression for damping is equivalent to stating that the energy lost per cycle per unit displacement amplitude is a constant, which is intuitively expected. Using these relations for effective stiffness and damping, the free strain of the actuator can be calculated at any given frequency in the range of 1-200 Hz and excitation voltage in the range 40-140 V. The comparision of experimentally measured free strain with predictions using this phenomenological model is shown in Figure 2.14, where the sample is excited at 80 V_{peak} and 120 V_{peak} at frequencies of 5 Hz, 25 Hz and 100 Hz. It can be seen that at lower frequencies, the damping is underpredicted and at higher frequencies, the damping is overpredicted. This is due to the rather simple

hyperbolic variation of the effective damping parameter assumed in Equation (2.17). A more complicated variation would yield more accurate results, but the accuracy of the present assumption is considered to be within acceptable limits.

It is worth mentioning here that the static free strain values can be obtained from the above equations by first setting $\dot{\varepsilon} = 0$ and then setting $f = 0$. The resulting equation for static free strain is

$$\varepsilon_{static} = \frac{V}{-2.44\text{x}10^{-3}V + 0.893} \tag{2.18}$$

The values of static free strain obtained by this equation are very close to the values obtained from Equation (2.6), though not completely the same. This is because Equation (2.6) represents the static behavior which has an inherent asymmetry between positive and negative excitation voltages due to remnant polarisation effects. This asymmetry decreases as the frequency of excitation increases. However, the model represented by Equation (2.12) assumes a solution which is inherently symmetric. Therefore, for static and low frequency behavior, Equation (2.6) should be used to obtain more accurate results while Equation (2.12) should be used for high frequency behavior.

2.5.3 Effect of DC bias

Several researches have reported the benefecial effects of operating piezoceramic actuators with a DC bias field. A DC bias field increases the value of d_{31} under stress [146]. This can be explained by the fact that a DC bias field has a stabilizing effect on the pinning of the domains [140]. The domains are better aligned under a DC bias and the domain walls become more difficult to move, which effectively reduces the extrinsic contribution to non-linear effects and losses in actuation. Figure 2.15 shows a strain-field hysteresis loop under a pure AC field and under the same AC field with a superimposed positive DC field of strength $0.5\text{V}_{\text{peak}}$. Only the AC component of the

strain is plotted for comparision. It can be seen that the area under the loop is less for the actuation with a bias than without bias. This shows that the losses have decreased due to the application of a DC bias. There is also a small decrease in the magnitude of peak free strain under bias.

2.6 Depoling behavior and dielectric breakdown

Although increasing the applied electric field is necessary in order to obtain larger deformations from the actuator, the magnitude of the electric field is constrained by two limits: depoling and dielectric breakdown. As the electric field applied along the poling direction increases, the dielectric breakdown eventually occurs in the piezoceramic material. However, this field usually corresponds to several hundreds of volts applied to the actuator, and is normally not encountered during operation. A more critical constraint is depoling of the piezoceramic. When exposed to a high electric field opposite to the poling direction, the piezoceramic loses most of its piezoelectric capability. The actuation is accompanied by large dielectric losses and poor effeciency. This is known as depoling of the piezoceramic and is accompanied by a permanent change in dimensions of the sample. This is probably due to large scale domain switching in the material. The DC depoling field of PZT-5H is approximately 5.5 kV/cm. For an AC excitation, the depoling field depends on the frequency. It is observed that under a dynamic excitation, the depoling field of the actuator becomes lower than the DC value. This trend is shown in Figure 2.16. As in other experiments, there is a relatively large scatter because of variations in the samples and their previous excitation history. A curve was fit to the experimental variation of depoling field with frequency.

$$E_{dep} = 2.292 \times 10^{-5}\ f^2 - 1.255 \times 10^{-2}\ f + 5.6 \tag{2.19}$$

where E_{dep} is the AC rms depoling field in kV/cm and f is the excitation frequency in Hertz. Figure 2.17(a) shows the effect of depoling on the actuator strain response. The PZT is excited at $4.7\text{kV}_{\text{rms}}/\text{cm}$ at 100 Hz. This is just at the depoling field, and the PZT usually takes a few seconds to depole, during which the strain-field hysteresis loop transforms slowly into the 'butterfly loop' which indicates that the sample has depoled. This process is accompanied by a rapid increase in current drawn. It can be seen that the area under the depoled loop is more than the area under the non-depoled loop which indicates that the energy losses are much larger in the case of the depoled actuator.

However, the application of an electric field along the initial direction of polarization reorients the domains along the poling direction, thus reversing the depoling action. The sample was depoled and then repoled by exposing it to a DC electric field of 5.9 kV/cm and 7.1 kV/cm for about 5 minutes. The free strain curves before and after repoling are shown in Figure 2.17(b). Though these repoling fields are much less than the initial poling field of the ceramic, which is usually of the order of 12 kV/cm, it is possible to recover most of the performance of the actuator. This may be useful in case of accidental depoling of actuators in smart systems. It was also observed that it is possible to repole the samples by means of exciting it with an AC field that is approximately 90% of the AC depoling field. An interesting observation during this kind of repoling is that after the actuator has depoled, it is necessary to shut off the excitation and let the actuator sit for 3-4 minutes before applying the repoling field. If this is not done, the repoling is not effective. Note that it is more difficult to repole actuators bonded onto structures since the tensile stresses created in the actuator by the application of the repoling field tend to impede domain reorientation. Care should be taken not to exceed the tensile failure stress of the piezoceramic, which will result in cracking of the bonded actuator.

2.7 Summary and conclusions

This chapter outlined a testing and characterization methodology for a commercially available piezoceramic sheet actuator. Such a procedure could also be extended to any generic actuator in order to obtain preliminary design data for a smart system. Several important conclusions can be drawn:

1. The effect of compressive stresses is well known and usually decreases the actuator performance. The effect of tensile stresses perpendicular to the direction of poling is small and increases the free strain of the actuator. An external tensile stress of 2500 psi causes an increase in the actuator free strain of the order of 10% at an excitation field of 3.937 kV/cm. However, during the design of smart systems, it is advisable to keep the stresses on the actuator to a minimum in order to obtain the best performance. Tensile stresses should especially be avoided since the ceramic is quite weak in tension.

2. Design of the actuator for use in DC applications has to take into account the drift phenomenon, which can be as high as 15% for moderately high fields. It appears possible to stabilize the drift by exposing the actuator to higher DC fields before the actual excitation.

3. A simple phenomenological model of the PZT free strain analogous to a mechanical single degree of freedom spring damper system is developed and validated experimentally.

4. A DC bias is beneficial during the AC operation of the actuators, since it reduces losses in the actuator. The application of a DC bias during actuation offers the added advantage of operating without as much danger of depoling the material as in a pure AC application.

5. Depoling of the actuators is a major problem in smart systems, especially since the depoling field decreases with excitation frequency. It is possible to repole the actuators by application of a positive DC field or an AC field. The recommended repoling technique is the application of an AC field along with a large positive DC bias. It should however be noted that while repoling actuators bonded onto structures, tensile stresses are induced in the actuator which might cause it to crack if the repoling field is too high. In such cases, repoling with an AC field along with a smaller DC bias may be appropriate.

The next chapter will address the direct piezoelectric effect, specifically the use of these piezoceramic sheets as sensors. The possibility of using the same element as both an actuator and a sensor is very advantageous for collocated control. A more detailed discussion of power consumption of the actuator, and methods to reduce the current drawn by the actuator, can be found in Chapter 4.

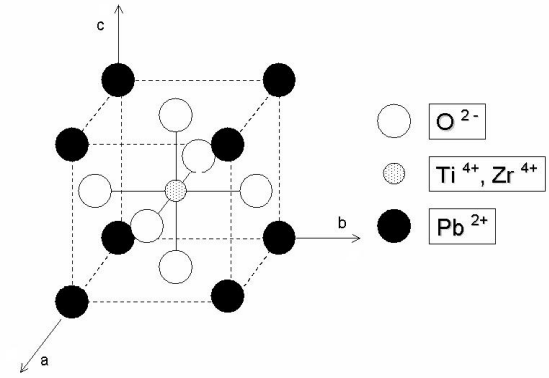

Figure 2.1 Typical PZT unit cell

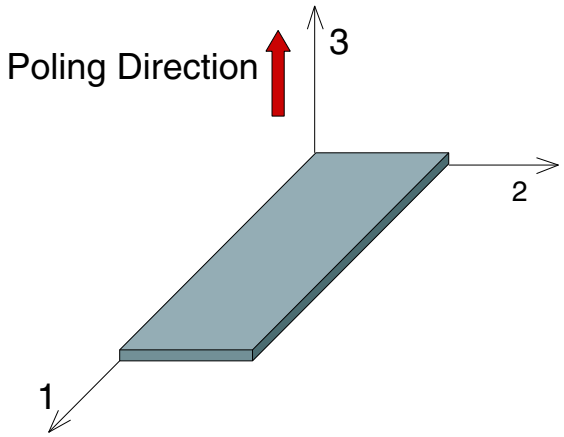

Figure 2.2 Piezoceramic sheet

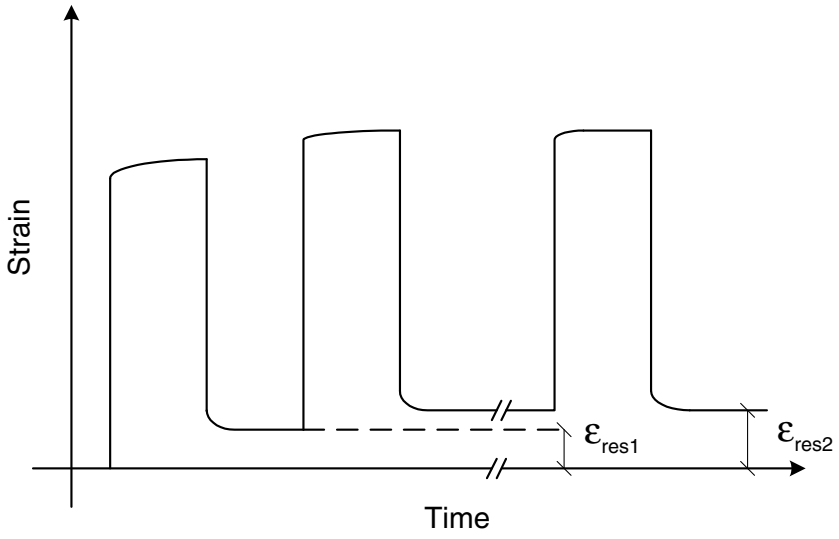

Figure 2.3 Strain during DC cycling

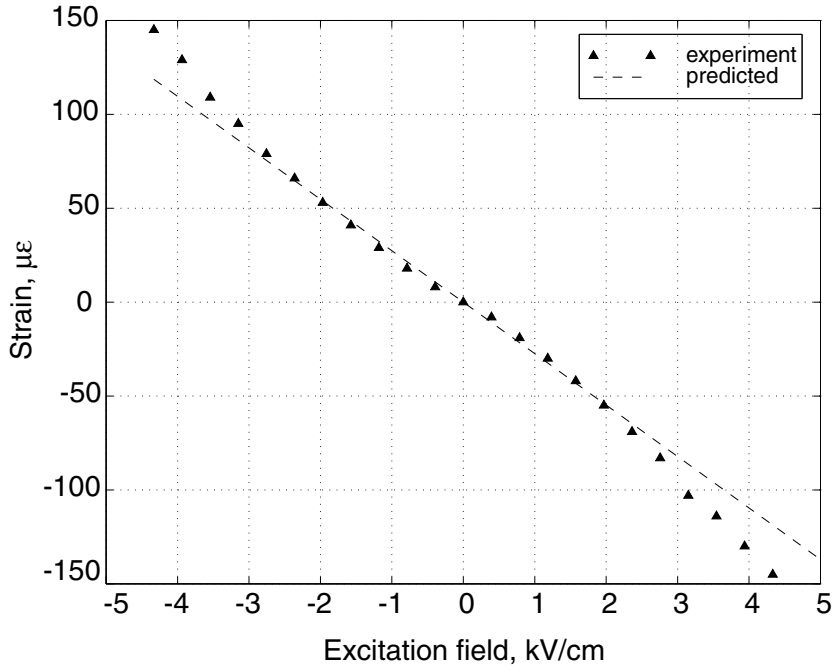

(**a**)Low excitation fields

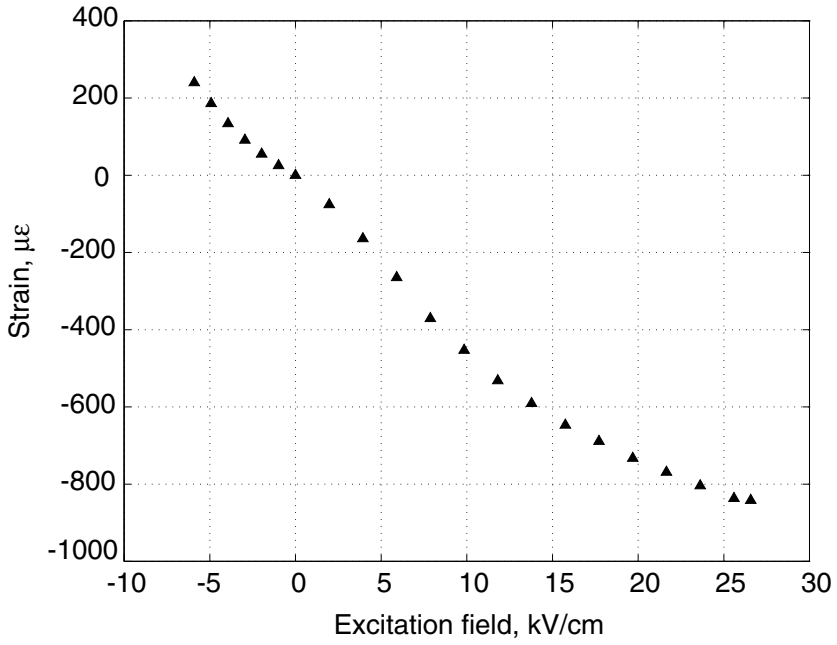

(**b**)High excitation fields

Figure 2.4 Static free strain behavior of PZT-5H

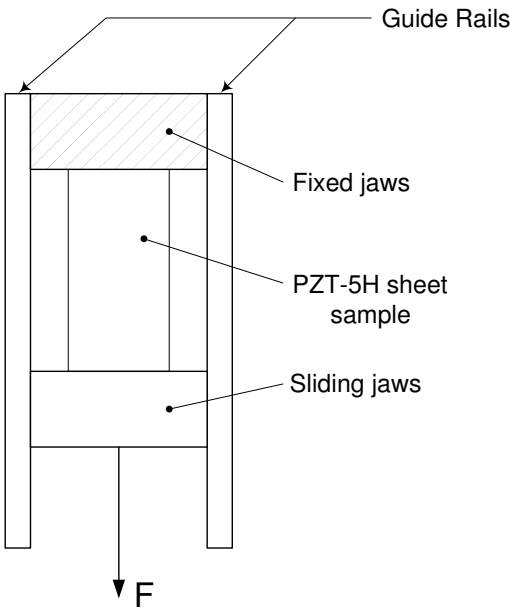

Figure 2.5 Tensile testing fixture

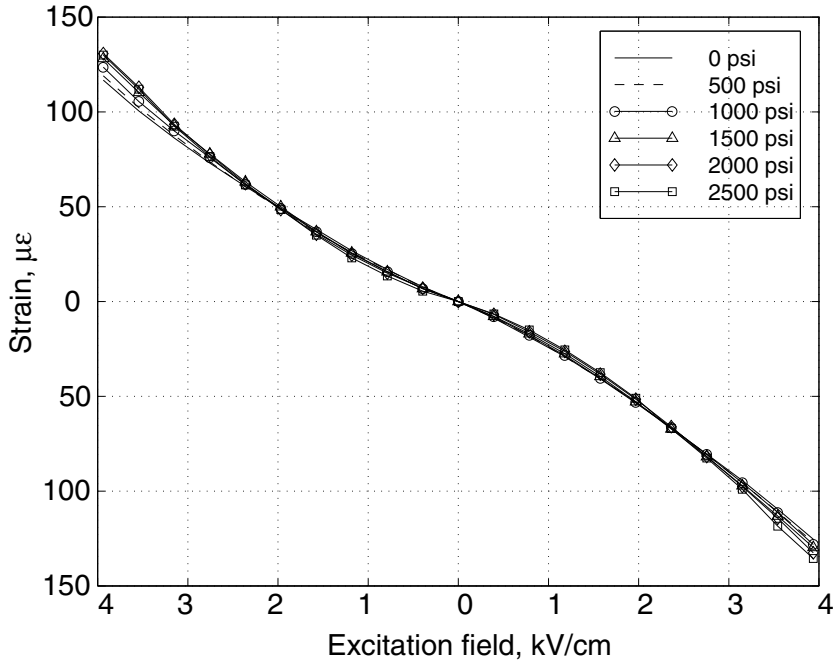

Figure 2.6 Variation of static free strain with transverse tensile stress

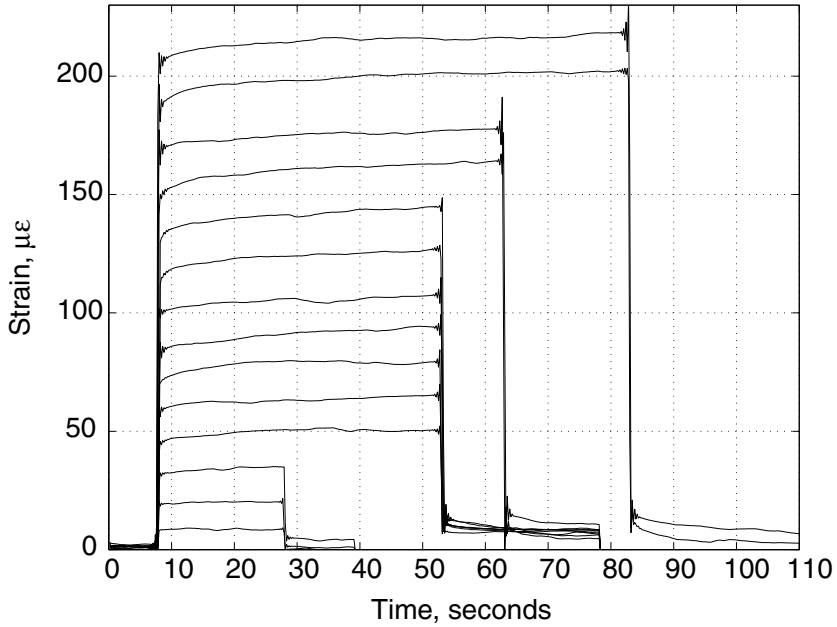

(**a**)Drift in the free strain

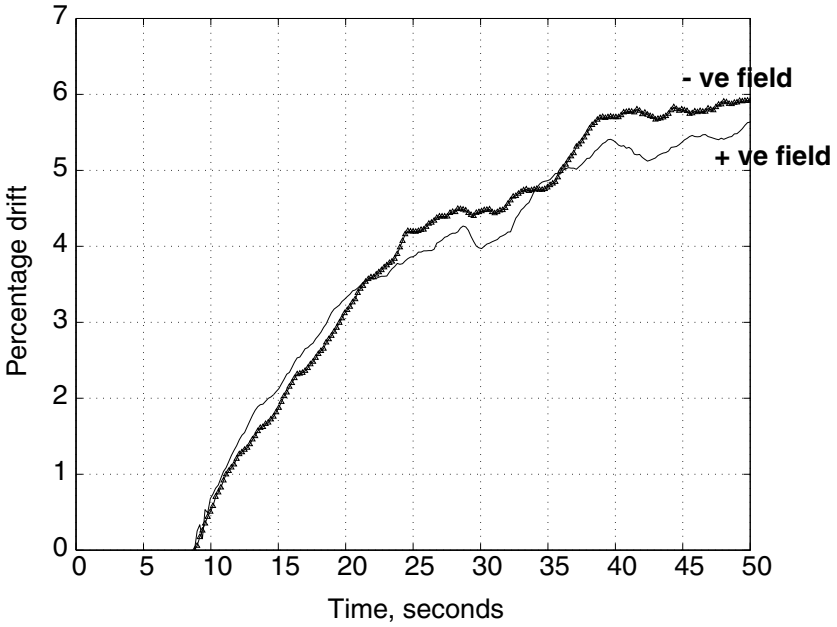

(**b**)Effect of field direction

Figure 2.7 Static strain drift behavior

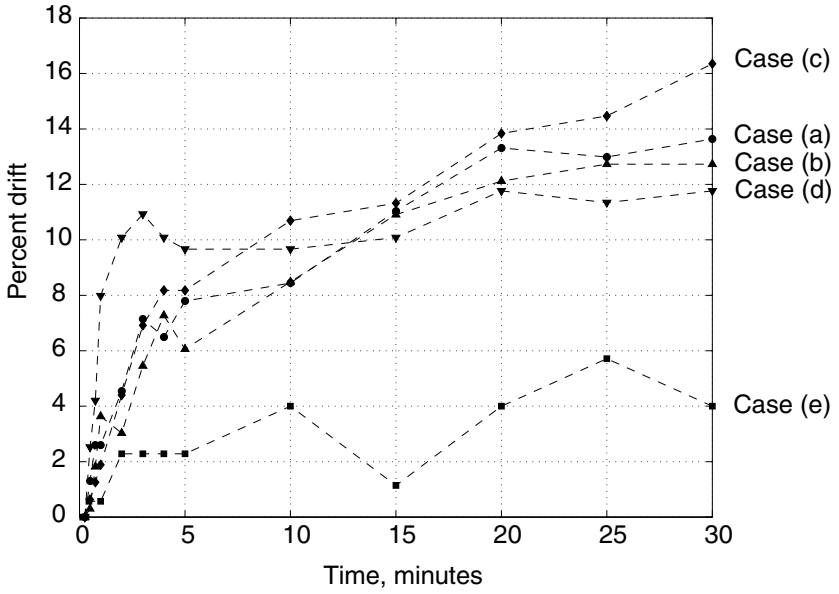

Figure 2.8 Drift under combined excitation

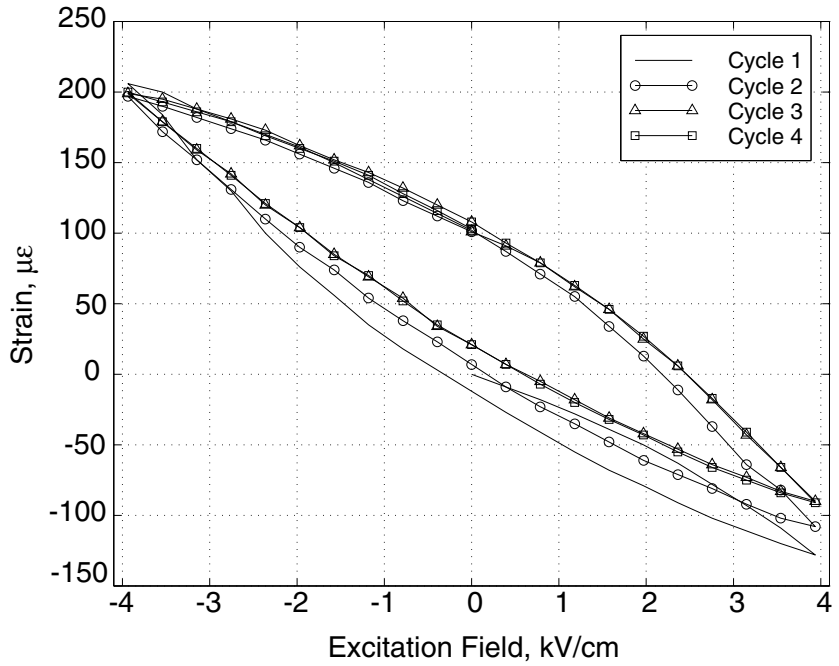

Figure 2.9 Quasi-static hysteresis curve, uncycled PZT

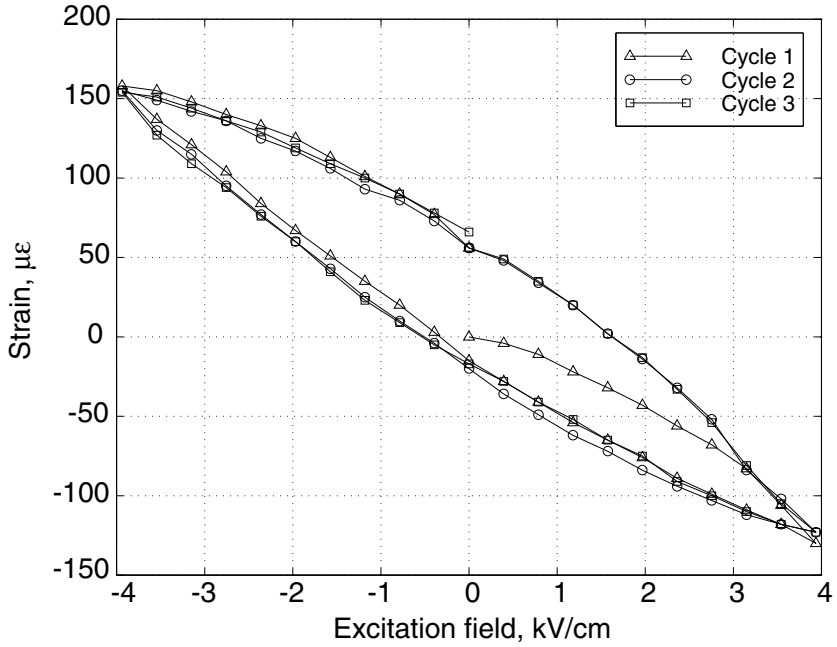

(**a**)Maximum field=3.937 kV/cm

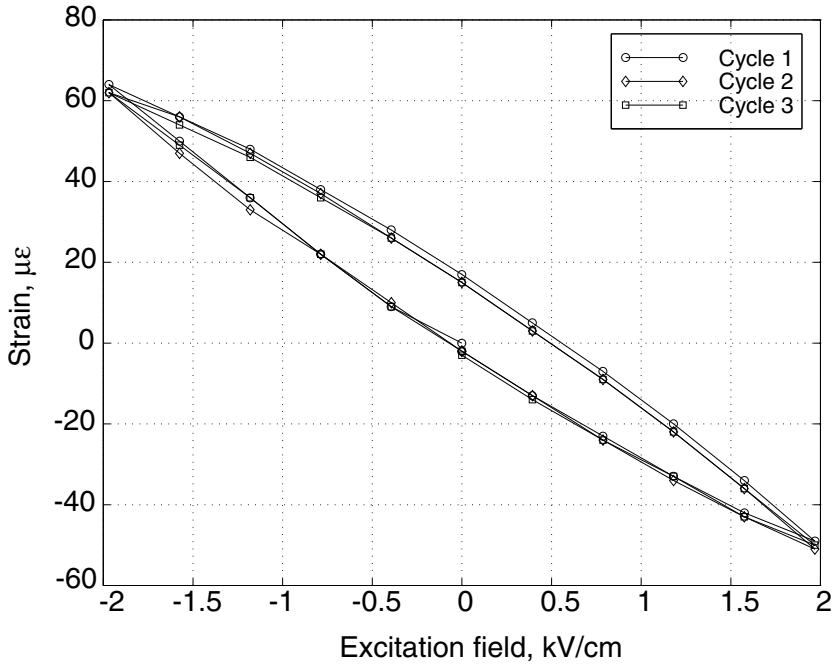

(**b**)Maximum field=1.968 kV/cm

Figure 2.10 Quasi-static hysteresis curves, after AC cycling

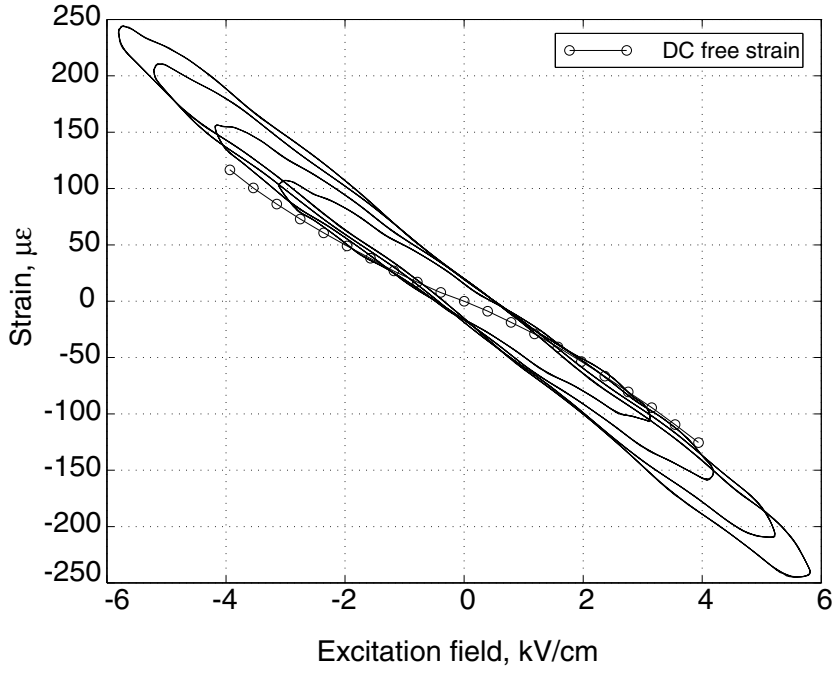

(**a**)Effect of increasing field, 5 Hz

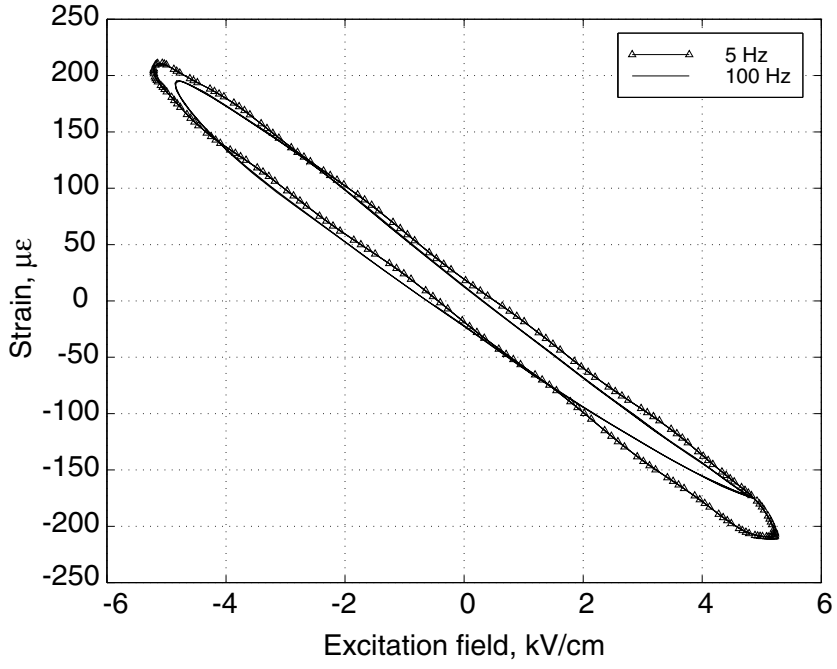

(**b**)Effect of increasing frequency

Figure 2.11 Variation of strain hysteresis with field and frequency for a free actuator

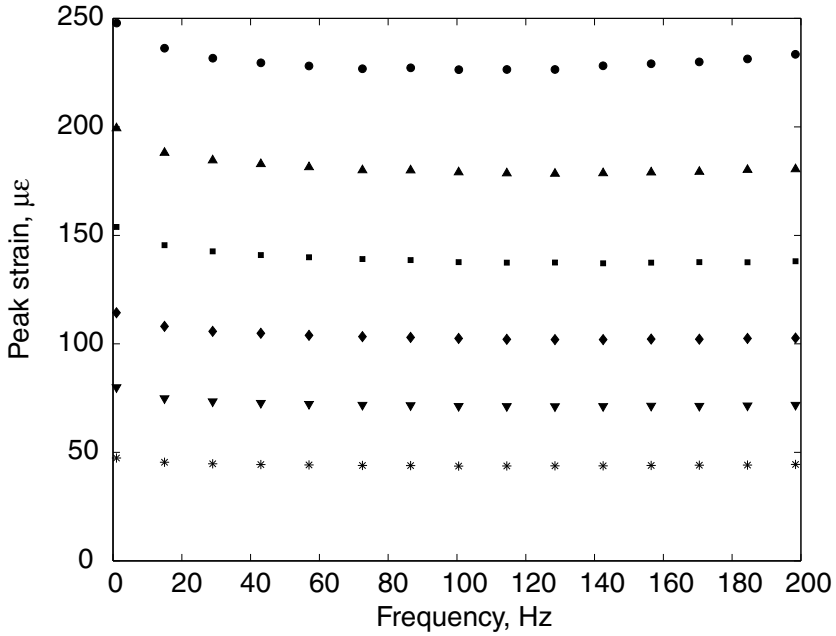

(**a**)Peak free strain

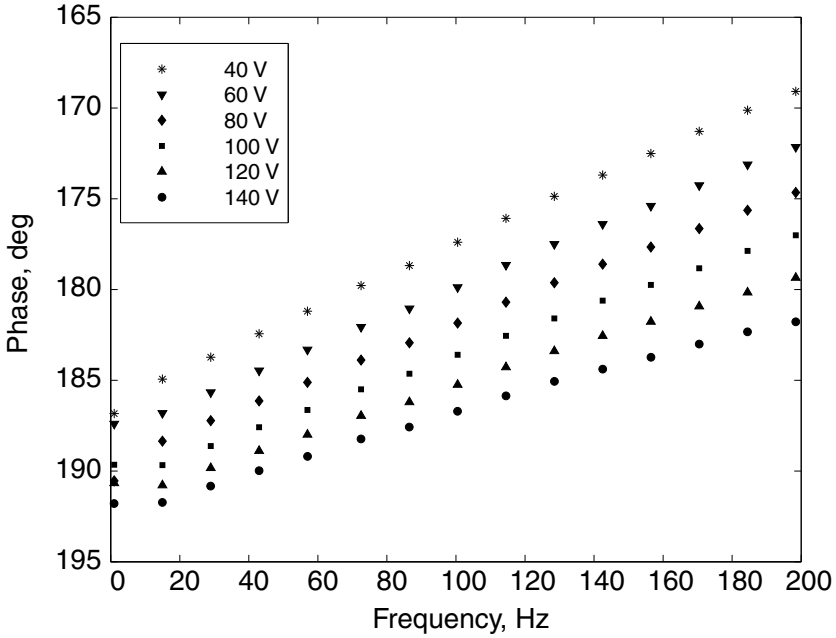

(**b**)Strain phase

Figure 2.12 Response of a free PZT actuator

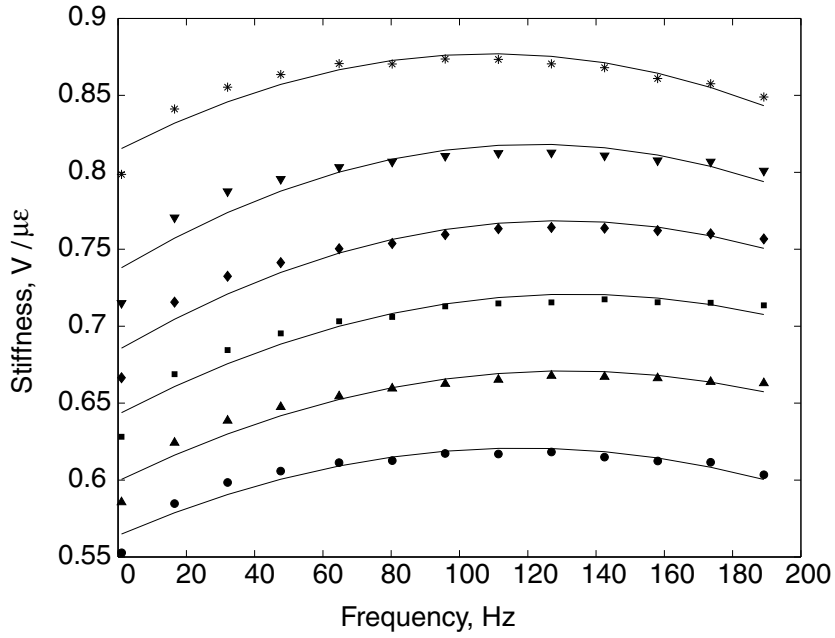

(**a**)Effective stiffness coefficient, *A*

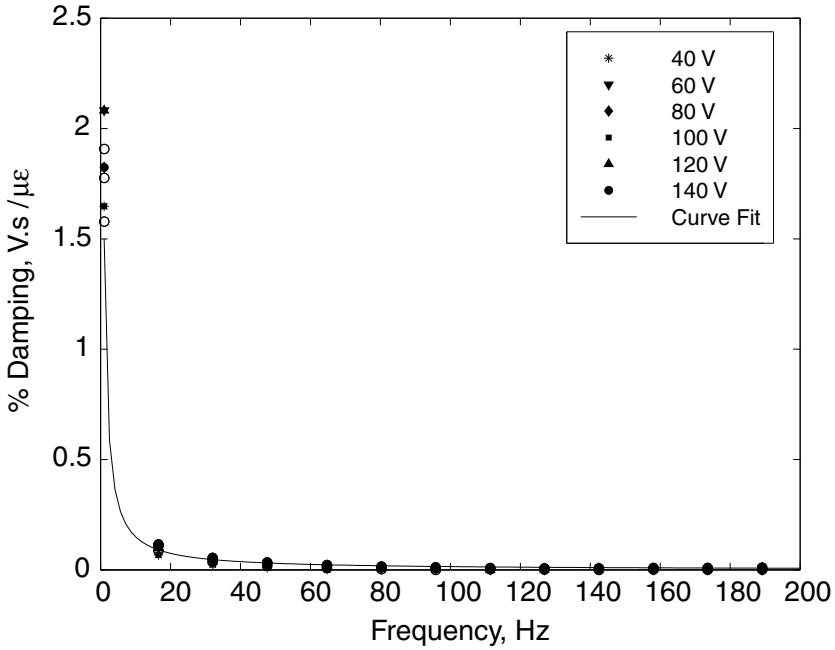

(**b**)Effective damping coefficient, *B*

Figure 2.13 Effective stiffness and damping variation, PZT-5H

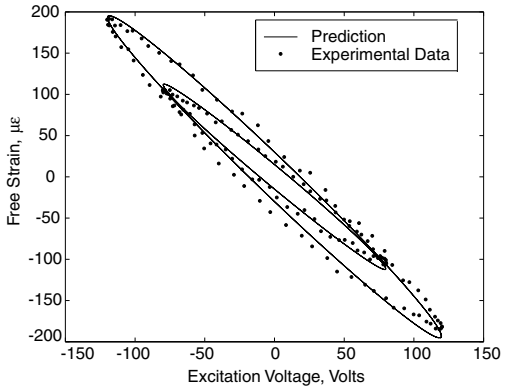

(**a**)5 Hz

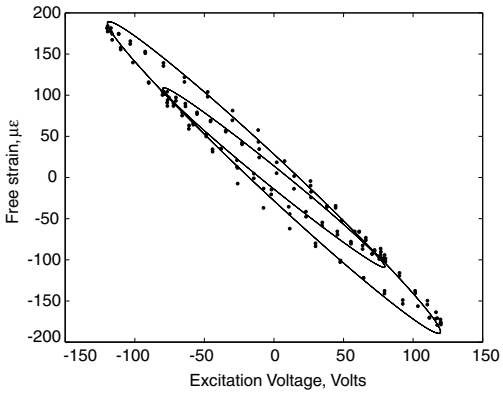

(**b**)25 Hz

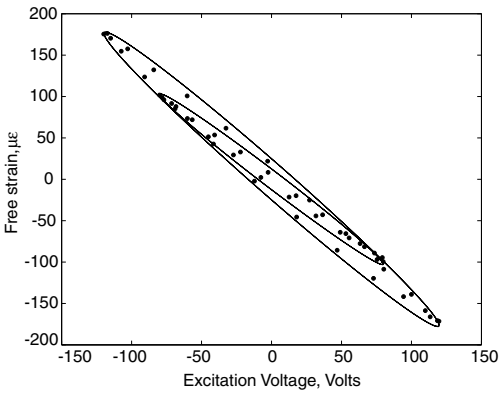

(**c**)100 Hz

Figure 2.14 Model validation at three different frequencies and two excitation voltages of 80 V_{peak} and 120 V_{peak}

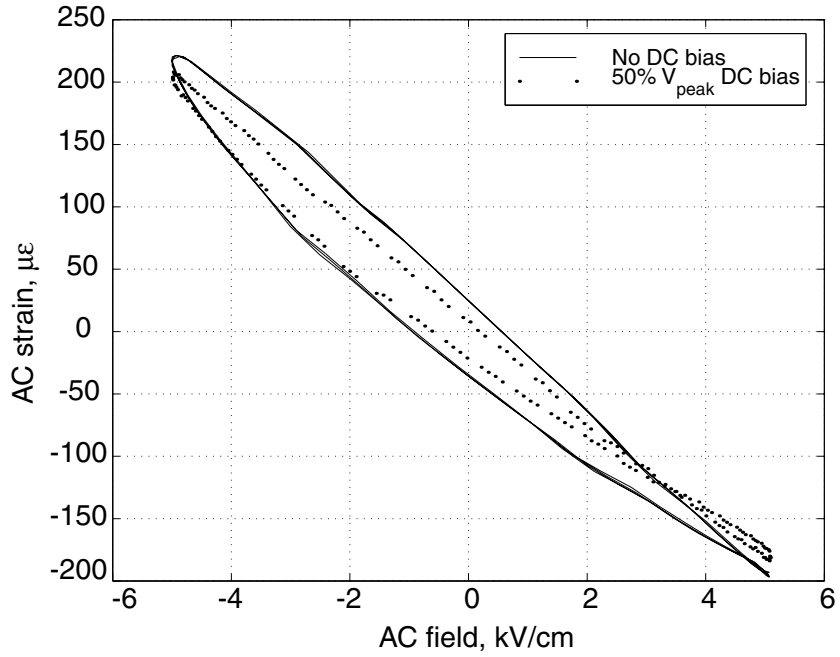

Figure 2.15 Effect of a DC bias field

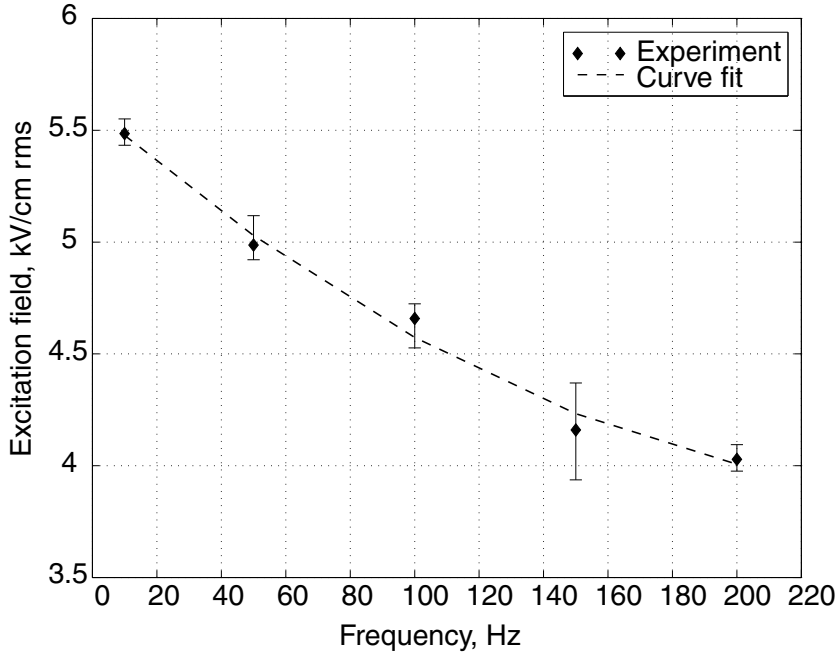

Figure 2.16 Variation of depoling field with excitation frequency

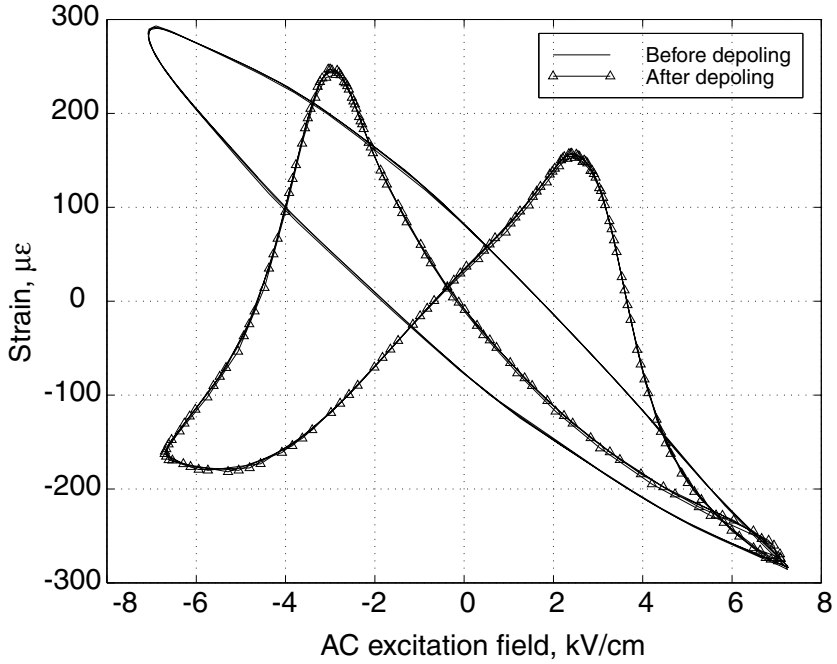

(**a**)Comparison of depoled and non-depoled strain response

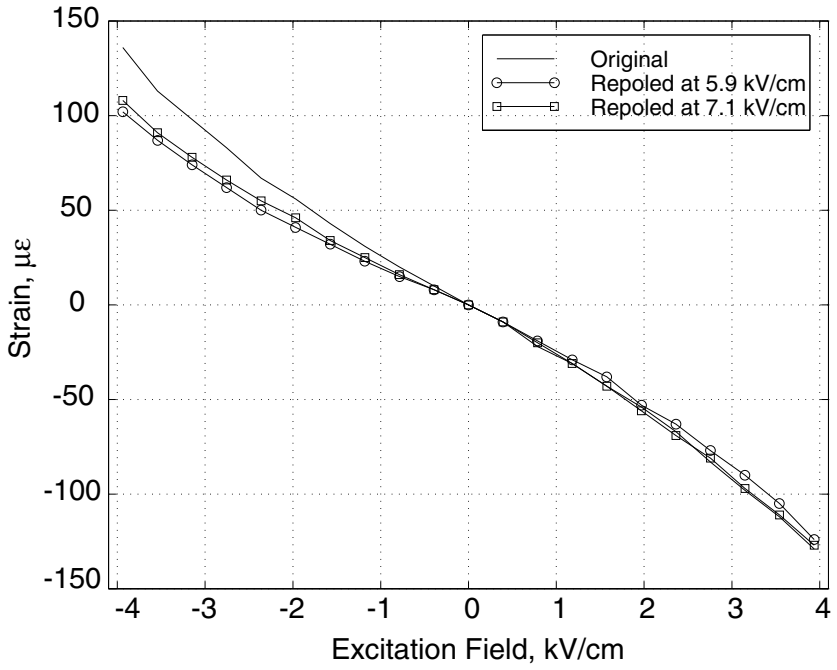

(**b**)Repoling effectiveness

Figure 2.17 Depoling behavior

Chapter 3

Piezoelectric Sensors

3.1 Introduction

Piezoelectric elements are commonly used in smart structural systems as both sensors and actuators [57]. A key characteristic of these materials is the utilization of the converse piezoelectric effect to actuate the structure in addition to the direct effect to sense structural deformation. Typically, piezoceramics are used as acutators and polymer piezo films are used as sensing materials. It is also possible to use piezoceramics for both sensing and actuation, as in the case of self sensing actuators [151]. Many researchers have used piezoceramic sheet elements as sensors in controllable structural systems [152] and also in health monitoring applications [153]. Most of these applications rely on the relative magnitudes of either the voltage or rate of change of voltage generated by the sensor, or the frequency spectrum of the signal generated by the sensor. Several investigations have been carried out on discrete piezoelectric sensor systems [152], active control of structures with feedback from piezoelectric sensors [154], and collocated sensors and actuators [151, 155]. However, limited attempt has been made to accurately calibrate the magnitude of the measured sensor voltage with actual structural strain.

Piezoelectric strain rate sensors have been investigated by [156] and [157] wherein their superior noise immunity as compared to differentiated signals from conventional foil gages has been demonstrated. The correlation between the piezoelectric gage reading and the foil gage measurement is quite good; however the comparison was performed only at one frequency, 25 Hz.

This chapter discusses the behavior of piezoelectric elements as strain sensors. Strain is measured in terms of the charge generated by the element as a result of the direct piezoelectric effect. Strain measurements from piezoceramic (PZT-5H) and piezofilm (PVDF) sensors are compared with strains from a conventional foil strain gage and the advantages of each type of sensor are discussed, along with their limitations. The sensors are surface bonded to a beam and are calibrated over a frequency range of 5-500 Hz. Correction factors to account for transverse strain and shear lag effects due to the bond layer are analytically derived and experimentally validated. The effect of temperature on the output of PZT strain sensors is investigated. Additionally, design of signal conditioning electronics to collect the signals from the piezoelectric sensors is addressed. The superior performance of piezoelectric sensors compared to conventional strain gages in terms of sensitivity and signal to noise ratio is demonstrated.

In addition to the possibility of performing collocated control, such actuators/sensors have other advantages such as compactness, sensitivity over a large strain bandwidth and ease of embeddability for performing structural health monitoring as well as distributed active control functions concurrently. These features, combined with the extremely good signal to noise ratio of piezoelectric sensors, make them ideally suited for smart rotor applications.

3.2 Basic sensing mechanism

A description of the basic piezoelectric mechanism was given in Section 2.1. The constitutive relations for a piezoelectric material can be rewritten as

$$\begin{bmatrix} \mathbf{D} \\ \varepsilon \end{bmatrix} = \begin{bmatrix} \mathbf{e}^{\sigma} & \mathbf{d}^{\mathbf{d}} \\ \mathbf{d}^{\mathbf{c}} & \mathbf{s}^{\mathbf{E}} \end{bmatrix} \begin{bmatrix} \mathbf{E} \\ \sigma \end{bmatrix} \tag{3.1}$$

The stress vector is written as

$$\sigma = \begin{bmatrix} \sigma_1 \\ \sigma_2 \\ \sigma_3 \\ \sigma_4 \\ \sigma_5 \\ \sigma_6 \end{bmatrix} = \begin{bmatrix} \sigma_{11} \\ \sigma_{22} \\ \sigma_{33} \\ \sigma_{23} \\ \sigma_{31} \\ \sigma_{12} \end{bmatrix} \tag{3.2}$$

Sensor applications are based on the direct effect (Equation (2.1)). The sensor is exposed to a stress field, and generates a charge in response, which is measured. In the case of a sensor, where the applied external electric field is zero, Equation (3.1) becomes

$$\begin{bmatrix} D_1 \\ D_2 \\ D_3 \end{bmatrix} = \begin{bmatrix} 0 & 0 & 0 & 0 & d_{15} & 0 \\ 0 & 0 & 0 & d_{24} & 0 & 0 \\ d_{31} & d_{32} & d_{33} & 0 & 0 & 0 \end{bmatrix} \begin{bmatrix} \sigma_1 \\ \sigma_2 \\ \sigma_3 \\ \sigma_4 \\ \sigma_5 \\ \sigma_6 \end{bmatrix} \tag{3.3}$$

This equation summarizes the principle of operation of piezoelectric sensors. A stress field causes an electric displacement to be generated Equation (3.3) as a result of the direct piezoelectric effect. Note that shear stress in the 1-2 plane, σ_6 is not capable of generating any electric response.

The electric displacement **D** is related to the generated charge by the relation

$$q = \iint \begin{bmatrix} D_1 & D_2 & D_3 \end{bmatrix} \begin{bmatrix} dA_1 \\ dA_2 \\ dA_3 \end{bmatrix} \tag{3.4}$$

where dA_1, dA_2 and dA_3 are the components of the electrode area in the 2-3, 1-3 and 1-2 planes respectively. It can be seen that the charge collected, q, depends only on the component of the infinitesimal electrode area **dA** normal to the displacement **D**. The charge q and the voltage generated across the sensor electrodes V_c are related by the capacitance of the sensor, C_p as

$$V_c = q/C_p \tag{3.5}$$

Therefore, by measuring the charge generated by the piezoelectric material, from Equations (3.3) and (3.4), it is possible to calculate the stress in the material. From these values, knowing the compliance of the material, the strain in the material is calculated.

The piezoceramic sensors used in this work are all in the form of sheets (Figure 2.2), with its two faces coated with thin electrode layers. The 1 and 2 axes of the piezoelectric material are in the plane of the sheet. In the case of a uniaxial stress field, the correlation between strain and charge developed is simple. However, for the case of a general plane stress distribution in the 1-2 plane, this correlation is complicated by the presence of the d_{32} term in the $\mathbf{d}^{\mathbf{d}}$ matrix.

While any piezoelectric material can be used as a sensor, the present study is focused to two types of piezoelectric materials, and they are piezoceramics and polymer piezoelectric film. The characteristics of each type of material are discussed below.

3.2.1 PZT sensors

PZT sensors exhibit most of the characteristics of ceramics, namely a high elastic modulus, brittleness and low tensile strength. The material itself is mechanically isotropic, and by virtue of the poling process, is assumed transversely isotropic in the plane normal to the poling direction as far as piezoelectric properties are concerned. This means that for PZT sensors, $s_{11} = s_{22}$, $s_{13} = s_{23}$, $s_{44} = s_{55}$, $d_{31} = d_{32}$ and $d_{15} = d_{24}$.

3.2.2 PVDF sensors

PVDF is a polymer (Polyvinylidene Flouride), consisting of long chains of the repeating monomer $(-CH_2 - CF_2 -)$. The hydrogen atoms are positively charged and the flourine atoms are negatively charged with respect to the carbon atoms and this leaves each monomer unit with an inherent dipole moment. PVDF film is manufactured by solidification of the film from a molten phase, which is then stretched in a particular direction and finally poled. In the liquid phase, the individual polymer chains are free to take up any orientation and so a given volume of liquid has no net dipole moment. After solidification, and stretching the film in one direction, the polymer chains are mostly aligned along the direction of stretching. This, combined with the poling, imparts a permanent dipole moment to the film, which then behaves like a piezoelectric material.

The process of stretching the film, which orients the polymer chains in a specific direction, renders the material piezoelectrically orthotropic, which means $d_{31} \neq d_{32}$ and $d_{15} \neq d_{24}$. The stretching direction is taken as the 1-direction. For small strains, however, the material is considered mechanically isotropic.

The typical characteristics of PZT and PVDF are compared in Table 3.1. The Young's modulus of the PZT material is comparable to that of aluminum, whereas that of PVDF is approximately 1/12th that of aluminum. It is therefore much more

	PZT-5H	**PVDF**
Youngs Modulus (GPa)	71	4-6
d_{31} (pC/N)	-274	18-24
d_{32} (pC/N)	-274	2.5-3
d_{33} (pC/N)	593	-33
e_{33} (nF/m)	30.1	0.106

Table 3.1 Typical properties at 25 °C

suited to sensing applications since it is less likely to influence the dynamics of the host structure as a result of its own stiffness. It is also very easy to shape PVDF film for any desired application. These characteristics make PVDF films more attractive for sensor applications compared to PZT sensors, in spite of their lower piezoelectric coefficients (approximately 1/10th of PZT). Also, PVDF is pyroelectric, and this translates to a highly temperature dependent performance compared to PZT sensors.

3.3 Sensor Calibration

3.3.1 Experimental setup

A dynamic beam bending setup was used to calibrate the piezoelectric sensors. A pair of PZT sheets is bonded at 20 mm from the root of a cantilevered aluminum beam of dimensions 280 x 11 x 1.52 mm, and connected so as to provide a pure bending actuation to the beam. A conventional foil type strain gage is bonded on the beam surface at a location approximately 50 mm from the end of the actuators, and a piezoelectric sensor is bonded at the same location on the other face of the beam so that both sensors are exposed to the same strain field. A sketch of the experimental setup is shown

in Figure 3.1. The strain reading from the foil gage is recorded using a conventional signal conditioning unit and the strain is calculated using standard calibration formulae. The output of the piezoelectric sensor is measured using conditioning electronics and converted to strain. A sine sweep is performed from 5-500 Hz and the transfer functions of the two sensors are compared.

3.3.2 Conversion of voltage output to strain

A typical piezoelectric sheet can be treated as a parallel plate capacitor, whose capacitance is given by

$$C_p = \frac{e_{33}^{\sigma} l_c b_c}{t_c} \tag{3.6}$$

where l_c, b_c and t_c are length, width and thickness of the sensor respectively. The relation between charge stored and voltage generated across the electrodes of the capacitor is given by Equation (3.5). Considering only the effect of strain along the 1-direction, from Equations (3.3), (3.4), (3.5) and (3.6) the voltage generated by the sensor can be expressed as

$$V_c = \frac{d_{31} Y_c b_c}{C_p} \int_{l_c} \varepsilon_1 dx \tag{3.7}$$

Assuming the value of ε_1 to be averaged over the gage length, and defining a sensitivity parameter

$$S_q = d_{31} Y_c l_c b_c \tag{3.8}$$

where Y_c is the Young's modulus of the piezoelectric material. The equation relating strain and voltage generated by the sensor is

$$\varepsilon_1 = \frac{V_c C_p}{S_q} \tag{3.9}$$

The measurement of the voltage V_c is discussed below.

3.3.3 Signal conditioning

The output of the piezoelectric sensor has to be passed through some signal conditioning electronics in order to accurately measure the voltage being developed by the sensor. This is because the piezoelectric sensor typically has a very high output impedance. Most oscilloscopes and data acquisition systems have an input impedance of 1MΩ. The primary purpose of the signal conditioning system is to provide a signal with a low output impedance while simultaneously presenting a very high input impedance to the piezoelectric sensor. There are several ways of achieving this [158, 159]. One way is to short the electrodes of the sensor with an appropriate resistance and measure the current flowing through the resistance by means of a voltage follower. Since current is the rate of change of charge, measuring the current flowing through the sensor is equivalent to measuring the strain rate directly [156, 157]. The procedure followed in the present work is to make use of a charge amplifier to measure the charge generated by the sensor, which is equivalent to measuring its strain.

The signal conditioning circuit used in this investigation is shown in Figure 3.2. The piezoelectric sensor can be modeled as a charge generator in parallel with a capacitance, C_p, equal to the capacitance of the sensor. The cables which carry the signal to the charge amplifier, collectively act as a capacitance C_c in parallel with the sensor. The charge amplifier has several advantages [158]. First, as will be shown below, the charge generated by the sensor is transferred onto the feedback capacitance, C_F. This means that once the value of C_F is known and fixed, the calibration factor is fixed, irrespective of the capacitance of the sensor. Second, the value of the time constant, which is given by $R_F C_F$ can be selected to give the required dynamic frequency range. It is to be noted, however, that there is always some finite leakage resistance in the piezoelectric material, which causes the generated charge to leak off. Therefore, though the time constant of

the circuit can be made very large to enable operation at very low frequencies, it is not possible to determine a pure static condition. This basic physical limitation exists for all kinds of sensors utilizing the piezoelectric effect. Third, the effect of the lead wire capacitance, C_c, which is always present for any physical measurement system, is eliminated. This has the important consequence that there are no errors introduced in the measurements by the lead wires.

Considering only the charge generated by strain in the 1-direction, the current i can be expressed as

$$i = \dot{q} = d_{31} Y_c l_c b_c \dot{\varepsilon_1} \tag{3.10}$$

$$= S_q \dot{\varepsilon_1} \tag{3.11}$$

Assuming ideal operational amplifier characteristics, the governing differential equation of the circuit can be derived to be

$$\dot{V_0} + \frac{V_0}{R_F C_F} = -\frac{S_q \dot{\varepsilon_1}}{C_F} \tag{3.12}$$

which, for harmonic excitation, has the solution

$$\bar{V_0} = -\left(\frac{j\omega R_F C_F}{1 + j\omega R_F C_F}\right) \frac{S_q \bar{\varepsilon_1}}{C_F} \tag{3.13}$$

$$= H(\omega)(-S_q^* \bar{\varepsilon_1}) \tag{3.14}$$

where the quantities with a bar represent their magnitudes, and ω is the frequency of operation. The quantity S_q^* is called the circuit sensitivity, representing the output voltage per unit strain input, and is given by

$$S_q^* = \frac{d_{31} Y_c l_c b_c}{C_F} \tag{3.15}$$

The magnitude and phase of the gain $H(\omega)$ are plotted in Figure 3.3(a) for different values of time constant, while keeping $R_F = 10 M\Omega$. It can be seen that this represents

a high pass filter characteristic, with a time constant $\Theta = R_F C_F$. As discussed before, the value of this time constant can be made very large for low frequency measurements. Another point to be noted is that the sensitivity of the circuit depends inversely on the value of the feedback capacitance, C_F. For a given strain, as the value of C_F decreases, the output voltage V_0 will increase. However, this capacitance cannot be decreased indefinitely. From Equation (3.13), it can be seen that the lower cutoff frequency of the circuit varies directly with C_F. This tradeoff is shown in Figure 3.3(b), assuming a fixed value of R_F of 10MΩ. Though larger time constants are possible with larger values of feedback resistance, it is not practical to increase the value of the feedback resistor R_F beyond the order of tens of megaohms due to various operational constraints. For a time constant of the order of 0.1 seconds, the circuit sensitivity is of the order of 10^4 volts/strain, which translates to an output voltage in the millivolt range in response to a one microstrain input. This sensitivity is achievable in a conventional foil strain gage only after extensive amplification and signal conditioning is incorporated. It can be seen that for larger time constants, the sensitivity drops, which means that as a pure static condition is approached, the output signal becomes weaker. Hence, as discussed before, it is not possible to measure pure static or quasi-static conditions. The major advantage of the charge amplifier comes from the fact that the circuit sensitivity, and therefore, the output voltage is unaffected by the capacitance of the sensor and stray capacitances like the input cable capacitance. The output depends only on the feedback capacitor. This makes it easy to use the same circuit with different sensors without changing the calibration factor.

3.4 Correction factors

It should be noted that the derivation of Equation (3.9) was based on the assumption that only strain in the 1-direction contributed to the charge generated, the effect of other strain components was negligible, and that there is no loss of strain in the bond layer. In reality however, a transverse component of strain exists and there are some losses in the finite thickness bond layer. Hence, the value of strain as calculated by this equation is not the actual strain which is measured by the strain gage. Several correction factors are required to account for transverse strain and shear lag losses in the bond layer. These correction factors are discussed below.

3.4.1 Poisson's ratio effect

The sensor on the beam is in reality exposed to both longitudinal and transverse strains. If the 1-direction is assumed to coincide with the length dimension of the beam and the 2-direction with the width direction of the beam, Equation (3.3) can be rewritten as

$$D = d_{31}Y_{11}\varepsilon_1 + d_{32}Y_{22}\varepsilon_2 \tag{3.16}$$

For a longitudinal stress, there will be a lateral strain due to Poisson's effect at the location of the sensor,

$$\varepsilon_2 = -\nu\varepsilon_1 \tag{3.17}$$

where ν is the Poisson's ratio of the host structure material, which in this case, is aluminum ($\nu = 0.3$). Hence, Equation (3.9) can be rewritten as

$$\varepsilon_1 = \frac{V_o}{K_p S_q^*} \tag{3.18}$$

where K_p is the correction factor due to Poissons effect. For PZT sensors, it can be seen that

$$K_p = (1-\nu) \tag{3.19}$$

for PVDF sensors, K_p is given by

$$K_p = (1 - \nu \frac{d_{32}}{d_{31}}) \tag{3.20}$$

This is a key distinction between piezoelectric sensors and conventional foil gages. The transverse sensitivity of a piezoelectric sensor is of the same order as its longitudinal sensitivity. However, for a conventional strain gage, the transverse sensitivity is close to zero and is normally neglected. Hence, in a general situation, it is not possible to separate out the principal strains of a structure using only one piezoelectric sensor. At least two sensors are required, constructed out of a piezoelectrically or mechanically orthotropic material. Therefore, this rules out the use of PZT sensors where both longitudinal and transverse strain measurements are required. For calibration, the transverse strain is known a priori, which enables the derivation of a correction factor.

3.4.2 Shear lag effect

The derivation of the correction factor to account for shear lag effects caused by a finite thickness bond layer proceeds along the lines of that presented by Crawley and DeLuis [160]. Consider a sensor of length l_c, width b_c, thickness t_c and Young's modulus Y_c bonded onto the surface of a beam of length l_b, width b_b, thickness t_b and Young's modulus Y_b. Let the thickness of the bond layer be t_s [161,162,163]. Assuming the beam to be actuated in pure bending, the forces and moments acting on the beam can be represented as shown in Figure 3.4.

Linear strain distribution across the thickness of the beam is assumed, and the actuator thickness is considered small compared to the beam thickness. The strain is assumed constant across the thickness of the actuator. Force equilibrium in the sensor along the x direction gives

$$\frac{\partial \sigma_c}{\partial x} t_c - \tau = 0 \tag{3.21}$$

and moment equilibrium in the beam gives

$$\frac{\partial \sigma_b}{\partial x} + \tau \frac{3b_c}{b_b t_b} = 0 \tag{3.22}$$

The strains can be related to the displacements by

$$\varepsilon_c = \frac{\partial u_c}{\partial x} \tag{3.23}$$

$$\varepsilon_b = \frac{\partial u_b}{\partial x} \tag{3.24}$$

$$\gamma = \frac{1}{t_s}(u_c - u_b) \tag{3.25}$$

where u_c and u_b are the displacements of the sensor and on the beam surface respectively, and γ is the shear strain in the bond layer.

Substituting Equations (3.23-3.25) in Equations (3.21) and (3.22), and simplifying leads to the relation

$$\frac{\partial^2 \zeta}{\partial x^2} - \left[\frac{G}{Y_c t_c t_s} + \frac{3b_c G}{Y_b b_b t_b t_s} \right] \zeta = 0 \tag{3.26}$$

where G is the shear modulus of the bond layer material and ζ is defined as the quantity $(\varepsilon_c/\varepsilon_b - 1)$. Making the substitution

$$\Gamma^2 = \frac{G}{Y_c t_c t_s} + \frac{3b_c G}{Y_b b_b t_b t_s} \tag{3.27}$$

leads to the governing equation for shear lag in the bond layer

$$\frac{\partial^2 \zeta}{\partial x^2} - \Gamma^2 \zeta = 0 \tag{3.28}$$

The general solution for this equation is

$$\zeta = A \cosh \Gamma x + B \sinh \Gamma x \tag{3.29}$$

with the boundary conditions

$$\text{at } x = 0 \qquad \zeta = -1 \tag{3.30}$$

$$\text{at } x = l_c \qquad \zeta = -1 \tag{3.31}$$

Solving these gives the complete solution as

$$\zeta = \frac{\cosh \Gamma l_c - 1}{\sinh \Gamma l_c} \sinh \Gamma x - \cosh \Gamma x \tag{3.32}$$

This variation is calculated both along the length and the width of the sensor, and the two effects are assumed to be independent, which means effects at the corners of the sensor are neglected. The function is plotted in Figure 3.5(a), along the length, for a PZT sensor of size 6.67 x 3.30 x 0.25 mm and in Figure 3.5(b), for a PVDF sensor of the same length and width, but of a thickness 56μm. The variations are plotted for different values of the bond layer thickness ratio, $\Xi = t_s/t_c$ for both types of sensors. The values of Ξ are calculated by varying the bond layer thickness for a constant sensor thickness. The PVDF sensor shows a much lower shear lag loss than the PZT sensor for a given bond layer thickness ratio. This is due to the combined effect of lower sensor thickness and lower Y_c in the case of PVDF in Equation (3.27). As a result, the shear lag effect is almost negligible for a PVDF sensor.

To quantify the effect of the shear lag, effective dimensions are defined along the length and width of the sensor such that the effective sensor dimensions are subjected to a constant strain, which is the same as the assumed strain on the beam surface. By doing this, the sensor is assumed to be of new dimensions, smaller than the actual geometrical dimensions, over which $\varepsilon_c/\varepsilon_b = 1$ identically. The values of the effective length and width fractions, l_{eff} and b_{eff} respectively, can be obtained by integrating the area under the curves in Figure 3.5. For the sensor under discussion, which had a bond layer thickness of 0.028 mm ($\Xi = 0.112$), the effective length fraction is 0.7646 and the effective width fraction is 0.4975. This means that only approximately 76% of the sensor length and 50% of the sensor width contribute to the total sensed strain. Because the whole geometric area of the sensor is no longer effective in sensing the beam surface strain, these correction factors must be inserted in the calibration equation

Equation (3.9), which becomes

$$\varepsilon_1 = \frac{V_0}{K_b S_q^*} \tag{3.33}$$

where K_b is the correction factor to take care of shear lag effects in the bond layer. The value of K_b is independent of the material properties of the sensor, and is dependent only on its geometry. For both PZT and PVDF sensors, K_b is given by

$$K_b = l_{eff} b_{eff} \tag{3.34}$$

It should be noted here that for a PVDF sensor, the value of K_b is very close to unity (Figure 3.5(b)) and the shear lag effect can be neglected without significant error.

The final conversion relation from output voltage to longitudinal strain is

$$\varepsilon_1 = \frac{V_0}{K_p K_b S_q^*} \tag{3.35}$$

3.5 Experimental results

Experiments were performed on the beam bending setup as described above. For the sine sweeps, the beam was actuated from 5-500 Hz. A conventional 350Ω foil strain gage was used, with a MicroMeasurements 2311 [164] signal conditioning system. For the piezo sensor, a charge amplifier was built using high input impedance LF355 operational amplifiers, with $R_F = 10M\Omega$ and $C_F = 10nF$.

A major advantage of using piezoelectric sensors as opposed to conventional foil strain gages is their superior signal to noise ratio and high frequency noise rejection. Shown in Figure 3.6 is the impulse response from both the conventional foil strain gage and a PZT strain sensor. Both readings were taken simultaneously after the beam was impacted at the tip. Both the responses are unfiltered and show the actual recorded voltages from the signal conditioners. Note the large amplitude background noise in the foil gage output, and the much higher signal to noise ratio of the PZT strain gage.

The foil strain gage operates by sensing an imbalance in a Wheatstone bridge circuit, which is on the order of microvolts. Therefore, at low strain levels, the signal to noise ratio of foil strain gages is quite poor. The superior signal to noise ratio of piezoelectric sensors makes them much more attractive in situations where there is a low strain or high noise level. This can be seen more clearly in Figure 3.7 that shows the frequency response of the beam to a small impulse as recorded by a conventional foil strain gage and a PZT sensor. The spikes in the frequency response at 60 Hz, 120 Hz, 240 Hz, 360 Hz and 420 Hz are overtones of the AC power line frequency. Since the foil strain gage requires an excitation, its output can get contaminated with a component of the AC power line signal. PZT sensors are inherently free from this contamination, however, the signal conditioning circuitry introduces some contamination into the PZT sensor output as well. It is worth mentioning here that the signal conditioning electronics associated with the foil strain gage is much more involved and bulky compared to that used in conjunction with the piezoelectric sensor.

The correlations between strain measured by a conventional strain gage and that measured by a PZT sensor are shown in Figures 3.8-3.10 for a sine sweep ranging from 5 Hz to 500 Hz. Figure 3.8 shows the correlation between the strain measurements from a strain gage and a PZT sensor after the appropriate correction factors are applied. The dimensions of the PZT sensor are 3.5 x 6.0 x 0.23 mm, and the value of C_F for this experiment is 1.1nF. Also shown for comparision is the strain calculated from the PZT sensor readings without application of the correction factors. It can be seen that the correction factors are very significant and after they are applied, there is very good agreement between the strains measured by the strain gage and the PZT sensor. Figure 3.9 shows a frequency sweep response at a very low excitation voltage, such that the strain response is only on the order of several microstrain. The sensor in this case is a PZT sensor of size 6.9 x 3.3 x 0.23 mm. Good correlation is observed over

the whole frequency range, both in matching resonant frequencies as well as magnitude of the measured strain at off-resonant conditions. Hence, it can be concluded that the PZT sensors are capable of accurately measuring both low and high strain levels. It is to be noted that the strain gage is not able to accurately pick out the peak amplitudes at low strain levels. This clearly demonstrates the superiority of piezoelectric sensors in such applications. The error between the foil strain gage and the PZT sensor is at most between 5-10% for off-peak conditions.

Figure 3.10 shows the results of replacing the PZT sensor with a PVDF sensor of size 7.1 x 3.6 x 0.056 mm, at higher strain levels. Again, good correlation is observed for lower frequencies, but at high frequencies, some discrepancy is apparent. Also plotted on the same figure is a prediction of the strain response at the sensor location calculated by an assumed modes method. The theoretical model uses a complex modulus with 3% structural damping. It can be seen that both sensors follow the same trend as that of the theoretical prediction. The discrepancy after the third resonant peak can be explained by a slight error in collocation of the foil strain gage and the PVDF sensor. This difference in position gives rise to a shift in the zeros of the transfer function and the dynamics of these zeros affect the shape of the transfer function in this frequency range. The correlation in Figures 3.8 and 3.9 is better, however, since these tests were carried on a different experimental beam setup.

3.6 General operating considerations

3.6.1 Effect of sensor transverse length

The size of the sensor is chosen on the basis of the desired gage length. The strain measurements from PZT sensors of three different sizes are shown in Figure 3.11. All three sensors have the same gage length of 0.125 inch, which is the same as the gage

length of the foil strain gage also. The width of the sensors is varied and is 0.5 inch in case (a), 0.375 inch in case (b) and 0.25 inch in case (c). It can be seen that there is good correlation between strain gage and piezoelectric sensor irrespective of the sensor size. The primary effect of the sensor size can be seen from Equation (3.15). For a given sensor material, the output depends only on the area of the sensor, $l_c b_c$. A larger sensor would therefore produce a larger sensitivity. Assuming the sensing direction to be along l_c, for a constant gage length, the sensitivity can be increased by increasing the width of the sensor, b_c.

The secondary effect of sensor size can be seen from Equations (3.27) and (3.32). For a given sensor thickness t_c and bond thickness t_s, as the sensor dimensions increase, the shear lag losses decrease and the strain is transferred more efficiently from the surface of the structure to the sensor. The good correlation between PZT sensor strain measurements and conventional foil strain gage measurements irrespective of sensor size validates the theoretically derived shear lag correction factor.

3.6.2 Effect of temperature on sensor characteristics

The properties of all piezoelectric materials vary with temperature. In the case of piezoelectric ceramics, the variation with temperature is highly dependent on the material composition [165]. Both the dielectric permittivity and the piezoelectric coeffecients vary with temperature. Since the charge amplifier effectively transfers the charge from the piezoelectric sensor onto a reference capacitor, the change in dielectric permittivity, and hence, the capacitance of the sensor with temperature has no effect on the sensor output. The only dependence of sensor output on temperature is due to the change in piezoelectric coefficients, as seen from Equation (3.15). As per the datasheets supplied by the manufacturer [142], the magnitude of d_{31} increases by approximately 10% from room temperature (25°C) to 50 °C . Tests were carried out in this temperature

range by placing the entire experimental setup in an environmental chamber. The results are plotted in Figure 3.12, which shows a negligible change in sensor output without the use of any temperature correction factors. PVDF film exhibits pyroelectricity in addition to piezoelectricity, and hence, it has highly temperature dependent properties. PVDF film is sometimes used in temperature sensing. Care must be taken, therefore, to take measurements from PVDF sensors at known temperature conditions, and to use the appropriate values of the constants for calibration.

3.7 Summary and conclusions

Piezoelectric materials show great promise in smart structural sensing applications. Using piezoceramic elements affords the possibility of constructing self-sensing actuators. These can then be used to implement a collocated control scheme, that has been shown to have many advantages. This chapter discussed the basic behavior of piezoelectric sensors and described a method to calibrate them. Several conclusions can be drawn

1. The performance of piezoelectric sensors surpasses that of conventional foil type strain gages, with much less signal conditioning required, especially in applications involving low strain levels, and high noise levels. It is also possible to accurately calibrate these sensors. Using orthotropic materials like PVDF, it is possible to construct strain sensor configurations which enable the separation of different components in a general two dimensional strain distribution. However, it is not advisable to use these sensors to measure strain levels more than the order of 150 microstrain since nonlinearities and change in material properties, especially d_{31}, with stress will affect the accuracy of the calibration.

2. A simple circuit can be used to perform signal conditioning on the output of the

piezoelectric sensor. The sensing system exhibits very good signal to noise output characteristics and its sensitivity can be adjusted by changing a component in the circuit, at the expense of frequency response.

3. For a constant gage length, sensitivity increases with increasing sensor area. Investigation of the effect of temperature conditions on the sensor response indicates that the output of the sensor needs no temperature correction over a moderate range of operating temperatures inspite of the fact that the piezoelectric coefficients are strongly temperature dependent.

4. The best strain sensitivity can be achieved by making the sensor area as large as possible, with the constraint of selecting an appropriate gage length for the application. It should also be pointed out that the sensor adds stiffness to the structure, and this additional stiffness increases with sensor size. This can be a significant factor in the case of PZT sensors, but will be normally negligible for PVDF sensors.

5. Good correlation with foil strain gage measurements has been demonstrated and the application of correction factors to the piezoelectric sensor output has been validated. It can be concluded that piezoelectric strain sensors are a simple, easy to use and reliable alternative to conventional resistance based foil strain gages in many applications.

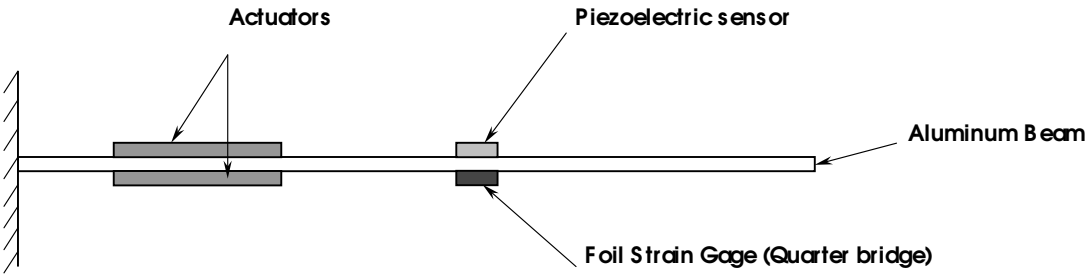

Figure 3.1 Calibration setup

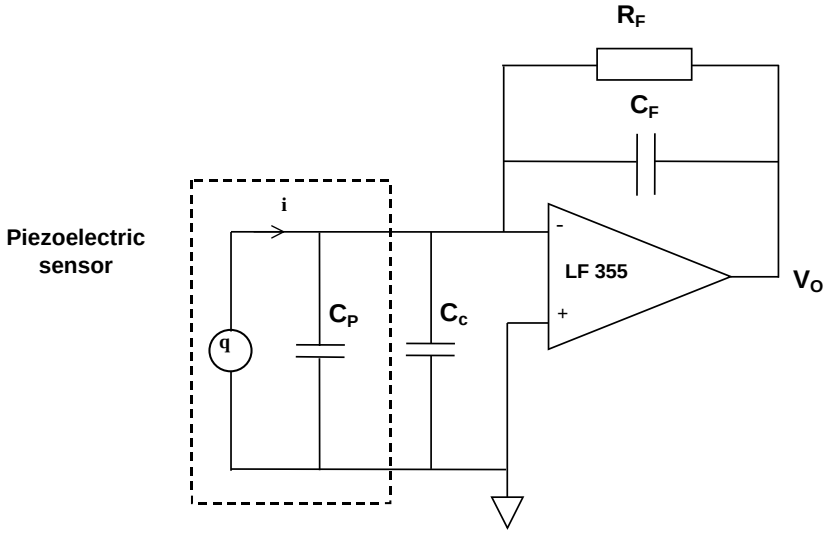

Figure 3.2 Charge amplifier circuit

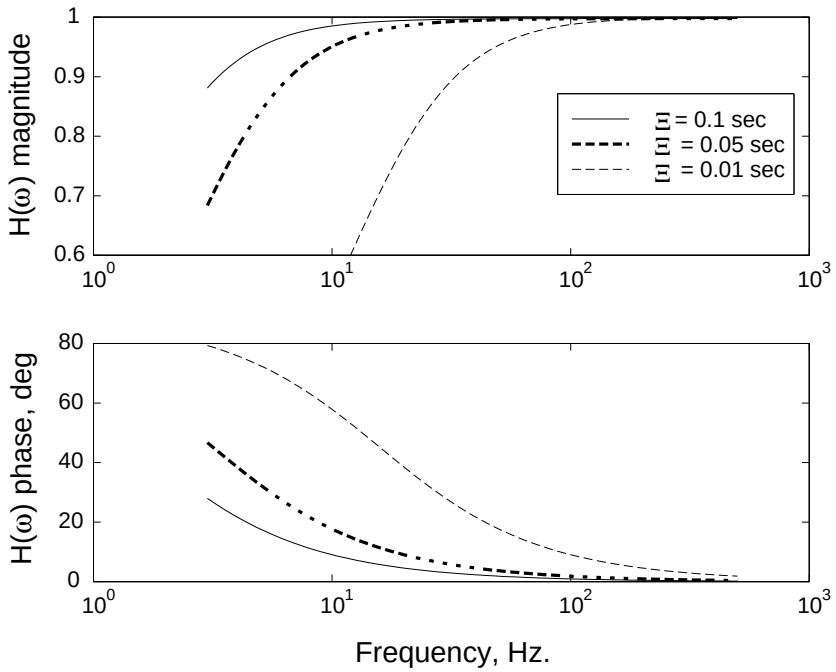

(**a**)Circuit transfer function, for different time constants

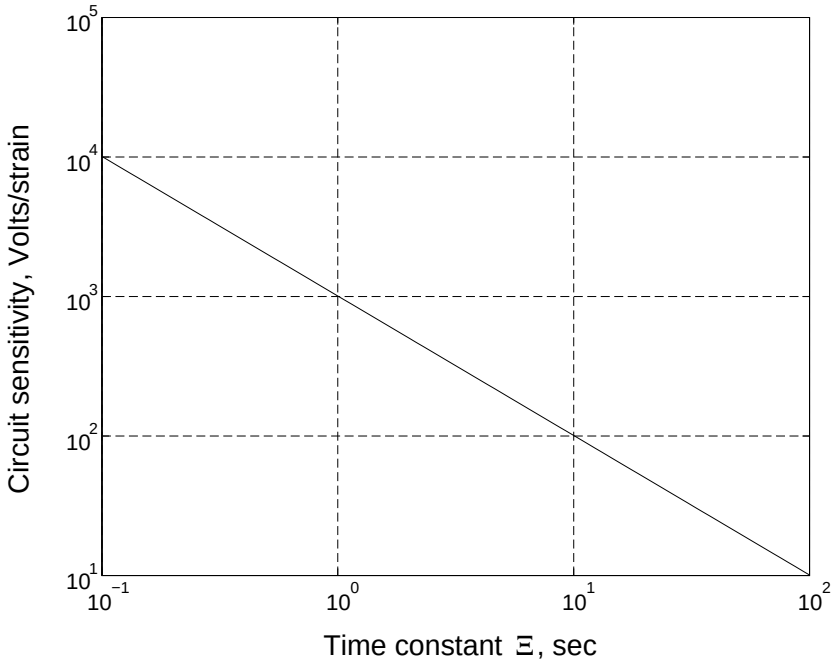

(**b**)Tradeoff between sensitivity and time constant

Figure 3.3 Circuit characteristics

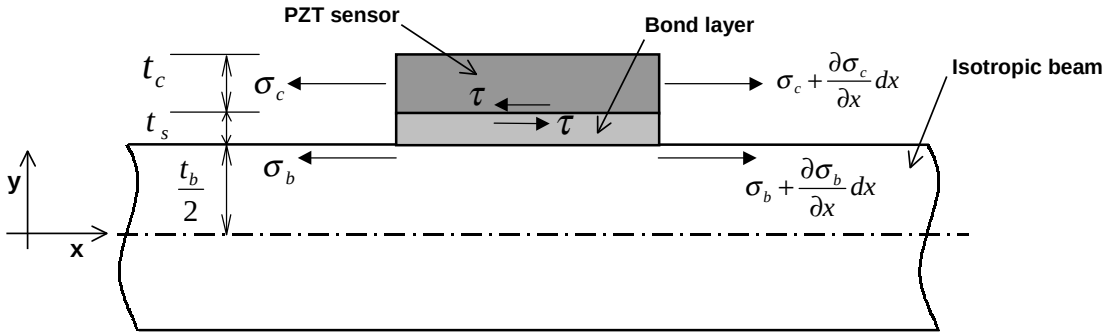

Figure 3.4 Forces and moments acting on the sensor

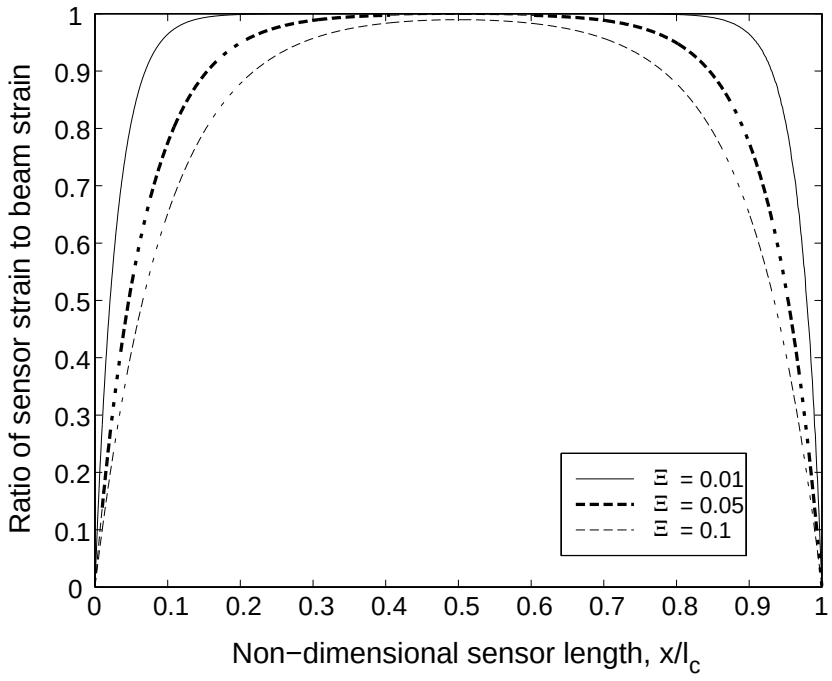

(**a**)0.25 mm thick PZT sensor

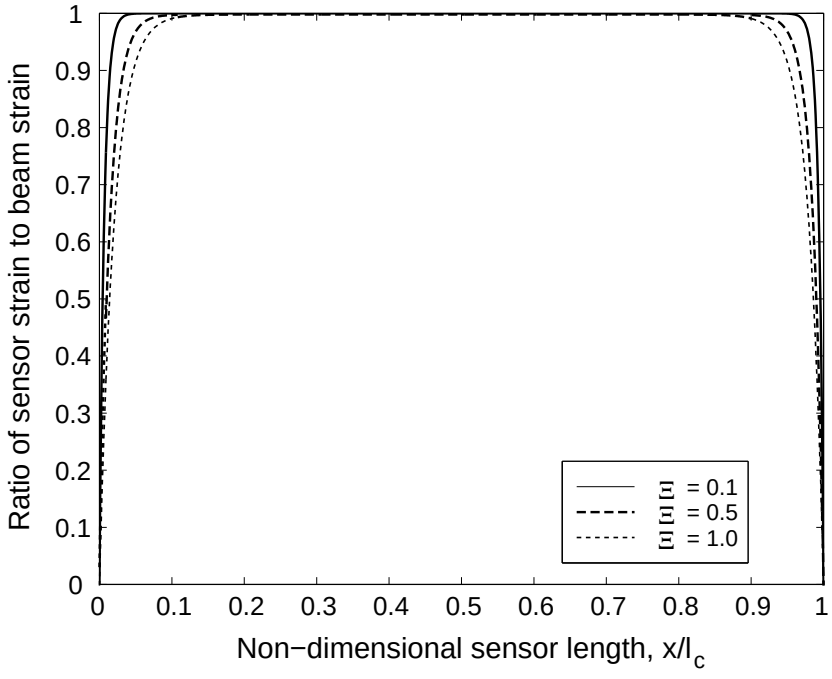

(**b**)0.056 mm thick PVDF sensor

Figure 3.5 Shear lag effects along sensor length

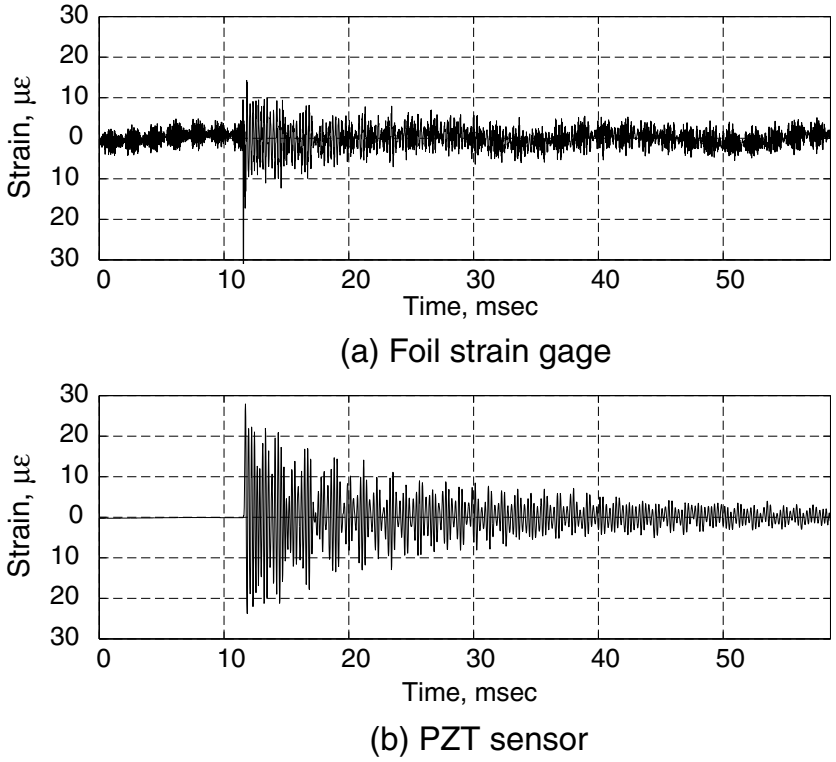

Figure 3.6 Foil strain gage and PZT sensor impulse response in the time domain

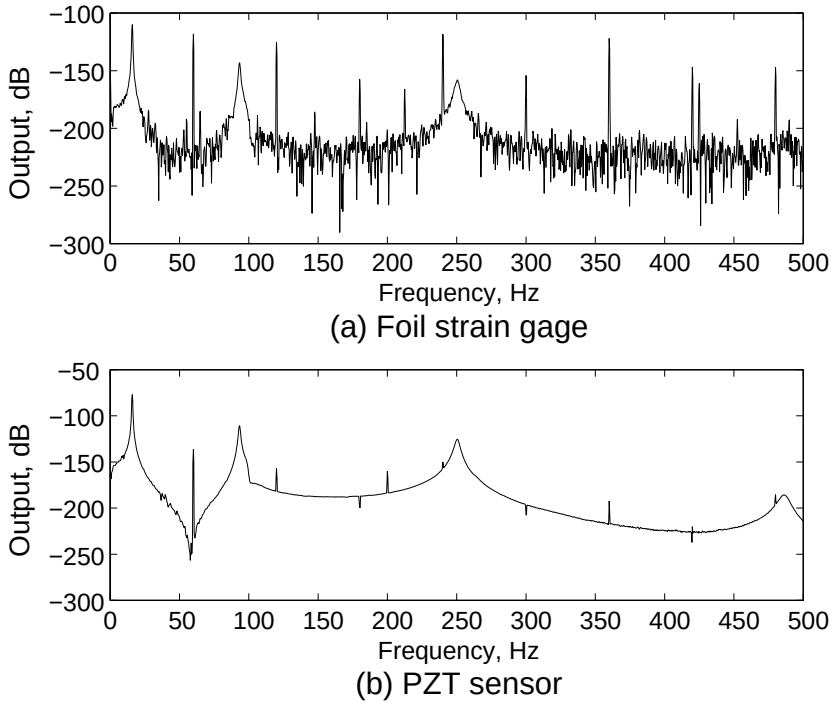

Figure 3.7 Foil strain gage and PZT sensor impulse response in the frequency domain

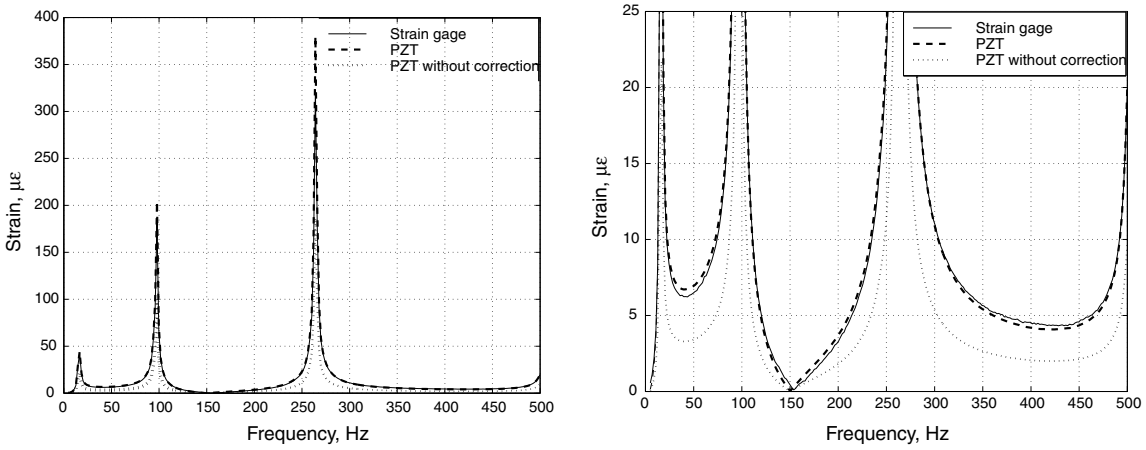

(**a**) Normal vertical scale (**b**) Expanded vertical scale

Figure 3.8 Correlation of PZT sensor and foil strain gage with correction factor

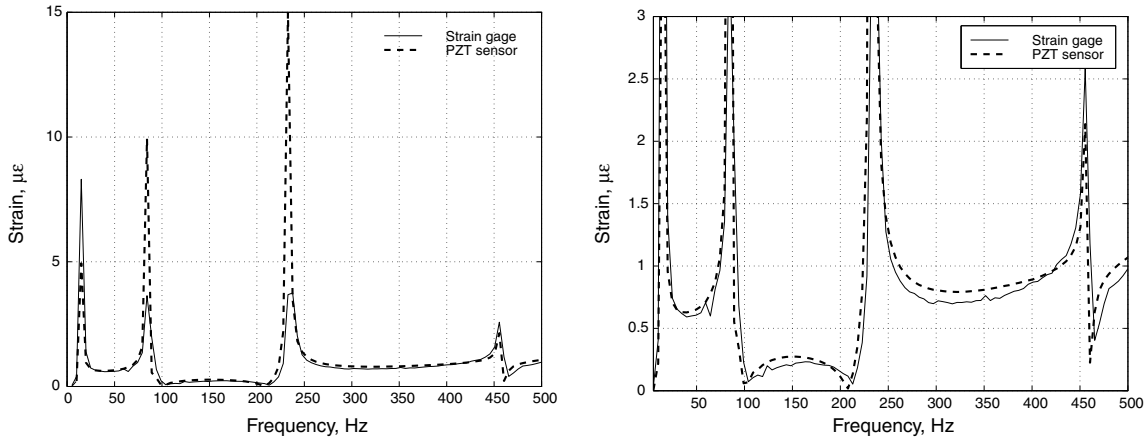

(**a**) Normal vertical scale (**b**) Expanded vertical scale

Figure 3.9 Correlation of PZT sensor and foil strain gage for response at low strain levels

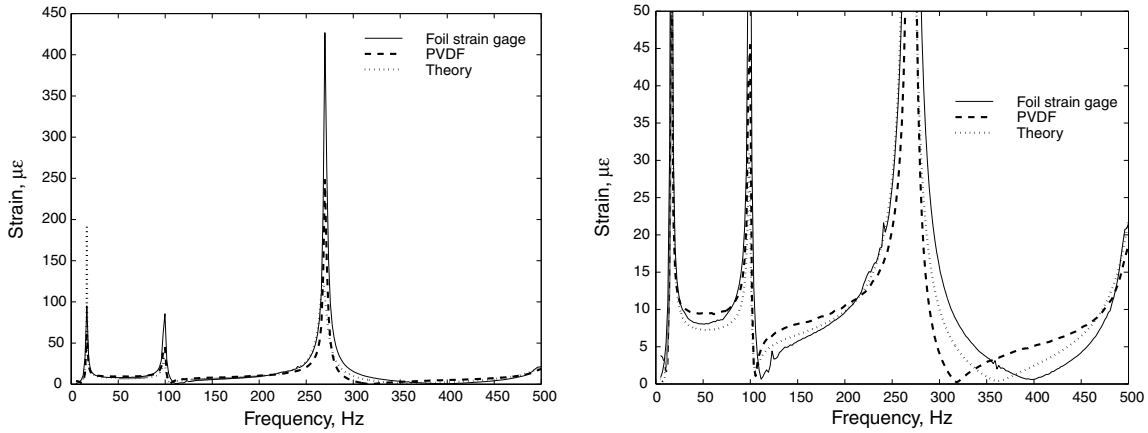

(**a**) Normal vertical scale (**b**) Expanded vertical scale

Figure 3.10 Correlation of PVDF sensor and foil strain gage response

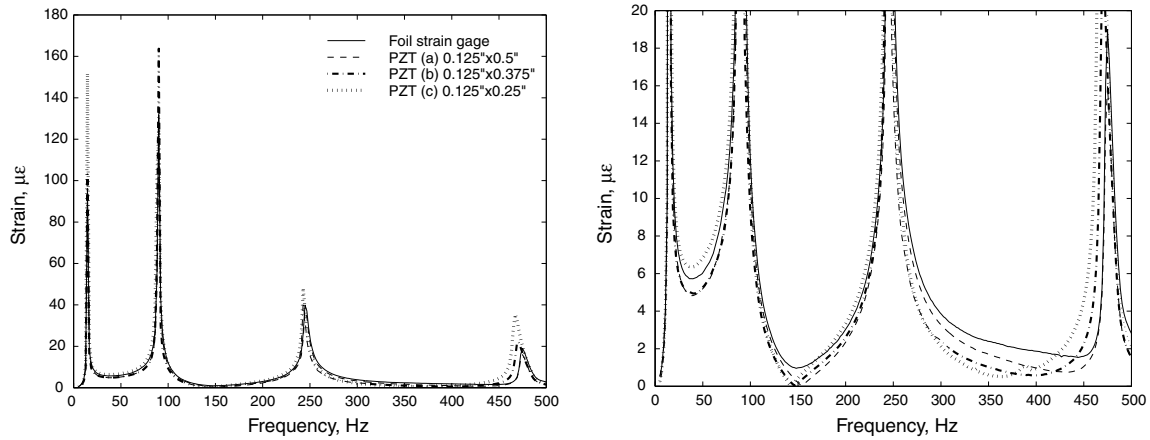

(**a**) Normal vertical scale (**b**) Expanded vertical scale

Figure 3.11 Correlation of foil strain gage and PZT sensors of different sizes, keeping gage length constant

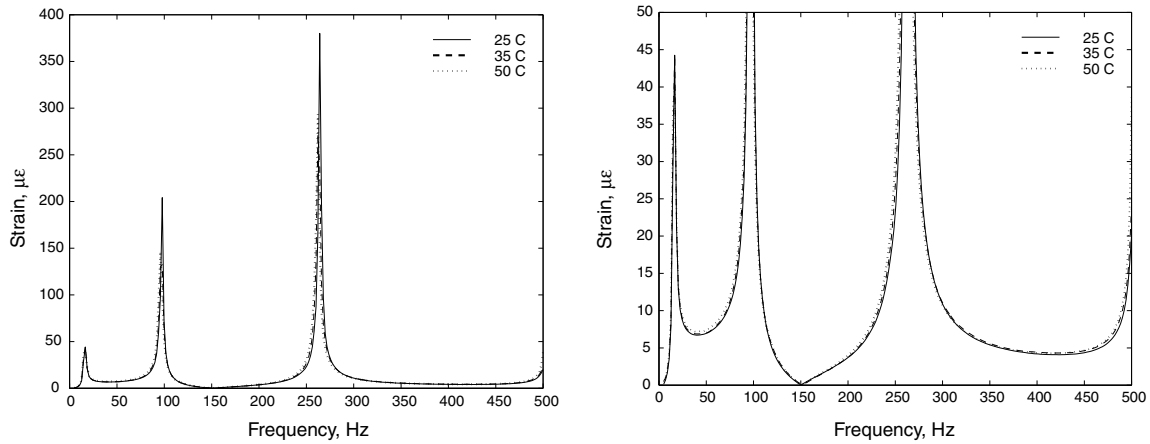

(**a**) Normal vertical scale (**b**) Expanded vertical scale

Figure 3.12 PZT sensor output variation with temperature

Chapter 4

Power Consumption of Piezoelectric Actuators

Piezoelectric actuators, as will be demonstrated in subsequent sections, behave as capacitive loads. As a result, special power amplifiers, capable of delivering large currents, are required to drive practical systems incorporating these actuators. The large currents result in excessive heat generation, and are a cause of concern in designing rotating actuation systems with sliprings for power transmission. In this chapter, the power consumption of piezoelectric actuators is discussed, and a theoretical model is experimentally validated. A means of reducing the current drawn from the power amplifier is described. This is accomplished by incorporating the actuator in a tuned L-C oscillator circuit. Non-ideal circuit performance is addressed, along with theoretical limits to possible power savings and practical difficulties in achieving them. The practical limitation of the size of a physical inductor needed for this purpose is recognised and the use of an active pseudo-inductor is investigated. This pseudo-inductor is connected in parallel with a commercially available power amplifier and reduction in current drawn from the amplifier is demonstrated.

4.1 Electro-mechanical impedance approach

The net impedance of an actuator bonded to a structure can be broken up into two parts: a purely electrical impedance, and a purely mechanical impedance. The energy supplied by the power source driving the actuator appears as an increase in electrical energy of the actuator, an increase in strain energy of the actuator and structure, electrical and mechanical losses, and any work output from the structure. It is therefore convenient to treat the impedance of the actuator and structure as a net electro-mechanical impedance seen by the power source. Once all the mechanical and electrical impedances have been lumped into an effective electro-mechanical impedance, it becomes easy to calculate the current drawn, and therefore the power requirements of the actuator-structure combination.

4.1.1 Electrical impedance of a free actuator

A free piezoelectric actuator, by virtue of its physical configuration, behaves primarily as a capacitive load. In the case of a piezoceramic sheet actuator, it can be treated as a parallel plate capacitor.

For an ideal capacitor, the electrical impedance is given by:

$$Z = \frac{1}{j\omega C} \tag{4.1}$$

where ω is the angular frequency of the applied field and C is the capacitance in Farads, which for an ideal parallel plate capacitor is given by:

$$C = \frac{eA}{t} \tag{4.2}$$

where e is the dielectric permittivity, A is the area of the plate and t is the distance between the plates, which in this case is the thickness of the piezoceramic sheet. If a sinusoidal voltage is applied to the capacitor, the current drawn leads the voltage

by exactly 90° . Real capacitors with dielectric media, however, have energy losses. These losses are due to conduction currents in the dielectric as well as molecular friction opposing the rotation of dielectric dipoles. This causes the current to lead the voltage by a phase angle δ less than 90° . The non-ideal capacitor is usually modelled by a simplified equivalent circuit incorporating a shunt resistance in parallel with an ideal capacitor. The energy losses appear as ohmic heating in the shunt resistance. The dissipation factor, given by $\tan\delta$, is therefore a measure of the energy loss in the capacitor and consequently, the power consumed by the actuator. The impedance of a non-ideal capacitor can be given in terms of a complex dielectric permittivity [166].

$$\bar{e} = e_o k' - j e_o k'' = e - j e \frac{k''}{k'} \tag{4.3}$$

where e_o is the permittivity of free space, k' is the relative permittivity of the dielectric and

$$\tan\delta = \frac{k''}{k'} \tag{4.4}$$

It is well known that the dielectric permittivity and the dissipation factor of piezoceramics increase with increasing field [167]. This information is essential for predicting the power consumption of systems incorporating piezoceramic actuators. For PZT-5H, these variations were calculated from the current consumption measurements in the experiments described above.

From Equations (4.2), (4.3) and (4.4), the electrical impedance of the piezoceramic sheet can be expressed as:

$$Z = \frac{t}{j\omega e_{33}^{\sigma}(1 - j\tan\delta)A} \tag{4.5}$$

The experimentally measured current drawn and the calculated dissipation is shown in Figure 4.1. Equating the impedance form Equation (4.5) to the value of impedance calculated from the experimentally measured voltage and current, the variation of e_{33}^{σ}

and $\tan\delta$ with field can be generated and is shown in Figure 4.2. Curves are fit to the experimental data, and the variation of e_{33}^{σ} and $\tan\delta$ with field can be calculated as:

$$K_e = 5.3187E^2 - 5.9754E + 7.32 \tag{4.6}$$

$$\tan\delta = 0.0662E + 0.0376 \tag{4.7}$$

where K_e is the percent increase in e_{33}^{σ} and E is the electric field in $\mathrm{kV_{rms}/cm}$.

4.1.2 Electro-mechanical impedance of the actuator

A short description of the derivation of the combined electro-mechanical impedance is given here [168]. The structural impedance of the active system is derived by considering a PZT actuator deforming along its length only, driving a single degree of freedom spring mass damper system. For an actuator of length l_c, width w_c and thickness t_c, and with an elastic modulus Y_{22}^{E}, the force exerted is given by

$$F = K_A l_c(\varepsilon_{mech} - \Lambda) \tag{4.8}$$

where K_A is the static stiffness of the PZT, given by $Y_{22}^{E} w_c t_c / l_c$, Λ is the free strain which is defined as $d_{31}V/t_c$, and ε_{mech} is the mechanical strain of the structure at the actuator location. For a PZT being excited along the 3-axis (or z-axis) and assuming it deforms only along the 1-axis (or x-axis), the constitutive relations (Equations (2.1) and (2.2)) can be rewritten as:

$$\varepsilon_1 = \bar{s}_{11}^{E}\sigma_1 + d_{31}E \tag{4.9}$$

$$D_3 = \bar{e}_{33}^{\sigma}E + d_{31}\sigma_1 \tag{4.10}$$

In these equations, ε_1 is the strain, σ_1 is the stress and $\bar{s}_{11}^{E}$ is the complex compliance. The equation of motion for a PZT vibrating in the x-direction is given by:

$$\rho\frac{\partial^2 u}{\partial t^2} = \bar{Y}_{11}^{E}\frac{\partial^2 u}{\partial x^2} \tag{4.11}$$

where $\overline{Y}_{11}^{E}$ is the complex modulus given by:

$$\overline{Y}_{11}^{E} = Y_{11}^{E}(1 + j\eta) \tag{4.12}$$

where η is the mechanical loss factor of the PZT. The complex dielectric permittivity $\overline{e}_{33}^{\sigma}$ is given by:

$$\overline{e}_{33}^{\sigma} = e_{33}^{\sigma}(1 - j\delta) \tag{4.13}$$

Assuming a solution to Equation (4.11) of the form

$$u = (a_1 \sin kx + a_2 \cos kx)e^{j\omega t} \tag{4.14}$$

where $k^2 = \omega^2\rho/\overline{Y}_{11}^{E}$, and applying the appropriate boundary conditions, it is possible to derive expressions for constants a_1 and a_2. A similar derivation can be performed to find the impedance of an actuator (assuming both electrodes shorted) under a constant force excitation. This gives an actuator mechanical impedance expressed as:

$$Z_A = -\frac{K_A(1 + \eta j)kl_c}{\omega \tan(kl_c)}\, j \tag{4.15}$$

4.1.3 Mechanical impedance of the structure

The mechanical impedance of the structure is defined as:

$$F = Z\dot{x} \tag{4.16}$$

The mechanical impedance of the beam in bending (from Equation (4.16)) is given by:

$$Z = \frac{4}{(t_b + t_c)^2}\frac{M}{(\theta_2 - \theta_1)\, j\omega} \tag{4.17}$$

where M is the actuation moment, θ_2 and θ_1 are the beam slopes at the ends of the actuator and t_b is the beam thickness. In the theoretical validation, the actuation moment M and the beam slopes θ_1, θ_2 are calculated using the Euler-Bernoulli model.

4.1.4 Electro-mechanical impedance of the actuator-structure combination

Using the expressions for the mechanical impedances of the actuator and the structure, and using the derived constants a_1 and a_2, the assumed displacement (Equation (4.14)) can be solved for. This is then substituted in the constitutive relations (Equations (4.9) and (4.10)) to obtain the value of the electric displacement D_3. The current is defined as:

$$I = \dot{q} = j\omega \int\int D_3 dxdy \tag{4.18}$$

The final expression for the consumed current is:

$$I = j\omega E w_c l_c \left(\frac{d_{31}^2 \overline{Y}_{11}^E Z_A \tan(kl_c)}{(Z+Z_A)kl_c} + \overline{e}_{33}^{\sigma} - d_{31}^2 \overline{Y}_{11}^E \right) \tag{4.19}$$

Note that for a free PZT actuator, though the actuator impedance Z_A is finite, the impedance of the structure, Z is zero. Also, the factor $\tan(\mathrm{kl_c})/(\mathrm{kl_c})$ is approximately equal to unity. The current drawn by the free PZT (Equation (4.19)) then reduces to:

$$I_{\mathrm{freePZT}} = j\omega E w_c l_c \overline{e}_{33}^{\sigma} \tag{4.20}$$

From this, the impedance of the free PZT can be written as

$$Z_{\mathrm{freePZT}} = \frac{\mathrm{V}}{\mathrm{I_{freePZT}}} = \frac{t_c}{j\omega E w_c l_c \overline{e}_{33}^{\sigma}} \tag{4.21}$$

Note that this expression for the impedance of the free PZT is the same as the expression derived considering the PZT to be a lossy capacitor (Equation (4.5)), considering $\tan\delta \approx \delta$. The experimentally measured current consumed by a free actuator and a pair of actuators bonded to a beam is compared with that predicted using Equation (4.19). The variation of e_{33}^{σ} and $\tan\delta$ given by Equations (4.6) and (4.7) is also incorporated in the theoretical predictions.

Experiments were performed on a free actuator and on a pair of actuators bonded to a cantilevered aluminum beam of dimensions 12” x 1” x 0.032”. The comparision of experimental and theoretically predicted current consumption is shown in Figures 4.3 and 4.4. The predicted values show very good agreement with experiment when the variation of e_{33}^{σ} and $\tan\delta$ is taken into account, and the agreement is poor when these parameters are assumed constant. This emphasizes the importance of incorporating these nonlinearities when attempting to predict the power consumption of such actuator systems.

Due to the highly capacitive nature of the actuators, though the actual energy dissipated in the actuator is small, a large current is drawn from the power amplifier driving it. This makes the driving circuit bulky and inefficient, and poses a challenge to compact smart systems with embedded electronics. The problem becomes even more critical for a rotary wing smart system where the transfer of power from fixed frame to rotating frame poses serious restrictions on the slip ring unit [129].

Several approaches to address this issue can be found in the literature, and can be broadly grouped under two methods: those that involve the design of efficient driving electronics to supply power to the actuator, and those that modify the effective impedance of the actuator by adding components to the actuator circuit. For example, in the first approach, special Pulse Width Modulated (PWM) amplifiers can be designed to decrease the power dissipated in the amplifier and make it more compact than conventional amplifiers. High power PWM amplifier designs have been proposed in the past to drive piezoelectric actuators and electrostrictive actuators [169, 170]. However, these amplifiers do not recover the energy necessary in charging the actuator capacitance, that is wasted on the negative half cycle of excitation. Hybrid techniques have also been suggested [171], wherein the charge used to displace the actuator is recirculated within the amplifier. This research is still in an early stage of development.

In the second approach, the effective impedance of the actuator is changed by adding passive or semi-active components to the actuator driving circuitry, through the modification of the driving circuit using an additional inductor in a series or parallel arrangement [172, 173]. Though the concept is theoretically feasible, the size of the correcting inductance required for practical applications can become prohibitive.

The feasibility of connecting a pseudo-inductor in the actuator driving circuit as a means of reducing the current drawn from the power amplifier is discussed in subsequent sections. Apart from power savings, the change in effective actuator impedance as a result of the pseudo-inductor has applications in other areas, such as semi-active damping augmentation. Though analyses of the behavior of L-C circuits can be found in the literature, they are often limited to ideal components. As seen from Section 4.1.1, piezoelectric actuators have a high degree of non-ideality. The discussion that follows below first goes through a detailed analysis of L-C circuits, emphasizing the effects of non-ideality in the components, that place an upper bound on the theoretically achievable performance gains. It then examines a parallel L-C circuit with the use of a gyrator circuit set up to simulate an inductance, as a means to circumvent problems inherent in purely passive physical inductors. Series and parallel R-L shunt circuits with a pseudo-inductor have been investigated in the past [174], but were limited to low power measurements of the system impedance. In the present work, the gyrator circuit, or pseudo-inductor is connected in parallel with an unloaded piezoceramic stack actuator, and is driven by the output of a commercially available power amplifier. As this configuration can effectively increase the driving capability of an off-the-shelf power amplifier, peak current drawn from the power amplifier is considered as the primary metric of the performance of the circuit. The power consumed by the pseudo-inductor itself is also measured and included in the overall system performance.

4.2 Theory of L-C oscillator circuits

A capacitor is an energy storage element and under a harmonic voltage excitation, it charges up during the positive half cycle of excitation and discharges during the negative half cycle. The current drawn by an ideal capacitor leads the applied voltage by a phase angle ϕ, of 90 degrees. Therefore, for an ideal capacitor, the net energy consumed in one cycle is zero. In the case of a non-ideal capacitor, that is modeled as a pure capacitor with a resistance in series, there is some energy dissipated by the resistance in the form of ohmic heating. This energy loss is unrecoverable and is supplied by the power supply, whereas the energy used in charging the capacitor in the first half cycle is returned to the power supply during the second half cycle. For a load drawing a current $\bar{I}$ at a voltage $\bar{V}$, the power consumption is given by [175]:

$$\bar{P} = \bar{V} * \bar{I} \tag{4.22}$$

where the bars represent complex quantities. The real part of this power is called the active power and represents the actual physical energy dissipated in the system. For the case of the nonideal capacitor, this is the ohmic heating loss. The active power is given by

$$P_{\text{active}} = Re(\bar{P}) = V * I * \cos\phi \tag{4.23}$$

where the quantities without bars represent the absolute values and $\cos\phi$ is known as the power factor of the circuit. In the case of an ideal capacitor, $\cos\phi = 0$ and so, the real power consumed (P_{active}) becomes zero. Even though the real power consumed is zero or close to zero in the case of an non-ideal capacitance, the power supply has to be designed to handle the current I, and the heat dissipation associated with it. Therefore, the power supply has to be rated for a much higher power output than the actual dissipation in the load, resulting in a much larger and heavier power supply than necessary. In order to increase the efficiency of the power circuitry, it is desirable to

increase the power factor and make it as close to unity as possible. This is equivalent to making the impedance of the circuit purely resistive.

It is possible to correct the power factor by adding an inductance in the circuit. An inductor is also an energy storage element, however, an ideal inductor causes the current to lag behind the applied voltage. Thus a combination of an inductor and a capacitor can cause the net phase difference between voltage and current in the circuit to be zero. This effectively causes the circuit to be purely resistive and the power factor becomes unity.

An inductor can be incorporated into the circuit in two fundamentally different ways. The inductor can be either connected in series with the capacitance (Figure 4.5(a)), or in parallel with the capacitance (Figure 4.5(b)). These two configurations are the ideal cases, where the inductor is a pure inductance and the actuator is a pure capacitance.

The net impedance of the circuit is:

$$\bar{Z}_{tot} = R + \bar{Z}_p \tag{4.24}$$

where $\bar{Z}_p$ represents the impedance due to the combination of capacitance and inductance, or in the ideal case, the net reactance of the circuit. For the series configuration, $\bar{Z}_p$ can be derived as

$$\bar{Z}_{p(\text{series})} = \frac{j(\omega^2 LC - 1)}{\omega C} \tag{4.25}$$

and for the parallel configuration, $\bar{Z}_p$ is given by

$$\bar{Z}_{p(\text{parallel})} = \frac{j\omega L}{1 - \omega^2 LC} \tag{4.26}$$

where ω is the circular frequency (radians/sec). From Equation (4.25), it can be seen that at a particular frequency ω_o, the series impedance $\bar{Z}_p$ goes to zero. This frequency is called the resonant frequency and is given by

$$\omega_o = \frac{1}{\sqrt{LC}} \tag{4.27}$$

At this point, since $\bar{Z_p}$ is zero, the net impedance of the circuit is R, which is purely resistive. At resonance, energy is continuously being transferred between the inductor, which stores the energy in a magnetic field, and the capacitor, which stores the energy in an electric field. Ideally, at this point, no external forcing is needed to sustain the oscillatory flow of current through the capacitor. In practice, however, resistive losses add damping to the system, and some energy needs to be input to the system to maintain the oscillations.

In the case of the parallel circuit, at the resonance frequency ω_o, from Equation (4.26), the value of $\bar{Z_p}$ goes to infinity. This means that there is no voltage drop across the resistance R and so no current flows from the power supply. Ideally, at this point, the voltage across the actuator is the same as the power supply voltage, and the current drawn by the actuator is supplied by the parallel inductive arm of the circuit. This current is maintained by the transfer of energy between the two arms at resonance. The net current drawn from the power supply is therefore zero. The parallel L-C oscillator concept is therefore pursued further in an attempt to minimize the absolute value of current drawn from the supply.

4.3 Development of non-ideal circuit behavior

In reality, an ideal inductor and an ideal capacitor are not possible. A piezoelectric actuator itself acts like a non-ideal capacitor, and can be modeled as an ideal capacitor with a resistor in series(Section 4.1.1). The total non-ideal impedance is given by

$$\bar{Z_c} = R_c + \frac{1}{j\omega C} \tag{4.28}$$

The series resistance can be mathematically modeled in terms of a complex

permittivity factor [166]. From Equation (4.5),

$$\bar{Z_c} = \frac{1}{j\omega\bar{C}} = \frac{\tan\delta - j}{\omega C(1+\tan^2\delta)} \approx \frac{\tan\delta - j}{\omega C} \tag{4.29}$$

since $\tan\delta \ll 1$. From Equations (4.28) and (4.29), the value of R_c is found to be

$$R_c = \frac{\tan\delta}{\omega C} \tag{4.30}$$

The resistive part of the impedance is related to the dissipation factor. This is because the constant reorientation of dipoles in the dielectric medium in the presence of an alternating electric field results in energy dissipation similar to ohmic heating. The value of this resistance drops as the frequency of excitation increases, which means that it is actually a pseudo-resistance since a real resistance is independent of frequency. A plot of the theoretical variation of R_c with actuator capacitance at different actuation frequencies is shown in Figure 4.6. This plot is obtained for a PZT-5H actuator material, with $\tan\delta = 0.035$ and a relative permittivity of 3400. The variation of e_{33}^{σ} and $\tan\delta$ with excitation field (Figure 4.2, Equations (4.6), (4.7)) is ignored in these calculations, for the sake of simplicity. Including this variation would only increase the non-ideality. For comparison, a plot of Z_c with capacitance is shown in Figure 4.7. It can be seen that R_c is negligible compared to Z_c, but as will be shown, still has a significant effect on system performance.

Any physical inductor has some finite resistance due to the coil windings. The non-ideal parallel L-C circuit is shown in Figure 4.8. A real inductor can therefore be represented by a pure inductance with a resistance in series as

$$\bar{Z_l} = R_l + j\omega L \tag{4.31}$$

The net non-ideal impedance of the parallel configuration can be derived to be:

$$\begin{aligned}\Re(\bar{Z_p}) &= \frac{\omega^2 C(R_l+R_c)(L+R_lR_cC)}{\omega^2C^2(R_l+R_c)^2+(\omega^2LC-1)^2} \\ &- \frac{(\omega^2LC-1)(R_l-\omega^2LCR_c)}{\omega^2C^2(R_l+R_c)^2+(\omega^2LC-1)^2}\end{aligned} \tag{4.32}$$

$$\begin{aligned}\Im(\bar{Z_p}) &= \frac{-(\omega^2LC-1)(L+R_lR_cC)\omega}{\omega^2C^2(R_l+R_c)^2+(\omega^2LC-1)^2} \\ &- \frac{\omega C(R_l+R_c)(R_l-\omega^2LCR_c)}{\omega^2C^2(R_l+R_c)^2+(\omega^2LC-1)^2}\end{aligned} \tag{4.33}$$

Because R_l and R_c are always positive, the denominators of Equations (4.32) and (4.33) can never be equal to zero, and therefore, $\bar{Z_p}$ can never be infinity. To make the impedance wholly resistive, the imaginary part of $\bar{Z_p}$ should be set to zero. Setting $\Im(\bar{Z_p}) = 0$ in Equation (4.33), frequency ω_{o1} at which this occurs is derived to be

$$\omega_{o1}^2 = \frac{L-R_l^2C}{(L-R_c^2C)LC} \tag{4.34}$$

It can be seen that $\omega_{o1} = \omega_o$ if either R_l and R_c are zero or R_l equals R_c. To see how the non-ideality affects the performance of the circuit, let us examine three cases:

4.3.1 Case (I): $R_l = R_c$

In this case, $\omega_{o1} = \omega_o$ and the reactance from Equation (4.32) reduces to:

$$Z_p = \frac{L}{2R_lC} + \frac{R_l}{2} \tag{4.35}$$

The values of inductance required in an ideal system to achieve resonance at 10 Hz, 50 Hz and 100 Hz are plotted versus actuator capacitance in Figure 4.9. The lower end of the capacitance scale ($\approx 0.1\mu$F) is a typical value for piezoceramic sheet acuators, while the higher end value ($\approx 7\mu$F) represents a typical piezoceramic stack actuator. It can be seen that the required value of the inductance increases rapidly as the excitation

frequency and actuator capacitance decrease. To get the best performance, as close to the ideal case as possible, Z_p should be as high as possible. From Equation (4.35), Z_p depends directly on the L/C ratio. It can be concluded that a high value of Z_p can be achieved if either L/C is very high, or R_l is as small as possible, or both.

Since the current drawn in the parallel case is $I_p = V_p/Z_p$, and the current drawn by the actuator in the absence of the inductor is $I_c = V_p/Z_c$, the relative current saving by adding the inductor is given by $(1 - Z_c/Z_p)$. Hence, the value of Z_p/Z_c is a direct indicator of the performance of the circuit. As long as $Z_p/Z_c > 1$, the addition of the inductance in parallel with the actuator decreases the current drawn from the supply. In order to achieve best performance, the dependence of Z_p/Z_c on system parameters must be investigated and the parameters should be set so as to give as high Z_p/Z_c value as possible at the operating point. Rewriting Equation (4.35) at resonance,

$$Z_p = \frac{1}{2\omega_o C}\left[\frac{1}{\tan\delta} + \tan\delta\right] \tag{4.36}$$

and from Equation (4.29)

$$Z_c = \sqrt{1+\tan^2\delta}\,\frac{1}{\omega_o C} \tag{4.37}$$

From the above two equations,

$$\frac{Z_p}{Z_c} = \frac{1}{2}\frac{\sqrt{1+\tan^2\delta}}{\tan\delta} \tag{4.38}$$

An interesting feature of this is that the maximum Z_p/Z_c is independent of the operating point (for $R_c = R_l$). The maximum gain achievable from the circuit, which is set by the maximum value of Z_p/Z_c, depends purely on the dissipation factor of the actuator. This gives a direct idea of the effect of non-ideality on performance. For a $\tan\delta = 0$, $Z_p/Z_c \to \infty$, which is the ideal case. For a $\tan\delta = 0.035$, $Z_p/Z_c \approx 14.3$, which translates to a theoretical maximum achievable current saving of 93%. Therefore, even in the presence of non-ideality, the achievable saving is significant.

4.3.2 Case (II): $R_l = 0$, $R_c \neq 0$

In order to study the effect of non-ideality in the actuator alone, let us consider a non-ideal capacitor with an ideal inductance in parallel, that is, set $R_l = 0$. Then, ω_{o1} from Equation (4.34) becomes

$$\omega_{o1}^2 = \frac{1}{C(L - CR_c^2)} \tag{4.39}$$

which is very close to the ideal ω_o. Substituing $R_l = 0$ in Equation (4.32) and simplifying leads to

$$Z_p = \frac{\omega^3 L^2 C \tan\delta}{(1 - \omega^2 LC)^2 + \tan^2\delta} \tag{4.40}$$

This results in

$$\frac{Z_p}{Z_c} = \frac{\omega^4 L^2 C^2 \tan\delta}{((1 - \omega^2 LC)^2 + \tan^2\delta)\sqrt{(1 + \tan^2\delta)}} \tag{4.41}$$

Since in this case, $\omega_{o1} \approx \omega_o$, $\omega_o^2 LC \approx 1$ and also since $\tan\delta \ll 1$, Equation (4.41) at the resonance point reduces to

$$\frac{Z_p}{Z_c} \approx \frac{1}{\tan\delta} \tag{4.42}$$

From this it can be seen that if the non-ideality is limited to the capacitor alone, the maximum theoretical Z_p/Z_c depends on the dissipation factor of the capacitor. As before, if $\tan\delta = 0$, $Z_p/Z_c \to \infty$. The dissipation factor of the capacitor is therefore a very important quantity and places a physical limit on the maximum achievable current saving.

4.3.3 Case (III): $R_c \neq R_l \neq 0$

This represents the most general case. The frequency at which $\bar{Z}_p$ becomes wholly resistive is given by Equation (4.34). From this, the value of the correcting inductance required can be derived to be

$$L = \frac{(C^2\omega_o^2 R_c^2 + 1) + \sqrt{(C^2\omega_o^2 R_c^2 + 1)^2 - 4C^2\omega_o^2 R_l^2}}{2C\omega_o^2} \tag{4.43}$$

For a solution to exist,

$$(C^2\omega_o^2R_c^2+1)^2-4C^2\omega_o^2R_l^2\geq 0 \tag{4.44}$$

which gives

$$R_l\leq\frac{1}{2C\omega_o} \tag{4.45}$$

This gives the maximum allowable value of R_l, the non-ideality in the inductor, for the circuit to function. However, substituting this value of R_l in Equation (4.32) leads to $Z_p/Z_c\approx 1$, at which point the addition of the inductor is ineffective.

For an operating frequency of 100 Hz, and an actuator capacitance of 10μF, the maximum R_l is 79.6Ω. For values of $R_l=10\Omega$, 50Ω and 75Ω, Figures 4.10 and 4.11 show the variation of required correcting inductance and Z_p/Z_c with actuator capacitance respectively, at an operating frequency of 10 Hz and 100 Hz. It can be seen that the value of R_l has a small effect on the inductance required, but has a large effect on the achievable value of Z_p/Z_c. As the non-ideality R_l and the actuator capacitance increase, the maximum possible Z_p/Z_c decreases. For this reason, the remainder of this paper addresses the behavior of a high capacitance piezoelectric stack actuator as opposed to a low capacitance piezoelectric bimorph actuator.

4.4 Implementation of the current reduction circuit

The power saving circuit should be able to operate over a range of frequencies for a given actuator. As an example, consider a typical stack actuator, with a capacitance of 7μF. The range of operating frequencies is 0-100 Hz, which corresponds to the frequency requirement for the application of the stack actuator in the smart trailing edge flap of a helicopter rotor system [129]. In such a system, the piezostack provides the actuation force to actively control vibration. However, for the purpose of this study, only

a free actuator is considered, performing no mechanical work output. Figure 4.12 shows the theoretical variation of Z_p/Z_c with excitation frequency for the actuator in parallel with a 1 H inductor. Both the ideal case ($R_c = R_l = 0$) and the non-ideal case (with nonzero dissipation and $R_l = 50\Omega$) are plotted for comparison. The circuit performs well only in a small range of excitation frequencies about the resonance frequency and the addition of the inductance actually degrades the performance of the actuator at excitation frequencies away from the resonance frequency of the circuit. Thus the operation of the system is limited to only a small range of frequencies.

However, if the circuit could be continuously tuned at each operating frequency, the variation of Z_p/Z_c for the same actuator could be extended over a range of frequencies, as shown in Figure 4.13. Apart from the difficulty in tuning the circuit to operate over the entire frequency range, from Figures 4.9, 4.10 and 4.11, it can be seen that the required inductance increases rapidly for low values of actuator capacitance and excitation frequency. It is in practice, difficult to obtain physical inductances in the range of tens of Henries. Physical inductors of such magnitude also tend to be very bulky and heavy, which make them inconvenient to integrate in a smart system such as a smart rotor blade. Such inductors also tend to have a high value of R_l. To overcome these disadvantages, the concept of a pseudo-inductor, or active inductor is used. Depending on the frequency of interest, a pseudo-inductor can be easily tuned to generate a large range of inductance values, and the size of the circuit is independent of the value of inductance. Inductance values as high as 10^6H have been reported in the literature [176], and are obtainable with just one operational amplifier.

4.5 Implementation of a pseudo-inductor

A pseudo-inductor is a gyrator circuit using an operational amplifier, which effectively inverts the impedance of a capacitor. Energy is no longer stored in a magnetic field, but as a charge on a capacitor in the pseudo-inductor circuit. The amplifier changes the phase of the current flowing in the circuit so that the input impedance is inductive.

Two circuits were investigated for this purpose. The first circuit [176, 177], was chosen for its simplicity since it uses only one operational amplifier and three other components. The second circuit [177,178] was discarded because of certain difficulties, which will be discussed below.

Pseudo-inductors have been widely used in Integrated Circuits and other small signal, high frequency circuits. Use of these circuits in power management applications has not been attempted before. Using a pseudo-inductor as compared to a physical inductor has many advantages. Firstly, the inductor is very compact, not exceeding the size of a single operational amplifier, and inductance values of the order of 100H can be easily achieved with no increase in size. The value of the inductance can be changed by changing the values of the capacitance or the resistance in the pseudo-inductor circuit. This is easily realized in practice by making use of a potentiometer by varying its resistance. Also, the effective value of the series resistance, R_l can be made smaller than the corresponding value for a physical inductor.

The main disadvantage of the pseudo-inductor is that by using an active element in the circuit, namely the operational amplifier, it now becomes necessary to supply power to the operational amplifier for its functioning. This must be supplied at a voltage equal to or above the peak voltage of the input signal, depending on the type of op-amp chosen for the purpose. However, the power supply for the amplifier will only be a simple DC power supply that is much more compact than the power amplifiers which

supply power to the actuator. Thus, by reducing the actuator current consumption, and thereby reducing the size of the power amplifier, the addition of a DC power supply will still result in an overall weight saving. Normally, sufficient DC power is available on any aircraft, justifying the use of the psuedo-inductor, and resulting in an overall weight reduction of the system.

Circuit-1 is shown in Figure 4.14 and is discussed in detail in the references [177]. Assuming an ideal unity gain amplifier, the impedance of this circuit can be derived to be

$$\bar{Z_{in}} = R_{in} + jwL_{in} \tag{4.46}$$

where R_{in}, which is the same as R_l, and L_{in} are

$$R_{in} = \frac{R_2(1+\omega^2C^2R_1R_2)}{1+\omega^2C^2R_2^2} \tag{4.47}$$

$$L_{in} = \frac{CR_2(R_1-R_2)}{1+\omega^2C^2R_2^2} \tag{4.48}$$

For the input impedance to be inductive, it can be seen that $R_1 > R_2$. The Q factor of the inductor is

$$Q = \frac{\omega C(R_1-R_2)}{1+\omega^2C^2R_1R_2} \tag{4.49}$$

where the Q factor is defined as $\omega L/R$, and can be shown to be equivalent to Z_p/Z_c. The Q of an inductor gives an indication of the amount of non-ideality present. To get a high value of Q, or as close to ideal performance as possible, $R_2 \ll R_1$, and so, $L_{in} \approx CR_1R_2$.

The value of Q however, depends on the frequency of operation. It can be shown that Q reaches a maximum when

$$\omega_o = \frac{1}{C\sqrt{R_1R_2}} \tag{4.50}$$

The corresponding maximum value of Q is

$$Q_{max} = \frac{1}{2}\sqrt{\frac{R_1}{R_2}} \tag{4.51}$$

If the capacitance C is chosen so that it is equal to the external tuning capacitance, which in this case is the actuator capacitance,

$$\omega = \frac{1}{\sqrt{LC}} = \frac{1}{C\sqrt{R_1 R_2}} \tag{4.52}$$

and

$$Q = \frac{1}{2}\sqrt{\frac{R_1}{R_2}} \tag{4.53}$$

This means that Q is independent of frequency and reaches the maximum possible value at each tuned resonant frequency of the circuit. This therefore represents the best possible design of the circuit. However, in practice, it was observed that the best performance was achieved if the capacitance C was less than the actuator capacitance, though of the same order of magnitude.

Circuit-2 [178] is shown in Figure 4.15. The L and Q of this circuit are

$$L = CR_1R_2 \tag{4.54}$$

$$Q = \frac{\omega CR_1R_2}{R_1 + R_2} \tag{4.55}$$

It is recommended to keep $R_1 = R_2$ for stability reasons. If the actuator capacitance is C_a, Equations (4.54), (4.55) become

$$\omega = \frac{1}{\sqrt{C_a CR_1R_2}} \tag{4.56}$$

and

$$Q = \frac{\omega CR_1}{2} = \frac{1}{2}\sqrt{\frac{C}{C_a}} \tag{4.57}$$

For the circuit to be effective, $Q \geq 1$ and so the minimum value of C is

$$C_{min} \geq 4C_a \tag{4.58}$$

This means that a large capacitance has to be used for the circuit to work effectively. The large size of this capacitor makes the construction and use of the circuit inconvenient and so it was decided to implement Circuit-1 for the pseudo-inductor.

4.6 Experimental results

The pseudo-inductor test circuit-1 was implemented using a PA88 high voltage operational amplifier. The resistance R_{in} (Equation(4.47)) varies almost quadratically with frequency, as the terms multiplying ω^2 in the numerator are typically several orders of magnitude larger than the terms multiplying ω^2 in the denominator. This is shown in Figure 4.16, where a pseudo-inductor is compared to a physical inductor, a 0.1 H choke coil. The pseudo-inductor was constructed with component values $R_1 = 10k\Omega$, $R_2 = 100\Omega$, and $C = 0.1\mu$F. The actual value of the pseudo-inductance is just under 0.1 H because 10% components were used throughout the circuit. This experiment was intended as a proof of concept and to demonstrate the low R_l values achievable in the frequencies of interest.

For the actuator L-C circuit, it was decided to choose component values that gave the worst performance, in order to demonstrate the feasibility of the concept at an adverse operating point. Therefore, from the non-ideal analysis described above, and from Figures 4.10 and 4.11, the actuator chosen was a commercially available piezoelectric stack actuator (P-804.10) [137] with a capacitance of 7μF. The value of R_{in} ($\approx R_2$) of the pseudo-inductor was chosen to be 100Ω, which, for the chosen actuator, is close to the maximum allowable R_l for circuit operation. The power saving circuit was implemented by connecting the pseudo-inductor in parallel with the stack actuator. A commercially available power amplifier (PI E-501.00 LVPZT-amplifier) [137] was used to drive the stack and the pseudo-inductor circuitry was driven off a DC power supply. To allow the pseudo-inductor to operate effectively independent of any DC bias present in the actuator excitation voltage, it was AC coupled to the actuator. The values of C and R_2 were held fixed at 1μF and 100Ω respectively, while R_1 was a $2M\Omega$ potentiometer to enable tuning of the pseudo-inductor at each operating frequency. This gave a maximum

achievable inductance of 200 H. It should be noted that such a high value of inductance is very difficult to achieve with a physical inductor.

Figure 4.17 shows the power savings obtained by connecting a 100 H pseudo-inductor in parallel with a stack actuator of capacitance 7μF, which gives a resonant frequency of $\approx$ 5Hz. The stack was actuated at 0-50 V. The power supply to the inductor was at $75V_{DC}$. The reduction in power consumption shown is the quantity $V * I$, which is the actual volt-amperes consumed from the power supply. Power consumed to run the pseudo-inductor is also plotted, and it can be seen that even after accounting for power consumed by the pseudo-inductor, significant overall power saving can be achieved. Since the circuit is tuned to $\approx$ 5 Hz, the maximum savings occurs at this frequency and drops off at other frequencies.

The op-amp circuit that acts as a pseudo-inductor can be run off any DC voltage greater than or equal to the peak excitation voltage, and so the power consumed by the pseudo-inductor and the actuator is not a direct indication of the effectiveness of the L-C circuit. Comparision of the actual current consumed by both the actuator and the pseudo-inductor, and the actual strain responses of the actuators, with and without the L-C circuit will yield more insight into the behavior of the circuit. Figure 4.18 shows the performance of the same configuration with operating frequencies from 10Hz to 50Hz. It can be seen that though the minimum current drawn from the power amplifier is around the resonant frequency of 20Hz, the minimun overall current drawn from the power amplifier and the DC supply of the psuedo-inductor ($I_{amp} + I_{DC}$) is at a slightly higher frequency. Figure 4.19 shows the voltage across the stack, currents drawn from the power amplifier and DC supply of the pseudo-inductor, and the strain output of the stack, while operating at 30 Hz. The current drawn from the amplifier in the absence of the pseudo-inductor is I_{stack}, current drawn from the amplifier when the pseudo-inductor is connected in parallel is I_{amp} and current drawn by the pseudo-inductor from

its DC supply is I_{DC}. For comparision, Figure 4.19(a) shows the voltages, currents and strains when the pseudo-inductor is disconnected and Figure 4.19(b) shows the same parameters when the pseudo-inductor is connected in parallel. The pseudo-inductor in this case was set for an inductance value of 10H, which results in a resonant frequency of approximately 20 Hz. It can be seen that the peak-to-peak magnitude of the strain output of the stack remains unaffected, and the only effect of the pseudo-inductor is to reduce the peak current being drawn from the power amplifier, while at the same time drawing some current from its DC supply.

One of the major advantages of the pseudo-inductor is that it can be tuned to any operating frequency, which is not possible in a physical L-C circuit without physically changing the inductors. The tuning of the operating frequency of the pseudo-inductor is accomplished by means of varying one of the resistances in its circuit. The test results of power savings achieved by continuously tuning the circuit is shown in Figure 4.20. Two different excitation voltages are shown, 0-50 V and 0-100 V, for which the supply voltages to the pseudo-inductor are $75V_{DC}$ and $125V_{DC}$ respectively. The actuator power saving and the overall system power saving are shown. The power savings decreases with frequency, which is in agreement with the trends shown in Figure 4.13. Figure 4.21 shows the power required for operation of the pseudo-inductor. It can be seen that the actuator power savings is relatively constant with excitation voltage, but power consumed by the pseudo-inductor increases with excitation voltage. Hence, at low frequencies, where the Z_p/Z_c value is inherently high, and at low excitation voltages, when the pseudo-inductor itself draws less power from its power supply, there is an overall saving in power. But at higher frequencies and higher excitation voltages, though the actuator power saving is still significant, the overall power saving is negative. This means that some extra power has to be supplied to the system to run the operational amplifier which forms the pseudo-inductor. However, as mentioned before, the power to

run the pseudo-inductor can be supplied by a compact DC power supply, thus resulting in a net saving in weight of the system.

4.7 Summary and conclusions

1. It is possible to predict the power consumption of free and surface bonded actuators fairly accurately using the impedance method, given the variation of the dielectric permittivity and dissipation factor with field for a free actuator. Once these variations are known for a specific actuator, and an expression for the mechanical impedance of the structure is obtained, the current drawn by the actuators bonded on the structure can be predicted. The accuracy of the prediction becomes lower at high values of field and frequency. Discrepancies are noticable for fields above $4.8 kV_{rms}/cm$ and frequencies above roughly 100 Hz due to non-linearities.

2. The highly capacitive nature of the actuators results in large currents being drawn from the power sources driving them in real applications. However, only a small part of this input power is dissipated by losses in the actuator. The concept of utilizing an L-C circuit, of which the actuator forms the capacitive arm is suggested as a means to reduce the current drawn by the actuator.

3. The effect of non-ideality of the components on the performance of a parallel L-C oscillator circuit was derived, and the limits of non-ideality for proper functioning of the circuit were identified. It was shown that assuming an ideal inductor, the maximum possible power saving depends only on $\tan\delta$, the dissipation factor of the actuator material. For a piezostack actuator of capacitance $7\mu F$, operating at a frequency of 20 Hz, which is representative of a typical vibration control application on a smart helicopter rotor, the value of inductance required for tuning

is on the order of 10H. This value is very dependent on the amount of series resistance associated with the inductor.

4. A physical inductor of this inductance value would be very large and would also have a large series resistance. In order to eliminate such problems inherent with physical inductors, the concept of using a pseudo-inductor is investigated. The performance of a simple pseudo-inductor, built out of a single operational amplifier, was measured. By demonstrating functioning of the circuit at an adverse operating condition, the concept of using pseudo-inductors to reduce current drawn from the power amplifier was experimentally validated. As this circuit was connected in parallel with the piezostack actuator, to the output of a conventional power amplifier, it was possible to increase the driving capability of existing amplifiers. A peak current saving of approximately 90% has been obtained for the piezostack described above, at a frequency of 5Hz, without affecting the piezostack output displacement.

5. The pseudo-inductor circuit was tuned to operating frequencies in the range of 5 - 100Hz and as expected from theory, the maximum achievable performance was observed to decrease with frequency. Because the pseudo-inductor is an active circuit, the power consumed by it was measured. When this power was included with the overall performance, the maximum power saving at the above operating condition was approximately 70%. The overall power savings, including the power consumed by the pseudo-inductor, decreases with an increase in operating frequency and is dependent on the selection of optimum values of circuit component.

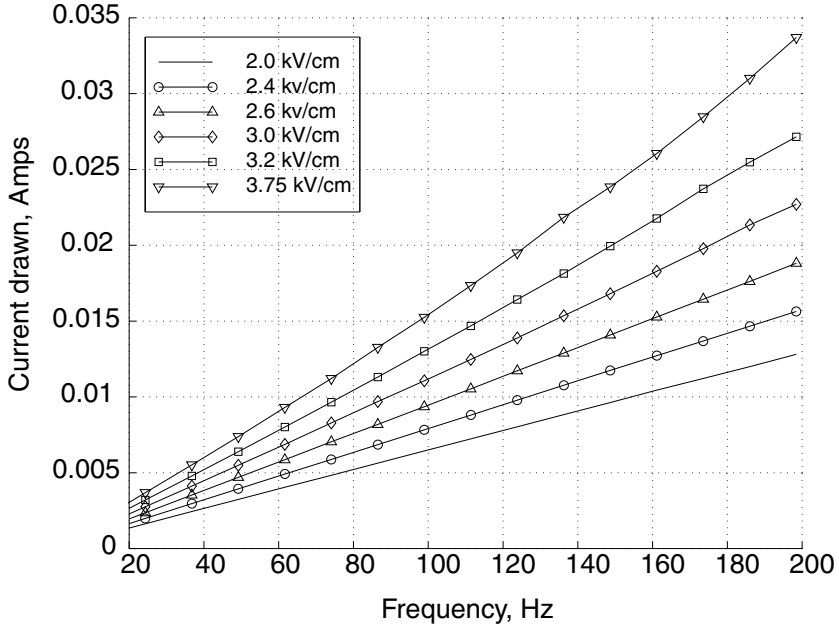

(**a**)Current drawn

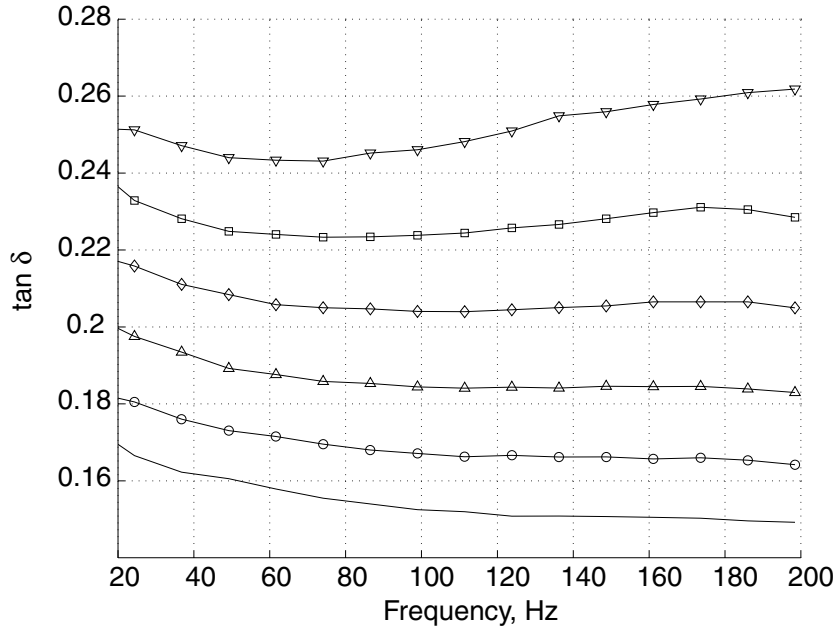

(**b**)Calculated tan δ

Figure 4.1 Experimentally measured current and tan δ for a free piezoelectric sheet

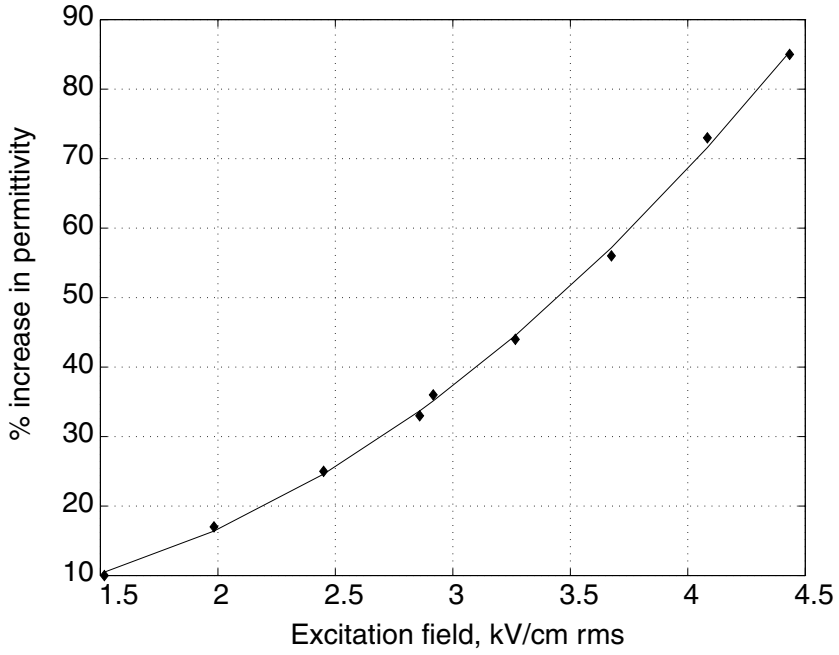

(**a**)Dielectric Constant

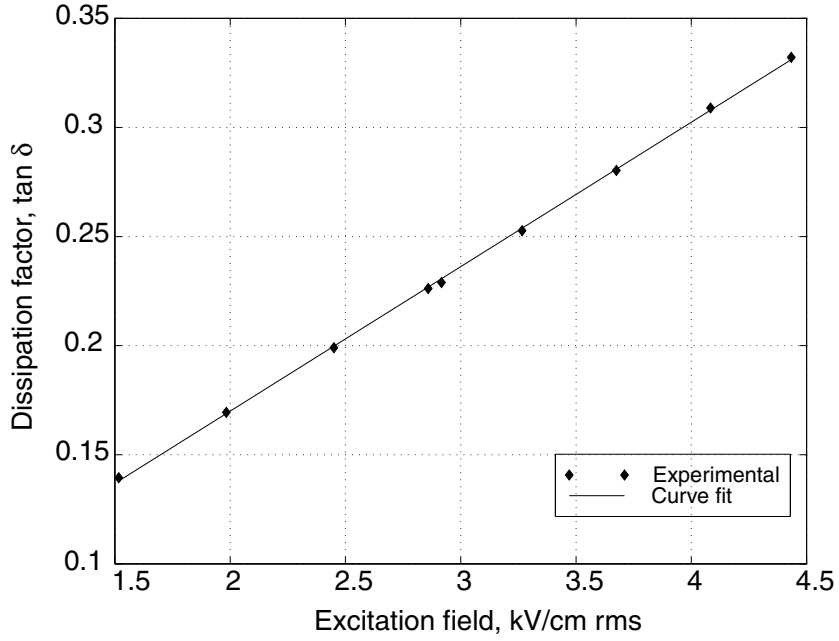

(**b**)Dissipation Factor

Figure 4.2 Variation in piezoelectric material constants with applied electric field

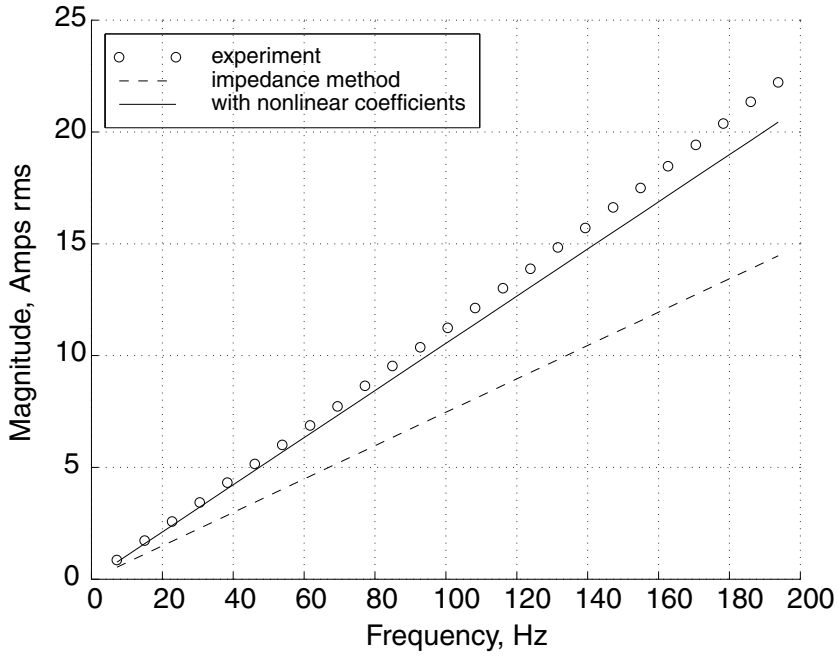

(**a**)Magnitude of current

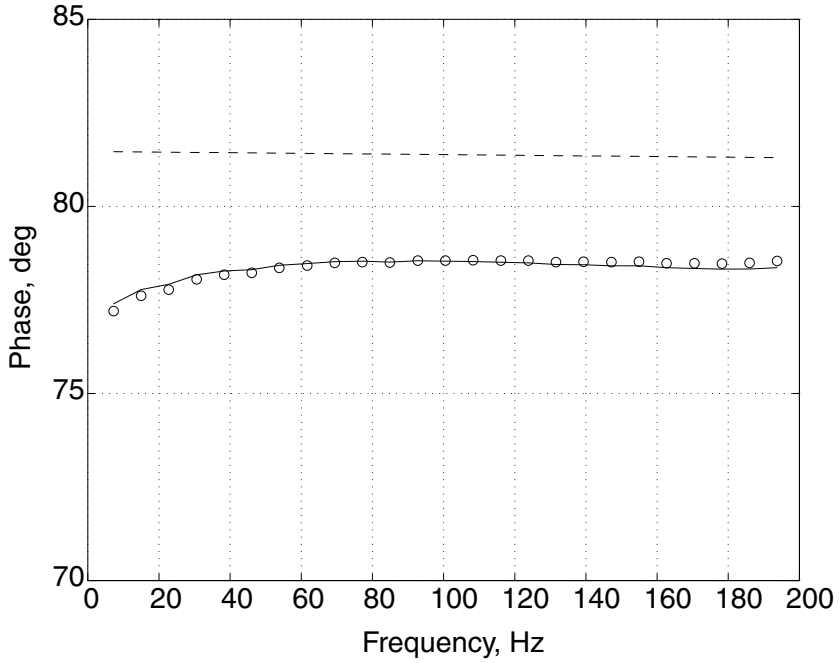

Phase of current

Figure 4.3 Current consumption predictions for a free actuator, $3.0 kV_{rms}/cm$

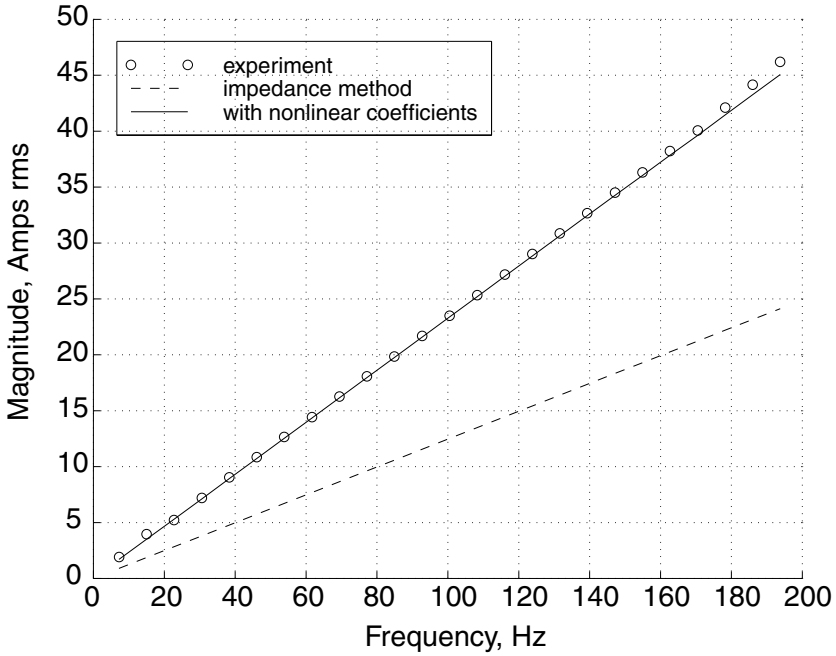

(**a**)Magnitude of current

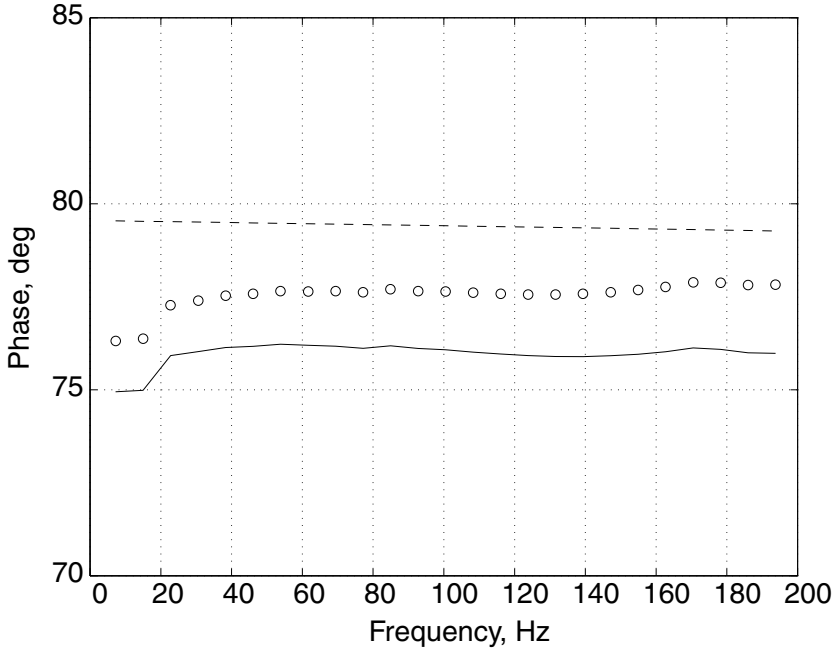

(**b**)Phase of current

Figure 4.4 Current consumption predictions for a pair of actuators bonded onto a beam, $3.0\text{kV}_{\text{rms}}/\text{cm}$

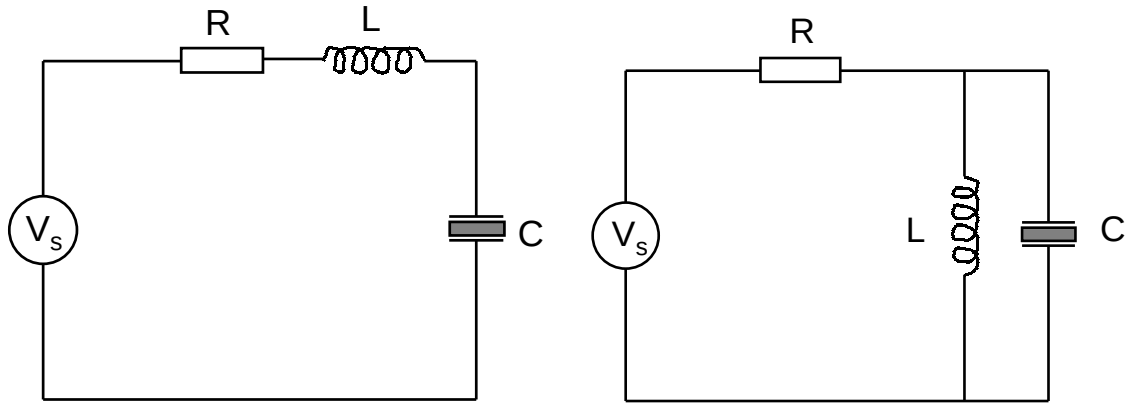

(**a**) Series (**b**) Parallel

Figure 4.5 Ideal series and parallel configurations

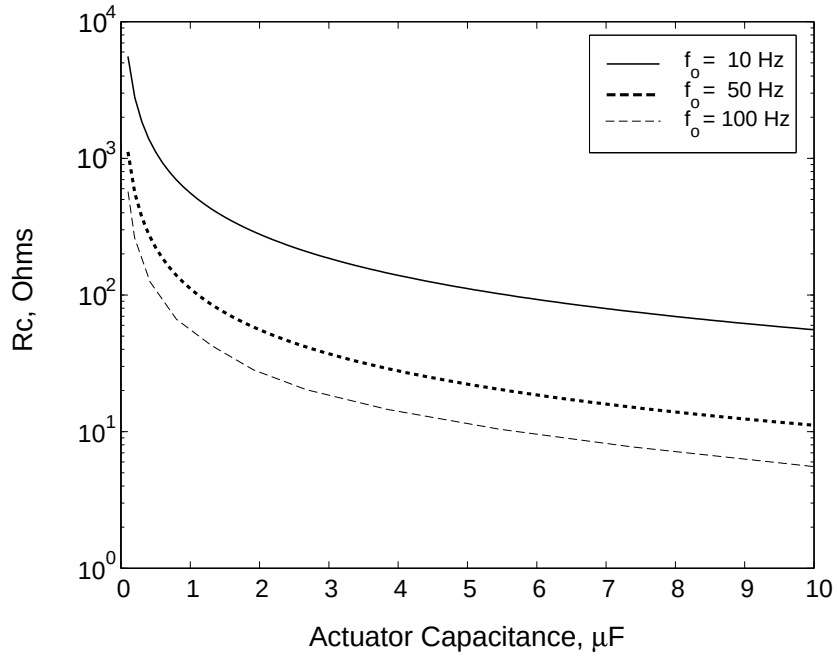

Figure 4.6 Variation of R_c for $\tan\delta$=0.035, relative permittivity of 3400

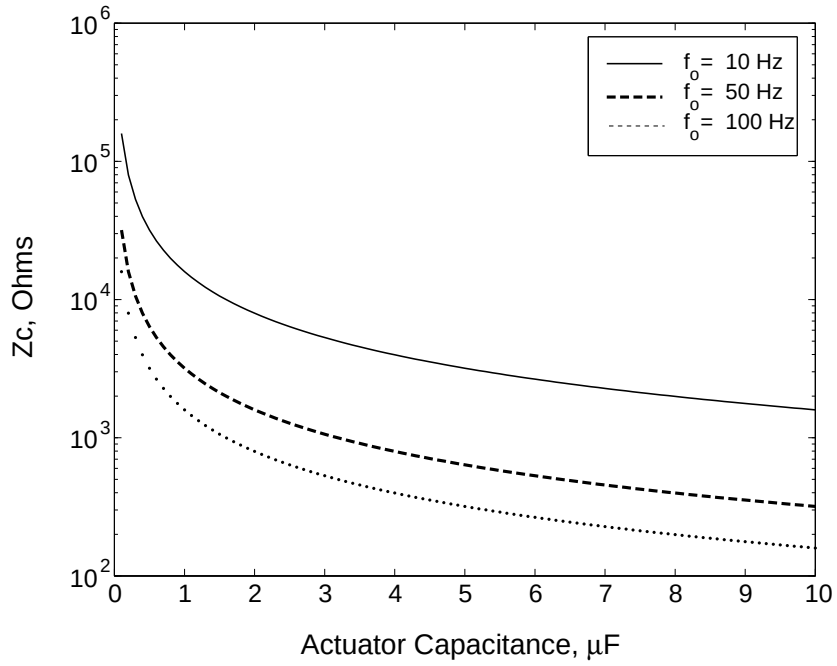

Figure 4.7 Variation of Z_c for $\tan\delta$=0.035, relative permittivity of 3400

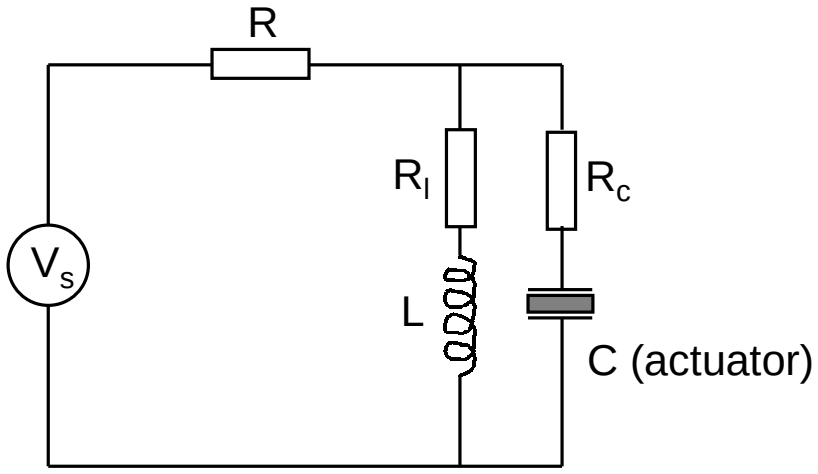

Figure 4.8 Non-ideal L-C circuit

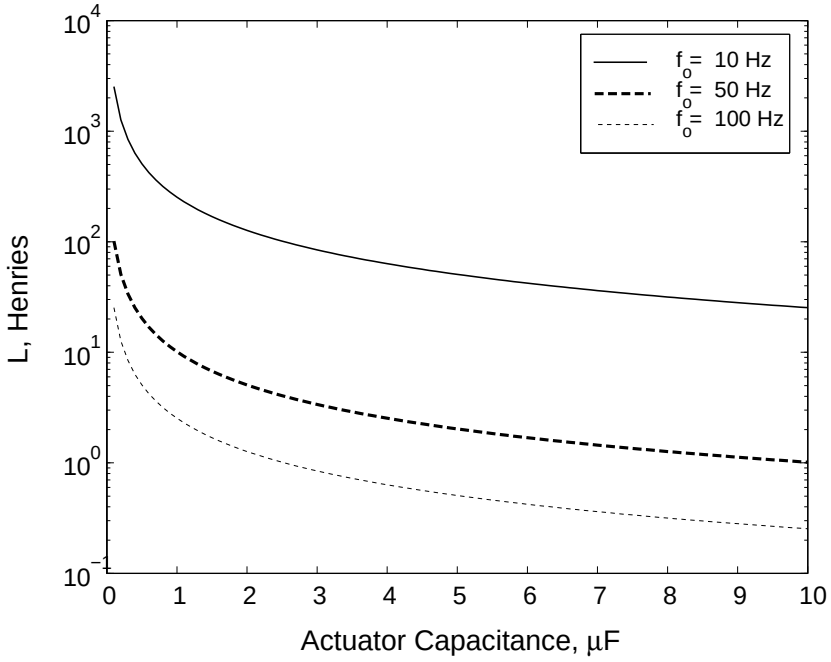

Figure 4.9 Inductance requirement, $R_c = R_l$

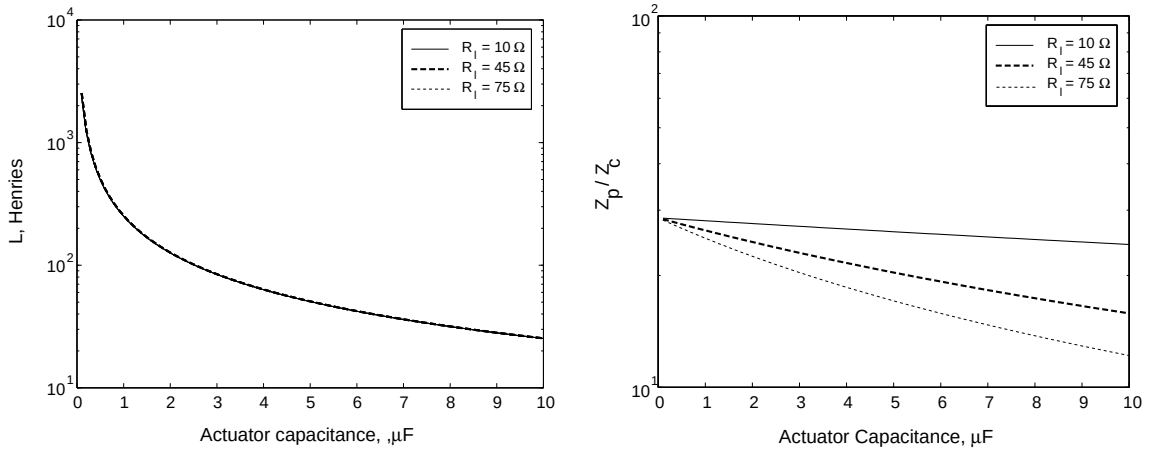

(**a**) (**b**)

Figure 4.10 Required inductance and Z_p/Z_c for $f = 10Hz$

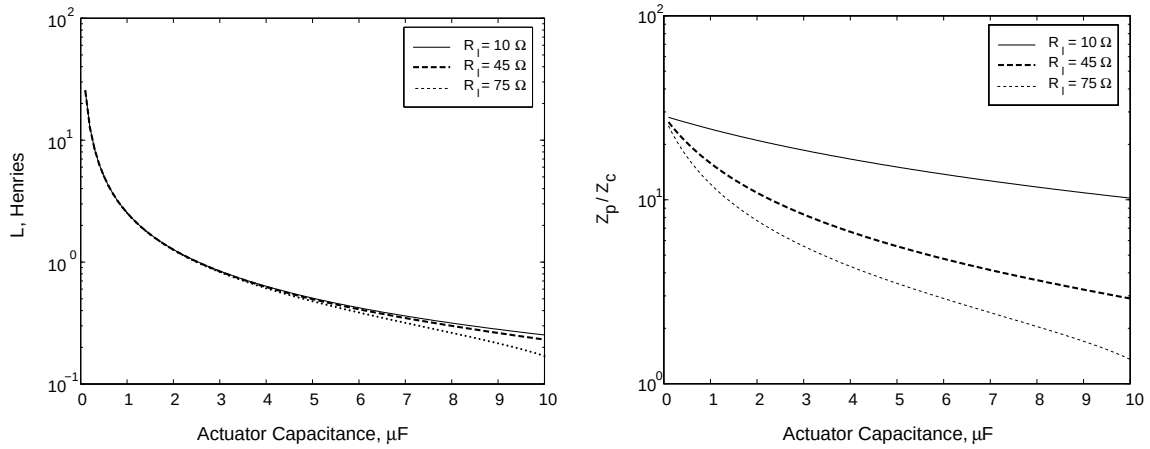

(**a**) (**b**)

Figure 4.11 Required inductance and Z_p/Z_c for $f = 100Hz$

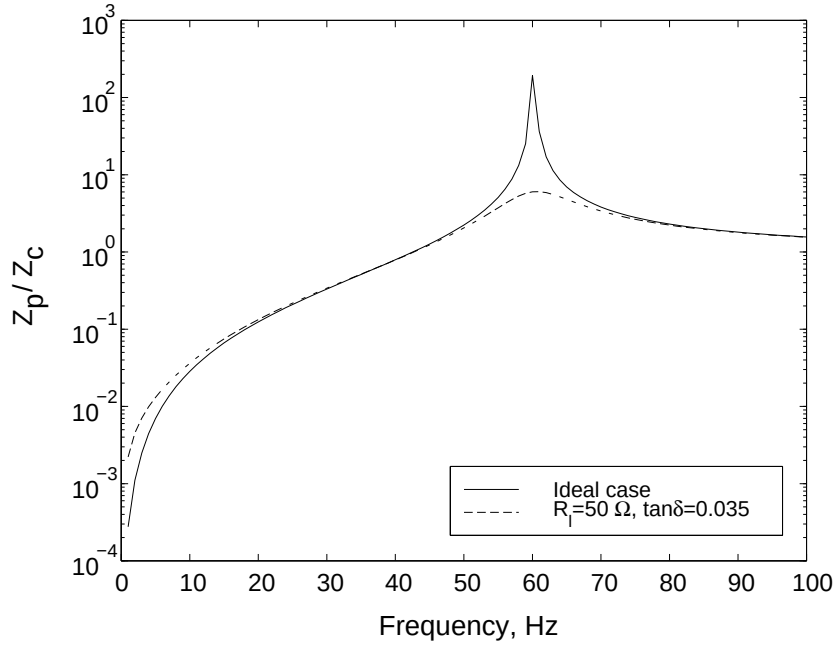

Figure 4.12 Variation of Z_p/Z_c with frequency for a 7μF actuator, in parallel with a 1H inductor

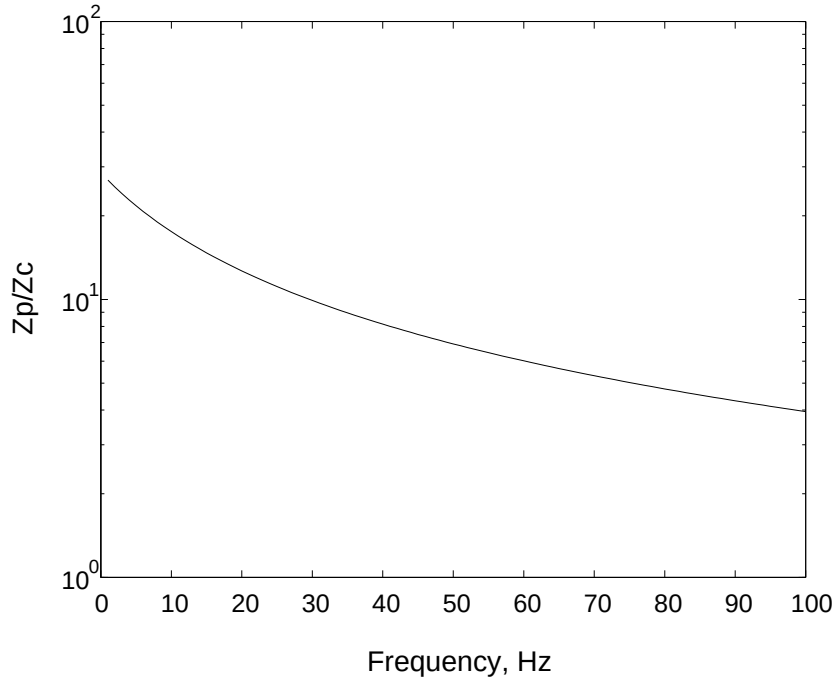

Figure 4.13 Z_p/Z_c achievable by continuous tuning, 7μF actuator, $R_l = 50\Omega$

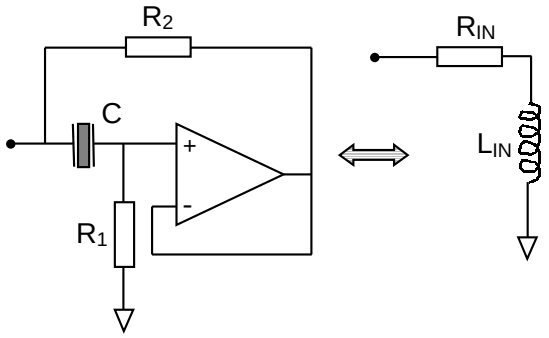

Figure 4.14 Pseudo-inductor circuit-1

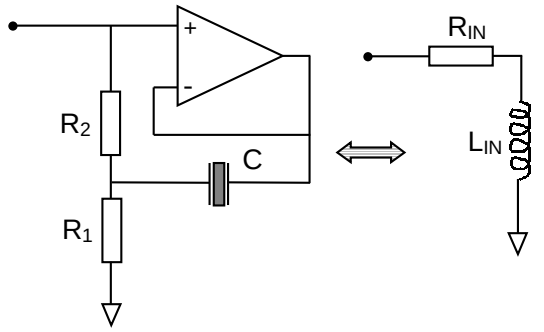

Figure 4.15 Pseudo-inductor circuit-2

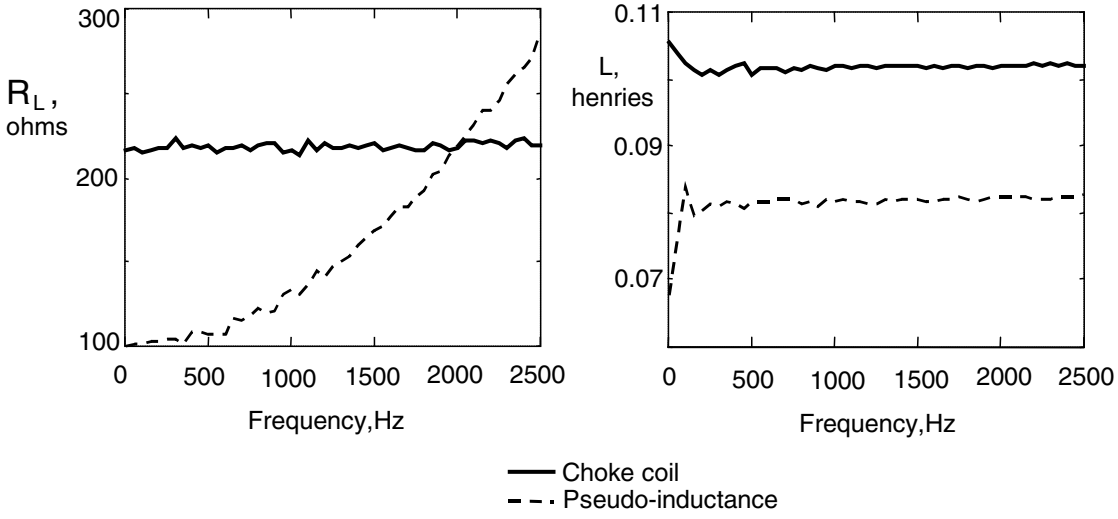

Figure 4.16 Comparison of choke coil and pseudo-inductor performance

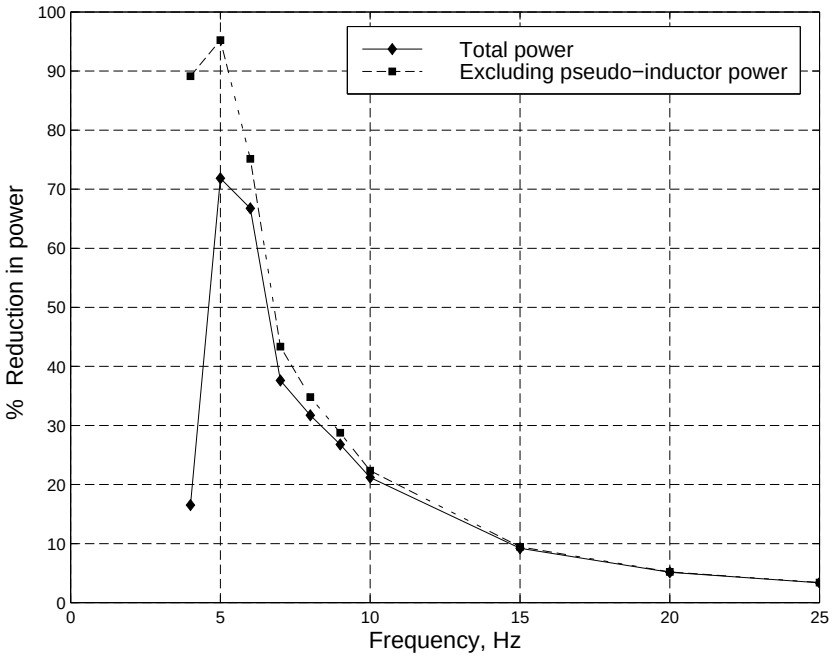

Figure 4.17 Pseudo-inductor circuit performance

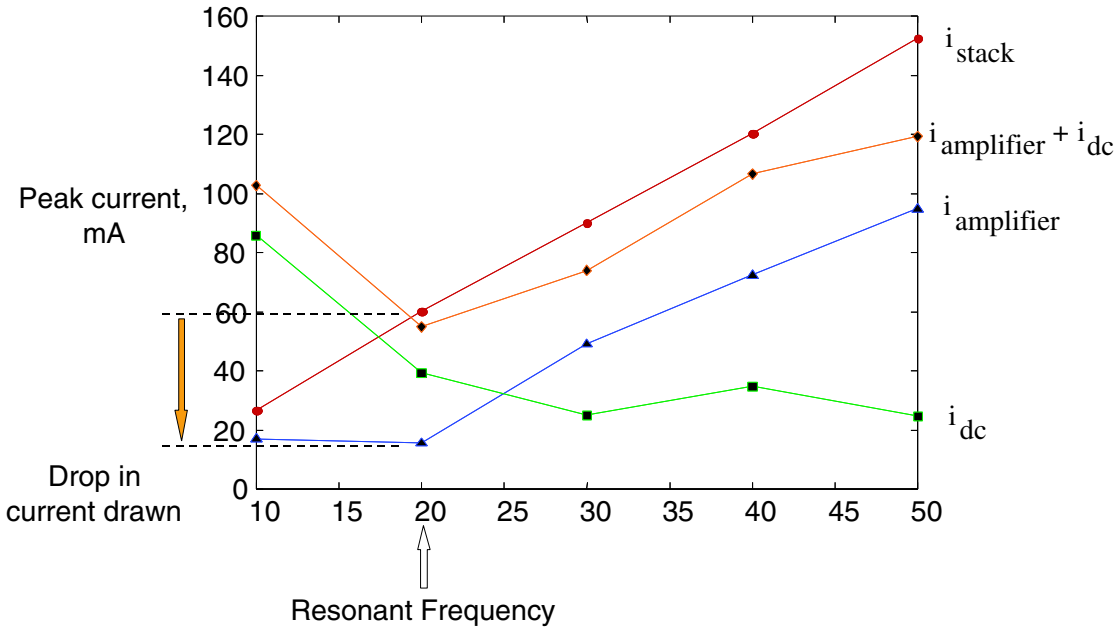

Figure 4.18 Variation of current drawn with frequency

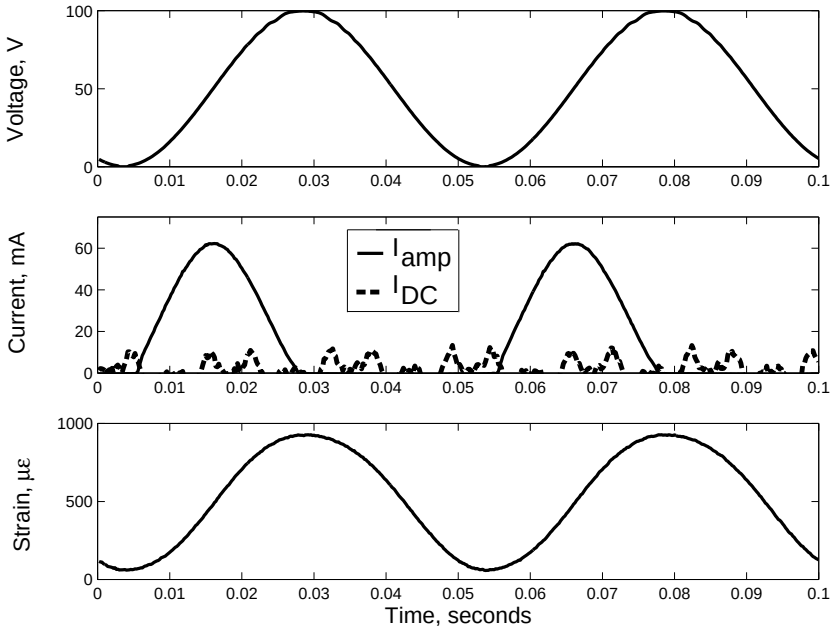

(**a**)Without pseudo-inductor

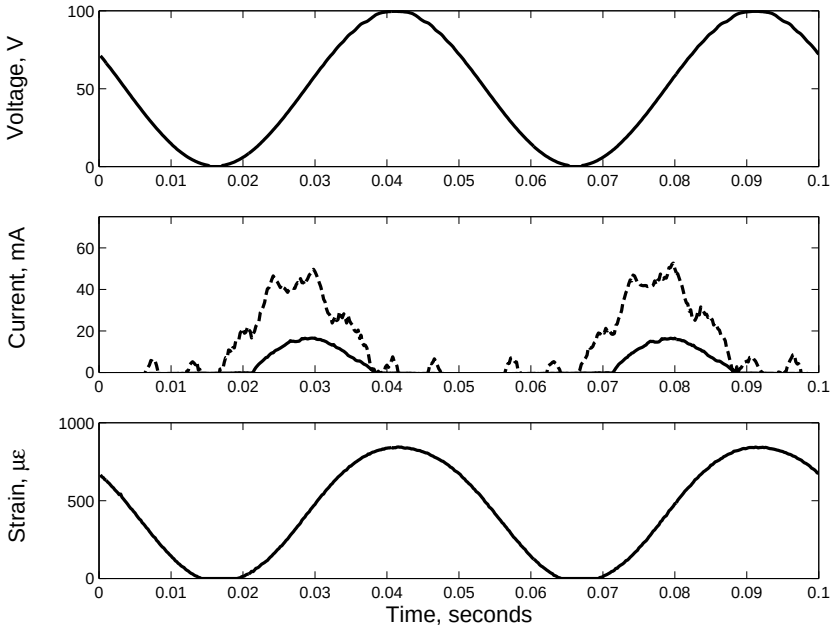

(**b**)With pseudo-inductor

Figure 4.19 Time variation of voltage, current and strain at 30 Hz

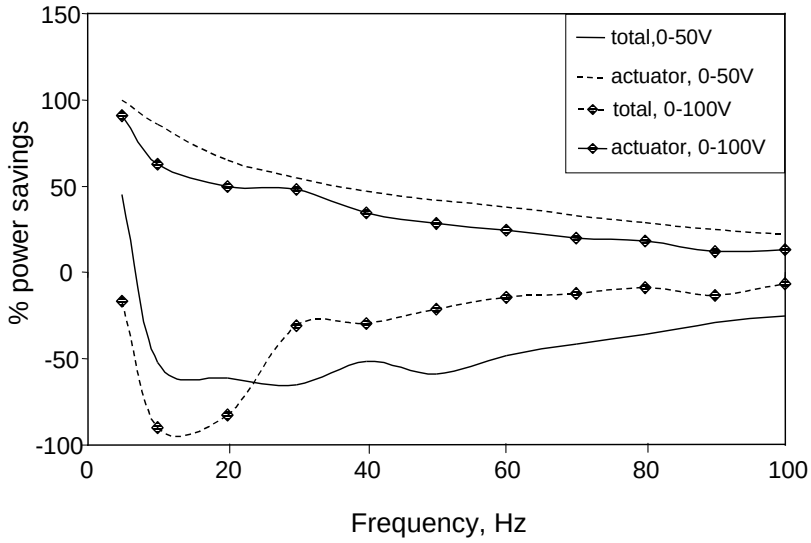

Figure 4.20 Pseudo-inductor circuit performance with adaptive tuning

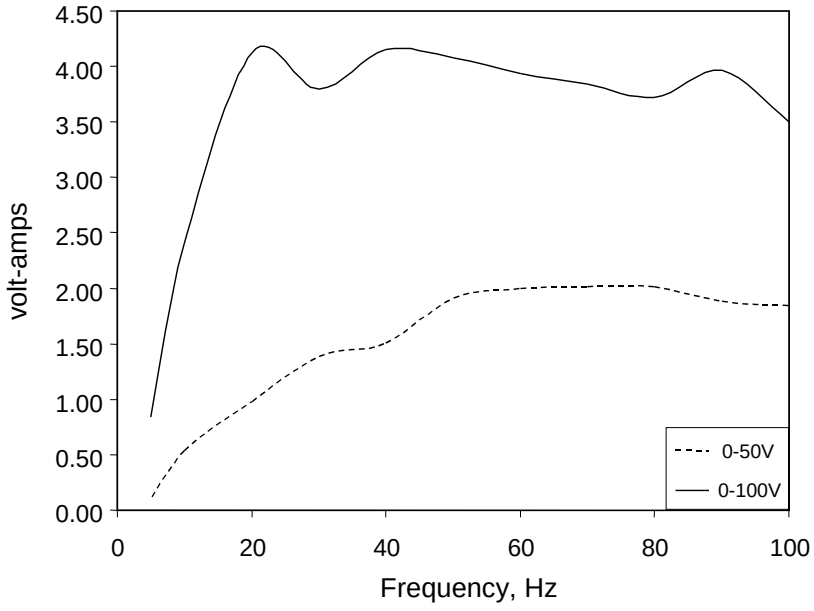

Figure 4.21 Pseudo-inductor power consumption

Chapter 5

Piezoelectric Hydraulic Hybrid Actuator: Design and Development

The previous three chapters discussed the various aspects of piezoceramic materials, from the point of view of their application in practical smart systems. As discussed in the Introduction Chapter 1, piezoceramic based mechanisms show great promise as potential actuators for aerospace applications, especially in the smart rotor concept. This is due to their high energy density and wide bandwidth as well as the low number of moving parts involved. The high energy density allows these actuators to meet the severe volumetric constraints imposed by smart rotor blade applications and the low number of moving parts decreases complexity and wear, and increases reliability of the system.

The major drawback of these actuators, however, is their low stroke. To overcome this problem, many different stroke amplification mechanisms have been investigated. These are discussed in more detail in Chapter 1. Amplification mechanisms in general involve many moving parts that contribute to actuation losses and degrade rapidly under high loading, especially the large centrifugal loads encountered on a helicopter rotor blade. In addition, the maximum practical amplification ratio is on the order of 15. At larger amplification ratios, the stiffness of the amplification mechanism itself becomes

a serious issue. Studies have shown that mechanical amplification leads to a 60-80% reduction in the overall energy density of the device, compared to that of the base active material [179].

Several actuation mechanisms based on the frequency rectification concept have been proposed in the past in order to increase the stroke of piezoceramic actuators without needing amplification mechanisms. The frequency rectification concept essentially trades off the high frequency actuation capability of piezoceramic actuators into a lower frequency mechanical output of the actuation device. This is achieved by a summation of small displacements of the piezoceramic actuator, over multiple actuation cycles, through an arrangement which can be thought of as a mechanical diode, into a larger net displacement. Several different methods of achieving frequency rectification have been proposed. Some of them, with brief descriptions, are listed below. A more detailed discussion can be found in Reference [180].

- **Inchworm motors** [181, 182, 183, 184]. These actuators utilize three or more piezostacks in order to achieve frequency rectification. Two groups of piezostacks are actuated in a specific sequence. One group of piezostacks provides the motive power, while the other group acts as a brake and alternately clamps the ends of the motive piezostack elements to a stationary rail or shaft. This results in a net displacement in only one direction. By actuating the motive stacks at a high frequency, the entire assembly can achieve moderately high linear velocities.

- **Rotary piezostack motors**. The concept is similar to the inchworm motors, except for the fact that the brake piezostacks engage a cylindrical stator and the motive piezostacks, which are mounted on a rotor, provide a torque about a central shaft [185]. Another rotary motor concept is based on rectifying the angular displacements created by a set of piezoelectric bimorphs vibrating at resonance

using a roller clutch [186, 187, 188]. As the roller clutch is a passive frequency rectification device, the construction of this device is much simpler than devices requiring active clamping by secondary piezoelectric actuators.

- **Ultrasonic motors** [138, 139, 70]. These motors are based on a traveling wave created in a ring of piezoelectric material. This ring is sandwiched between two fixed stator rings and presses against them. The motion of the traveling wave in the piezoelectric ring creates a frictional force between it and the stator. This results in a rotary motion. Several different types of this motor exist, travelling wave motors, standing wave ultrasonic motors, multi-mode ultrasonic motors and hybrid transducer ultrasonic motors. All these concepts are based on the same fundamental principle. Ultrasonic motors have been used to actuate control surfaces in an unmanned aerial vehicle as part of the Smart Wing program [75, 76]

- **Micropulse actuators**. This actuator is similar to an inchworm actuator, but in addition to linear motion along a drive element, it is capable of operating in a rotary mode [189]. Each actuator has four piezoelectric elements wedge shaped elements. The elements are energized in pairs, at ultrasonic frequencies. One pair causes the drive element to move to the right, and another pair causes it to move to the left. The basic principle is that due to the shape of the piezoelectric wedges, the expansion of the elements in response to an electric field causes the point of maximum gripping force to be off the center of the element. The unbalance in forces causes the element to move in one direction or the other.

5.1 Piezoelectric hydraulic actuation concept

A common feature of all the actuation mechanisms described above is their reliance on friction to achieve relative motion. As a result of this friction, the surfaces in contact

undergo a large amount of wear, that leads to a short useful lifetime of the actuator. These actuators also have to be built to very tight tolerances in order to achieve efficient frequency rectification. The wear of the surfaces adversely affects these tolerances and therefore affects the performance of the actuators. For example, the ultrasonic motor actuators used in the Smart Wing program have a lifetime on the order of a few hundred hours. In addition, the blocked force of the actuator depends on the maximum friction that can be achieved between the stationary and moving parts.

Recent years have seen the introduction of the piezoelectric hydraulic actuation concept. Although this concept is also based on the frequency rectification principle, it is not friction based. In addition, the hydraulic actuator system, with accumulators, has the capability of meeting high transient output requirements, which is very difficult to achieve by other means. The piezoelectric hydraulic actuation concept combines the advantages of piezoelectric actuation with hydraulic load transfer. A piezoelectric actuator is excited at a high frequency, displacing a fluid in a constrained volume referred to as the pumping chamber, through a displacement rectification device. The rectification device is a set of uni-directional flow valves, that allow the fluid to flow in only one direction. These valves are usually passive, for example, conventional ball type check valves, but several current research efforts are focussed on active valves. The piezoelectric actuator, pumping chamber and valves form a unit called a piezoelectric pump.

A large amount of research has been focused recently, especially in the biomedical field, into piezoelectrically driven micropumps [190, 191] for moving small quantities of fluid. Shoji et. al. [190] have compiled an extensive review of microflow devices. One microflow concept has been developed as a hybrid energy harvesting transducer [192]. Some of these designs also dispense with mechanical valves and achieve flow directionality by means of appropriately designing the geometry of

the inlet and outlet ports [193, 194, 195]. Several micropumps utilize piezoelectric unimorphs or bimorphs as their actuators, which are of relatively low stiffness but large free displacement. Other micropump concepts include peristalic pumps [196] and resonantly driven pumps [197]. However, most of these devices operate on the microscale and are too small to meet the output requirements of a smart rotor, both in terms of stroke and force.

Consider the operation of a generic piezoelectric pump, below its first fundamental frequency. For a given blocked force, the output flow rate, and therefore the output power, varies linearly with the free displacement of the piezoelectric actuator, and with the frequency of pumping. Hence, by increasing the fundamental frequency of the pumping assembly, it is possible to increase the maximum operating frequency, amd therefore the maximum power output. For this reason, it is not sufficient to have a piezoelectric actuator with a large free displacement. The actuator should also have a large blocked force, which implies a large stiffness. This translates into a high fundamental frequency of the assembly. It is for this reason that piezoelectric stacks are ideally suited as actuators for the piezoelectric pump.

In conjuction with an output actuator, and appropriate flow control valves, the piezoelectric pump forms a piezoelectric hydraulic hybrid actuator, also referred to in this thesis as the *device*. A schematic of the entire system is shown in Figure 5.1. The piezoelectric pump pressurizes the working hydraulic fluid, which then flows in a fixed direction according to the check valves installed in the pumping head. A high pressure accumulator and a low pressure accumulator are installed near the outlet and inlet ports of the pump respectively. The accumulators perform several important functions. Firstly, as shown in a subsequent section (Section 5.5.3), the stiffness of the accumulator is small compared to the stiffness of other elements in the system. Because of this, the load is effectively isolated from the piezostack, which as a result, sees a relatively

constant mechanical impedance irrespective of the load condition. This means that a set of system parameters can be calculated to optimize the pump performance relatively independent of load. Secondly, the accumulators filter out the high frequency pressure pulses generated by the pump. Thirdly, the accumulator stores energy, which can be made available to the load during times of sudden demand. However, in the interests of compactness, the device tested in this thesis does not include accumulators. The piezoelectric pump is directly connected to the output hydraulic actuator.

The output section of the device consists of a Wheatstone bridge network of flow control valves, and an output hydraulic actuator. The direction of actuation of the output is controlled by the network of flow control valves. The directional control could also be achieved with a single 4-way directional control valve. The directional control valves are actuated at the desired output frequency. Alternatively, in the case of using active valves in the pumping head, the functions of the check valves and the flow control valves could be combined and executed by the active valves alone. A study is being conducted into the feasibility of replacing the mechanical valves on the arms of the Wheatstone bridge as well as the check valves on the pump system with active magneto-rheological valves [198]. This will help to achieve a system with no moving parts, which will offer large benefits in terms of reduced complexity and improved lifetime.

Piezoelectric hydraulic hybrid actuators are not to be confused with hydraulic amplification devices [199, 200, 201]. Several such concepts have been proposed, that utilize a hydraulic fluid, contained in passages of appropriate geometry, purely as a stroke amplifier. These devices do not have any frequency rectification and are also limited in terms of the maximum achievable amplification ratio by the compressibility of the hydraulic fluid.

The present device was developed in conjunction with the Smart Material Actuated Servo Hydraulics (SMASH) program. The goal of SMASH technology development is

the creation of devices and systems that allow application of mechanical power output through hydraulics without the need for traditional hydraulic distribution lines. The result would be a compact, self-contained, localised actuation system physically situated at the required output location, for example, a control surface on a wing. The long range goal of this work is to actively control a flap on a rotor blade, to minimize vibration and noise.

Typical requirements for the output of the device are shown in Figure 5.2. As the present device is intended to be the next generation actuator for a typical smart rotor system, the output design goals are along the lines of a recently developed trailing edge flap actuator driven by piezoelectric stacks [131]. The above mentioned actuator was designed for a full scale MD-900 Explorer rotor blade section, with a force requirement of 18 lbs peak at 43 mils displacement. The final actuator achieved a blocked force of 9 lbs and a free stroke of approximately 80 mils.

5.2 Current state of the art

Recently, several actuator systems based on the concept of hybrid actuation are under development. Mauck and Lynch [202, 203, 204, 180, 205, 206] investigated a system consisting of a pump driven by a high voltage piezostack of length 10.2 cm and cross-sectional area 1.9 cm $\times$ 1.9 cm. Several versions of designs have been investigated, with accumulators incorporated into later designs. The final device achieved a blocked force of 61 lbs and an output actuator velocity of 7 cm/sec. The large current requirements and heating of the piezostack limited the pumping frequency of the system to 60 Hz. The overall performance of the system is analytically examined in terms of actuation efficiencies, and the effect of the viscosity of the hydraulic fluid was experimentally determined. A lumped parameter theoretical model of this system has been developed.

Nasser et.al. [207] presented a piezohydraulic actuation system that makes use of the compressibility of the working fluid in order to eliminate accumulators and 4-way valves. Use of active bidirectional valves is envisaged to control output actuator motion. One of the main goals of this work is to determine the effects of friction of the actuator on its performance. The piezostack driving this pump has a free stroke of 100μm and a capacitance of 40μF. The system was run at 10 Hz at an input voltage amplitude of 150 V, and demonstrated an overall amplification factor of 1.42. As this device made use of commercially available solenoid valves as active check valves, operation of the device was limited to very low pumping frequencies. As a result, it functions more as a hydraulic amplification device as opposed to a frequency rectification device. Theoretical modeling using a mechanical lumped parameter analogy has been developed [208], and the efficiency of piezohydraulic and piezopneumatic actuation has been analyzed [209].

A magnetostrictive water pump, which is conceptually similar to a pump driven by a piezoelectric stack, has been developed by Gerver et. al. [210]. This pump operates at a relatively low pressure, on the order of 5psi, and makes use of an additional hydraulic stroke amplification scheme to increase the flow rate. A flow rate of 15ml/sec at an output pressure of 5psi has been reported.

Konishi et. al. [211, 212] have developed a piezoelectric hydraulic hybrid actuator using a piezostack of length 55.5mm and diameter 22mm. The operating voltage of this piezostack is -100V to +500V and its free strain and blocked force are 60μm and 10.8kN respectively. This piezoelectric pump was excited at 300 Hz and delivered an output power of approximately 34 W. Mathematical models were developed and the possibility of using fluid resonance to increase the output power was investigated [213, 214].

5.3 Basic working principle

A simplified diagram of the working cycle of the piezoelectric pump is shown in Figure 5.3. This working cycle assumes that the working hydraulic fluid is an ideal fluid, that has an infinite bulk modulus. The part of the curve labeled OA corresponds to the compression stroke of piezoelectric pump. In this part of the cycle, the pumping chamber pressure increases at essentially zero displacment of the piezostacks, till the point A, at a pressure P_{load}. At this point, the force in the output hydraulic actuator is equal to the external load. The outlet check valve then opens and the piezostacks expand to the point B, which is their maximum displacement state δ_o. Useful external work is done in the segment BC, wherein the output load undergoes some displacement. The segment BC is the return stroke of the piezostacks, where the pumping chamber pressure falls back to the original value and the piezostacks subsequently deform to their initial length. The work output from the piezostacks is equal to the area OABCO. The theoretical efficiency of such a system can be shown to be twice that of the same piezostacks driving a simple spring type load [202], in which case the work output per cycle is the area OBCO.

However, in practice, all fluids have a finite bulk modulus. This results in deformation of fluid under an external pressure and leads to the actual working cycle of the piezoelectric pump as shown in Figure 5.4. The compression stroke, OB now has a slope less than 90° due to the finite stiffness of the working fluid. The limits of operation of the device are defined by the points B and C. The point B is the point of intersection of the fluid stiffness line and the piezostack load line. At this point, all the deformation of the piezostack actuator goes into deformation of the fluid in the pumping chamber. The work output of the actuator is essentially stored as potential energy in the fluid and is returned to the actuator in the return cycle. Hence, the net work output of the device is

zero, and this condition is the output blocked condition. The corresponding force at the output hydraulic actuator is the blocked force of the device. At point C, the only force on the piezostacks is due to the required cracking pressure of the check valves. Once this is overcome, the fluid flows freely through the circuit. At this point, the maximum flow rate, or no-load flow rate of the piezostack pump is achieved. The output work of the device is however, zero, as the output load in this condition is zero. Maximum work output of the device is achieved at an intermediate point. This is discussed in more detail in Section 5.5.

It is worth mentioning here that Figure 5.4 also contains some level of idealization. In reality, the segments AC and OD will have a non-zero slope, corresponding to the effective stiffness of the working fluid throughout the circuit. However, as the volume of fluid in the circuit is large compared to the volume of fluid in the pumping chamber, the stiffness of the fluid in the circuit, which effectively means the slope of these segments, will be much less than that of the segments OB and CD. Hence, this slope is approximated to be zero, and for the remainder of this thesis, the segments AC and OD are assumed to be horizontal.

5.4 Prototype design and construction

A schematic of the piezoelectric pump is shown in Figure 5.5. Technical drawings of the parts are included in Appendix A. An exploded assembly drawing of the piezoelectric pump is shown in Figure 5.6. The main components of the pump are the piezostack assembly, piston assembly, pump body, pumping head and preload assembly.

The piezoelectric stack assembly consists of two commercially available low voltage piezostacks (model P-804.10, Physik Instrumente) [137]. These piezostacks were chosen on the basis of a previous study by Lee et. al. [131, 130] that demonstrated

that these piezostacks have the highest energy density out of 15 other commercially available piezostacks investigated. The piezostacks are bonded together, end to end, with a steel end cap bonded on one end. The steel end cap has one spherical face, that comes into contact with the piston and pushes against it. The spherical face eliminates any adverse bending moments from being transferred to the piezostack. The other end of the piezostacks is bonded to a preload mechanism, that can be moved in and out by means of a preload screw. All bonding was by means of a cyanoacrylate type adhesive.

The preload assembly consists of a preload base fixture and a preload screw. The preload screw serves to adjust the position of the piezostack assembly relative to the pump body as well as to provide a compressive preload to the piezostacks. The compressive preload is necessary to maintain the physical inegrity of the piezostacks, which have very low tensile strength.

The piezostack assembly is in contact with the piston assembly, which is a steel piston bonded to a diaphragm. The steel piston has a tight running fit with a bore in the pump body. The diaphragm is fabricated out of a 0.002” thick C-1095 spring steel sheet. The piston serves two purposes. Firstly, it constrains the deflected shape of the diaphragm to remain flat over most of its surface, except around its circumference, and therefore maximizes the displaced volume per cycle. Secondly, the tight fit of the piston with the pump body eliminates, to a large extent, any rocking motion of the piston. The main purpose of the diaphragm is to provide a leak-proof seal, and to increase the stiffness of the piezostack-piston assembly. While one face of the pumping chamber is formed by the movable piston, the other face is formed by the pumping head. This part of the pump contains the two check valves, as well as a pressure transducer for measuring the pumping chamber pressure.

The first prototype was fabricated out of C-1018 steel, however, in order to save weight, the final design could be fabricated out of aluminum. The parts of the

piezoelectric pump are shown in Figure 5.7(a) and the assembled piezoelectric pump is shown in Figure 5.7(b). A sealing ring was also fabricated to measure the piston displacement. This part is exactly like the pumping head, with the center bored out, leaving behind only the seat that clamps the diaphragm to the pump body. The sealing ring is replaced with the pumping head after measuring the piston displacement, prior to filling the device with hydraulic fluid. The overall length of the entire piezoelectric pump assembly is under 4" and it has a square cross-section with each side of length 1.5". Strain gages are bonded on the piezostacks to measure the strain of the piezostacks during operation and their temperature is measured using a thermocouple, not shown in the figure, that is mounted directly on the piezostacks. The sizing of the various geometrical parameters of the piezoelectric pump is discussed below.

5.5 Preliminary sizing considerations

5.5.1 Quasi-static pumping assumption

The performance of the device is highly sensitive to the dimensions of both the pumping chamber and the output hydraulic actuator. The viscosity of the fluid, diameter of the tubing, and the modulus of elasticity of the tubing material also play important roles in the frictional losses that occur in the device as well as its frequency response. However, for an initial design, it is convenient to neglect any frequency dynamics of the system, and assume a constant response at all pumping frequencies. As a result of this quasi-static pumping assumption, the volumetric flow rate of the pump, Q, at any given pumping frequency is equal to the product of the volumetric displacement of the pump per cycle, Δ_{pump} and the pumping frequency f_{pump}.

$$Q = \Delta_{\text{pump}} f_{\text{pump}} \tag{5.1}$$

The large flexibility in trading off force and stroke afforded by the use of hydraulics results in many possible combinations of pumping chamber and output actuator dimensions. The final design is therefore very dependent on the output requirements of the device. Keeping in mind the ultimate goal of maximizing output power density, for a device of known external dimensions, the output power is considered to be the primary performance metric.

The major variables on which the power output depends are:

1. Pumping chamber diameter, d_{cham}
2. Output actuator diameter, d_{out}
3. Pumping chamber height, Δ_{gap}
4. Piezostack characteristics
    (a) Blocked force F_{block}
    (b) Free displacement δ_{free}
5. Fluid compressibility, β

A piezostack which is known to have a high energy density [131], PI-804.10 [141] is chosen to drive the pump, and hence the piezostack characterisitics are assumed to be constant for this tradeoff study. Similarly, the fluid compressibility is also assumed constant, because a low viscosity standard hydraulic oil, MIL-H-5606F was chosen as the working fluid.

5.5.2 Work output per cycle: load-line analysis

The power output of the device is given by the area under the load-force curve (area OABCO, Figure 5.8). As a result of the quasi-static pumping assumption

(Equation (5.1)), to maximize the output power, it is sufficient to maximize the work done by the device per pumping cycle.

The work done per cycle is given by

$$\Delta W_{\text{cyc}} = F_{\text{o}}\delta_{\text{o}} \tag{5.2}$$

The equation of the piezostack load line is given by

$$\delta = \delta_{\text{free}}\left(1 - \frac{F}{F_{\text{block}}}\right) \tag{5.3}$$

In order to calculate the area under the curve, it it necessary to derive expressions for the locations of the points A, B and C. This involves calculating the stiffness K_{f}. At this point, it would be worthwhile exploring the stiffness of each constituent of the hydraulic circuit and developing an equivalent system model.

5.5.3 Simplified system model

The overall system can be represented as an arrangement of single degree of freedom spring-mass systems. As the present analysis is quasi-static, the mass terms are ignored (Figures 5.9and 5.10), yielding a static solution for deformations of the system. It should be noted that Figure 5.9 is the equivalent system representation when the outlet valve is open, and the output hydraulic cylinder is assumed clamped. The effective stiffness obtained from this configuration will give the slope of the segments AB and CO. The equivalent system when both valves are closed, which leads to the stiffness K_{f} is shown in Figure 5.10. This stiffness is only due to the fluid in the pumping chamber.

Neglecting inertia terms is considered sufficient as a first approximation of the system for the purposes of designing overall system parameters. The effect of viscosity is also neglected in this analysis. It may be possible to improve the performance of subsequent designs by including dynamic effects in the analysis by taking into

consideration inertial terms. The system model can be broken down into the following elements

1. Pump body
2. Piezostack internal stiffness
3. Piston and Diaphragm
4. Fluid and Tubing
5. Accumulators

Each element can be considered as a linear mechanical spring element with a force-deflection characteristic of the form

$$\Delta F = K_{\text{spring}} \Delta x \tag{5.4}$$

where ΔF is the change in force in the spring, K_{spring} is the spring constant and Δx is the change in length of the spring.

Alternatively, the stiffness of element can be expressed in terms of its compressibility as [215, 216]

$$\Delta P_e = \beta_{\text{eff}} \frac{\Delta \mathbb{V}_e}{\mathbb{V}_e} \tag{5.5}$$

where ΔP_e is the change in pressure in the element, β_{eff} is the effective bulk modulus, or compressibility of the element and $\mathbb{V}_e$ and $\Delta \mathbb{V}_e$ are the volume and change in volume of the element respectively. From the above two equations, for an element of cross-sectional area A_e

$$\beta_{\text{eff}} = \frac{K_{\text{spring}} \mathbb{V}_e}{A_e^2} \tag{5.6}$$

5.5.4 Pump body

The stiffness of the pump body depends on its cross-sectional area, and the material used in its construction. The stiffness is calculated based on simple linear elastic theory and is designed to be much larger than the piezostack stiffness.

5.5.5 Piezostack internal stiffness

Investigations into piezostack characteristics carried out in the past [130, 131] have shown that their output displacement amplitude is independent of the preload applied to the piezostack. Hence, the bias pressure in the circuit, which acts as a preload on the piezostacks, does not directly affect their output stroke. The piezostack itself can be modeled as a spring of stiffness K_{p}, which is the internal stiffness of the piezostack, acted on by a force F_{block} that is equal to the blocked force of the piezostack. The stiffness of the piezostack, K_{p} is given by

$$K_{\mathrm{p}} = \frac{F_{\mathrm{block}}}{\delta_{\mathrm{free}}} \tag{5.7}$$

5.5.6 Piston and diaphragm

The piston is assumed rigid and the diaphragm is modeled as an annular plate undergoing pure bending deflections. For such a geometry, assuming the outer edge is perfectly clamped, and the inner edge, which is bonded to the rigid piston undergoing only an axial degree of freedom, the central deflection w_{max} is given by [217]

$$w_{\mathrm{max}} = K_{\mathrm{d}} \frac{P_d \, r_{\mathrm{inner}}^4}{Y t^3} \tag{5.8}$$

where the constant K_{d} is

$$K_{\mathrm{d}} = \frac{3(1-\nu^2)}{16} \left[1 - \left(\frac{r_{\mathrm{inner}}}{r_{\mathrm{outer}}} \right)^4 - 4 \left(\frac{r_{\mathrm{inner}}}{r_{\mathrm{outer}}} \right)^2 \log \frac{r_{\mathrm{inner}}}{r_{\mathrm{outer}}} \right] \tag{5.9}$$

In the above equations, P_{d} is the differential pressure acting on the diaphragm, r_{inner} and r_{outer} are the inner and outer radii of the annulus, t is the diaphragm thickness, and Y and ν are the Youngs Modulus and Poissons ratio respectively of the diaphragm material. From these equations, an expression for $K_{\mathrm{diaphragm}}$ can be derived. From Figure 5.11, it can be seen that the force-displacement characteristic is quite linear and the assumption of pure bending deformations is justified.

5.5.7 Fluid and tubing

The fluid and tubing can be treated as two elements with their stiffnesses adding like springs in series. The effect of the tubing stiffness can be treated as an effective change in the bulk modulus of the fluid. The compressibility of the tubing, β_{tube} is given by [215]

$$\beta_{\mathrm{tube}} = \frac{d_{\mathrm{i}}}{4\delta r} \tag{5.10}$$

where d_{i} is the inner diameter of the tube and δr is the radial displacement of the tube, given by

$$\delta r = \frac{d_i P_i}{2Y_{\mathrm{tube}}} \left[\frac{d_i^2 + d_o^2}{d_o^2 - d_i^2} + \nu_{\mathrm{tube}} \right] \tag{5.11}$$

where d_o is the outer diameter of the tube, subjected to an internal pressure rise P_i. The Youngs Modulus and Poissons ratio of the tube, which is made of aluminum in the present system, is Y_{tube} and ν_{tube}.

5.5.8 Accumulators

The accumulators used in the present system are commercially available, 1 pint capacity accumulators of the bladder type, charged with nitrogen gas. The stiffness of the bladder itself is ignored in this analysis and only the stiffness of the gas in the accumulator, with a volume V_{gas} and a pressure P_{gas} is considered. For this volume of gas, assuming the

change in volume due to the pumping is an adiabatic process,

$$P_{\text{gas}} V_{\text{gas}}^{\gamma} = \text{Constant} \tag{5.12}$$

where γ is the gas constant. This leads to

$$\beta_{\text{gas}} = -\gamma P_{\text{gas}} \tag{5.13}$$

Comparing the relative magnitudes of the above stiffnesses for a typical set of system parameters, it can be seen that the stiffness of the accumulators is small compared to the large stiffness of the fluid and tubing. The diaphragm stiffness is approximately 10% of the piezostack stiffness in the current design. As a result of this, the fluid and tubing can be considered rigid, the accumulator stiffness can be ignored, and the system can be approximated to a piezostack working against the load stiffness alone.

5.5.9 Work done per cycle: calculation of operating points

In the analysis, an effective load-force curve of the piezostack is used. This is obtained by re-scaling the original load line to account for the decrease in free stroke and block force of the piezostack-diaphragm assembly as a result of the diaphragm stiffness.

From Figure 5.8, and Equation (5.3),

$$\delta_{\text{o}} = \delta_{\text{free}} - F_{\text{o}} \left[\frac{1}{K_{\text{p}}} + \frac{1}{K_{\text{f}}} \right] \tag{5.14}$$

where K_{f} is the stiffness of the column of fluid in the pumping chamber and K_{p} is the stiffness of the piezostack. Defining an effective stiffness, K_{eff}

$$\delta_{\text{o}} = \delta_{\text{free}} - \frac{F_{\text{o}}}{K_{\text{eff}}} \tag{5.15}$$

It can be seen that the effective stiffness is just the series combination of the piezostack and fluid stiffnesses. From Equations (5.15) and (5.2), the work output of

the device per cycle is

$$\Delta W_{\text{cyc}} = F_{\text{o}} \left[\delta_{\text{free}} - \frac{F_{\text{o}}}{K_{\text{eff}}} \right] \tag{5.16}$$

This work is expressed in terms of pressure and displacement inside the pumping chamber. Figure 5.12 shows a schematic of the fluid column between the pumping chamber and the output actuator. The pumping chamber has a cross-sectional area A_{p} and a displacement δ_{p}, while the output actuator has a cross-sectional area A_{out} and a displacement δ_{out}. The area ratio is given by

$$A_{\text{R}} = \frac{A_{\text{out}}}{A_{\text{p}}} \tag{5.17}$$

The work output per cycle can be rewritten in terms of the force and displacement of the output actuator

$$\Delta W_{\text{cyc}} = \frac{F_{\text{out}}}{A_{\text{R}}} \left[\delta_{\text{free}} - \frac{F_{\text{out}}}{A_{\text{R}} K_{\text{eff}}} \right] \tag{5.18}$$

5.5.10 Stiffness of the fluid in the pumping chamber

The stiffness of fluid in the pumping chamber can be derived using Equations (5.4), (5.5) and (5.6). Consider a fluid filled chamber, of uniform cross-sectional area A_{cham}, with a movable piston at one end (Figure 5.13). Under an axial force F, the piston moves by δx, deforming the fluid volume. The initial volume of fluid is $\mathbb{V} = A_{\text{cham}} \Delta_{\text{gap}}$. The rise in pressure of the fluid ΔP is given by

$$\begin{aligned} \Delta P &= -\beta \frac{\Delta \mathbb{V}}{\mathbb{V}} \\ &= -\beta \frac{A_{\text{p}}^2 \delta x}{A_{\text{p}} \Delta_{\text{gap}}} \end{aligned} \tag{5.19}$$

Using Equation (5.4), this results in an expression for the stiffness of the fluid in the pumping chamber

$$K_{\text{f}} = \beta \frac{A_{\text{p}}}{\Delta_{\text{gap}}} \tag{5.20}$$

For given working fluid, β is fixed, and A_p may be constrained by other factors, especially overall size. However, the designer is relatively free to decide on a value for the pumping chamber height, Δ_{gap}, which gives him a powerful method of adjusting the fluid stiffness. Substituting the expression for fluid stiffness back in Equation (5.18), the expression for output work per cycle is

$$\Delta W_{cyc} = \frac{F_{out}}{A_R}\delta_{free} - \frac{F_{out}^2}{A_R^2 K_p} - \frac{F_{out}^2 \Delta_{gap}}{A_R^2 \beta A_p} \tag{5.21}$$

5.5.11 Maximum output work

The dimensions of the output actuator are fixed by overall geometric constraints; a commercially available 0.5" bore hydraulic actuator was chosen for the present device. This fixes the value of A_{out} and the only parameters that remain to be fixed are the diameter and height of the pumping chamber.

It should be noted here that although maximum work output is the primary goal of the device in order to achieve maximum possible power density, the application specifications may dictate a certain displacement requirement at a certain bandwidth (Figure 5.2). This requirement directly translates into the flow rate of the piezoelectric pump. A given output power, being the product of force and velocity, can be achieved with a high force and low velocity or a low force and a high velocity. Therefore, in addition to sizing the parameters of the device for maximum per cycle output work, the constraint of achieving the required output displacement must also be included in the design process.

Plots of the variation of output work with A_{out} and Δ_{gap} are shown in Figure 5.14. In Figure 5.14(a), the work output per cycle is plotted as a function of pumping chamber diameter for various output loads, with a pumping chamber height of 0.05". The maximum work output per cycle is achieved at a certain value of pumping chamber

diameter, and this maximum decreases with output load. Figure 5.14(b) shows the work output per cycle as a function of pumping chamber height, for a pumping chamber diameter of 1". The maximum work output increases monotonically (at a slower rate) with decreasing pumping chamber height. This is to be expected as a smaller pumping chamber height increases the stiffness of the fluid and essentially provides a direct energy transfer to the output load. As this function has no extremum, a value of pumping chamber height between 0.02" and 0.05" can be chosen depending on other factors such as machinability and clearances.

The condition for maximum output work per cycle, which is equivalent to the maximum output power, is obtained by differentiating Equation (5.21) with respect to the two parameters A_p and Δ_{gap}

$$\frac{\partial(\Delta W_{cyc})}{\partial A_p} \Rightarrow A_p = F_{block}\frac{A_{out}}{2F_{out}} - \Delta_{gap}\frac{K_p}{2\beta} \tag{5.22}$$

If $\beta \rightarrow \infty$ in the above equation, the value of A_p reduces to an impedance matched condition, i.e., at the midpoint of the piezostack load line. This is as expected, since the maximum power output is known to occur at an impedance matched condition [203, 202].

Based on the above discussion, taking into consideration any geometric constraints on the overall size of the device, an optimum pump geometry can be arrived at for a given output load. The fluid compressibility, which is a key parameter on which the power output of the device depends, can be very different from the reference value specified in the data sheet. The actual compressibility depends on several factors, like the system bias pressure and the amount of air entrained, and can be as low as 10% of the reference value [216]. This can have a significant effect on the output performance. It should be noted that the reference fluid bulk modulus is specified at 2500 psi, with no

entrained air. The actual fluid bulk modulus is given by [218]

$$\beta_{\text{fluid}} = E_{\text{p}} \times E_{\text{a}} \times \beta_{\text{ref}} \tag{5.23}$$

where E_{p} and E_{a} are the correction factors for bias pressure and entrained air, and β_{ref} is the reference fluid bulk modulus, which for the current fluid is given as 260,000 psi (Table 5.1. For the current system bias pressure of 50 psi, $E_{\text{p}} = 0.9$. The fraction of entrained air is assumed to be 1%, which is not an uncommon value for hydraulic systems. For this amount of entrained air, $E_{\text{a}} = 0.1$. It can be seen that the entrained air has a strong influence on the effective fluid bulk modulus, however, dissolved air is known to have no effect on the effective bulk modulus [216]. Substituting these values into Equation (5.23), the effective fluid bulk modulus is obtained as

$$\beta_{\text{fluid}} = 0.9 \times 0.1 \times \beta_{\text{ref}} = 23400 \text{ psi} = 0.16 \text{ GPa} \tag{5.24}$$

For the present proof of concept experimental device, the diameter of the pumping chamber was set at 1” and the height of the pumping chamber was set at 0.05”. A list of all the important parameters of the current design is shown in Table. 5.1. The piezostack data provided is for each piezostack [131].

In order to get a rough estimate of the blocked force of the device and the no-load cylinder velocity, an approximate calculation can be performed, with the quasi-steady pumping assumption. From Figures 5.4 and 5.8, the blocked force, or the maximum output force of the device F_{max} is obtained when $\delta_{\text{o}} = 0$. Applying this condition to Equation (5.14) leads to

$$F_{\text{max}} = \frac{\delta_{\text{free}}}{1/K_{\text{p}} + 1/K_{\text{f}}} \tag{5.25}$$

The value of K_{f} for the present parameters can be calculated using Equation (5.20). After substituting these numbers in the above equation, the estimated $F_{\text{max}} = 30.7$ lbs.

To estimate the no-load cylinder velocity, assuming a piston deflection of 0.8 mils, and given the device geometry in Table 5.1, the output swept volume per cycle is

Piezostack – Model P-804.10		
Number of piezostacks	2	
Length	0.3937	in
Width	0.3937	in
Height	0.7087	in
Blocked Force (0-100V)	1133	lbs
Free strain (0-100V)	1035	$\mu\varepsilon$
Free displacement (0-100 V)	≈ 12	μm
Maximum voltage	120	V
Minimum Voltage	-24	V
Capacitance	$\approxeq 7$	μF
Hydraulic Fluid – MIL-H-5606F		
Density	859	gm/cc
Kinematic Viscosity	15	centistokes
Reference Bulk Modulus β_{ref}	260,000	psi
Pumping Chamber		
Diameter	1	in
Height	0.050	in
Output Actuator - Double Rod		
Bore diameter	0.5	in
Shaft diameter	0.25	in
Stroke	2	in

Table 5.1 Prototype device parameters

0.6283×10^{-3} in^3. This is the same as the flow into the output hydraulic actuator, which gives, for a pumping frequency of 300 Hz, a no-load cylinder velocity of 1.2797 in/sec. It should be noted that since the above estimate neglected fluid compressibility and flow resistance, this estimate represents an upper bound on the actual no-load cylinder velocity.

5.6 Pumping head and check valves

The pumping head and check valves are the most important part of the piezoelectric pump. As mentioned above, the pumping chamber height is a very important parameter on which the output of the device depends. In the present device, this is set as 0.050“. The pumping head also has a port to allow measurement of the pumping chamber pressure with a pressure transducer. As real fluids have a non-zero viscosity, there is a flow resistance and therefore a pressure drop associated with the fluid flowing through the check valves. The ideal check valve would have a zero flow resistance in the forward flow direction, infinite flow resistance in the reverse flow direction and an infinite bandwidth.

Real check valves, however have a finite flow resistance and some amount of leakage in the reverse flow direction, which however is small enough to neglect for all practical purposes. Real check valves also have a finite bandwidth and their response starts rolling off at high frequencies. From the point of view of the piezoelectric pump, this is a major disadvantage. As discussed above, as the pumping frequency of the piezoelectric pump increases, the flow rate increases and therefore the output power increases. However, if the pumping frequency starts approaching the resonant frequency of the check valves, the phasing of the opening and closing of the check valves with respect to the pumping becomes significant and the flow rate starts to deteriorate. At even higher pumping

frequencies, the check valve ceases to respond to the pressure pulses caused by the pumping, and the flow rate goes to zero. Any potential increase in output performance obtained as a result of increasing the pumping frequency would be negated by using check valves with a low bandwidth. Therefore, in order to achieve as high an output power density as possible, it is imperative to have check valves with a bandwidth significantly larger than the pumping frequency.

Two types of check valves were tested in the present piezoelectric pump.

1. **Type I** Ball type check valves
2. **Type II** Reed valves

5.6.1 Type I valves

The Type I valves are commercially available ball type check valves [218]. A cross-sectional view of one of these valves is shown in Figure 5.15(a). The spring ensures that under zero external differential pressure, the valve is in a closed condition, and a positive pressure differential in the flow direction is required to open it. This pressure differential is called the cracking pressure. From the construction of the valves, it can be seen that the valve can be approximated as a single degree of freedom mass-spring-damper system, with the appropriate frequency response. By increasing the stiffness of the spring, the natural frequency of the valves can be increased, but this also consequently increases the cracking pressure. Figure 5.15(b) shows a pair of these valves assembled in the pumping head.

5.6.2 Type II valves

The Type II valves were reed valves designed and fabricated in-house. A cross-sectional view of one of the reed valves is shown in Figure 5.16(a). The reeds were machined

from a sheet of 0.002” thick C-1095 spring steel. The base of the reed was attached to the body of the valve by a bead of solder, in order to make the valve as simple and compact as possible. Comparing Figures 5.15(a) and 5.16(a), it can be seen that the inertia of the oscillating member, which is the ball in the case of the Type I valves, and the reed in the case of the Type II valves, is much lower in the Type II valves. Therefore, it is expected that the bandwidth of the Type II valves will be much larger than that of the Type I valves. Assuming a perfectly clamped condition at the solder bead, the Type II valves were designed to have their first resonant frequency around 3 KHz. However, as the solder bead is not a rigid boundary condition, the actual resonant frequency is expected to be somewhat lower than the calculated value. Type II valves are shown installed in the pumping head in Figure 5.16(b). It can be seen that the Type II valves can easily fit into the same diameter pumping head as the Type I valves. In fact, the pumping head can be shorter in the case of the Type II valves, because they are much shorter than the Type I valves.

Multiple check valves can be installed in the pumping head in order to decrease their effective flow resistance.

5.7 Delivery of electrical power

As the piezoelectric pump is basically an electrical to mechanical energy conversion device, the delivery of electrical power to the device is an important aspect of the design. As discussed in Chapter 4, the piezoceramic stacks present a predominantly capacitive load to the power amplifier driving them. A low voltage piezostack was chosen to drive the piezoelectric pump in order to avoid the hazards of high voltages. The maximum working voltage of the piezostack, 100 V, is also well within the range of the power supply buses widely used on modern aircraft. The total capacitance of the two

piezostacks driving the present piezoelectric pump is approximately 14 μF (Table 5.1). At an operating frequency f Hz, the peak current i_{p} drawn by the piezostacks will be

$$i_{\mathrm{p}} = 50 \times 2 \times \pi f C_{\mathrm{p}} = 4.396 f \quad \mathrm{mA} \tag{5.26}$$

At an operating frequency of 100 Hz, this translates to a current of approximately 0.44 Amps. Although a large part of the power supplied is reactive in nature and is returned to the power amplifier, supplying such large currents would necessitate big amplifiers. The piezoelectric hydraulic hybrid actuator would then require large heavy amplifiers to drive it, effectively reducing the attractiveness of the device as a compact actuation solution [219]. A more detailed discussion on the topic of power consumption by piezoceramic actuators can be found in Chapter 4. Several solutions exist to this problem. The use of L-C oscillatory circuits to reduce the current drawn is not feasible in this case, because the operating frequency is very high, resulting in a low L/C ratio, and consquently, low performance benefits. Switching power amplifiers can be used, resulting in a large decrease in weight and volume compared to conventional linear amplifiers.

5.7.1 Piezostack driver

A completely different solution to the problem is to recognize that the piezostacks need not be excited by a sinusoidal voltage. For a given peak displacement, as the swept volume per cycle is constant, the only parameter of consequence to the performance of the device is the frequency of excitation. Figure 5.17 shows the schematic circuit diagram of a piezostack driver based on this idea, that was designed and fabricated in-house. This driver will be referred to as the *switched driver* in subsequent discussions, and should not be confused with a switched mode power supply, or a switching power amplifier. Examples of this same driving concept can be found in the device of Konishi

et. al. [211, 212] and also in various types of droplet generators, such as in inkjet printers. The circuit basically consists of two N-channel MOSFETS, labeled A and B. The piezostack is represented by a capacitance, C_p and is connected in series to the MOSFETS by a current limiting resistance, R_{LIM}. The drain of MOSFET A is connected to a DC power supply, V_{DC}, which for example, would be the DC power bus on an aircraft. Depending on the level of the control voltage, the MOSFETS exist in one of two states:

1. MOSFET A is ON and MOSFET B is OFF → In this state, the series combination of R_{LIM} and C_p is shorted to V_{DC}. The piezostack charges up to the DC bus voltage exponentially with a time constant depending on the values of the current limiting resistance and the piezostack capacitance.

2. MOSFET A is OFF and MOSFET B is ON → In this state, the series combination of R_{LIM} and C_p is shorted to ground. The piezostack discharges exponentially.

As a result of the piezostack charging and discharging between states 1 and 2, the voltage appearing at the electrodes of the stack approximates a square wave (Figure 5.18). As the peak voltages of the sinusoidal excitation and the switch driver waveform are the same, the peak displacement of the piezostack is the same in both cases, which is a direct consequence of the high bandwidth of the piezostacks. Also, as the area under the switch driver waveform is larger than that under the sinusoid, it is expected that the switch driver will deliver more power to the piezostacks, and consequently, the power output of the device will increase. The charging and discharging roll-offs are useful in decreasing transient loads on the piezostacks, which would otherwise respond to sharp changes in slope of the excitation voltage, creating potentially damaging internal stresses.

The main advantage of this method of exciting the piezostacks is that it is very compact. A prototype circuit was built in the lab on a circuitboard with an overall footprint of less than 3 square inches. This is mainly because the power dissipation in the driving circuit is almost zero, as a result of the low values of $R_{DS(ON)}$ of the MOSFETS. The only power that is dissipated in the circuit is in the current limiting resistance, R_{LIM}. The value of this resistance is chosen depending on the allowable peak current that can be drawn from the DC bus. The peak current is approximately given by V_{DC}/R_{LIM}.

This method is inherently inefficient in terms of electrical efficiency. As the primary requirement is output power of the device, the challenge in this particular application is not so much the electrical efficiency, as the electric power delivery to the device. In this case, electrical efficiency is sacrificed for compactness.

In the experiments conducted on the device, the piezoelectric pump was excited using both a conventional linear power amplifier and the switch driver. The conventional linear amplifier was a HERO precision power amplifier (Model PA9810), custom designed by Rohrer Meß-& Systemechanik [220]. The model PA9810 amplifier is a 700 Watt amplifier with a $\pm$500 V, $\pm$1.5 A output. Using the PA9810, it was possible to excite the piezoelectric pump to a maximum frequency of 600 Hz. With the switch driver, the piezoelectric pump was tested to a maximum frequency of 1KHz.

5.8 Experimental setup

Experiments to measure the performance and output power of the device were conducted under two broad categories:

1. Performance evaluation of the piezoelectric pump

2. Output power of the device

These experiments were carried out under a variety of test conditions, including exciting the piezoelectric pump with different drivers, operating the piezoelectric pump at different frequencies, investigation of the effect of bias pressure and several heat dissipation mechanisms to prevent the piezostacks from overheating. A short description of these experiments is given below. All data acquisition was performed on a Windows NT based PC with a National Instruments PCI-6031E 16-bit DAQ card, using a virtual instrument application programmed in LabVIEW™ 5.1.

5.8.1 Performance evaluation of the piezoelectric pump

This was the first set of experiments performed after the assembly of the prototype pump. The main goal of these experiements was to evaluate the pumping performance of the piezoelectric pump and to validate the performance with analytic predictions. This enabled identification of any mechanical problems with the assembly and served as a proof of concept for the next phase, which was the installation of the pump in the piezoelectric hydraulic hybrid actuator.

A schematic diagram of the experimental setup is shown in Figure 5.19(a). The port labeled 'Bleed' and the neighboring valves were used to fill the hydraulic circuit. The filling was carried out by first pouring the hydraulic fluid into the reservoir at the bleed port. A vacuum was then applied at this port, drawing out all the air from the system. After all the air bubbles stopped appearing, the vacuum was released and the circuit was pressurised to the operating bias pressure. The bias pressure in the circuit serves two functions

1. Applies a preload on the piezostacks in the pump
2. Increases the minimum pressure occuring in the hydraulic fluid, which has the effect of reducing cavitation.

After the circuit was pressurised to the bias pressure, the bleed valves are closed. By clamping the output hydraulic cylinder and keeping valves V1 and V2 open, the piezoelectric pump transfers fluid from the low pressure accumulator to the high pressure accumulator. The pressure rise created in the accumulators, given by $P_{\text{outlet}} - P_{\text{inlet}}$ was measured over a period of 5 minutes, for several bias pressures and pumping frequencies. The excitation voltage to the piezostacks was kept constant, at 0-100 V. The quantities measured were the excitation voltage to the piezostacks, current drawn by the piezostacks, temperature of the piezostacks, strain of the piezostacks, and pumping chamber pressure.

The output signals of the pressure transducers and strain gages were conditioned/amplified with 2311 Signal Conditioning Amplifiers (Measurements Group, Inc. [164]). The pressure transducers were PX600 series subminiature millivolt output type pressure transducers manufactured by Omega [221]. These transducers were excited at 5 V_{DC}, with a gain of 500. The strain gages were EA-06-125BZ-350, manufactured by Measurements Group, Inc., and were excited at 1 V_{DC} with a gain of 1000. The gage length of the strain gage was 0.125" and each piezostack was instrumented with a strain gage. The strain gage installation was calibrated by monitoring the piezostack deflection at a frequency of 1 Hz and below with a dial gage. This was done in order to eliminate any errors introduced by the fact that the gage length of the strain gage did not cover the entire length of the piezostack.

5.8.2 Output power of the device

After validation of the piezoelectric pump performance, the next set of experiments involved measuring the output power of the device. As mentioned in Section 5.1, the device under consideration does not have accumulators in the hydraulic circuit, to reduce the size of the final hybrid actuator. Referring to Figure 5.19(a), valves V1 and

V2 were closed, cutting off the accumulators from the rest of the hydraulic circuit. The piezoelectric pump was therefore directly connected to the output hydraulic actuator, also referred to as the output *cylinder*. A 10μm line filter was included upstream of the pump inlet in order to prevent any contamination in the working fluid from affecting the operation of the pump. Deadweights were hung off the end of the output hydraulic cylinder, and its position, *h*, was measured using a linear potentiometer. This sensor was also excited by $1V_{DC}$, with a gain of 1, using the Measurements Inc., 2311 signal conditioning unit. A suitable value of system bias pressure, chosen from the observations of the previous experiment as 50psi, was applied to the circuit and kept constant. The output cylinder velocity, which when multiplied by the load weight gives the output power, was measured as a function of pumping frequency, piezostack driving method, load mass and fluid viscosity.

The cylinder output in this case, however, is unidirectional. After each measurement of cylinder velocity, the valves had to be manually opened, and the cylinder position adjusted to zero. The final device would have a bi-directional output, which can be achieved by means of a 4-way valve as shown in Figure 5.19(b). A commercially available 4-way spool valve was installed in the setup, and some preliminary bi-directional actuation data were taken. This spool valve was a HR Textron Model 27A50 R-DDV [222] spool valve, chosen because of its compactness and frequency response. The overall dimensions of the valve are 1.3”$\times$3.4”$\times$2.08”, which is comparable to the dimensions of the piezoelectric pump itself. Bidirectional no-load cylinder velocity tests were performed, however, due to a failure in the 4-way spool valve, these experiments could not be completed. A picture of the experimental setup is shown in Figure 5.20 and pictures of the piezoelectric pump, bleed port, output cylinder, and 4-way spool valve are shown in Figure 5.21.

The results of these experiments, observations made, and the consequent changes

made to the device in order to improve its performance, will be elaborated in Chapter 7.

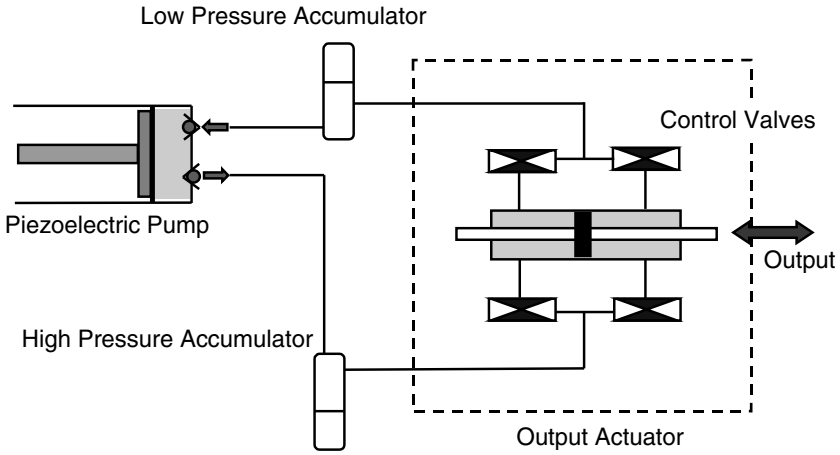

Figure 5.1 Schematic of piezoelectric hydraulic hybrid actuator

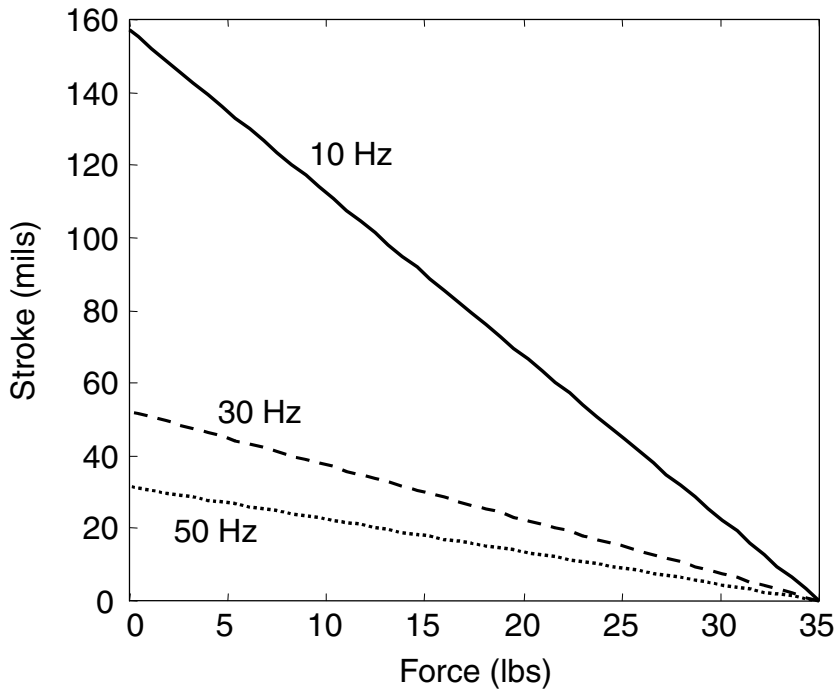

Figure 5.2 Nominal output design goals

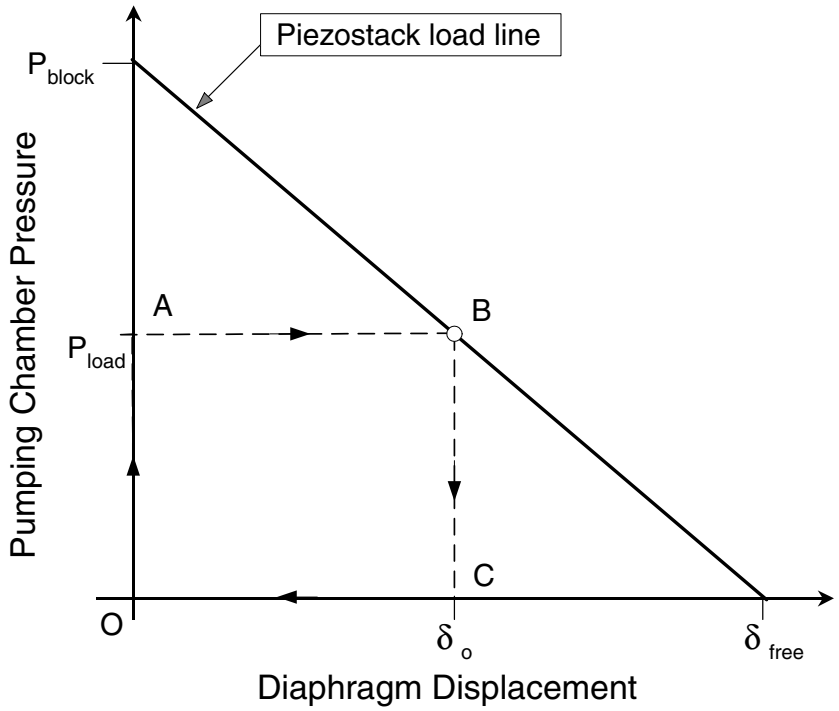

Figure 5.3 Pumping cycle for an ideal incompressible working fluid

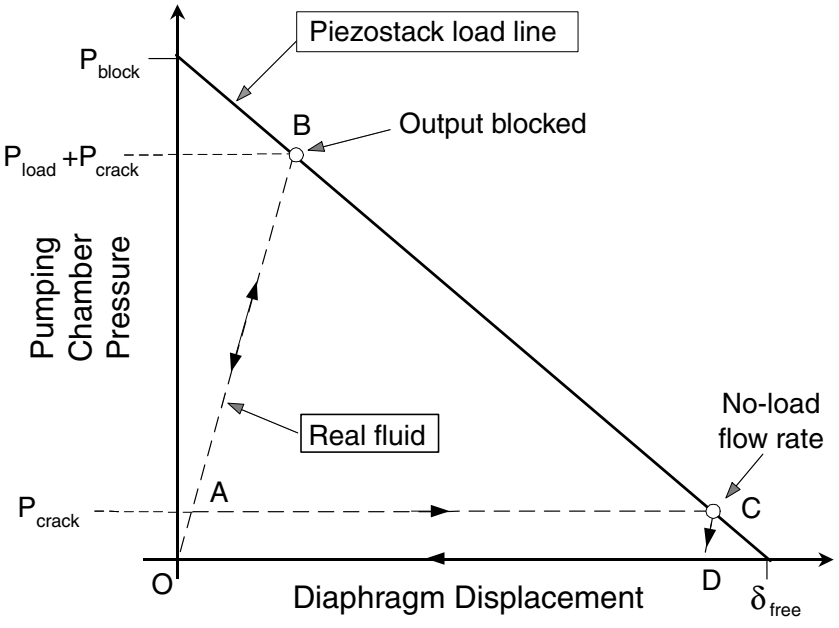

Figure 5.4 Pumping cycle for a real working fluid

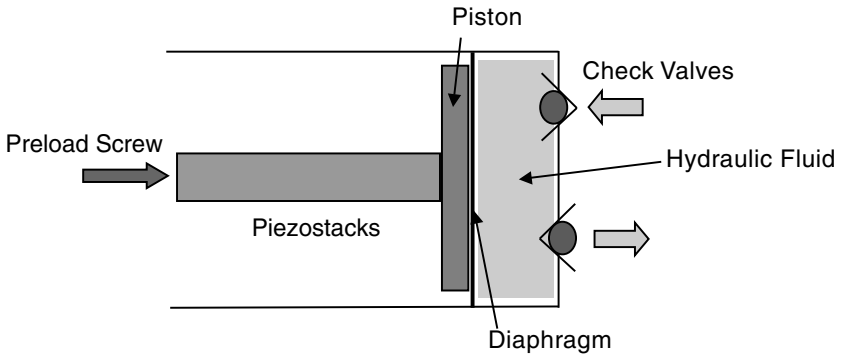

Figure 5.5 Schematic of the piezoelectric pump

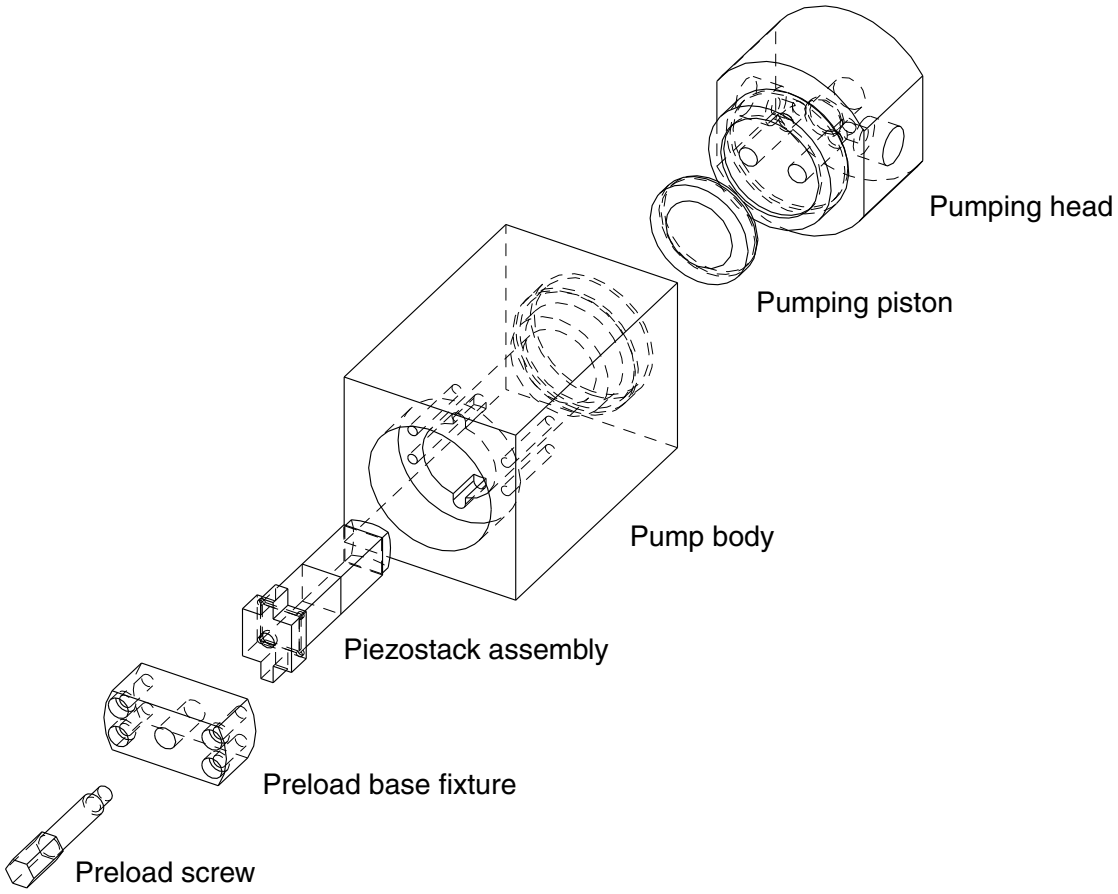

Figure 5.6 Exploded view of the piezoelectric pump assembly

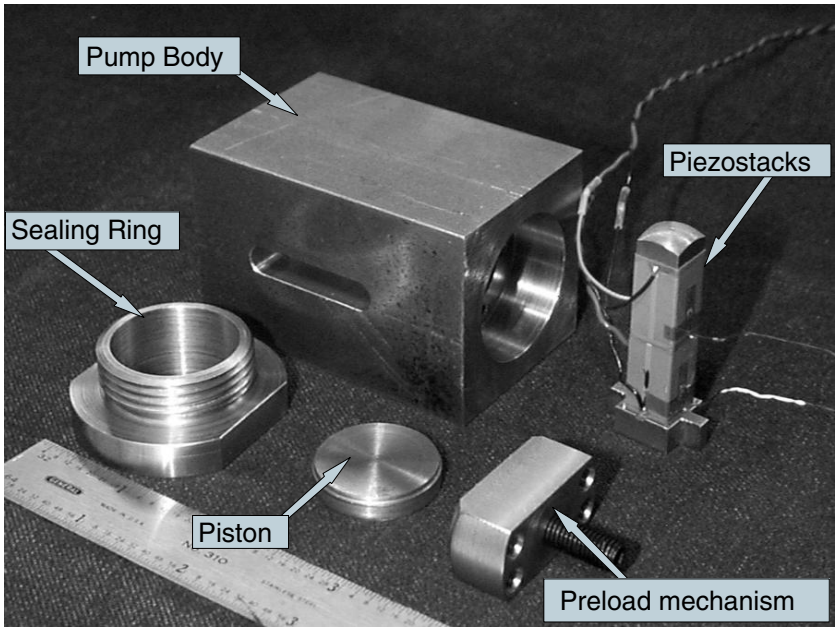

(**a**)Parts of the piezoelectric pump

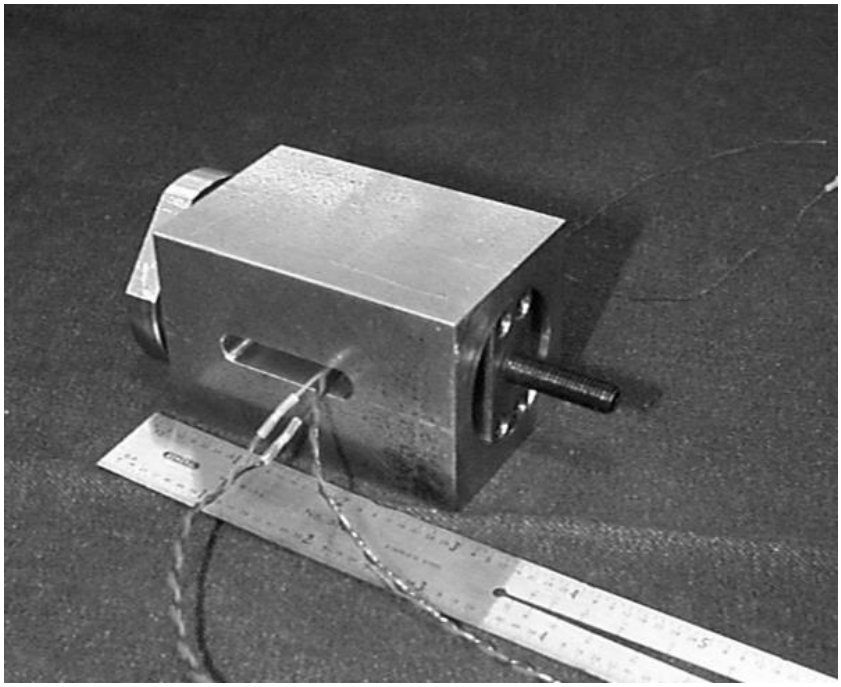

(**b**)Assembled piezoelectric pump with sealing ring

Figure 5.7 First prototype of the piezoelectric pump

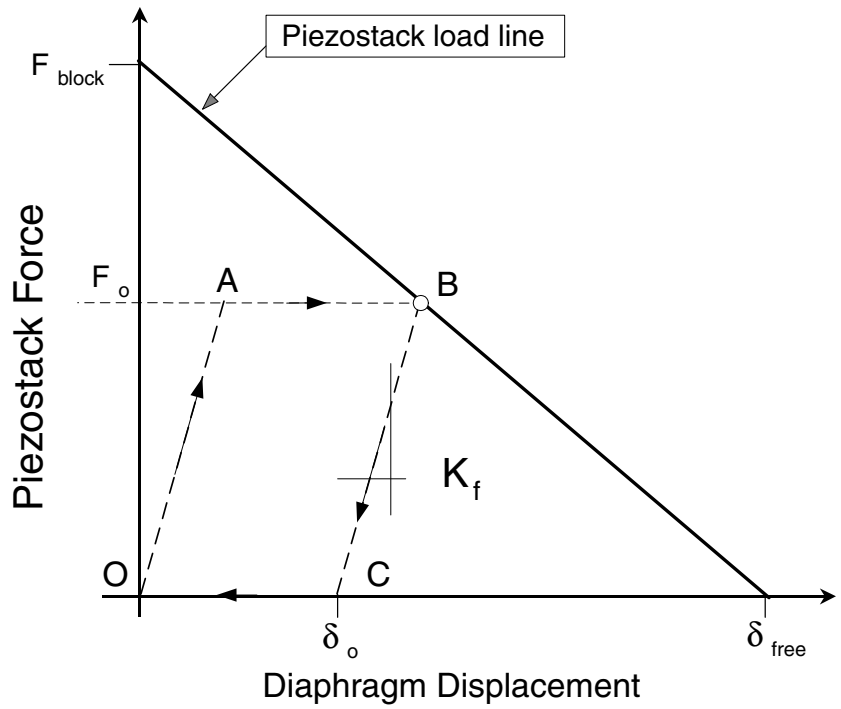

Figure 5.8 Load-line analysis

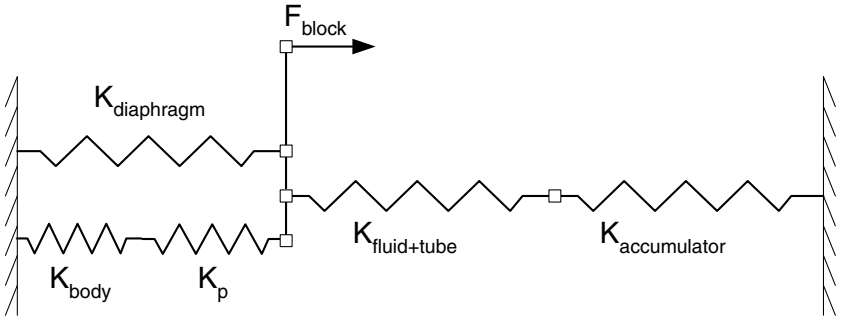

Figure 5.9 Simplified system model, outlet valve open

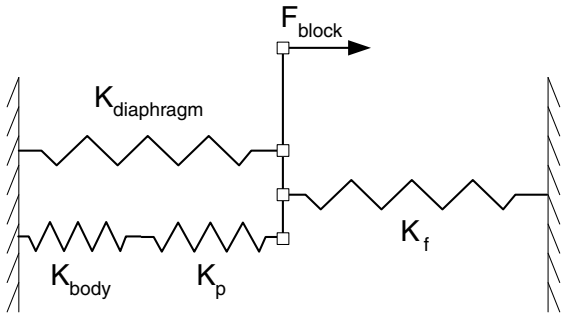

Figure 5.10 Simplified system model, pumping chamber

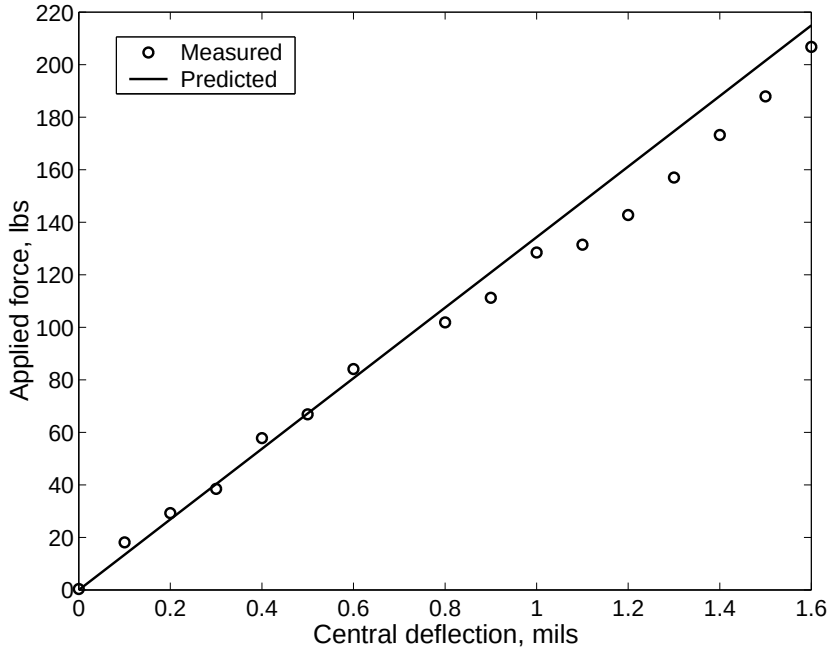

Figure 5.11 Correlation between theoretical and measured diaphragm stiffness

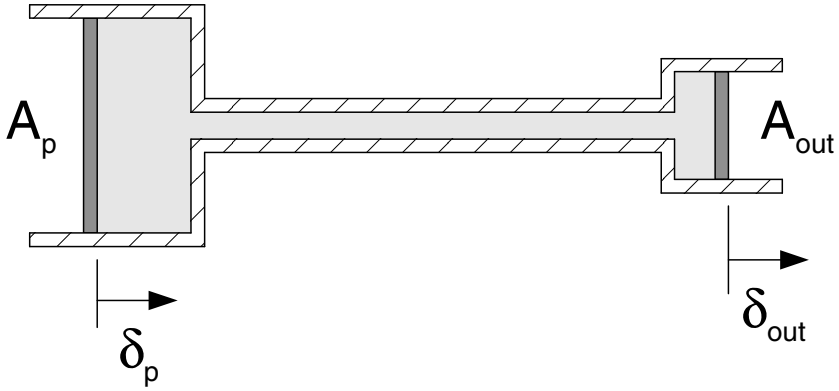

Figure 5.12 Fluid line between pumping chamber and output actuator

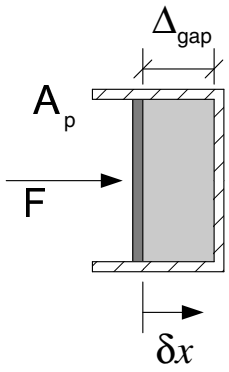

Figure 5.13 Equivalent spring stiffness of fluid in the pumping chamber

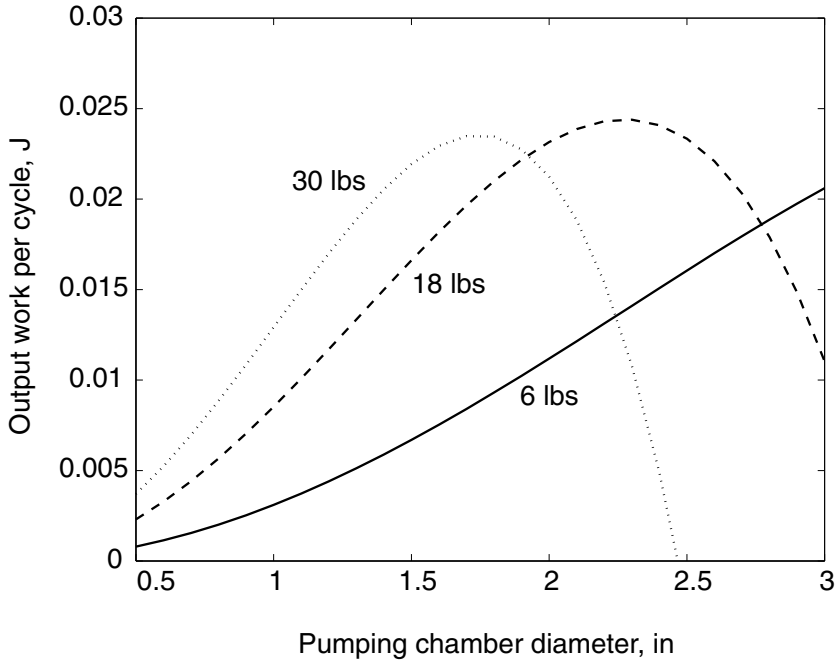

(**a**)Work output as a function of pumping chamber diameter

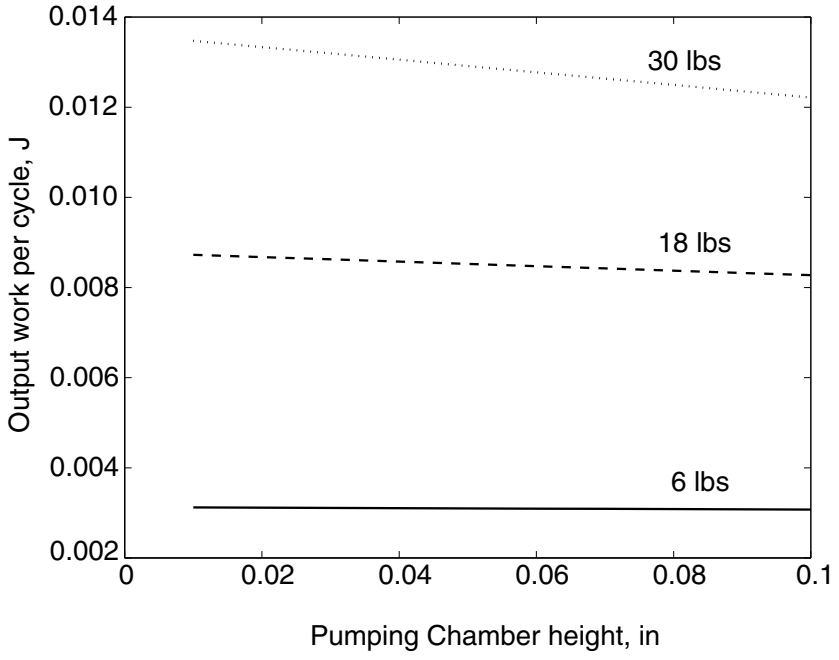

(**b**)Work output as a function of pumping chamber height

Figure 5.14 Dependence of work output per cycle on pumping chamber geometry, $\Delta_{\text{gap}} = 0.05''$

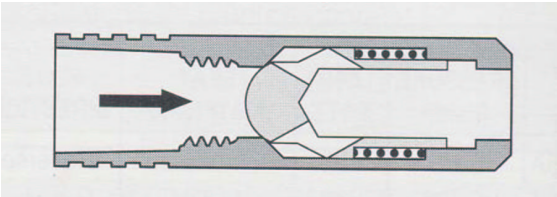

(**a**)Cross-sectional view [218]

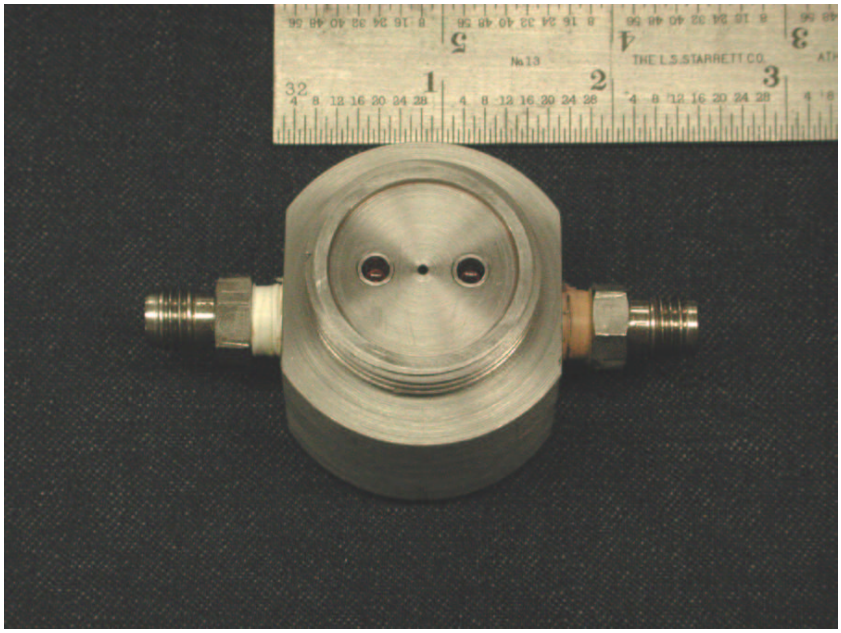

(**b**)Valves assembled in the pumping head

Figure 5.15 Type I: Ball type check valves

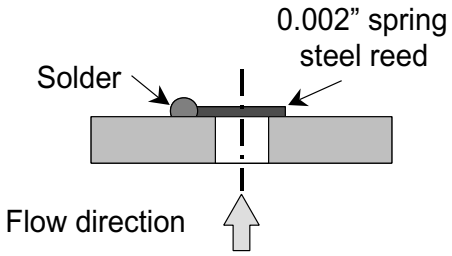

(**a**)Cross-sectional view

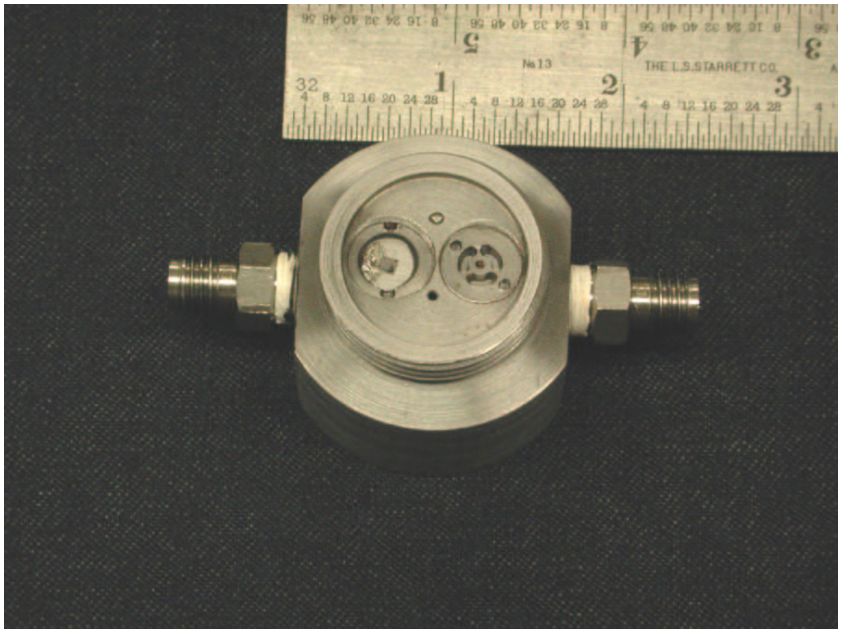

(**b**)Valves assembled in the pumping head

Figure 5.16 Type II: Reed valves

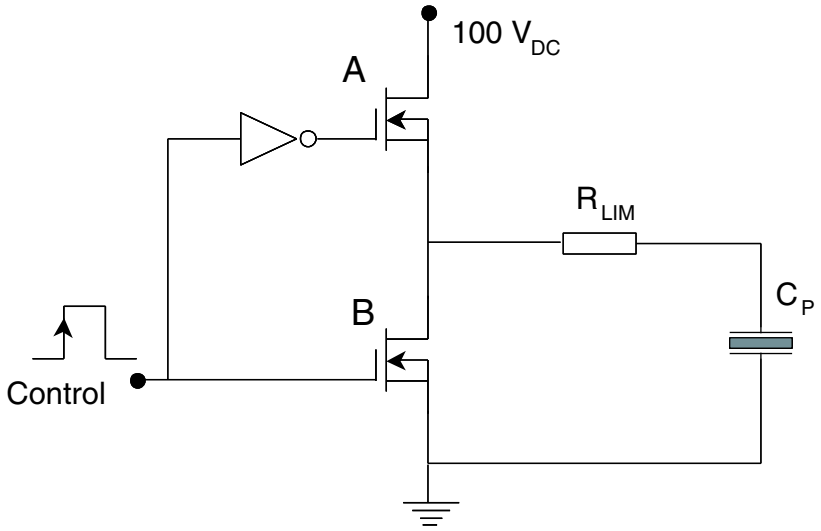

Figure 5.17 Schematic of the piezostack switched driver circuit

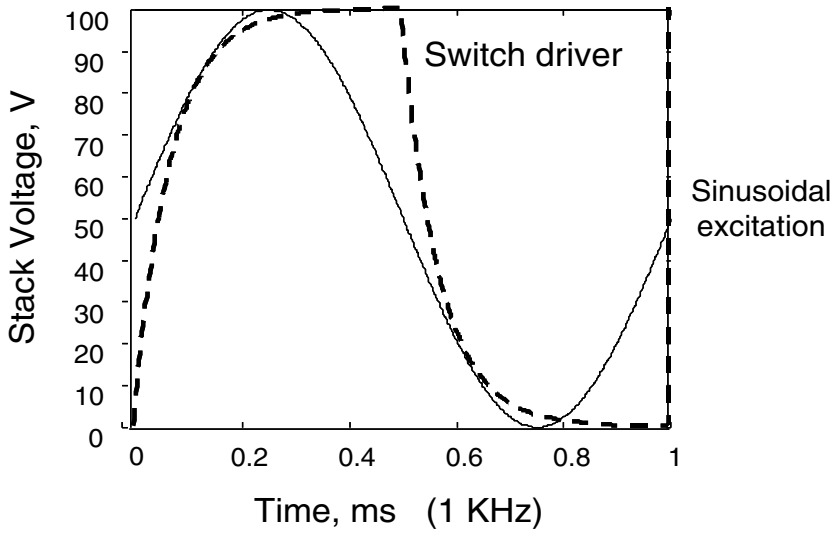

Figure 5.18 Comparison of sinusoidal waveform and switch driver waveform

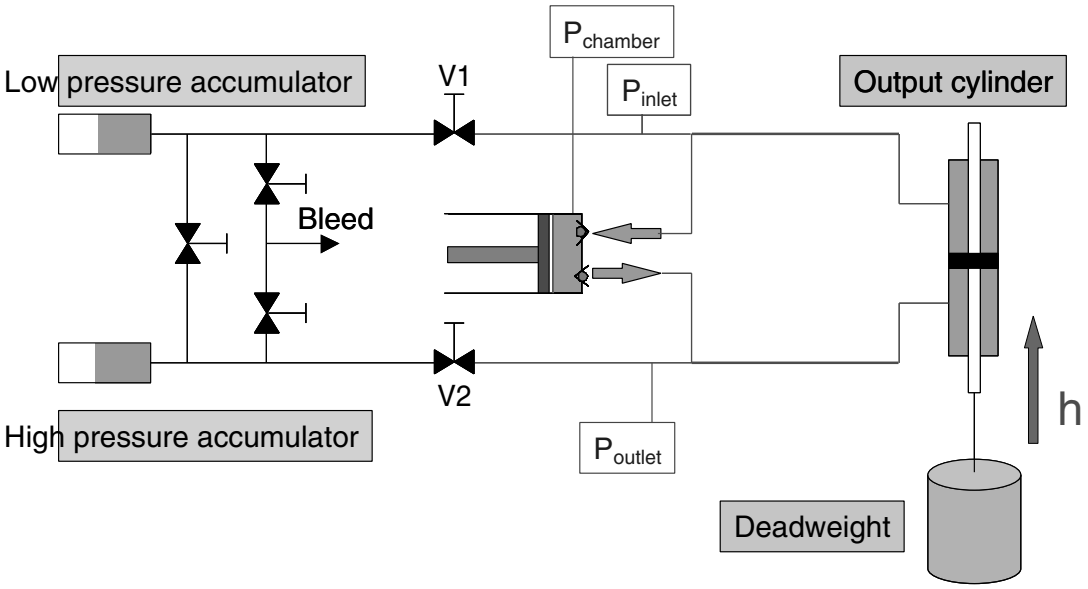

(**a**)Uni-directional output

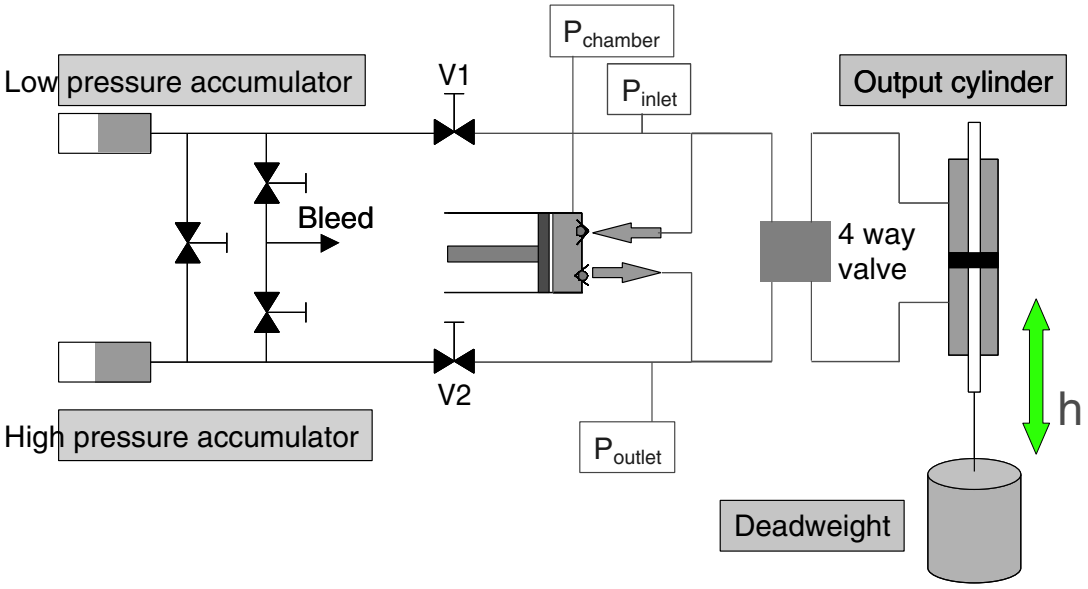

(**b**)Bi-directional output, with 4 way valve

Figure 5.19 Experimental setup for the evaluation of device performance

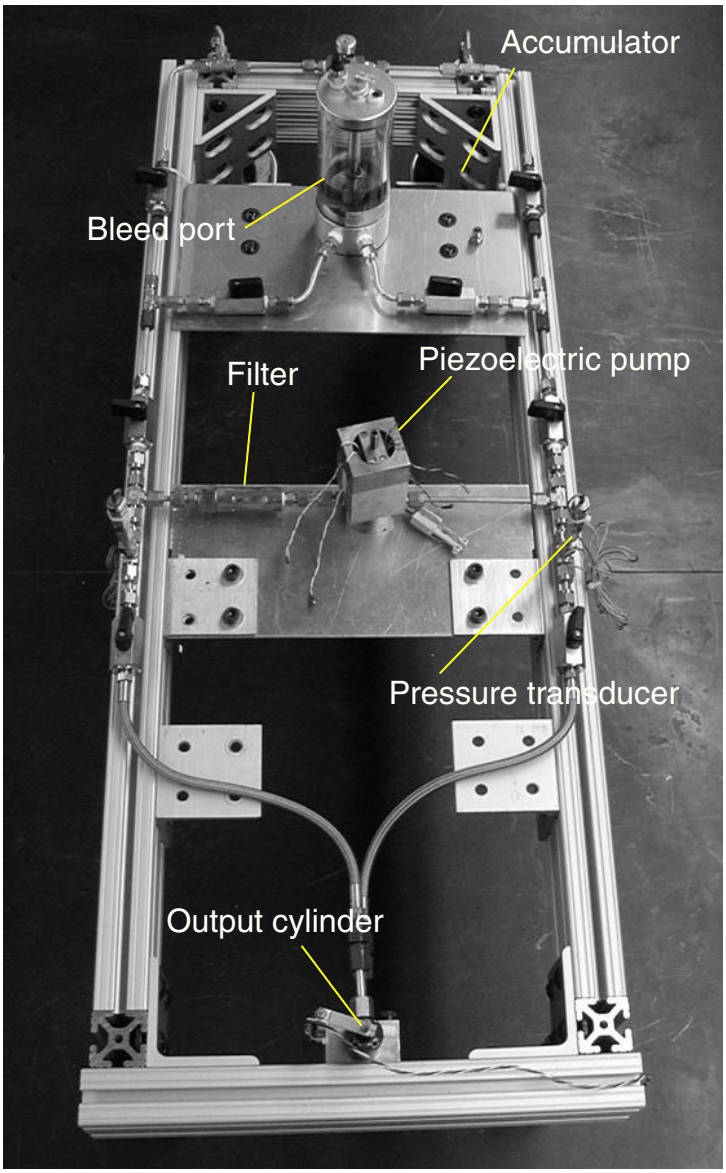

Figure 5.20 Experimental setup

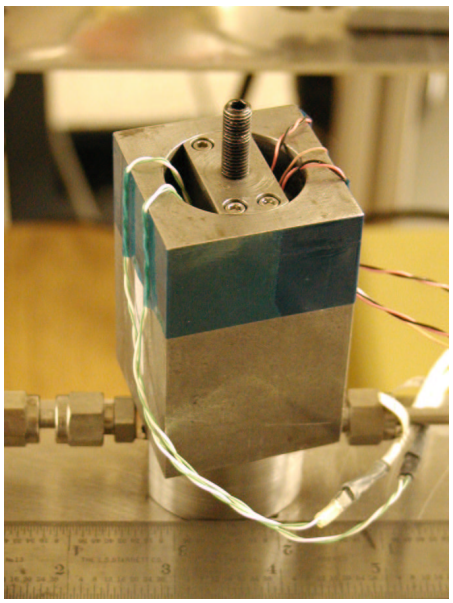

(**a**)Piezoelectric pump

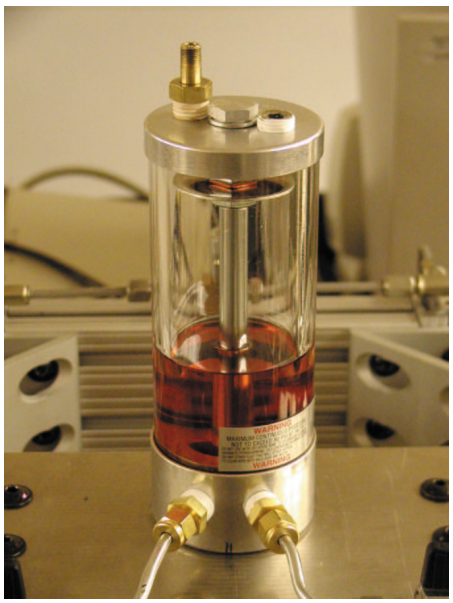

(**b**)Bleed port

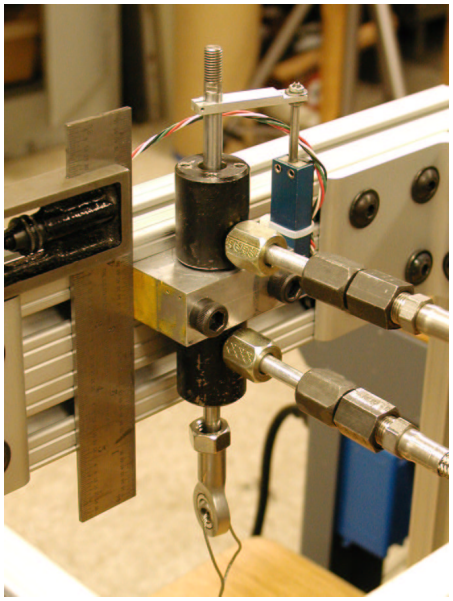

(**c**)Output hydraulic cylinder

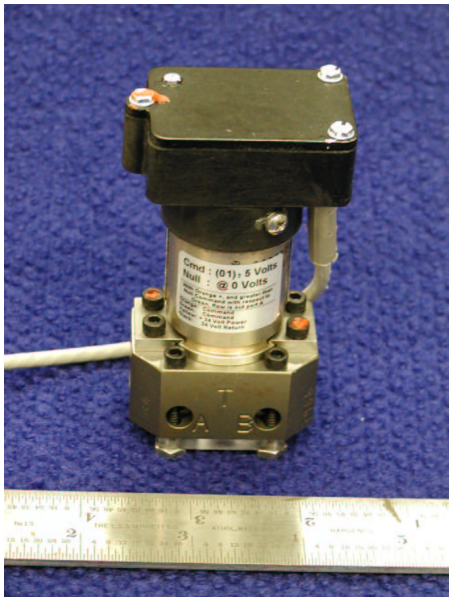

(**d**)4 way spool valve [222]

Figure 5.21 Parts of the experimental setup

Chapter 6

Theoretical Modeling

This chapter discusses the theoretical modeling of the pumping mechanism, as well as the self-heating phenomenon of the piezostacks. The goal of this modeling is two fold. Firstly, to verify the correct functioning of the system, by comparing measured performance with theoretical predictions. This will enable the identification of any mechanical or design flaws in the system. Secondly, the modeling will help to understand and quantify the observed physical phenomena. For example, if the relationship between the physical parameters of the pump and the output performance is known, the device can be scaled to achieve a specified performance. The key to achieving a high energy density with this device is through pumping the fluid at as high a frequency as possible. One of the major barriers to this is the self-heating of the piezostacks. Once this phenomenon is quantified, and the causes identified, steps can be taken to control the temperature rise.

In the discussion below, the term *device* is used to refer to the entire piezoelectric-hydraulic hybrid actuator, while *pump* specifically refers to the piezoelectric stack-piston assembly with the pumping head and check valves. *Output of the device* refers to the displacement of the output hydraulic actuator.

The experiments from which data was obtained to validate the models is described in

Chapter 5. Two main sets of experiments were carried out. The first set was to measure the pumping capability of the pump, wherein the differential pressure generated by the pump is measured over a period of 5 minutes. The second set was to measure the output of the device under various mechanical loads. During these tests, the temperature of the piezostacks was monitored. The theoretical modeling follows in the same order as the experiments.

6.1 Modeling of the pumping chamber and check valves

Understanding the behavior of the fluid in the pumping chamber, along with the behavior of the two check valves, is key to understanding the behavior of the system as a whole. Though the flow field in the pumping chamber is very complex, the resistance to fluid flow produced by the pumping chamber, piston and check valve assembly have been calculated by other researchers using ANSYS FLOTRAN [206]. Such an analysis can provide important information regarding the selection of an appropriate pumping chamber geometry. In this thesis, however, the details of the flow inside the pumping chamber are ignored. A simplified model of the pumping chamber is constructed, using a basic control volume approach.

6.1.1 Derivation of governing equation using a control volume approach

The pumping chamber can be modeled as a rigid hollow cylinder with one deformable face and two check valves embedded in the other face. The outlet valve is connected to an accumulator of pressure P_{high} and the inlet valve is connected to an accumulator of pressure P_{low}. The pump diaphragm, forming the deformable face, is driven by the piezostack actuator. Consider a control volume enclosed by the pumping chamber, that

deforms along with the diaphragm(Figure 6.1).

The equation of conservation of mass for a control volume is [223]

$$\left(\frac{dm}{dt}\right)_{\text{system}} = \frac{d}{dt}\left(\iiint_{\text{CV}} \rho d\mathbb{V}\right) + \iint_{\text{CS}} \rho\left(\vec{\upsilon}\cdot\hat{n}\right) dA = 0 \tag{6.1}$$

When applied to the control volume in the pumping chamber, the above equation leads to

$$\frac{\mathbb{V}_{\text{cham}}}{\rho}\frac{d\rho}{dt} + \frac{d\mathbb{V}_{\text{cham}}}{dt} + \frac{\dot{m}_{\text{cham}}}{\rho} = 0 \tag{6.2}$$

where $\mathbb{V}_{\text{cham}}$ is the initial volume of the pumping chamber, $\dot{m}_{\text{cham}}$ is the mass flow rate of the fluid leaving the chamber and ρ is the fluid density.

By the definition of fluid compressibility [215], for a fluid of bulk modulus β, the change in pumping chamber pressure, dP_{cham} in response to a change in pumping chamber volume $d\mathbb{V}_{\text{cham}}$ is given by

$$dP_{\text{cham}} = -\frac{\beta}{\mathbb{V}_{\text{cham}}} d\mathbb{V}_{\text{cham}} = \frac{\beta}{\rho} d\rho \tag{6.3}$$

Using this result, the first term in Equation (6.2) reduces to

$$\frac{\mathbb{V}_{\text{cham}}}{\rho}\frac{d\rho}{dt} = \frac{\mathbb{V}_{\text{cham}}}{\beta}\frac{dP_{\text{cham}}}{dt} \tag{6.4}$$

The second term in Equation (6.2) is a boundary deformation term, which is prescribed by the motion of the diaphragm, and therefore of the piezostack. For a harmonic excitation of the piezostack at a circular frequency ω, this term can be expressed as

$$\frac{d\mathbb{V}_{\text{cham}}}{dt} = \frac{d}{dt}\left[\Delta\mathbb{V}_{\text{cham}} \sin\omega t\right] = \Delta\mathbb{V}_{\text{cham}}\omega\cos\omega t \tag{6.5}$$

where $\Delta\mathbb{V}_{\text{cham}}$, the peak volumetric displacement of the diaphragm, is approximated to be

$$\Delta\mathbb{V}_{\text{cham}} = a_{\text{cham}}\Delta x \tag{6.6}$$

where a_{cham} is the cross-sectional area of the pumping chamber and Δx is the peak deflection of the piezostack.

The third term in Equation (6.2) gives the net volumetric flow rate of the fluid from the pumping chamber. The fluid flows into and out of the pumping chamber through the check valves, which offer a resistance to the flow. This resistance is expressed in terms of a flow rate factor, C_{fq}, that relates the differential pressure ΔP across the valve to the volumetric flow rate Q of the fluid flowing through the valve.

$$Q = C_{\text{fq}}\sqrt{\Delta P} = C_{\text{fq}}\sqrt{P_{\text{cham}} - P_o} \tag{6.7}$$

If the inlet valve is open, the pumping chamber would be connected to the low pressure accumulator, and $P_o = P_{\text{low}}$. Similarly, if the outlet valve is open, the pumping chamber would be connected to the high pressure accumulator, and $P_o = P_{\text{high}}$. It is assumed that only one of the valves can be open at any given point in time. Because fluid can only flow from high pressure to a lower pressure, Equation (6.7) can be rigorously expressed to include flow direction as

$$Q = C_{\text{fq}}\sqrt{\|P_{\text{cham}} - P_o\|} * sign(P_{\text{cham}} - P_o) \tag{6.8}$$

6.1.2 Modeling of the check valves

The check valves are modeled by a cracking pressure, P_{crack} and a hysteresis pressure, P_{hyst}, that define the conditions under which they open or close (Figure 6.2). The inlet valve is considered open when either of the following two conditions is met

$$\begin{aligned} &P_{\text{cham}} < (P_{\text{low}} - P_{\text{crack}}) \\ &\quad \text{or} \\ &P_{\text{cham}} < (P_{\text{low}} - P_{\text{crack}} + P_{\text{hyst}}) \quad \text{and} \quad \frac{dP_{\text{cham}}}{dt} > 0 \end{aligned} \tag{6.9}$$

Similarly, the outlet valve is considered open if

$$P_{\text{cham}} > (P_{\text{high}} + P_{\text{crack}})$$

$$\text{or} \tag{6.10}$$

$$P_{\text{cham}} > (P_{\text{high}} + P_{\text{crack}} - P_{\text{hyst}}) \quad \text{and} \quad \frac{dP_{\text{cham}}}{dt} < 0$$

As shown in Figure 6.2, the valve remains closed if the pressure differential across it is less than the cracking pressure, P_{crack}. In this condition, the flow rate factor is zero. As the backpressure increases, causing the pressure differential across the valve to increase, the valve starts opening once the pressure differential reaches P_{crack}. The flow rate factor is then assumed to increase linearly till the valve is fully open, which occurs at a differential pressure of P_{full}. At this point, the flow rate factor remains constant at C_{fqo} for all larger differential pressures. For subsequently decreasing differential pressures, the reverse process occurs, with a small hysteresis given by P_{hyst}.

It should be noted that in the present analysis, the dynamic characteristics of the valves themselves are ignored. The flow rate factor, C_{fq}, of the valve depends on the valve geometry and hydraulic fluid being used, and is normally specified by the valve manufacturer. In the present model, the exact value of the valve cracking pressure, valve hysteresis pressure, and flow coefficient are backed out from experiment. The variation of C_{fq} with pressure differential is expressed as

$$C_{\text{fq}} = \begin{cases} 0 & \text{if} \quad \Delta P < P_{\text{crack}} \\ \dfrac{\Delta P - P_{\text{crack}}}{P_{\text{full}} - P_{\text{crack}}} * C_{\text{fqo}} & \text{if} \quad P_{\text{crack}} \leq \Delta P < P_{\text{full}} \\ C_{\text{fqo}} & \text{if} \quad \Delta P \geq P_{\text{full}} \end{cases} \tag{6.11}$$

Similar relations can be derived for the case when ΔP is decreasing. Combining Equations (6.2), (6.4), (6.5), (6.6) and (6.8) leads to the final governing equation for flow through the pumping chamber

$$\frac{dP_{\text{cham}}}{dt} = -\frac{\beta}{\mathbb{V}_{\text{cham}}} \left[\Delta \mathbb{V}_{\text{cham}} \omega \cos \omega t + C_{\text{fq}} \sqrt{\|P_{\text{cham}} - P_o\|} * sign(P_{\text{cham}} - P_o) \right] \tag{6.12}$$

Note that if the check valves are closed, the last term in Equation (6.12) would go to zero, and the equation would reduce to that of purely the compression of the fluid in the pumping chamber.

6.1.3 Numerical solution

The above equation is solved numerically with the valve operation specified by Equations (6.9), (6.10) and (6.11) to yield the pumping chamber pressure as a function of time, and the net fluid flow rate through the pumping chamber. This is accomplished using the ODE45 subroutine in MATLAB [224]. The pumping chamber governing equation (Equation (6.12)) is complicated by the valve dynamics, which can however be included in the numerical solution scheme. Another complication arises from the fact that the boundary conditions, which are the pressures at the inlet and outlet, are not constant through the solution time. These pressures keep changing depending on how much fluid is pumped from one accumulator to another.

In order to account for the changing boundary conditions, the entire time period of interest, which in the case of these experiments was 5 minutes, is divided into smaller regions of time. During these smaller time periods, the pressures at the inlet and outlet are assumed to remain constant. This assumption is justified by the fact that the volume of fluid pumped into the accumulator in each pumping cycle is small compared to the overall volume of gas in the accumulator, as a result of which the change in accumulator pressure over one pumping cycle is negligibly small. The above numerical formulation, Equation (6.12), is then solved for the small time period, with the appropriate boundary conditions, that are the inlet and outlet pressures, P_{low} and P_{high}. The volume of fluid flowing into the high pressure accumulator and out of the low pressure accumulator is then calculated from Equation (6.8). This quantity appears as a change in volume of gas in the corresponding accumulator. The resultant change in pressure in the accumulator

is calculated using the gas law. For the volume of gas in the accumulator, assuming the change in volume due to pumping is an adiabatic process, the following holds good

$$P_{\text{gas}} V_{\text{gas}}^{\gamma} = \text{Constant} \tag{6.13}$$

where γ is the gas constant. The boundary conditions are then updated with the new calculated changes in accumulator pressure and the process is repeated for the next time period. In this manner, the change in accumulator pressures over the entire 5 minute period is calculated.

Correlation between measured and calculated differential accumulator pressures are shown in Figure 6.3. The correlation is quite good for a pumping frequency of 50 Hz, but starts to deteriorate with time for the higher pumping frequency. This can be explained by the fact that the model does not include the effect of check valve dynamics, that contribute significantly to the volumetric flow rate of fluid through the pumping chamber, especially at a higher frequency. In addition, effects like surface friction and viscosity of the fluid are not considered in the analysis. The viscosity of the working fluid is considered small enough to be neglected. However, the basic dynamics of the pumping chamber is captured with sufficient accuracy by this model. Such an analysis can be used in order to assess the effectiveness of the design of the pumping mechanism with respect to expected volumetric flow rates, and to predict the effect of changing system parameters like check valve parameters, fluid properties and pumping chamber geometry.

6.2 Modeling of the overall device performance

6.2.1 Lumped parameter - state space method

Several methods of calculating the output cylinder displacement in response to a piezostack excitation at a given voltage and frequency can be found in the literature. Konishi et. al. [213, 214] solved the coupled governing differential equations of the piezostack and the hydraulic fluid circuit. Nasser et. al. [208] has expressed the overall device in terms of a mechanical mass-spring-damper lumped parameter analogy. Oates et. al. [206] developed a state-space representation of the device, which was subsequently solved using MATLAB.

The direct solution of the differential equations has been shown to correlate well with experimental data at 300 Hz, which was the operating frequency of that particular device [211, 212, 213, 214]. The lumped parameter model also showed good correlation with experiment, but was validated only upto operating frequencies of 100 Hz. The correlation of theory with experiment is shown by Oates et. al. [206] for pumping frequencies of upto 100 Hz. It was not possible to investigate higher pumping frequencies due to limitations in their experimental setup. The model was able to predict the behavior in this frequency range but the effect of the assumptions inherent in the model on higher frequency predictions is not clear.

The modeling technique used in this thesis is based on the state-space method and is similar to the one developed by Oates et. al. [206]. This technique was chosen for its simplicity and ability to quickly predict the overall device performance based on a given set of input parameters. Also, the opening and closing of the check valves can be easily modeled using this method, as opposed to techniques utilizing mechanical and electrical analogies of the hydraulic circuit. Once the dependence of the output on the input parameters has been established, the device parameters can be scaled appropriately

to achieve the desired output. In this thesis, experimental data are obtained for pumping frequencies upto 600 Hz, and hence the extent of the limitations on the high frequency prediction capabilities of the model can be explored.

6.2.2 States of the device

Consider the schematic diagram of the device as shown in Figure 6.4. The output hydraulic actuator, or cylinder, is shown connected to an external load, that is a mass M_{out} and a spring of stiffness K_{out}. Quantities with a subscript '1' refer to quantities in the region '1' in the figure, which is the upper part of the output hydraulic actuator. For example, C_3 refers to the fluid capacitance of the fluid in the upper part of the output hydraulic actuator. The same notation holds for regions '2', which is the lower part of the output hydraulic actuator and 'C', which is the pumping chamber. The goal of the model is to predict the output cylinder displacement x_{out} in response to the excitation voltage V_{p} applied to the piezostacks. However, by setting up the system in state-space form, the time response of any of the other states of the system can be calculated without rewriting the equations of the system. Only one-way operation of the device is modeled, with fluid flowing out through the outlet check valve R_{out} into the lower end of the output hydraulic actuator, causing the load mass to move upwards.

The state variables of the system are (Figure 6.4)

$$
\begin{aligned}
&x_1 \rightarrow x_{\mathrm{p}} \quad \text{Displacement of the pump piston} \\
&x_2 \rightarrow x_{\mathrm{out}} \quad \text{Displacement of the output hydraulic actuator} \\
&P_2 \quad \text{Pressure in the upper part of the output hydraulic actuator} \\
&P_1 \quad \text{Pressure in the lower part of the output hydraulic actuator} \\
&P_{\mathrm{c}} \quad \text{Pressure in the pumping chamber} \\
&x_3 \rightarrow \dot{x}_{\mathrm{p}} \quad \text{Velocity of the pump piston} \\
&x_4 \rightarrow \dot{x}_{\mathrm{out}} \quad \text{Velocity of the output hydraulic actuator}
\end{aligned}
\tag{6.14}
$$

6.2.3 Setting up the state-space equations

From the above definitions, the state space equations can be set up as follows

$$\dot{x}_1 = x_3 \tag{6.15}$$

and

$$\dot{x}_2 = x_4 \tag{6.16}$$

By equating forces acting on the pumping piston,

$$m_{\mathrm{p}}\ddot{x}_{\mathrm{p}} + b_{\mathrm{p}}\dot{x}_{\mathrm{p}} + k_{\mathrm{p}}x_{\mathrm{p}} = C_{\mathrm{v}}V_{\mathrm{p}} - P_{\mathrm{c}}a_{\mathrm{p}} \tag{6.17}$$

where m_{p}, b_{p} and k_{p} are the effective mass, damping and stiffness of the piston-piezostack assembly, respectively. From energy considerations, it can be shown that one-third of the mass of the piezostack also needs to be added to the mass of the piston, to get the effective mass of the combination, m_{p}. k_{p} is the effective stiffness of the diaphragm and piezostack, in parallel. a_{p} is the area of the pumping piston and V_{p} is the voltage applied to the piezostack. The constant C_{v} is an effective piezoelectric

coefficient expressed in terms of the blocked force of the piezostack and the voltage at which the piezostack is excited to obtain the specified blocked force.

$$C_{\mathrm{v}} = \frac{F_{\mathrm{block}}}{V_{\mathrm{max}}} \tag{6.18}$$

Using the state variables and rewriting Equation (6.17),

$$\dot{x}_3 = -\frac{k_{\mathrm{p}}}{m_{\mathrm{p}}} x_1 - \frac{a_{\mathrm{p}}}{m_{\mathrm{p}}} P_{\mathrm{c}} - \frac{b_{\mathrm{p}}}{m_{\mathrm{p}}} x_3 + \frac{C_{\mathrm{v}}}{m_{\mathrm{p}}} V_{\mathrm{p}} \tag{6.19}$$

Similarly, by equating forces acting on the output hydraulic actuator piston,

$$M_{\mathrm{out}}\ddot{x}_{\mathrm{out}} + B_{\mathrm{out}}\dot{x}_{\mathrm{out}} + K_{\mathrm{out}}x_{\mathrm{out}} = (P_2 - P_1)a_{\mathrm{out}} - M_{\mathrm{out}}g - f_{\mathrm{friction}} \tag{6.20}$$

where B_{out} is the damping at the output hydraulic actuator, g is the acceleration due to gravity and f_{friction} is the frictional force in the output actuator as a result of the tight fit between the piston and the inner bore of the cylinder. In the present set of experiments, there was no external spring, K_{out}, but it is included in the analysis for completeness. Using the state variables, the above equation is rewritten as

$$\dot{x}_4 = -\frac{a_{\mathrm{out}}}{M_{\mathrm{out}}} P_1 + \frac{a_{\mathrm{out}}}{M_{\mathrm{out}}} P_2 - \frac{K_{\mathrm{out}}}{M_{\mathrm{out}}} x_2 - \frac{B_{\mathrm{out}}}{M_{\mathrm{out}}} x_4 - \frac{(M_{\mathrm{out}}g + f_{\mathrm{friction}})}{M_{\mathrm{out}}} \tag{6.21}$$

6.2.4 Fluid impedance

The next step is to find a relation between the pressures P_1, P_2 and the flow rate of fluid through the inlet and outlet valves, given the flow factor of the valves and the geometry of the circuit. In order to do this, it is convenient to express the circuit in terms of an equivalent fluid impedance. The fluid circuit can either be expressed as a continuous system and solved using the wave equation or approximated as a lumped parameter system. Such lumped parameter impedance models are commonly used in hydraulic power theory, and a large number of references can be found in the

literature [225,226,227,216,215]. The similarity to electrical impedances that arises as a result of this formulation can also be utilized in solving the flow in such hydraulic power systems. For example, Bourouina et. al. have used an electrical equivalent network to model a fluid micropump [228]. As the analogy also extends to mechanical systems, a lumped parameter mass-spring-damper model can also be used to model such a system as described by Nasser et. al. [208]. The continuous system approach is necessary to capture certain dynamic phenomena, but it is expected that the lumped parameter model would have sufficient accuracy for the present application, at low frequencies where the dynamics of the system are not dominant.

A simple lumped parameter representation for the impedance of a fluid line is [216],

$$Z_{\mathrm{f}} = \frac{\Delta P}{Q} = R_{\mathrm{f}} + \frac{1}{sC_{\mathrm{f}}} + sL_{\mathrm{f}} \tag{6.22}$$

where R_{f}, C_{f}, and L_{f} are the resistance, capacitance and inductance of the fluid line, respectively. ΔP is the pressure differential across the fluid line, causing a volumetric flow rate of Q to occur. A brief discussion of the units of each of these components is necessary at this point, in order to avoid any confusion.

The pressure differential, ΔP has the units N/m^2, while the volumetric flow rate, Q has the units m^3/s. The fluid impedance, Z_{f} has the units of $Pa.s/m^3$, which are the same units as the terms in the above equation. The flow resistance, R_{f} is given by an empirical formula, that is considered sufficiently accurate for the present purpose. A more detailed calculation of R_{f} can be attempted depending on flow parameters and geometry. For example, Oates et. al. [206] calculated the flow resistance of the pumping chamber using ANSYS FLOTRAN. In the present discussion, however, the flow resistance of the pumping chamber is neglected, and only the flow resistance of the check valves and tubing is considered. By examining the relative magnitudes of the flow resistance of each of the constituent parts of the circuit, it can be seen that most of the flow resistance

originates from the check valves, justifying the preceeding assumption. Assuming laminar flow, a simple expression for flow resistance of a tube of inner diameter D and length L, with a fluid of dynamic viscosity μ is given by [229, 216, 215]

$$R_{\mathrm{f}} = \frac{128\mu L}{\pi D^4} \tag{6.23}$$

The fluid resistance term represents the viscous losses in the fluid, and depends directly on the fluid dynamic viscosity. The fluid capacitance, C_{f} is a measure of the compliance of the fluid, or the energy stored in the form of volumetric deformation. This has the units m^3/Pa and for a tube of length L, cross-sectional area A, filled with a fluid of bulk modulus β is given by [216, 215]

$$C_{\mathrm{f}} = \frac{AL}{\beta} \tag{6.24}$$

In practice, the tubing exhibits some degree of compliance as well, and this can be accounted for by replacing the fluid bulk modulus with an effective bulk modulus, β_{eff}, to take into account tubing stiffness. The effective bulk modulus is basically derived by considering the fluid stiffness in series with the tubing stiffness and is given by

$$\frac{1}{\beta_{\mathrm{eff}}} = \frac{1}{\beta} + \frac{1}{\beta_{\mathrm{tubing}}} \tag{6.25}$$

The bulk modulus of the tubing is derived by considering a tube of internal diameter d_i and external diameter d_o, constructed of a material of Young's modulus Y_t and Poisson's ratio ν_t. When subjected to an internal pressure rise ΔP, the internal volumetric change ΔV_t is [230]

$$\frac{\Delta V_t}{V_t} = \frac{2\Delta P}{Y_t}\left[\frac{d_i^2 + d_o^2}{d_o^2 - d_i^2} + \nu_t\right] \tag{6.26}$$

This expression can be substituted in Equation (6.3) to obtain a value for β_{tubing}.

The last term in the fluid impedance, Z_{f}, is the fluid inductance, which is a measure of the inertia, or mass of the fluid. Fluid inductance has the units $Pa.s^2/m^3$, and for a

fluid in a tube of length L and cross-sectional area A, can be expressed as

$$L_{\mathrm{f}} = \frac{\rho L}{A} \tag{6.27}$$

Using the expression for fluid impedance, along with the continuity equation, a relation between the flow rates and pressures in the pumping circuit can be derived.

By eliminating the fluid density ρ, the continuity equation for a control volume Equation (6.2) can be rewritten as

$$\frac{d\mathbb{V}_{\mathrm{CV}}}{dt} + \frac{\mathbb{V}_{\mathrm{CV}}}{\beta}\dot{P}_{\mathrm{CV}} + (Q_{\mathrm{out}} - Q_{\mathrm{in}}) = 0 \tag{6.28}$$

where P_{CV} is the pressure in the control volume, which is assumed constant throughout the control volume. Also, if the volumetric flow rates of fluid through the inlet and outlet check valves are denoted as Q_{in} and Q_{out} respectively,

$$Q_{\mathrm{in}} = \frac{P_1 - P_{\mathrm{c}}}{R_1 + R_{\mathrm{in}}} \tag{6.29}$$

$$Q_{\mathrm{out}} = \frac{P_{\mathrm{c}} - P_2}{R_2 + R_{\mathrm{out}}} \tag{6.30}$$

where R_1 and R_2 are the flow resistances of the inlet tubing and outlet tubing respectively, and R_{in} and R_{out} are the flow resistances of the inlet check valve and outlet check valve respectively. In the above equations, two important assumptions have been made. Firstly, the compliance of the tube and fluid have been ignored. In the physical system, the volume of fluid in the tube is small compared to the volume of fluid in the output hydraulic actuator, and hence this assumption is justified, atleast for low frequencies. Secondly, the mass of the fluid in the tube is also neglected. These two terms can be included without much difficulty by adding two more states to the model. However, as a first approximation, and especially at low frequencies, the error introduced by these assumptions is expected to be small. At higher frequencies, there will definetely be a significant contribution from these two terms to the overall

dynamics, but this simple model will allow us to investigate the extent of importance of the frequency dynamics of the system.

Since the rate of change of pumping chamber volume is given by

$$\frac{d\mathbb{V}_{\mathrm{CV}}}{dt} = -a_{\mathrm{p}}\dot{x}_{\mathrm{p}} \tag{6.31}$$

the continuity equation, Equation (6.28), applied to the pumping chamber leads to

$$a_{\mathrm{p}}\dot{x}_{\mathrm{p}} + C_{\mathrm{c}}\dot{P}_{\mathrm{c}} + Q_{\mathrm{out}} - Q_{\mathrm{in}} = 0 \tag{6.32}$$

Using Equations (6.29) and (6.30), this can be simplified to

$$\dot{P}_c = \frac{P_1}{C_{\mathrm{c}}(R_1 + R_{\mathrm{in}})} + \frac{P_2}{C_{\mathrm{c}}(R_2 + R_{\mathrm{out}})} + \frac{P_{\mathrm{c}}}{C_{\mathrm{c}}}\left[-\frac{1}{R_1 + R_{\mathrm{in}}} - \frac{1}{R_2 + R_{\mathrm{out}}}\right] + \frac{a_{\mathrm{p}}}{C_{\mathrm{c}}}x_3 \tag{6.33}$$

Similarly, applying the continuity equation, Equation (6.28) to the upper and lower sides of the output hydraulic actuator,

$$\dot{P}_1 = -\frac{P_1}{C_1(R_1 + R_{\mathrm{in}})} + \frac{P_{\mathrm{c}}}{C_1(R_1 + R_{\mathrm{in}})} + \frac{a_{\mathrm{out}}}{C_1}x_4 \tag{6.34}$$

$$\dot{P}_2 = \frac{P_2}{C_2(R_2 + R_{\mathrm{out}})} - \frac{P_{\mathrm{c}}}{C_2(R_2 + R_{\mathrm{out}})} - \frac{a_{\mathrm{out}}}{C_2}x_4 \tag{6.35}$$

where a_{out} is the cross-sectional area of the output hydraulic actuator. C_1 and C_2 are calculated using Equation (6.24).

6.2.5 Assembly of the state-space matrices

Equations (6.15), (6.16), (6.34), (6.35), (6.33), (6.19) and (6.21) can be combined into the familiar state space matrices

$$\begin{aligned} \dot{\tilde{y}} &= \mathbf{A}\tilde{y} + \mathbf{B}\tilde{u} \\ \tilde{y} &= \mathbf{C}\tilde{x} + \mathbf{D}\tilde{u} \end{aligned} \tag{6.36}$$

The terms in the above equations are as follows

$$\tilde{y} = \begin{Bmatrix} x_1 \\ x_2 \\ P_2 \\ P_1 \\ P_c \\ x_3 \\ x_4 \end{Bmatrix} \tag{6.37}$$

$$\mathbf{A} = \begin{bmatrix} 0 & 0 & 0 & 0 & 0 & 1 & 0 \\ 0 & 0 & 0 & 0 & 0 & 0 & 1 \\ 0 & 0 & -\frac{1}{C_2(R_2+R_{out})} & 0 & \frac{1}{C_2(R_2+R_{out})} & 0 & -\frac{a_{out}}{C_2} \\ 0 & 0 & 0 & -\frac{1}{C_1(R_1+R_{in})} & \frac{1}{C_1(R_1+R_{in})} & 0 & \frac{a_{out}}{C_1} \\ 0 & 0 & \frac{1}{C_c(R_2+R_{out})} & \frac{1}{C_c(R_1+R_{in})} & -\frac{1}{C_c(R_1+R_{in})} - \frac{1}{C_c(R_2+R_{out})} & \frac{a_p}{C_c} & 0 \\ -\frac{k_p}{m_p} & 0 & 0 & 0 & -\frac{a_p}{m_p} & -\frac{b_p}{m_p} & 0 \\ 0 & -\frac{K_{out}}{M_{out}} & -\frac{a_{out}}{M_{out}} & \frac{a_{out}}{M_{out}} & 0 & 0 & -\frac{B_{out}}{M_{out}} \end{bmatrix} \tag{6.38}$$

$$\mathbf{B} = \begin{bmatrix} 0 & 0 \\ 0 & 0 \\ 0 & 0 \\ 0 & 0 \\ 0 & 0 \\ \frac{C_v}{m_p} & 0 \\ 0 & \frac{-M_{out}g - f_{friction}}{M_{out}} \end{bmatrix} \tag{6.39}$$

$$\tilde{u} = \begin{Bmatrix} V_p \\ 1 \end{Bmatrix} \tag{6.40}$$

The **C** matrix can be set depending on the states of interest. In the present case, the cylinder displacement is the output, which makes the **C** matrix

$$\mathbf{C} = \begin{bmatrix} 0 & 1 & 0 & 0 & 0 & 0 & 0 \end{bmatrix} \tag{6.41}$$

The **D** matrix is taken as zero

$$\mathbf{D} = \begin{bmatrix} 0 & 0 \end{bmatrix} \tag{6.42}$$

6.2.6 Numerical solution

For specified initial conditions, the above state space equations are solved over a given time period, using the **lsim** routine in MATLAB. The program developed to calculate the response of the device based on the above theoretical development is included in Appendix B. The directionality of the check valves and their opening and closing are modeled by means of the values of R_{in} and R_{out}. Based on the pressures P_c, P_1 and P_2, conditions similar to Equations (6.9) and (6.10) are evaluated and the values of check valve resistance are assigned. If the valve is open, the check valve resistance is assigned an experimentally determined value of flow resistance (Equation (6.7)) and if the valve is closed, the check valve resistance is assigned a value of infinity. The changing value of valve resistance means that the **A** matrix is not constant with time. Also, other entries in the **A** matrix are also dependent on the state vector, for example, the fluid capacitances of the upper and lower parts of the output hydraulic actuator, C_1 and C_2. However, in order to solve the system, it is assumed time invariant for short periods of time. In each of these short periods, the state space system is solved and the values of the various states are computed. A new **A** matrix is calculated and the system

is solved over the next period of time, using the state vector computed in the previous time step as its initial condition. In this manner, the solution is calculated over the entire time period of interest.

Once the cylinder displacement is obtained over the entire time period of interest, the slope of the curve determines the cylinder velocity. This is then compared to experimentally measured cylinder velocities. Table 6.1 gives a list of the main parameters and their values as used in the present model.

Figure 6.5(a) shows the correlation between theoretical and experimental cylinder velocities for the device with ball type check valves, and Figure 6.5(b) shows the correlation for the device with reed valves. As expected, the predictions are poor at high frequencies. However, at frequencies upto approximately 200 Hz for the ball type valves and 250 Hz for the reed valves, the theory is able to predict the experimentally observed behavior with sufficient accuracy. This indicates that the valve dynamics is more important for the ball type check valves than the reed valves, a result which is consistent with previous observations. The theory is sufficient for the purposes of parameter identification and sizing the device to achieve required performance specifications. In order to capture the high frequency behavior, and to explore the possibility of harnessing the high frequency dynamics to improve the performance of the device, it is necessary to treat the fluid circuit as a continuous system, and especially explore the frequency dynamics of the fluid and tubing connecting the pump to the output hydraulic actuator.

6.3 Modeling of piezostack self-heating

The current drawn by the piezostack and the self-heating of the piezostacks are major concerns in the operation of the pump. These two quantities impose limits on the maximum operating frequency of the piezostack, which should be as high as possible

Piezostack – Model P-804.10		
Blocked force F_{block}	5000	N
Peak applied voltage V_{p}	100	V
Free displacement	22.5	μm
Piezostack mass (each)	16	gm
Hydraulic Fluid – MIL-H-5606F		
Density	859	gm/cc
Kinematic Viscosity	15	centistokes
Bulk Modulus (measured)	0.11	GPa
Pumping Chamber and Piston		
Diameter	25.4	mm
Height	1.27	mm
Piston mass	17	gm
Piston damping B_{p}	2×10^3	Ns/m
Tubing – Aluminum		
External diameter	3.175	mm
Internal diameter	4.76	mm
Length	15	mm
Output Actuator – Double Rod		
Bore diameter	0.5	in
Shaft diameter	0.25	in
Stroke	2	inch
Piston and rod mass	50	gm
Piston damping B_{out}	2×10^2	Ns/m
Friction	17.6	N
Check valves – Ball type		
Cracking pressure	5	psi
Fully open pressure P_{full}	15	psi
Hysteresis pressure P_{hyst}	1	psi
Check valve resistance R_{in}, R_{out}	43×10^9	pas/m^3

Table 6.1 Values of various parameters used in the state-space model

to maximize power output of the device.

Considering a piezoelectric sheet actuator driving a mechanical load, with a harmonic excitation of peak voltage V at a circular frequency ω, the current drawn can be predicted using an electro-mechanical impedance approach. Details of this can be found in Chapter 4. The current drawn by the piezoelectric sheet is given by (Equation (4.19)). By looking at the relative magnitude of the terms in this equation, it can be seen that the current drawn is dominated by the electrical impedance and an acceptable approximation to the current drawn can be obtained by ignoring the mechanical impedance terms.

Because the piezostack is composed of several sheets of PZT-5H, the total electrical impedance of the piezostack is equal to the electrical impedance of each piezoelectric sheet multiplied by the number of sheets in the piezostack. The final expression for the electrical impedance of the piezostack is

$$\overline{Z}_c = \frac{\tan\delta}{\omega C_{\text{stack}}(1+\tan^2\delta)} + \frac{1}{j\omega C_{\text{stack}}(1+\tan^2\delta)} \tag{6.43}$$

where C_{stack} is now the capacitance of the entire piezostack. Empirical equations for the variation of e_{33}^{σ} and $\tan\delta$ with excitation field for piezoceramic material of the piezostacks can be obtained as described in Chapter 4. These correction factors can be applied to the constants in Equation (6.43) and the current drawn by the piezostack can be calculated.

From Equation (6.43), it can be seen that in addition to a capacitance, the electrical impedance of the piezostack also contains a frequency dependent resistive term

$$R_{\text{stack}} = \frac{\tan\delta}{\omega C_{\text{stack}}(1+\tan^2\delta)} \tag{6.44}$$

It is this term which is the cause of heat generated in the piezostack [231,232] and is analogous to the energy loss due to damping in mechanical structures [233]. This self-heating of the piezostack is a major concern in operation of the system. Although the

specifications of the piezostack [137] show that its strain output is relatively unaffected upto temperatures of 55°C , the effect of higher temperatures is unknown. The manufacturer of the piezostack specifies an absolute limit of 80°C for the operating regime of the piezostack. At higher temperatures than this, the manufacturer warns that the bond layers between the individual piezoelectric sheets would degrade [137]. Additionally, the temperature rise of the piezostack may have adverse effects on its fatigue properties. Hence, it is very important to be able to predict the temperature rise in the piezostack. Several approaches to thermal modeling can be found in the literature [234,235,232], however, in this thesis, the temperature rise is calculated using a simple one-dimensional thermal model.

As mentioned above, the mechanical impedance of the piezostack and load are neglected while calculating the current drawn by the piezostack. This means that for the purpose of calculating the temperature rise of the piezostack, the work output of the piezostack is neglected. Figure 6.6 shows the temperature rise of the piezostack while operating under a 50 psi bias pressure and a 150 psi bias pressure, at a pumping frequency of 250 Hz. Though the work output of the piezostack is clearly larger in the case of the 150 psi bias operation, the temperature rise in both cases is almost the same. Flint et. al. [236] have calculated the self induced temperature rise of piezostack actuators with both the inclusion of host structure mechanical impedance and the purely capacitive behavior. These results show that the effect of including the mechanical impedance of the host structure is significant only at the resonant frequencies of the coupled system. Neglecting the mechanical work output of the piezostacks while calculating the self induced temperature rise appears a reasonable assumption.

Applying the law of conservation of energy to a control volume enclosing the piezostack [237](Figure 6.7) results in

$$\dot{E}_{\text{generated}} = \dot{E}_{\text{dissipated}} + \dot{E}_{\text{stored}} \tag{6.45}$$

The term energy in this context is understood to specifically refer to heat. For a piezostack being excited by a peak voltage of V_{stack}, at a circular frequency ω, the energy generated in the piezostack is purely due to ohmic heating, which from Equation (6.44) becomes

$$\dot{E}_{\text{generated}} = \frac{V_{\text{stack}}^2}{R_{\text{stack}}} = \frac{V_{\text{stack}}^2 \omega C_{\text{stack}} (1 + \tan^2 \delta)}{\tan \delta} \tag{6.46}$$

Because the mechanical load is ignored in this analysis, the energy dissipated is just the heat lost to the surroundings by thermal convection. This is given by

$$\dot{E}_{\text{dissipated}} = hA_s (T_{\text{stack}} - T_{\text{ambient}}) \tag{6.47}$$

where h is the convective heat transfer coefficient for the present system configuration and A_s is the surface area of the sides of the piezostack. It is assumed that a negligible amount of heat is dissipated from the ends of the piezostacks.

The stored energy leads to an increase in temperature of the piezostack, T_{stack}, depending on the mass of the piezostack, m_{stack}, and the specific heat of the piezostack material, c

$$\dot{E}_{\text{stored}} = \frac{d}{dt} [m_{\text{stack}} c T_{\text{stack}}] \tag{6.48}$$

Figure 6.8 shows the temperature rise in the piezostack actuators over the 5 minute actuation period. During this period, the piezostacks were cooled only by natural air convection. Also shown for comparison is the predicted temperature rise, calculated as described above, which is in good agreement with experimentally measured values. These results justify the assumptions of neglecting the mechanical work output of the piezostacks and neglecting the heat transfer through the ends of the piezostacks.

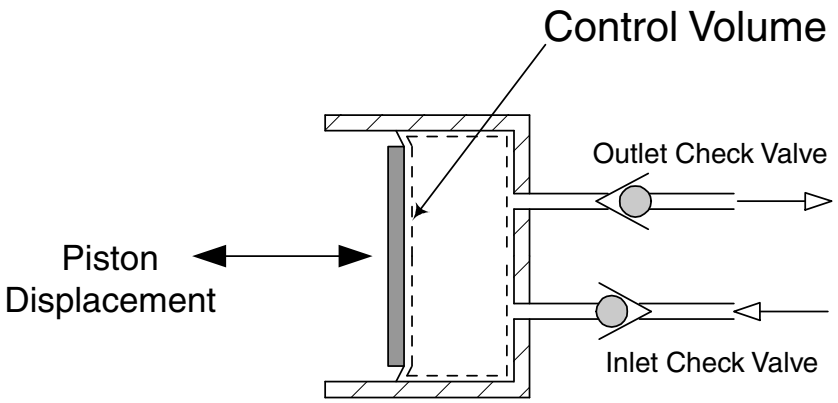

Figure 6.1 Control volume in the pumping chamber

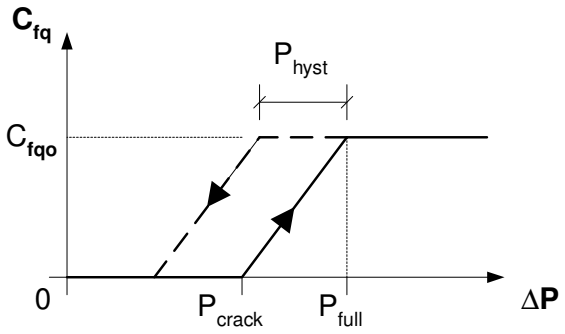

Figure 6.2 Check valve flow factor

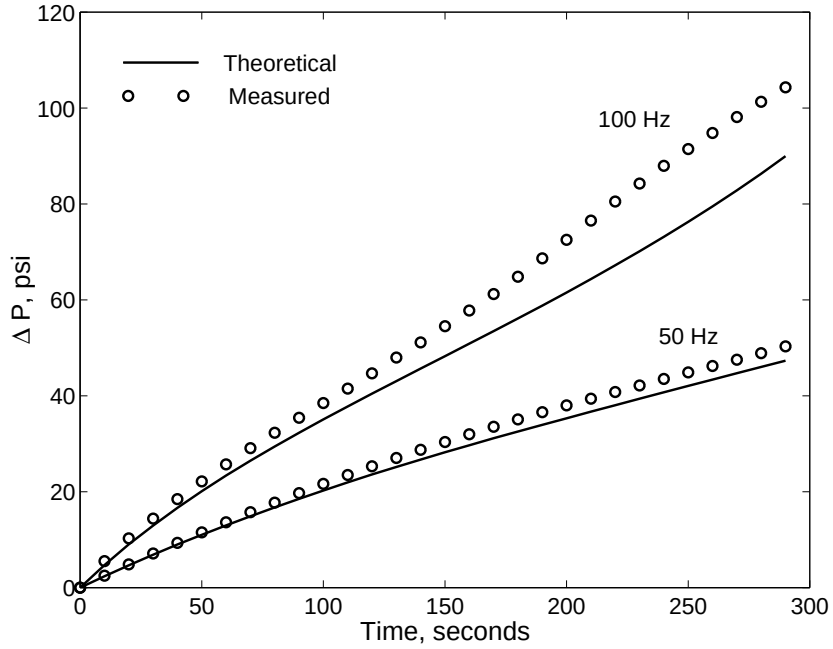

Figure 6.3 Correlation of measured differential pressure rise with theory, 50 psi bias pressure

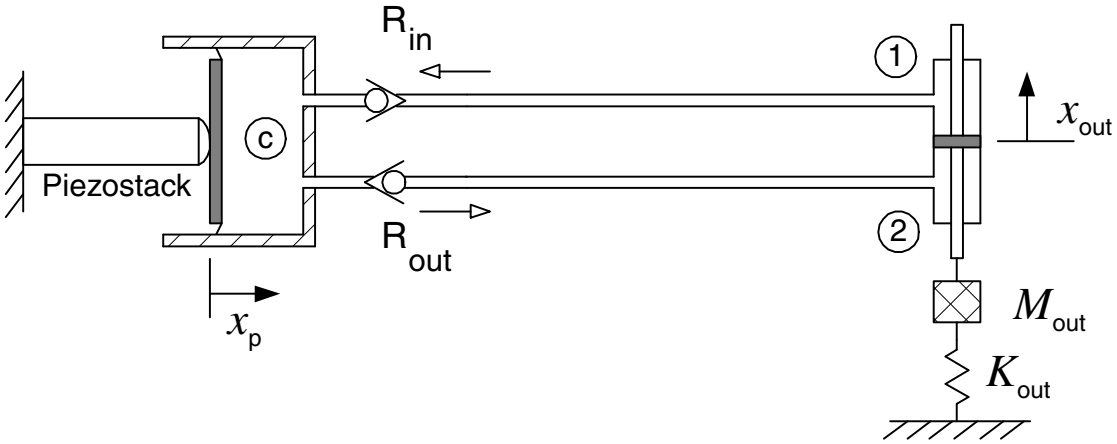

Figure 6.4 Schematic of the device

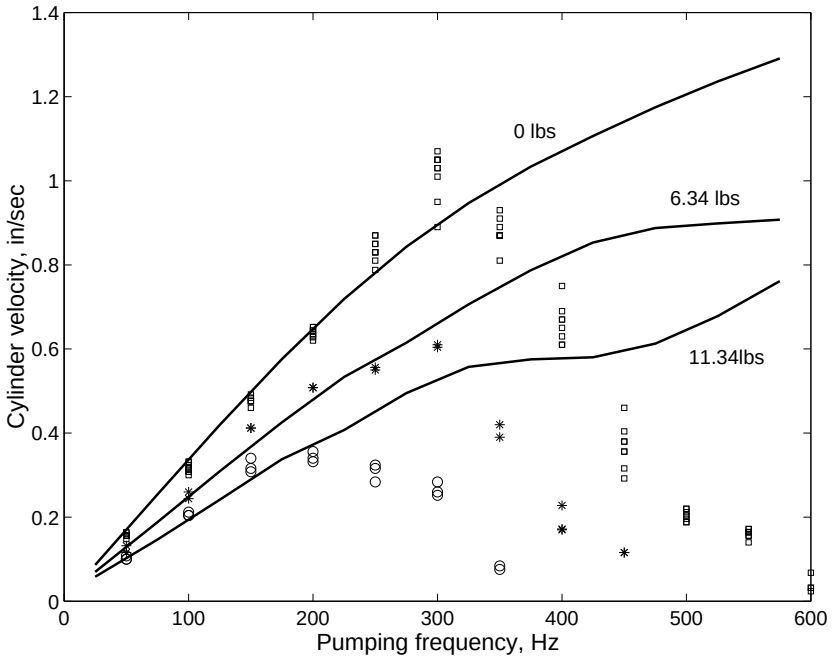

(**a**)With ball type check valves

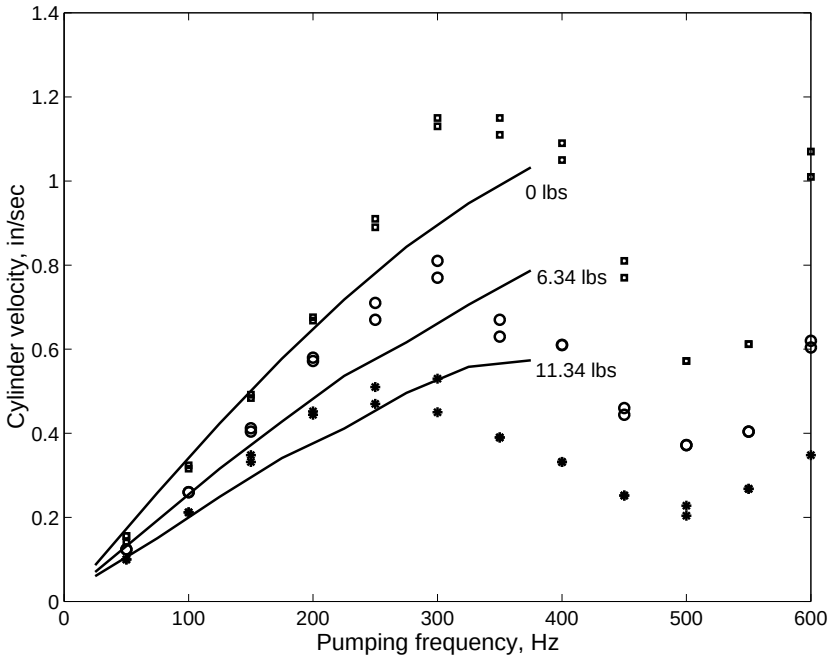

(**b**)With reed valves

Figure 6.5 Correlation of theoretical device output performance with experimentally measured values

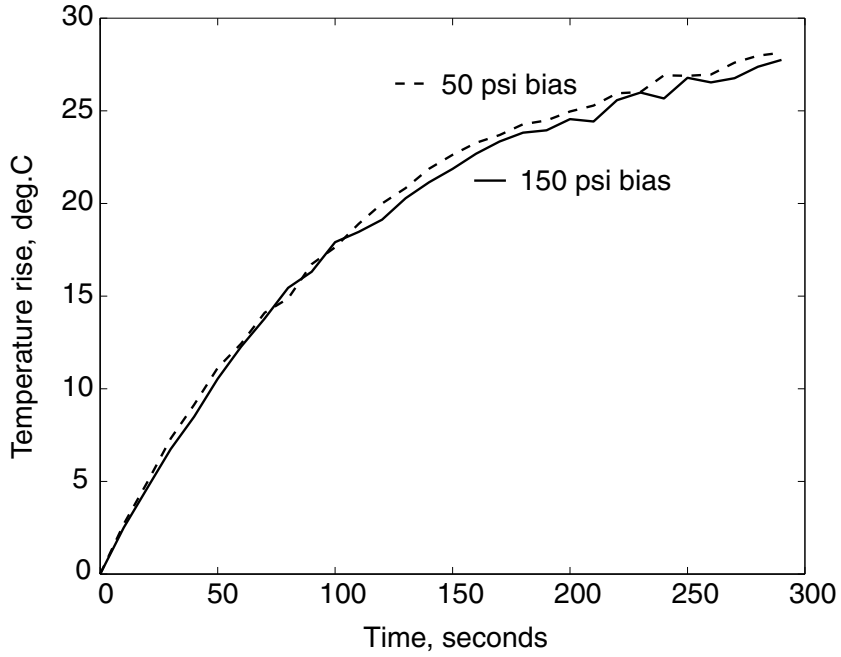

Figure 6.6 Temperature rise in the piezostacks at 50 psi bias and 150 psi bias pressure, 250 Hz excitation

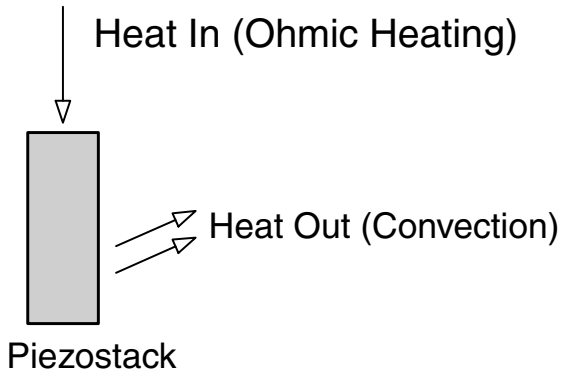

Figure 6.7 Heat transfer from the piezostack

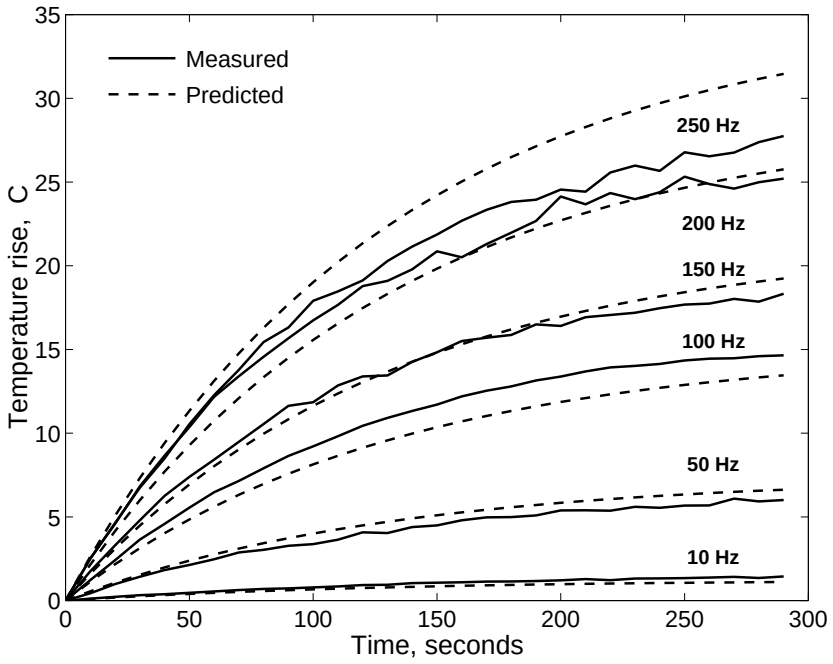

Figure 6.8 Correlation of measured piezostack temperature rise with theory

Chapter 7

Experimental Results and Discussion

This chapter will discuss the results of the experiments described in Section 5.8. Based on these observations, several important conclusions will be drawn, especially regarding the design of the piezoelectric hydraulic hybrid actuator.

Following the guidelines of Section 5.8, the experiments will be discussed in the following order

1. Performance of the piezoelectric pump
    (a) Effect of system bias pressure
    (b) Effect of piezostack actuation method
2. Output power of the device
    (a) Effect of system bias pressure
    (b) Effect of check valves
    (c) Effect of pumping frequency and piezostack actuation method
    (d) Effect of diaphragm stiffness and bonding method
    (e) Effect of fluid viscosity
    (f) Bidirectional actuation

7.1 Performance of the piezoelectric pump

In order to quantify the performance of the piezoelectric pump, the output flow rate was measured as a function of pumping frequency. The performance was measured at two different values of bias pressure and using two different piezostack driving methods. The piezoelectric pump was connected between two accumulators, and the actuation of the pump resulted in the transfer of fluid from the inlet accumulator (also called the low pressure accumulator) to the output accumulator (also called the high pressure accumulator). The differential pressure rise in the accumulators created by the pump was measured over a period of 5 minutes (Section 5.8.1). As the initial pressures in the accumulators is constant, the rate of increase of pressure in the accumulator is related to the flow rate of hydraulic fluid by the gas law. As a result of the low stiffness of the accumulators, the pump is working against almost no load. The rate of differential pressure rise in the accumulators is therefore a direct measure of the flow rate of the pump.

The differential pressure rise at a bias pressure of 50 psi is shown in Figure 7.1(a). Two important observations can be made from this figure. Firstly, the parameter of interest is the initial slope of the curve, which is a measure of the flow rate of the pump. It can be seen that for low frequencies, the slope has an approximately linear dependence on pumping frequency. This is to be expected as the frequency of pumping is low enough to be considered quasi-static, and hence the flow rate depends linearly on pumping frequency. At higher frequencies, however, the dynamics of the system becomes important, and the flow rate is no longer linearly dependent on frequency. It can be seen that the flow rate peaks at a frequency of between 100-200 Hz and then decreases. This attenuation in the flow rate is attributed to bandwidth limitations imposed by the check valves. While dynamic effects of the hydraulic circuit are also

expected to have a strong influence on the flow rate, the dominant factor is the check valves.

The second observation is that the differential pressure as a function of the time of operation is initially linear, but slowly starts saturating. This is attributed to the effect of emptying of the low pressure accumulator, in conjunction with other effects such as the dynamics of the accumulator bladder. As a result, this part of the curve should be ignored and only the initial linear region should be considered.

7.1.1 Effect of system bias pressure

The experiment was carried out at two different bias pressures, 50 psi and 150 psi. From the gas law, it can be seen that the change in pressure caused by a change in volume of the gas is dependent on the initial pressure and initial volume of the gas. Hence, for a higher initial pressure, and constant initial volumes of fluid in the accumulators, a higher increase in pressure is expected with a higher system bias pressure.

Figure 7.1 shows the measured data at two bias pressures, with the Type I valves installed in the pumping head. As expected, the differential pressure is greater in the case of the higher system bias pressure. The most important observation from these results is that the maximum rate of differential pressure rise occurs between pumping frequencies between 100 Hz and 200 Hz, which is the same for both the 50 psi case and the 150 psi case. This is as expected because the stiffness of the accumulators is small compared to the other components in the system and therefore does not have a large impact on the dynamic response of the system. The dynamics of the system is dominated by the dynamics of the check valves. As the pumping frequency increases above about 150 Hz, the rate of differential pressure rise decreases. This indicates that the dynamics of the Type I check valves becomes significant at frequencies above 150 Hz. This is a relatively low frequency compared to the bandwidth of the piezostack, and

therefore imposes a severe constraint on the achievable output power of the device.

It is important to note that the goal of these initial experiments was primarily to verify the effectiveness of the piezoelectric pump, and the overall performance of the device was not an issue. The satisfactory operation of the piezoelectric pump assembly was confirmed by validating the differential pressure rise measurements with theoretical predictions, as described in Section 6.1.

7.1.2 Effect of piezostack actuation method

The pressure rise experiments described above were also performed by actuating the piezoelectric pump by two different methods. The first method involved actuating the piezoelectric pump with a linear power amplifier (HERO model PA9810 [220]). A 0-100 V sinusoidal waveform was applied to the piezostacks at several frequencies. The differential pressure rise in the accumulators was compared to that measured when the piezoelectric pump was actuated with the switched driver (described in Section 5.7.1). With this switched driver, the piezostacks were actuated with a waveform that was approximately a square wave, with the same voltage levels (0-100 V), as in the case of the sinusoidal waveform. As a result, the deflection of the piezostacks, and therefore the volume swept by the pumping piston per cycle, was expected to be same for both actuation methods. A comparison between the increase in differential pressure due to the two actuation methods measured at a pumping frequency of 100 Hz and a bias pressure of 150 psi is shown in Figure 7.2. It can be seen that the flow rate increased by approximately 25% when the piezoelectric pump was actuated by the switched driver approach, as compared to the sinusoidal waveform. This is probably due to the larger impulsive pressures generated in the case of the switched driver waveform compared to the sinusoidal waveform. Hence, it can be concluded that in addition to compactness, the switched driver results in a performance increase of the piezoelectric pump and is a

more attractive option for actuating the piezoelectric pump.

7.2 Output power of the device

As described in Section 5.8.2, these experiments were performed to quantify the output of the device. The piezoelectric pump was connected to an output hydraulic cylinder, and the accumulators were initially charged to the system bias pressure. The accumulators were subsequently isolated from the rest of the hydraulic circuit, effectively coupling the piezoelectric pump directly to the load. This resulted in a system with very different stiffness and dynamic characteristics as compared to the configuration used to quantify the performance of the piezoelectric pump.

It is worth recalling that for quasi-steady operation, the blocked force of the device depends only on the device geometry and piezostack characteristics, while the no-load velocity of the output actuator depends on the device geometry, piezostack characteristics and frequency of pumping.

Figure 7.3(a) shows the output cylinder velocity as a function of output load and driving frequency. The maximum force and the maximum no-load velocity of the actuator are approximately 20 lbs and 0.65 in/sec respectively. These correspond to the blocked force and free strain quantities of the piezoelectric actuator. Each data point is the mean value of three different experimental measurements. True measurement of the blocked force of the device is not possible. The value of blocked force is therefore obtained by fitting a straight line to the force-velocity data, and extrapolating it to the zero velocity condition. Consequently, the value of blocked force is highly dependent on experimental scatter and is subject to some degree of uncertainty.

Theoretically, the blocked force of the device is expected to be independent of the pumping frequency, and the no-load velocity of the device is linearly proportional

to the pumping frequency. However, in the present experiment, the load is lifted through a finite distance during each pumping cycle. The inertia forces resulting from accelerations of the load result in a decrease in output force of the device with pumping frequency. It is expected that this effect would be decreased by introducing an accumulator in the circuit, which filters out the large pressure impulses. Also, such an effect would be absent in a purely spring type load. From Figure 7.3(a), it can be seen that the blocked force is slightly different for pumping frequencies of 50 Hz and 100 Hz. This difference may be largely due to the experimental scatter. The decrease in output force capability due to the effect of inertia loading is more apparent in the case of the higher pumping frequencies of 200 Hz and 300 Hz. This is to be expected, because the inertia forces depend on the square of the excitation frequency. Additionally, it can be seen that the no-load velocity follows the theoretically expected linear variation with pumping frequency at the lower frequencies of 50 Hz and 100 Hz, but is less than expected at the higher pumping frequencies of 200 Hz and 300 Hz. This variation can be more clearly seen in Figure 7.4 and this effect is discussed in greater detail in Section 7.2.2.

7.2.1 Effect of system bias pressure

Measurements were made of the output cylinder velocity for various deadweights at two different bias pressures, 50 psi and 150 psi. As discussed in Section. 7.1.1, for a hydraulic circuit with accumulators, a higher bias pressure would be desirable because it leads to a higher differential pressure rise and therefore a larger output force capability. More importantly, it would be better to adjust the bias pressure and accumulator properties in order to achieve an impedance matched condition with the piezostacks. This would concievably lead to the maximum work output by the device. However, for simplicity and compactness, the present device has no accumulators in

it. Consequently, the only effect a larger bias pressure would have is to decrease the possibility of cavitation and increase the fluid compressibility.

Figure 7.3 shows the effect of system bias pressure on the output performance. It can be seen that the performance is approximately the same at both the bias pressures. At the higher bias pressure of 150 psi, the no load cylinder velocity appears slightly less than that of 50 psi case. This is believed to be due to seizing of the piston in its bore due to possibly higher off-axis loads. A longer piston with a smaller clearance between the bore and the piston would solve this problem. For the time being, 50 psi is chosen as an acceptable working bias pressure for the device.

7.2.2 Effect of check valves

The output power of the device was measured with the Type I ball check valves as well as Type II reed valves installed in the pumping head. As operation at a high pumping frequency is one of the key goals of the design, the Type II valves were specifically intended to permit larger flow rates at higher frequencies than the Type I valves. It should be noted that while reed valves are routinely used in devices such as air compressors and two stroke engines, such devices have a much larger volumetric flow rate per cycle than the pump presently under study, where leakage is expected to be a critical factor. Although it is intutively expected that the reed valves would lead to an increase in performance, careful measurements of the performance of the device with the Type II reed valves is essential to evaluate its feasibility.

Figure 7.4 shows a comparison of the output cylinder velocity with Type I and Type II valves installed at no load and maximum tested load conditions. As expected, the Type II valves with a higher natural frequency show a larger flow rate. For the maximum tested deadweight of 11.34 lbs, at a pumping frequency of 300 Hz, the Type II valves permit approximately 2.8 times more flow rate than the Type I valves. Therefore, in

terms of the increasing the pumping frequency of the device and consquently its output power, the Type II valves provide a better solution than that with the conventional Type I valves.

At this point, it is worth looking into the effects of the dynamics of the check valves, as seen by measurements of the pumping chamber pressure. Figure 7.5 shows the measured pumping chamber force-displacement curves for several output deadweights, at a pumping frequency of 50 Hz and a bias pressure of 50 psi. Multiplying the pumping chamber pressure by the piston area gives the force on the piezostacks, plotted on the Y-axis. Also plotted on the same graph is the piezostack load line. In this case, a 0.01" thick steel diaphragm was installed, restricting the effective displacement of the piezostack to 0.8 mils. The piezostack load line has therefore been scaled appropriately, eliminating the stroke lost due to the presence of the diaphragm. As the pumping frequency is relatively low, the dynamics of the check valves is not expected to be significant. This is confirmed by observing the shape of the pumping chamber pressure traces, that are very close to the ideal parallelogram shape discussed in Chapter 5. From these measurements, the value of fluid stiffness in the pumping chamber, K_f can be calculated, and an effective value of the fluid bulk modulus can be identified. This value is 0.11 GPa, which is almost 10% of the reference fluid bulk modulus for the fluid. Including the appropriate corrections [218] to the reference fluid bulk modulus for the system bias pressure of 50 psi, and an entrained air fraction of 1%, the effective bulk modulus becomes 0.16 GPa (Section 5.5.11), which is in close agreement with the measured value. The importance of the fluid bulk modulus can be easily understood from this graph. A large part of the force capability of the piezostack is untapped as a result of the low stiffness of the fluid in the pumping chamber. Since some amount of entrained air is usually unavoidable in any hydraulic system, this stiffness can be increased by increasing the bulk modulus of the working fluid as well as decreasing

the pumping chamber height. As shown in Section 5.5.11, the height of the pumping chamber is a very important parameter in matching the device to the output load.

Figure 7.6 shows the force-displacement results at a pumping frequency of 50 Hz and 300 Hz with Type I valves installed. The bias pressure is maintained at 50 psi for both cases. At the frequency of 300 Hz, the dynamics of the Type I valves becomes a significant factor affecting the pressure history in the pumping chamber. This is evidenced from the shape of the force-displacement curves, which are far from ideal. Additionally, some smaller loops can be seen in the these curves, which are indicative of large phase mismatches between the piston displacement and pressure response.

Figure 7.7 shows the pumping chamber force-displacement curves at 50 Hz and 300 Hz, at a bias pressure of 50 psi, with the Type II valves installed. Comparing Figures. 7.7(a) and 7.6(a), it can be seen that there is almost no change in behavior at the low pumping frequency of 50 Hz. However, comparing Figures. 7.7(b) and 7.6(b), it can be seen that the pressure response of the Type II valves is more well behaved than that of the Type I valve at the pumping frequency of 300 Hz. This provides further evidence that the Type II valves are a better solution than the Type I valves for high frequency pumping.

7.2.3 Effect of pumping frequency and piezostack driving method

As discussed in Chapter 5, in order to increase the output power of the device, the pumping frequency must be increased. However, in practice, several factors restrict the maximum frequency that can be achieved. These factors are

1. Maximum current limitations of the driving power amplifier
2. Dynamics of the check valves
3. Dynamics of the hydraulic circuit

4. Piezostack self heating

Using the linear amplifier (Rohrer PA9810 [220]), the excitation frequency of the piezoelectric pump is limited to 300 Hz because of the output current limitations of the amplifier. This actuation frequency was achieved with the piezostacks connected in parallel to the amplifier output. Using two PA9810 amplifiers, one for each piezostack, the maximum excitation frequency was increased to 600 Hz. Using the switched driver, it was possible to test the device at a pumping frequency of 1 kHz.

Figure 7.8 shows the no-load output cylinder velocity of the device as a function of pumping frequency, with the Type II valves installed. The roll-off in pump flow rate with frequency is evident in this figure. However, the flow rate starts increasing again after around 400 Hz. This decrease of flow rate in the region around 400 Hz is believed to be due to the dynamics of the tubing and hydraulic circuit. These dynamics are not been addressed in this dissertation and are a very important factor in refining the design of the device to increase the output power.

Another observation that can be made from this figure is that the flow rates are larger in the case of exciting the piezostacks with the switched driver. This observation is consistent with the discussion in Section. 7.1.2.

At this point it would be worthwhile to discuss the effects of piezostack self-heating, since it is a major factor limiting the maximum excitation frequency of the piezostacks. A detailed discussion of the causes of piezostack heating and its quantification was presented in Chapter 6. Two techniques of limiting the maximum temperature of the piezostacks were attempted.

1. Passive heat dissipation - thermal compound

2. Active heat transfer - Thermoelectric Modules (TEMs)

The simplest way to prevent the piezostacks from overheating is to dissipate as much of the heat as possible through conduction from the piezostacks to a large thermal sink. In this case, the body of the pump itself is a large heat sink, and it would concievably be attached to the structure of an aircraft creating an even larger heat sink. The main issue is to provide a heat transfer path from the piezostack to the pump body. The solution that was adopted in this case was to fill the gaps between the piezostacks and the pump body with a thermally conductive, but electrically insulating silicone compound (CHO-THERM 1642 [238]). Due to its extremely low shear stiffness, the compound does not affect the deformation of the piezostacks. Because of its large thermal conductivity, it provides an effective heat transfer path to the pump body.

Figure 7.9 shows a test specimen used to measure the effectiveness of the passive cooling method. The test specimen represents a cross-section of the piezoelectric pump, with a piezostack and the thermal compound. A strain gage was bonded to the piezostack, and the temperature of the piezostack was measured using a surface mounted thermocouple. Even though this led to the measurement of a reduced temperature than that at the core of the piezostack, the level of error was considered acceptable for the present purpose. The test specimen was excited in the same manner as the piezoelectric pump and the temperature was measured over a given time period till the system reached steady state. These measurements are shown in Figure 7.10.

At an excitation frequency of 1 kHz, the piezostack temperature stabilized at approximately 70°C . As the manufacturer specifies 80°C as the maximum recommended operating temperature, the maximum excitation frequency of the piezoelectric pump using passive cooling was restricted to 1kHz. The present prototype pump has a body made of steel, which has a low thermal conductivity compared to aluminum. Therefore, the steady state temperature of the piezostacks achievable by fabricating the pump body out of aluminum is expected to be lower than that of the

present device.

Another approach to control the temperature of the piezostacks is by using active cooling, with TEMs. The TEMs operate off a $5V_{DC}$ supply and draw a current on the order of 1-2 Amps. When an electric current is passed through them, they transfer heat from a cold side to a hot side, acting as heat pumps. The TEMs can therefore be installed in the pump body with one side in contact with the piezostacks and the other side in contact with the pump body. In this way, they would transfer the heat generated in the piezostacks from the piezostacks to the pump body.

Figure 7.11 shows a test setup to measure the effectiveness of active cooling. A commercially available TEM [239] was installed on a piezostack, which was instrumented with a strain gage and a thermocouple. The other side of the TEM was in contact with an aluminum heat sink, which however is not shown in the figure. The results of the active cooling experiment are shown in Figure 7.12. It can be seen that the TEMs caused a significant reduction in the temperature of the piezostack. Unfortunately, the efficiency of these devices is quite low, and much more power needs to be supplied to the TEMs than the amount of heat they actually transfer from one side to the other. In addition, they are difficult to integrate in the pump body. For these reasons, this method was not chosen as the final solution for the piezostack heat dissipation problem. Passive cooling was considered to be sufficient for the present purpose, and the active cooling was retained as an option if more cooling is required in future tests.

7.2.4 Effect of diaphragm stiffness and bonding

The first prototype of the piezoelectric pump had a steel diaphragm of thickness 0.01”. The stiffness of this diaphragm caused a reduction in the effective free displacement of the piezostack-piston assembly from 1 mil to 0.8 mil. Correlations of the

experimentally measured diaphragm stiffness with theoretical predictions are discussed in Section 5.5.6. Additionally, measurements of the displacement of the diaphragm made using a scanning laser vibrometer showed some amount of rocking of the piston-diaphragm assembly. This was attributed to the large stiffness of the diaphragm causing the diaphragm to debond from the piston. The asymmetric debonding would cause an asymmetric forcing on the piston, resulting in a rocking motion of the piston in its bore. Because of this rocking motion, a considerable fraction of the volumetric displacement per cycle was lost, leading to lower cylinder velocities than expected. This can be seen by comparing the experimentally observed block force and no-load cylinder velocity of 20 lbs and 0.65 in/sec respectively with the estimated values of 30 lbs and 1.2 in/sec (Section 5.5.11).

In order to increase the volumetric displacement of the pump as well as to decrease the stresses in the diaphragm, the 0.01" thick steel diaphragm was replaced by a 0.002" thick diaphragm made of C-1095 tempered spring steel. The reduced stiffness of the 0.002" thick diaphragm resulted in an increase in the effective free displacement of the piezostack-piston assembly from 0.8 mils to 0.9 mils. As the stiffness of the fluid in the pumping chamber (approximately 2.5×10^5 lbs/in) is on the same order as the diaphragm stiffness (approximately 1.3×10^5 lbs/in), the decrease in stiffness of the diaphragm is not expected to have a large impact on the frequency response of the pumping assembly. The output performance of the device with the 0.002" thick diaphragm is shown in Figure 7.13. The blocked force of the device is approximately 33 lbs and the maximum no-load cylinder velocity achieved is about 1.2 in/sec at a pumping frequency of 300 Hz. These values are much closer to the estimated values (from Section 5.5.11).

The diaphragm was bonded to the piston using a cyanoacrylate type adhesive(M-Bond 200 [164]). This provided a thin bond with a high shear stiffness, and was

expected to have good fatigue properties. However, the performance of the device was observed to degrade with pumping cycles of the piezostacks, as shown in Figure 7.14. Additionally, the curves plotted in Figure 7.14 were obtained on consecutive days, with the piezostack-diaphragm assembly being kept under the system bias pressure between experimental runs. On disassembling the pump, it was observed that the diaphragm was slowly debonding from the piston. The debonding is expected to have occured due to a combination of fatigue failure of the bond layer and a gradual degradation of the bond layer due to the constant stress created by the system bias pressure. This resulted in the loss of a constraint on the angular displacement of the piston and hence allowed the piston to undergo a rocking motion in its bore. Consequently, the swept volume of the pump per cycle decreased with progressive operation of the pump. In order to solve this problem, several methods of bonding the diaphragm to the piston were investigated. The best results were achieved by bonding the diaphragm to the piston with film adhesive(Cytek 123-2 [240]). A circular piece of the film adhesive, of diameter 0.95" was placed between the diaphragm and the piston. A clamping pressure was applied and the assembly was cured in an oven at 250° F for 3 hours. The output performance of the device was measured and the results are shown in Figure 7.15. The amount of scatter in the experimental data can be seen from the error bars plotted in the figure. This scatter represents the variation between measurements, while the error in measurement of each point is calculated to be smaller than the size of the legend in the plot.

The performance of the device is now more repeatable over several experimental runs. The effect of the high bandwidth Type II valves on the performance of the device is again evident from the larger flow rates at higher pumping frequencies. Also shown in Figure 7.16 is the output no-load cylinder velocity with the Type II valves installed upto a pumping frequency of 1 kHz. The dip in the output velocity at around 500 Hz is

believed to be caused by the dynamics of the hydraulic circuit and tubing.

7.2.5 Effect of fluid viscosity

Experiments by Mauck et. al. [180, 205] showed the effect of the viscosity of the working fluid, which resulted in a 50% increase in the flow rate of the pump when the viscosity of the working fluid was decreased from 100 cst to 0.65 cst. However, these experiments were performed at pumping frequencies below 100 Hz. It can be expected that viscosity would have a greater effect on the performance of the device at higher pumping frequencies as a result of the higher fluid velocities.

Analyses by Zhang and Cadou [241] showed that viscosity does not have a significant effect on the performance of this device upto pumping frequencies of about 2kHz. In order to experimentally evaluate the effect of viscosity on the performance of the present device, especially at high frequencies, the output power experiments described above were repeated with a low viscosity hydraulic fluid. The low viscosity fluid used was a Mobil Velocite No. 3 spindle oil, with a viscosity of 2 cst. This is compared to the baseline performance of the device with MIL-H-5606F hydraulic fluid of viscosity 15 cst. The experiments were performed with the Type II check valves installed in the device.

The results of the experiment can be seen in Figure 7.17. The output cylinder velocities measured with the low viscosity oil are plotted as solid lines, and the velocities measured with the baseline hydraulic oil are plotted as dashed lines. No significant change in the performance is observed at higher frequencies. However, at low frequencies, the cylinder velocities are lower for the lower viscosity oil. The reason for this behavior is not well understood, but may be attributed to the leakage behavior of the reed valves.

7.2.6 Bidirectional actuation

Most of the experiments measuring the output power of the device were performed by actuating the output cylinder in only one direction. This was as a result of directly connecting the piezoelectric pump to the output cylinder, without a 4-way valve (Figure 5.19(a)). Experiments were performed in this fashion in order to minimize the complexity of the system for preliminary testing and validation. At the end of each run, the cylinder was returned to its zero position by manually opening the valves in the circuit and bypassing the piezoelectric pump. However, in the final application, bi-directional operation of the output cylinder is necessary. Therefore, after performing the preliminary output power experiments with uni-directional actuation, and validating the results with theoretical predictions, a 4-way valve was incorporated in the circuit (Figure 5.19(a)). The 4 way valve was a commercially available spool valve (HR Textron Model 27A50 R-DDV [222]), chosen specifically for its compactness and frequency response. It should be pointed out here that the size of the 4-way valve is comparable to the size of the piezoelectric pump itself, which means that the power density of the overall system is decreased by almost half to accomodate bi-directional actuation. Conceptually, one way to address this issue could be by installing active check valves, whose opening and closing could be controlled electronically. Thus, by adjusting the phasing of the valves, the direction of the output cylinder displacement could be changed.

Some initial experiments were performed on the bi-directional actuation of the output cylinder with no external load. Introducing the 4-way valve in the hydraulic circuit is expected to affect the flow rate of the device. In order to quantify this effect, the 4-way valve was kept fully open in one direction, effectively resulting in unidirectional actuation of the device, and the no-load cylinder velocities were measured as a function

of pumping frequency. These measurements are plotted in Figure 7.18. The hydraulic oil used in this case was the low viscosity 2 cst oil. Comparing these results to the no-load cylinder velocities measured without the 4-way valve (Figure 7.17), it can be seen that the introduction of the 4-way valve in the hydraulic circuit results in a decrease of approximately 20% in the no-load cylinder velocity at a pumping frequency of 300 Hz. Additionally, the shape of the curve is different, which is to be expected, since the change in geometry of the hydraulic circuit changes its dynamic response.

The next stage of experiments involved actuation of the 4-way valve with an oscillatory signal, resulting in bidirectional motion of the output cylinder. The 4-way valve was excited by a square waveform at frequencies of upto 10 Hz. Figure 7.19 shows the output cylinder displacement at an operating frequency of 5 Hz. The high frequency spikes are noise originating from the linear potentiometer. The pumping frequency in this particular case was 100 Hz. Figure 7.20 shows the peak to peak output cylinder displacement at output frequencies of upto 10 Hz, for various pumping frequencies ranging from 50 Hz to 300 Hz, with no external load. As the flow rate of the piezoelectric pump is constant, the product of the peak to peak output displacement and the output frequency is expected to be constant. Therefore, the theoretical shape of the output displacement as a function of pumping frequency is a rectangular hyperbola, which is closely matched by experimental measurements.

Further measurements of bidirectional actuation performance were performed with an external spring load attached to the device. The spring load consisted of a cantilevered beam, with its tip connected to the output hydraulic cylinder of the device. Steel and aluminum beams of the same geometry were used as the spring loads, thus achieving two different spring stiffnesses, of approximately 60 lbs/in and 180 lbs/in. The external load was chosen to be of a purely spring type, with no deadweight, so that there would be no bias force acting on the device. As all the testing was open loop, a

bias force would have caused the zero position of the output displacement to drift.

A linear potentiometer on the output shaft of the device provided measurements of the output displacement, while a load cell connected between the output shaft and the load spring provided output force data. A stepped sinusoidal voltage of amplitude 5V, at a frequency from 2 Hz to 20 Hz was input to the 4-way valve. The pump was operated at a constant frequency of 300 Hz, with a sinusoidal voltage of 0-100 V. It should be noted that in the frequency range considered, the open loop transfer function of the device is not significantly affected by the dynamics of the 4-way valve. According to the manufacturer supplied data [222], the bandwidth of the 4-way valve is approximately 200 Hz.

The amplitude and phase of the output displacement of the device is plotted in Figure 7.21. The output of the device under no-load condition, and with external spring loads of stiffness 60 lbs/in and 180 lbs/in are shown. As expected, the amplitude of output displacement decreases with increasing load. However, as the output frequency increases, the amplitude of the output does not vary much with load, as a result of the low spring forces at low amplitudes. The decrease in phase angle with increasing frequency is partly due to the response of the 4-way valve, which according to the specifications provided by the manufacturer [222], has a phase lag of 10° at a frequency of 20 Hz.

Since the analytical model developed in Chapter 6 does not include a model for the 4-way valve, a theoretical limiting curve for output displacement amplitude as a function of output frequency is obtained using the no-load unidirectional velocity data plotted in Figure 7.18. This is compared to the experimentally measured output displacement amplitudes, at a pumping frequency of 300 Hz, in Figure 7.22. It can be seen that the shape of both the curves is the same, whereas the experimental data is lower by a constant offset of approximately 0.03 in. This is attributed to the leakage in the 4-way

valve.

7.3 Conclusions

The design, analysis and testing of a compact piezoelectric hydraulic hybrid actuator is described in Chapters 5, 6 and 7. The device under development in the present study is envisaged as a potential actuator for a trailing edge flap on a smart rotor. As discussed in Chapter 1, while actuators based on active materials, especially piezoceramics, are very attractive for this application, their small stroke remains a major challenge to achieve sufficient control authority. Current actuator designs rely on mechanical stroke amplification of the small displacements of piezoelectric stacks to obtain required output displacements. Such devices typically are limited by the maximum possible amplification ratio and have energy densities on the order of 0.15 J/kg. It should be noted that in the present application, while energy density with respect to mass is very important from the point of view of weight penalty, energy density with respect to volume is also very important, considering the small volume enclosed within a rotor blade. The basic motivation for developing the piezoelectric hydraulic hybrid actuation concept is to increase the energy density of actuators based on active materials. The output bandwidth requirement, which in the present application is on the order of 40 Hz, should also be considered while evaluating the actuation performance.

The piezoelectric hydraulic hybrid concept combines the high energy density of piezostacks with the power transmission versatility of a hydraulic system. While the concept is based on frequency rectification, it does not suffer from the wear and tolerance problems inherent with other rectification concepts such as inchworm motors and ultrasonic motors.

It is worth pointing out here that the basic frequency rectification principle relies on

the conversion of a small stroke, high frequency input to a larger stroke, lower frequency output. Therefore, in order to increase the bandwidth of the output, it is important to have as high an input frequency as possible. Hence, in the present device, the design is focused on enabling as high a pumping frequency as possible. The present device was operated upto a pumping frequency of 1 kHz. However, the maximum fluid flow rate was observed at a pumping frequency of approximately 300 Hz.

Several challenges exist to operate the device at high pumping frequencies. Solutions to these issues are attempted in the present prototype and are discussed below :

- **Dynamics of the passive check valves :** Approximately 30% more flow rates at high pumping frequencies were achieved using the high frequency Type II passive check valves as opposed to the commercially available Type I ball type valves. From measurements of the output flow rates, as well as pressure traces in the pumping chamber of the pump, it can be concluded that the Type II valves are better suited for high frequency pumping.

- **Delivery of electrical power :** Using conventional linear amplifiers, supplying a sinusoidal excitation to the piezostacks, the large currents drawn by the highly capacitive piezostacks at high excitation frequencies would make the driving power amplifiers bulky. Any advantage obtained by the compactness of the device would be negated by the large power amplifiers. In the present design, the piezostacks were driven by a compact switched driver, that was designed and fabricated in-house and which enabled excitation of the piezostacks upto 1kHz. This helped to obtain better output flow rates than those observed while driving the pump with a sinusoidal waveform.

- **Piezostack self-heating :** Keeping the temperature of the piezostacks under

80°C appears imperative as per the specifications from the manufacturer. In the current design, this is achieved using a passive method to conduct heat away from the piezostacks. This results in a steady state piezostack temperature of approximately 70°C at a pumping frequency of 1kHz. If further cooling is required, active heat transfer using TEMs is a possible solution.

- **Piston-diaphragm assembly :** The diaphragm is a very important part of the current design. It serves two main functions. Firstly, it provides a seal between the pumping chamber and the piezostacks. Secondly, it increases the stiffness of the piston, and constrains it to move purely in an axial degree of freedom along its bore. Initial experiments on the device were carried out with a 0.01" thick low carbon steel diaphragm installed, that was bonded to the piston with cyanoacrylate adhesive. It was observed that there were large stresses being created in the circumference of the diaphragm, that coupled with poor fatigue properties of the cyanoacrylate adhesive, caused the diaphragm to debond from the piston. This resulted in a rocking displacement of the piston in its bore, with a consequent loss in volumetric displacement of the pump. The subsequent improved design incorporated a 0.002" thick C-1095 tempered spring steel diaphragm bonded to the piston with film adhesive. The high yield strength of the spring steel allows it to withstand the high stresses around the circumference of the piston, while its low thickness allows it to conform easily to the shape of the displaced piston. The film adhesive was also observed to have excellent fatigue properties. As a result, a 20% improvement in flow rates was observed and repeatable performance was recorded over several days.

It should be noted that in the present design, the maximum excitation frequency of 1 kHz was limited not by electrical power delivery issues, but by the maximum

temperature of the piezostacks as a result of self-heating.

The present device was designed to meet the specifications of a previous generation trailing-edge flap actuator, based on piezostacks with an amplification mechanism [131], that achieved a blocked force of 9 lbs and a free stroke of 80 mils, upto frequencies of approximately 100 Hz. The prototype piezoelectric hydraulic hybrid actuator developed in the course of the present research effort achieved a blocked force of approximately 33 lbs with a maximum no-load velocity of 1.2 in/sec, while being operated in the uni-directional output mode. In order to achieve bi-directional output, a 4-way valve was introduced in the device, which resulted in a loss of output displacement of approximately 20% due to internal leakage. At a frequency of 5 Hz, which is approximately 1/rev, the amplitude of the output displacement was measured to be 32 mils under no external load, dropping to 15 mils under an external spring load of 180 lbs/in. The no-load output displacement amplitude drops to 12 mils at a frequency of 10 Hz. It can be concluded that while the present prototype meets the blocked force and quasi-static free stroke requirements, it does not achieve the required bandwidth for active vibration control purposes. In its present form, the prototype is more suited for quasi-static applications, involving a long output stroke at a low frequency, as opposed to oscillatory output at a short stroke and high frequency. This is because a major feature of this actuation concept is that the uni-directional stroke can be virtually limitless. An example of an application where the present device would perform very well is the deployment and locking of a control surface on an aircraft.

The low bandwidth of the device is directly a result of the non-linear variation of flow rate with pumping frequency. While the state-space model described in Chapter 6 satisfactorily predicts the behavior of the system upto pumping frequencies of around 100 Hz, it fails to represent the behavior of the system at higher pumping frequencies. A comprehensive model of the system including the dynamics of the fluid and tubing

is necessary to predict, and consequently, increase the output of the device at higher pumping frequencies.

As the present device is in its early phase of development, and is intended to serve as a test setup for measuring performance, it is not prudent to compare its power density with other well-developed actuators. However, in terms of active material alone, the present device uses two piezostacks, whereas the previous generation actuator uses five of the same piezostacks. It is expected that the deficiency in output bandwidth of the present device could be overcome by designing the system to operate more efficiently at higher pumping frequencies.

7.4 Recommendations for future work

The output of the device was observed to be highly non-linear above pumping frequencies of approximately 300 Hz. This was attributed to dynamics of the hydraulic tubing and fluid. In order to understand this phenomenon better, and possibly utilize these effects to increase the output flow rate of the device, a detailed analytical model of the device including valve dynamics, hydraulic circuit dynamics, and fluid inertia needs to be developed and validated. An increase in the output stroke and bandwidth is only possible by increasing the flow rate of the pump. Future research efforts should focus on increasing the flow rate of the pump at high frequencies.

The issue of electrical power delivery, which is one of the major obstacles to high frequency pumping operation, was addressed in the present research by means of actuating the piezostacks with the switched driver. However, the long term effects of actuating the piezostack in this manner, with respect to fatigue failure, has not been addressed. This would be of considerable importance in a real application and should be investigated in future research.

The maximum pumping frequency of 1kHz was dictated by temperature limits of the piezostacks. In future devices, a careful design of heat transfer mechanisms is necessary. For example, construction of the pump body out of aluminum would reduce the steady state temperature of the piezostacks for the same frequency excitation. The possibility of integrating TEMs in the pump body should also be evaluated in the event of insufficient passive heat transfer.

Bi-directional output of the device is achievable only through the use of a 4-way valve installed on the output of the piezoelectric pump. However, the smallest conventional 4-way valves are almost as big as the piezoelectric pump itself, effectively reducing the power density of the device by almost half. This is a major limitation of the present design, and future efforts should be directed towards active check valves, that would perform both the functions of the passive check valves and the 4-way valve.

From the point of view of smart rotor applications, it is very important to evaluate the effect of centrifugal loads on the device, both in the design stage as well as by experimental validation.

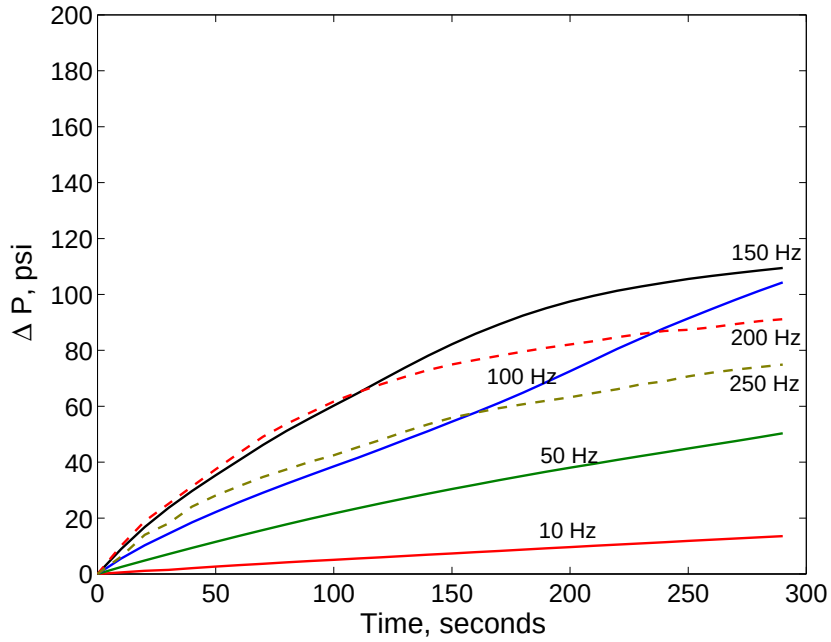

(**a**)Bias pressure 50 psi

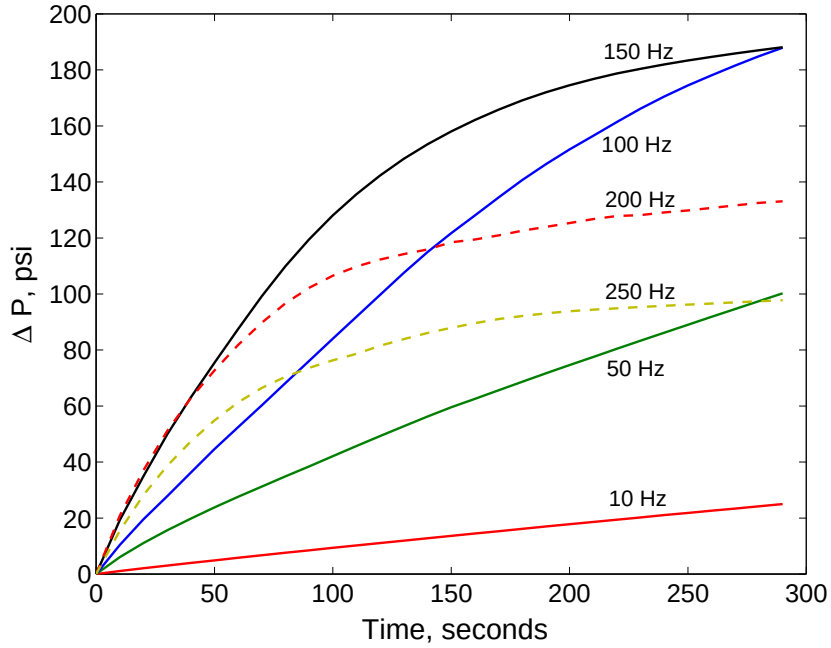

(**b**)Bias pressure 150 psi

Figure 7.1 Effect of system bias pressure on differential pressure rise in the accumulators

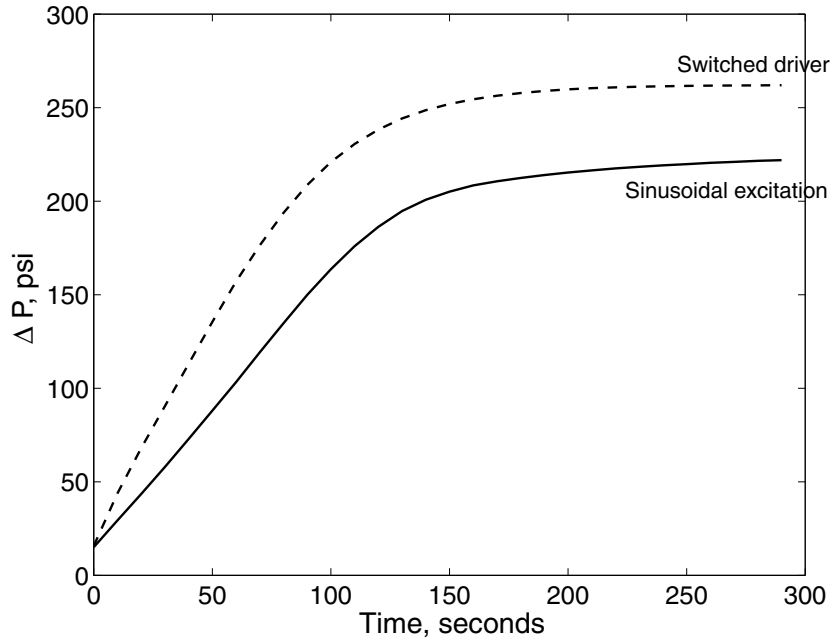

Figure 7.2 Comparison of differential pressure rise with two piezostack excitation methods; switched driver and sinusoidal excitation

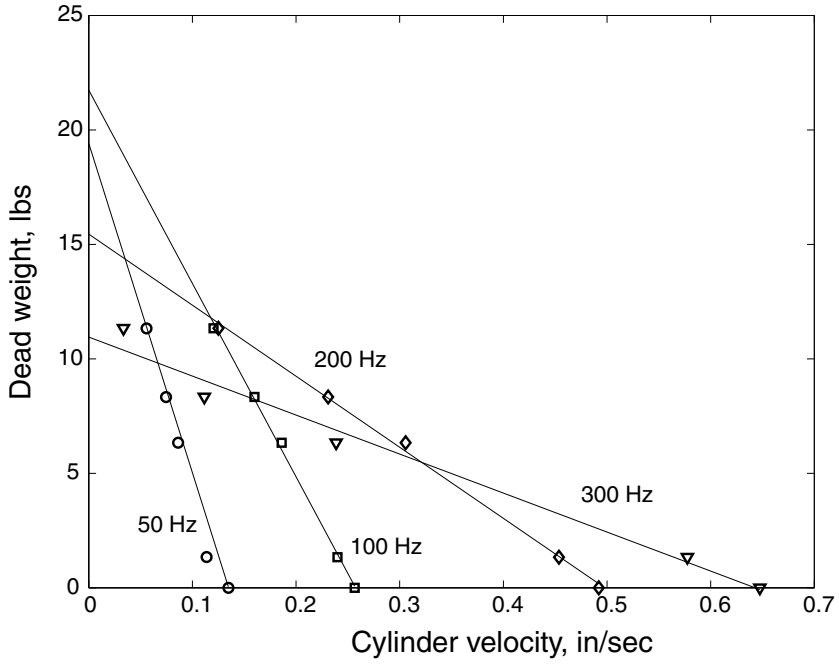

(**a**)Bias pressure 50 psi

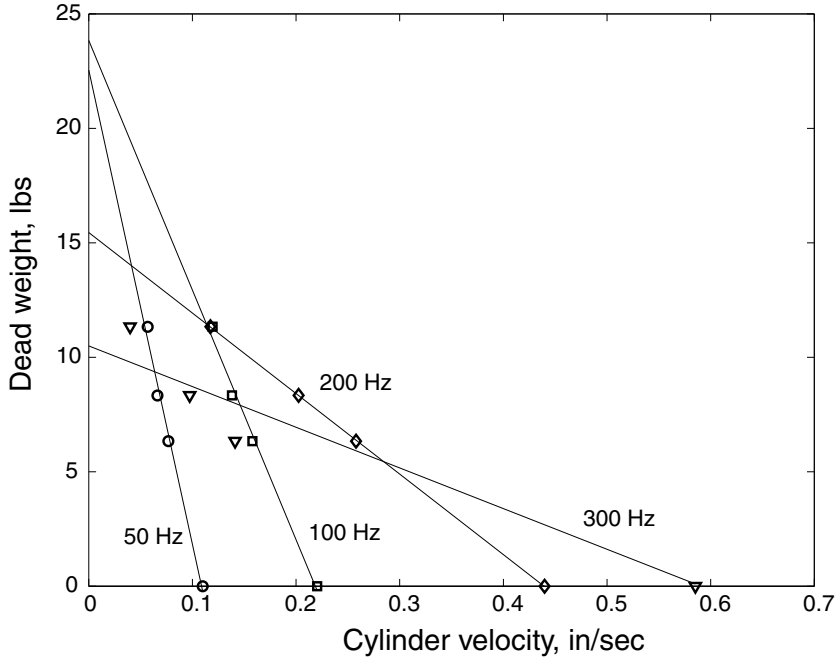

(**b**)Bias pressure 150 psi

Figure 7.3 Effect of system bias pressure on device output with 0.01” steel diaphragm, Type I valves

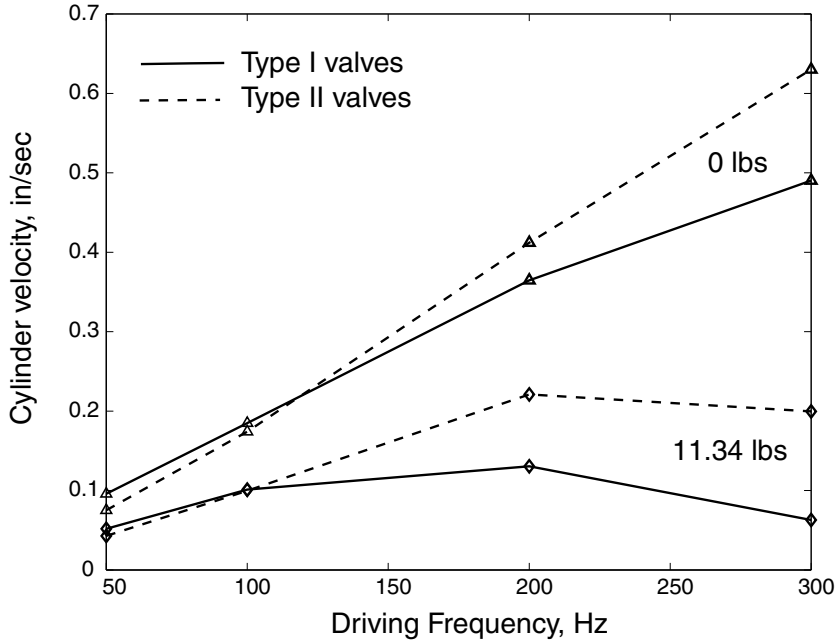

Figure 7.4 Comparison of output performance with Type I and Type II valves

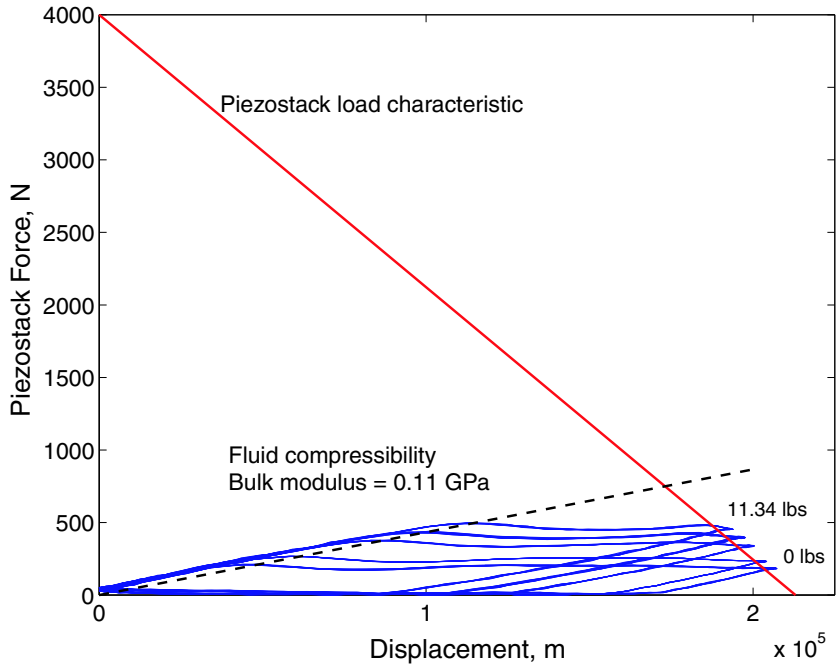

Figure 7.5 Measured pumping chamber force-displacement curves, for 50 Hz pumping frequency, and 50 psi bias pressure, Type I valves

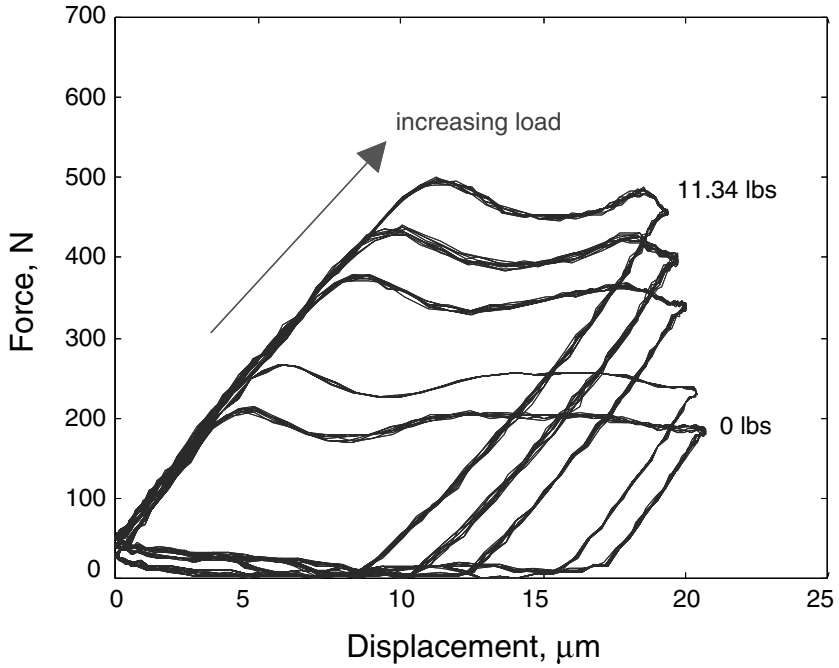

(**a**)Pumping frequency of 50 Hz

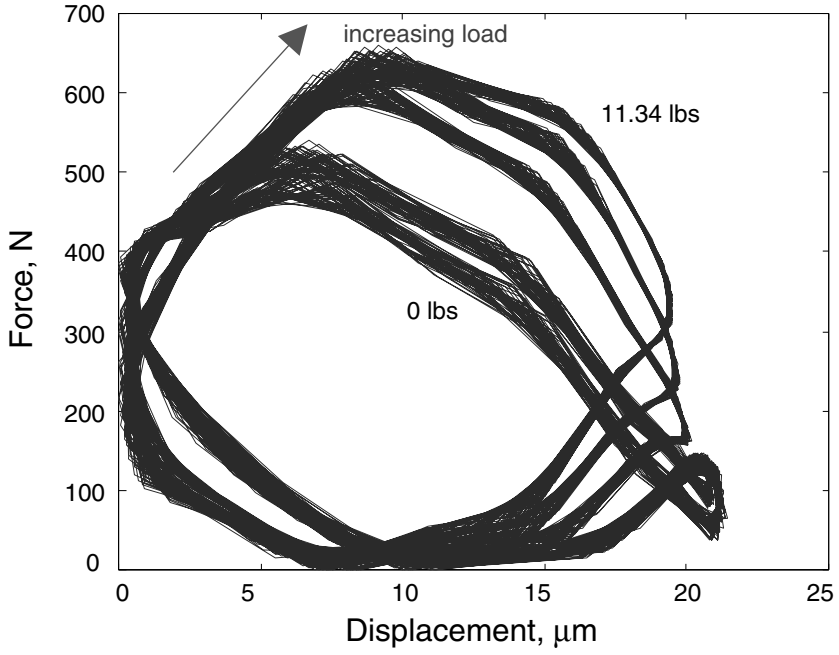

(**b**)Pumping frequency of 300 Hz

Figure 7.6 Pumping chamber force-displacement curves, Type I valves, 50 psi bias pressure

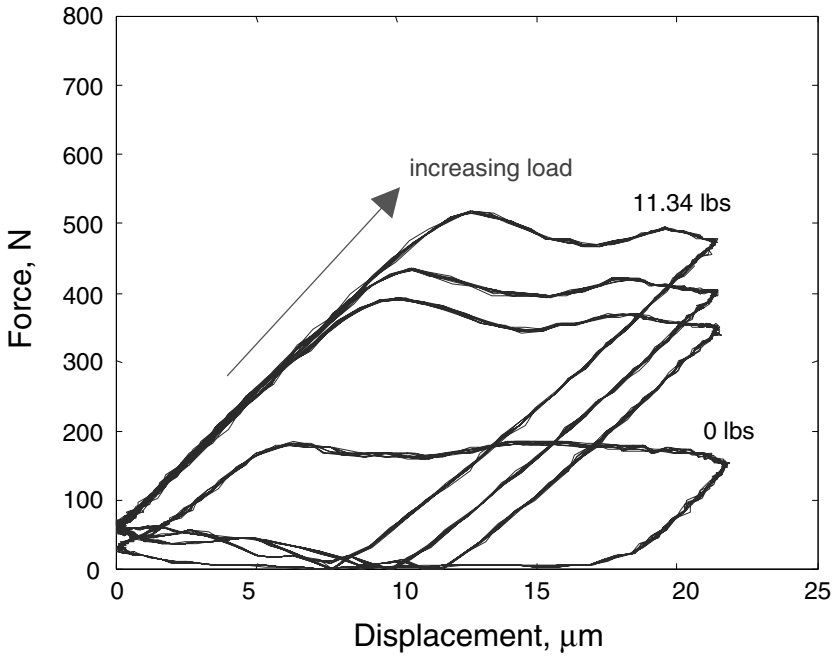

(**a**)Pumping frequency of 50 Hz

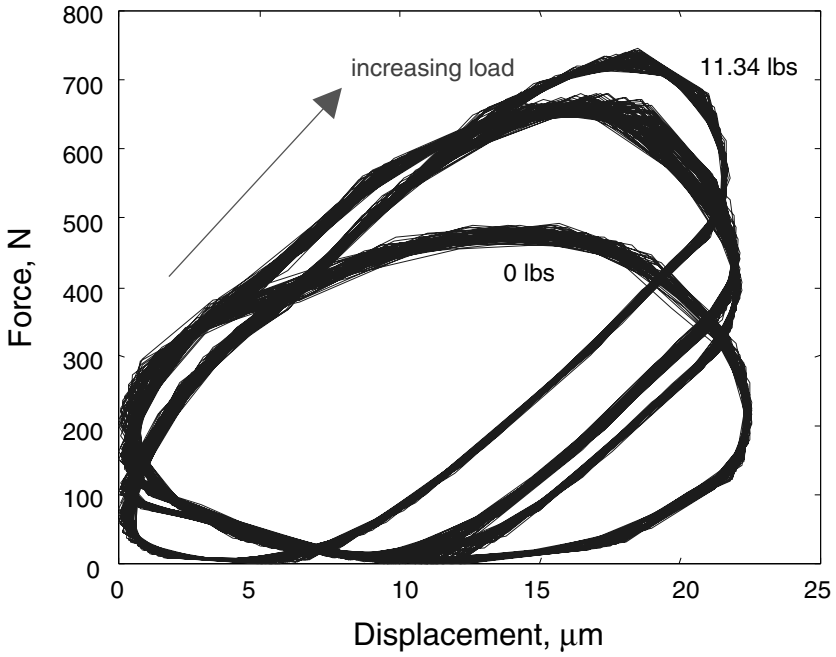

(**b**)Pumping frequency of 300 Hz

Figure 7.7 Pumping chamber force-displacement curves, Type II valves, 50 psi bias pressure

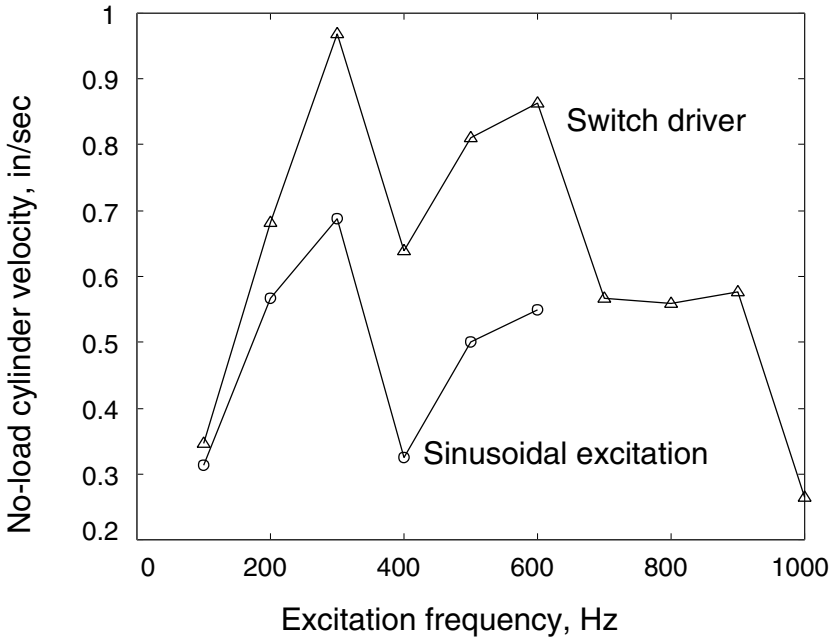

Figure 7.8 High frequency excitation

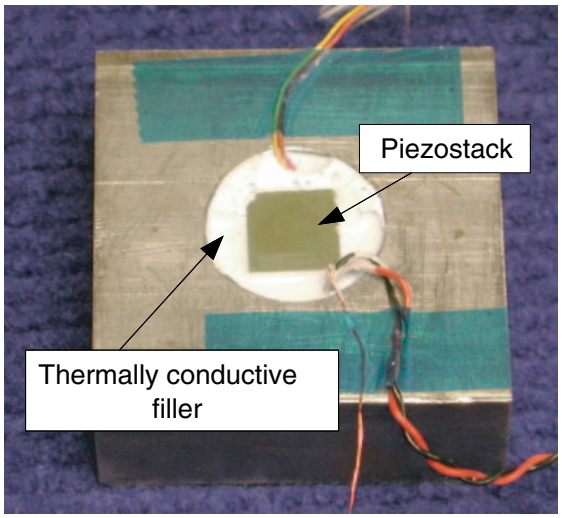

Figure 7.9 Test specimen for measuring passive cooling effectiveness

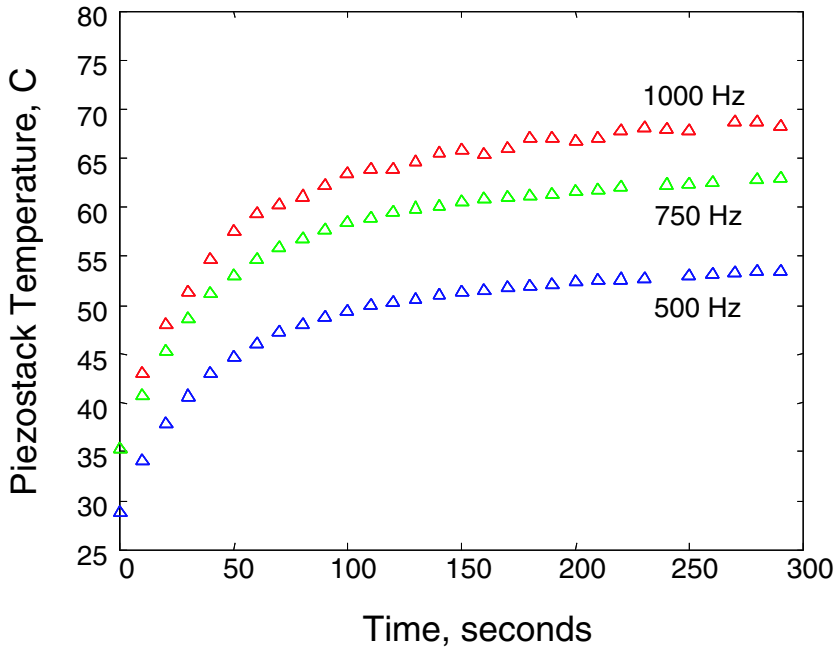

Figure 7.10 Steady state piezostack temperatures, passive cooling

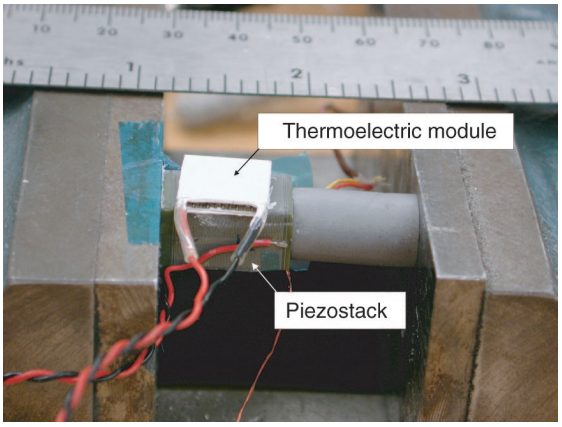

Figure 7.11 TEM cooling test setup

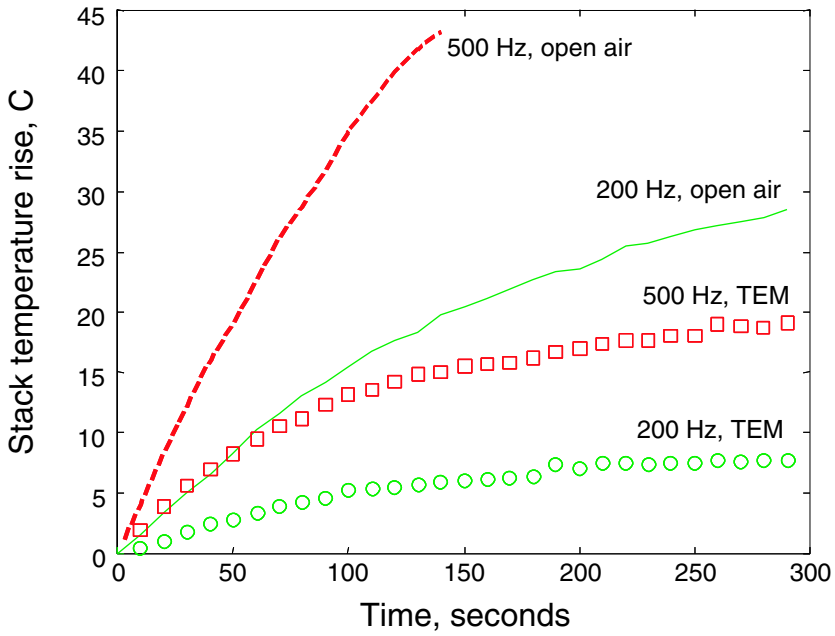

Figure 7.12 Effect of TEM on temperature rise of piezostacks

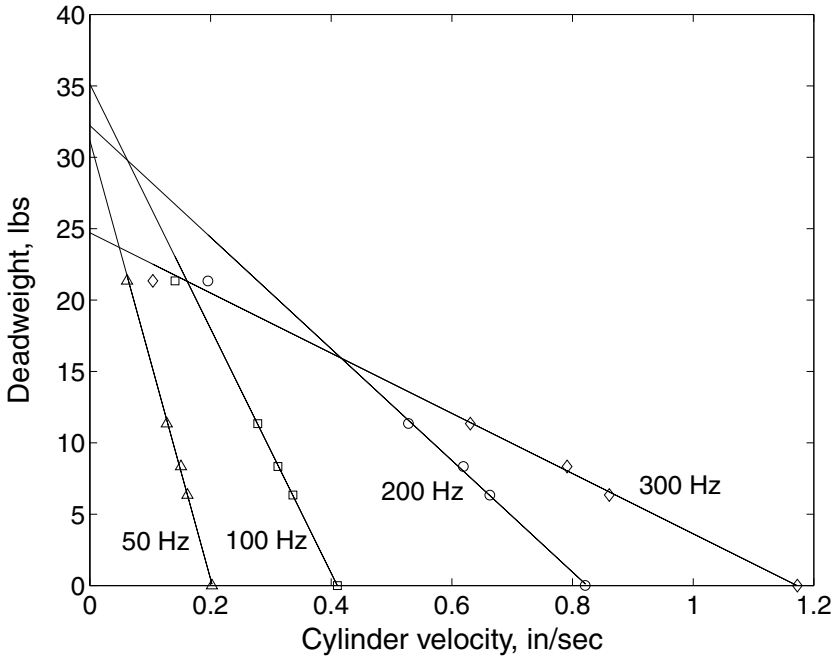

Figure 7.13 Output force-velocity curves with 0.002" spring steel diaphragm, Type II valves, 50 psi bias pressure

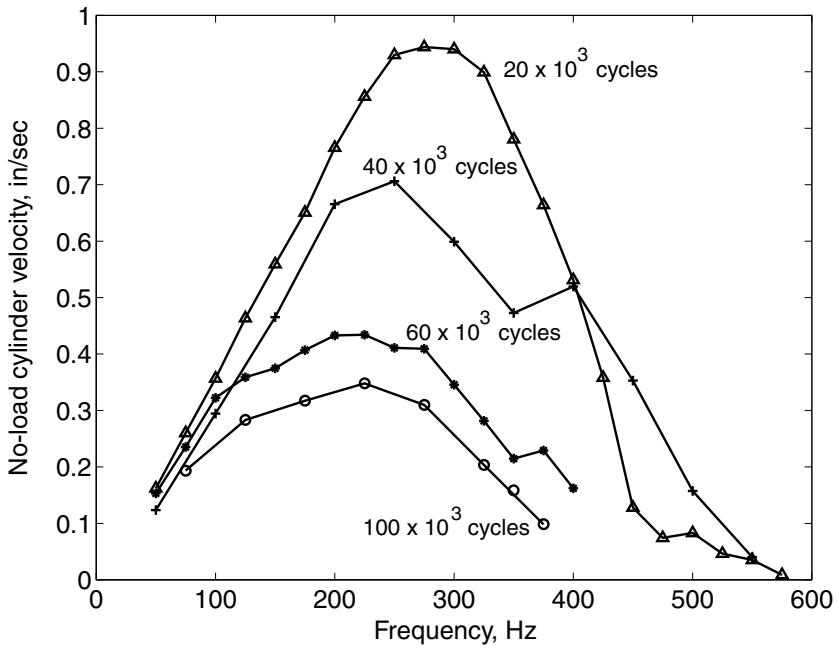

Figure 7.14 Degradation in device performance with pumping cycles

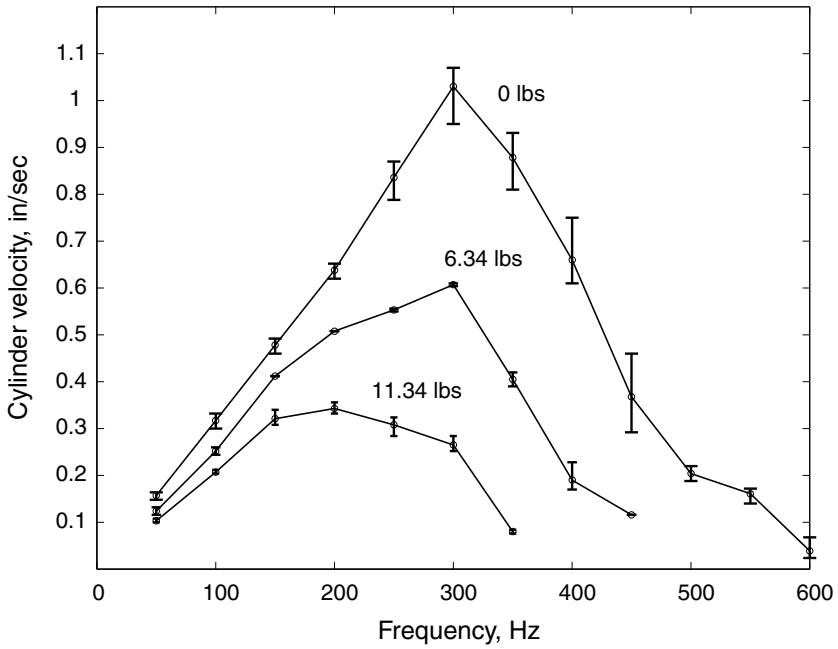

(**a**)Type I valves

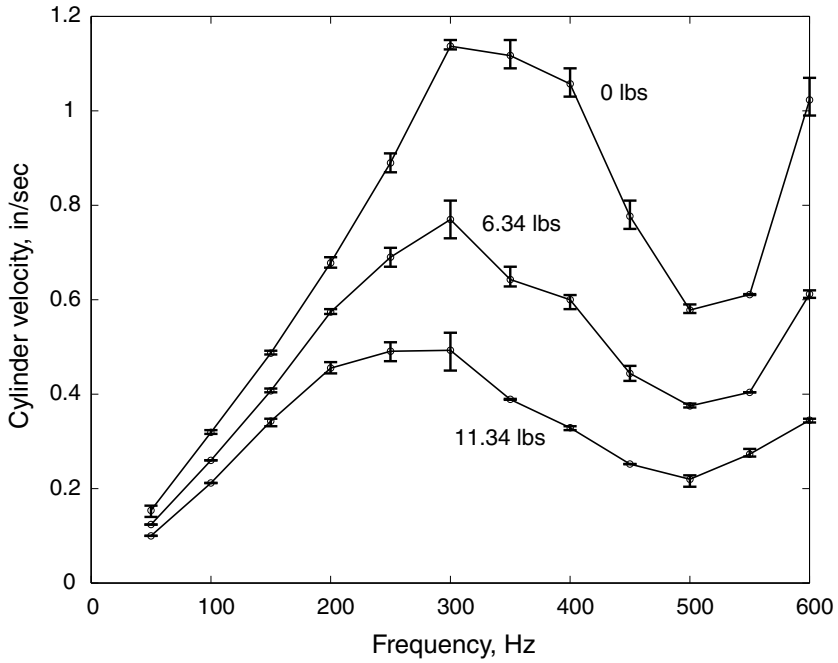

(**b**)Type II valves

Figure 7.15 Output cylinder velocity as a function of load and pumping frequency, 50 psi bias pressure

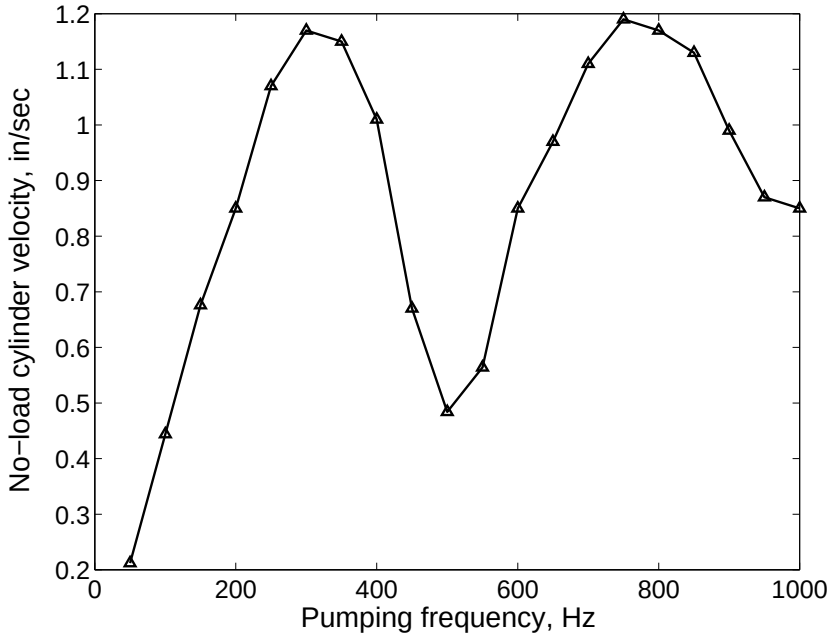

Figure 7.16 No-load cylinder velocity with pumping frequency, Type II valves and using switched driver

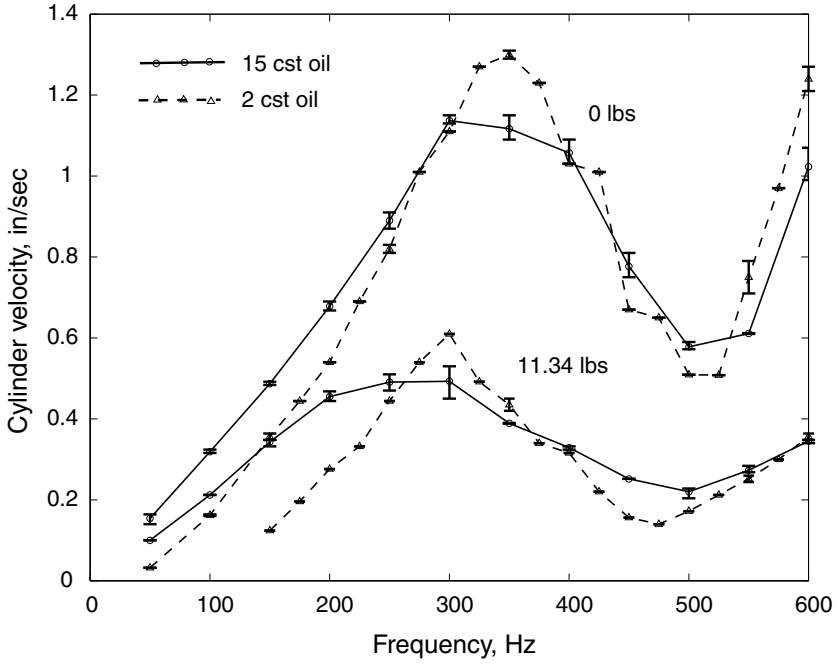

Figure 7.17 Effect of fluid viscosity on performance, with Type II valves

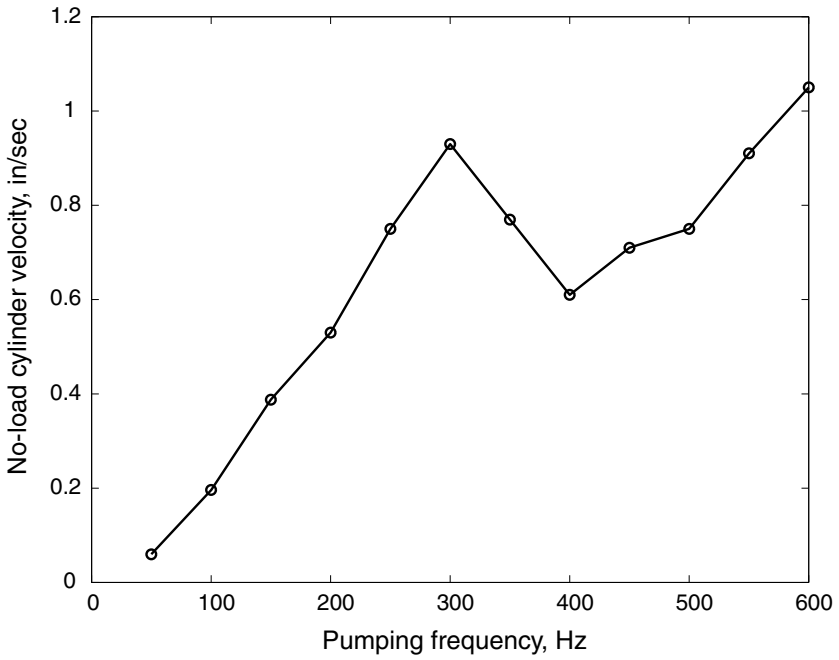

Figure 7.18 Output cylinder no-load velocity, with the 4 way valve and 2cst oil

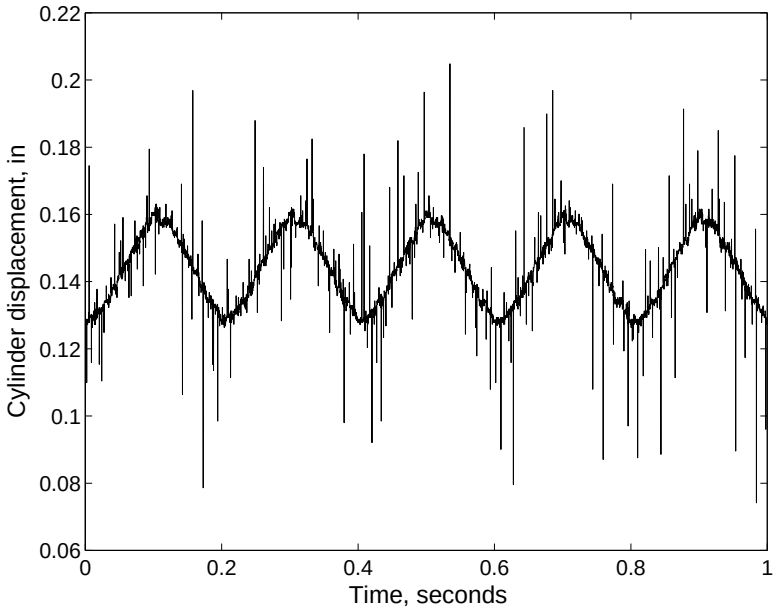

Figure 7.19 Output no-load cylinder displacement at 5 Hz, with a pumping frequency of 100 Hz, and with 50 psi bias pressure

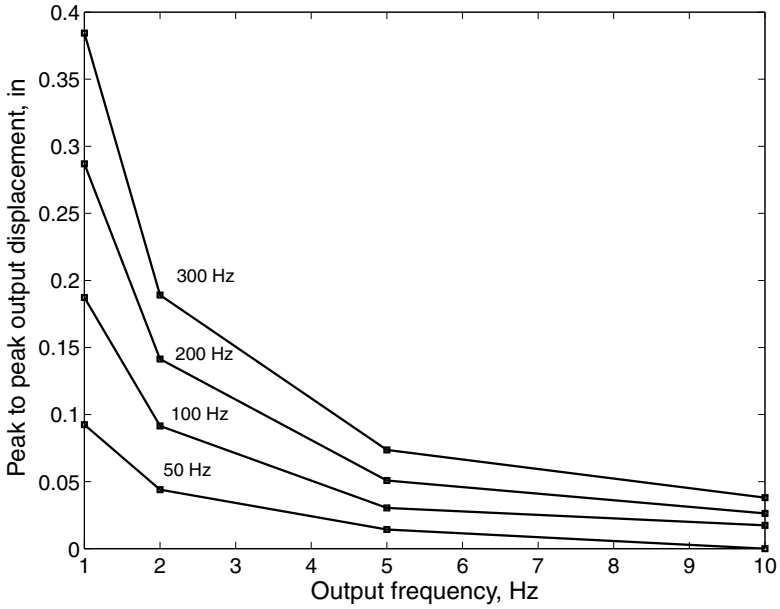

Figure 7.20 Output cylinder stroke as a function of output frequency, at various pumping frequencies, no external load

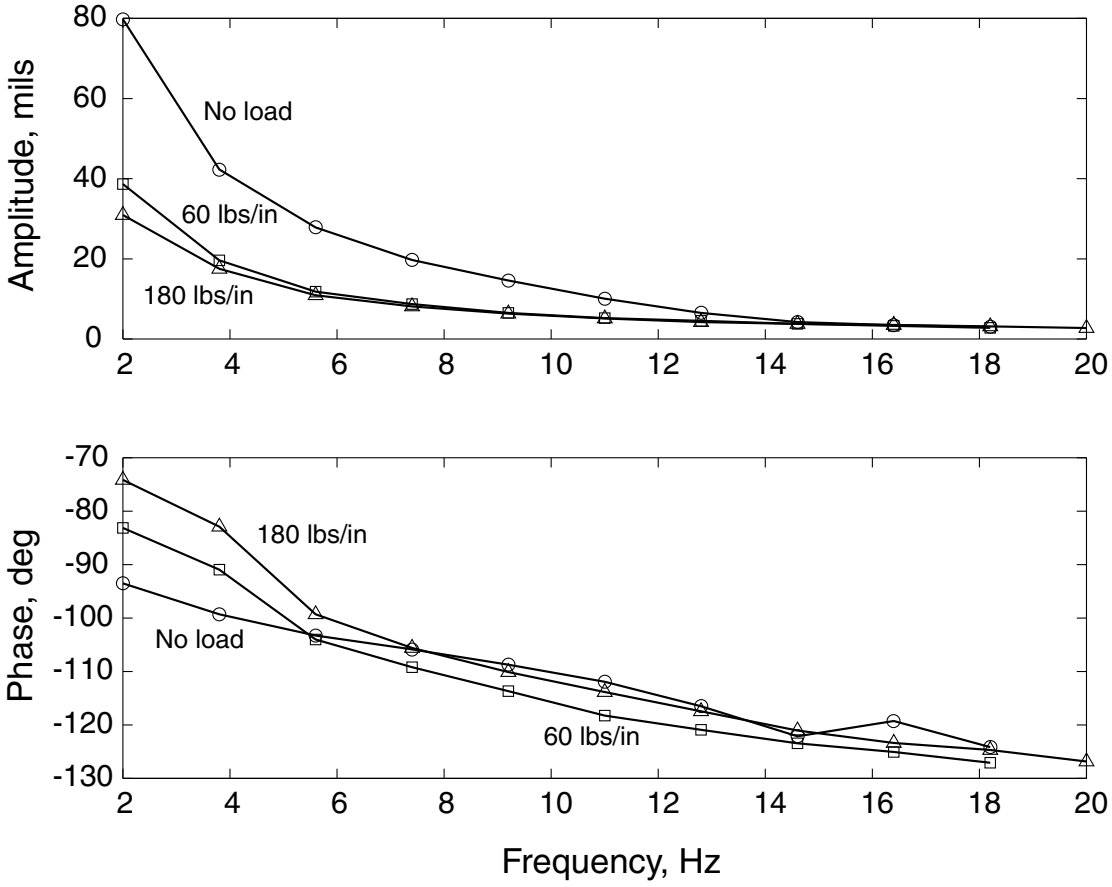

Figure 7.21 Output cylinder stroke as a function of output frequency, with external spring load, at 300 Hz pumping frequency

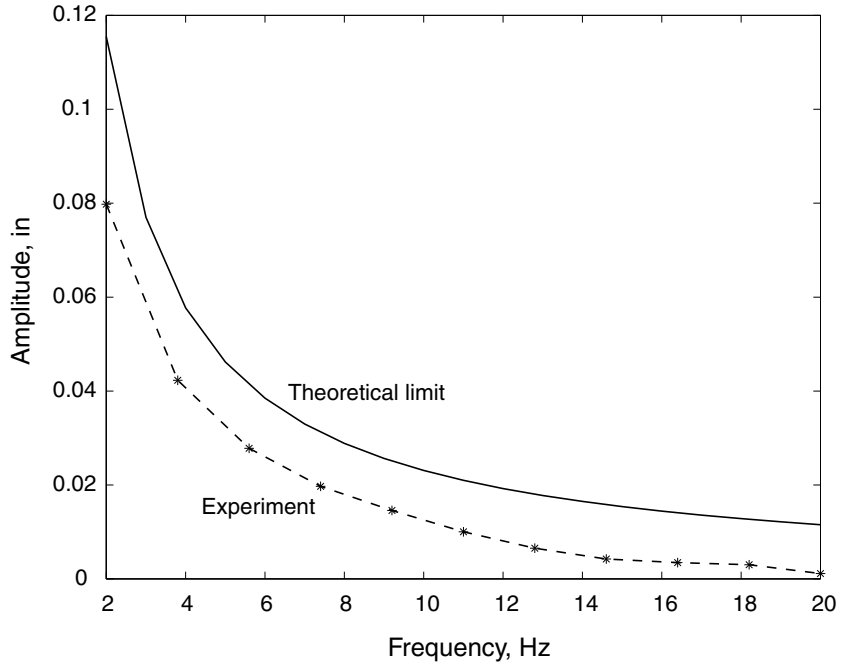

Figure 7.22 Correlation of measured no-load output displacement with theory at 300 Hz pumping frequency

Appendix A

Piezoelectric Pump: Technical Drawings

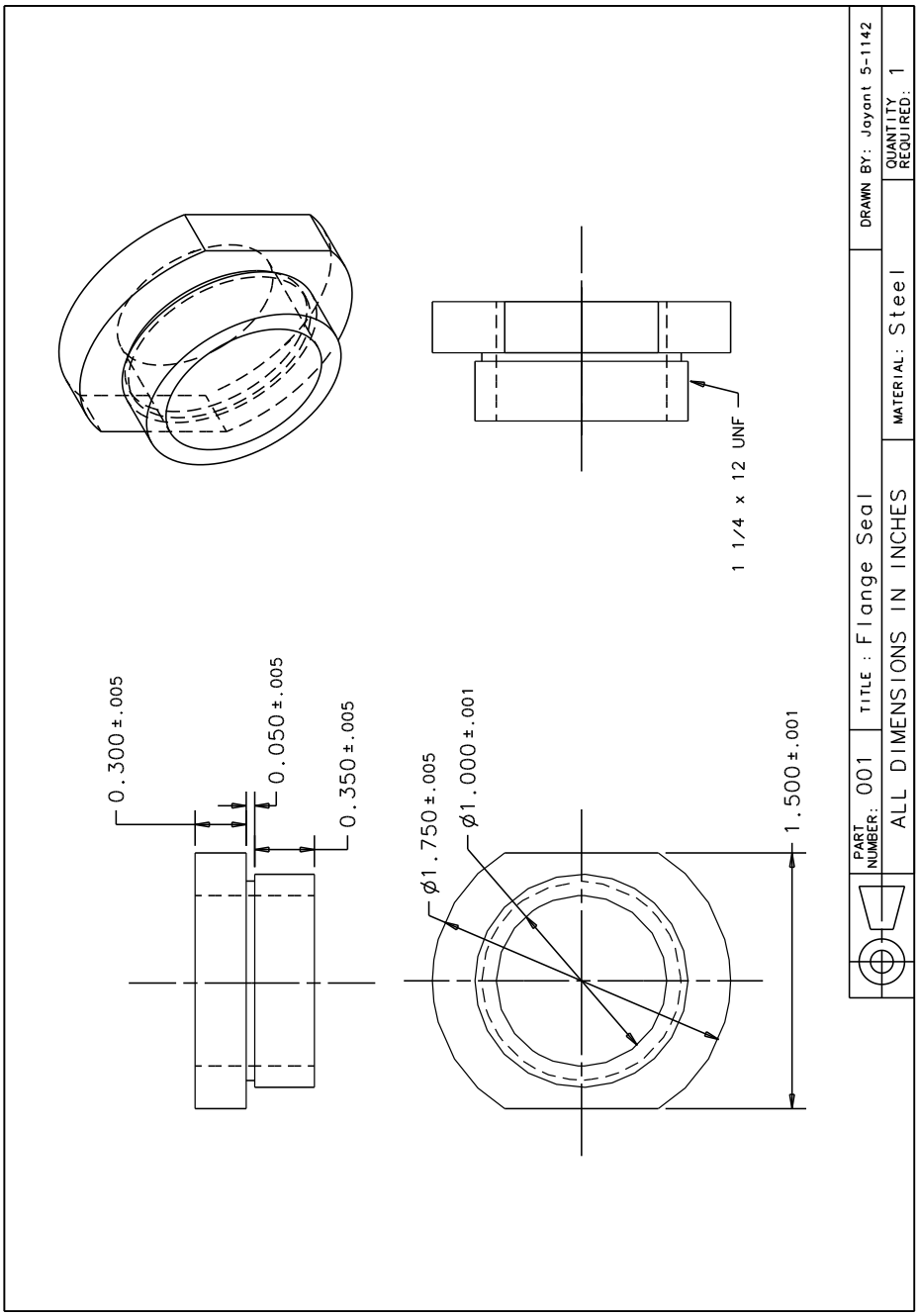

Figure A.1 Sealing ring

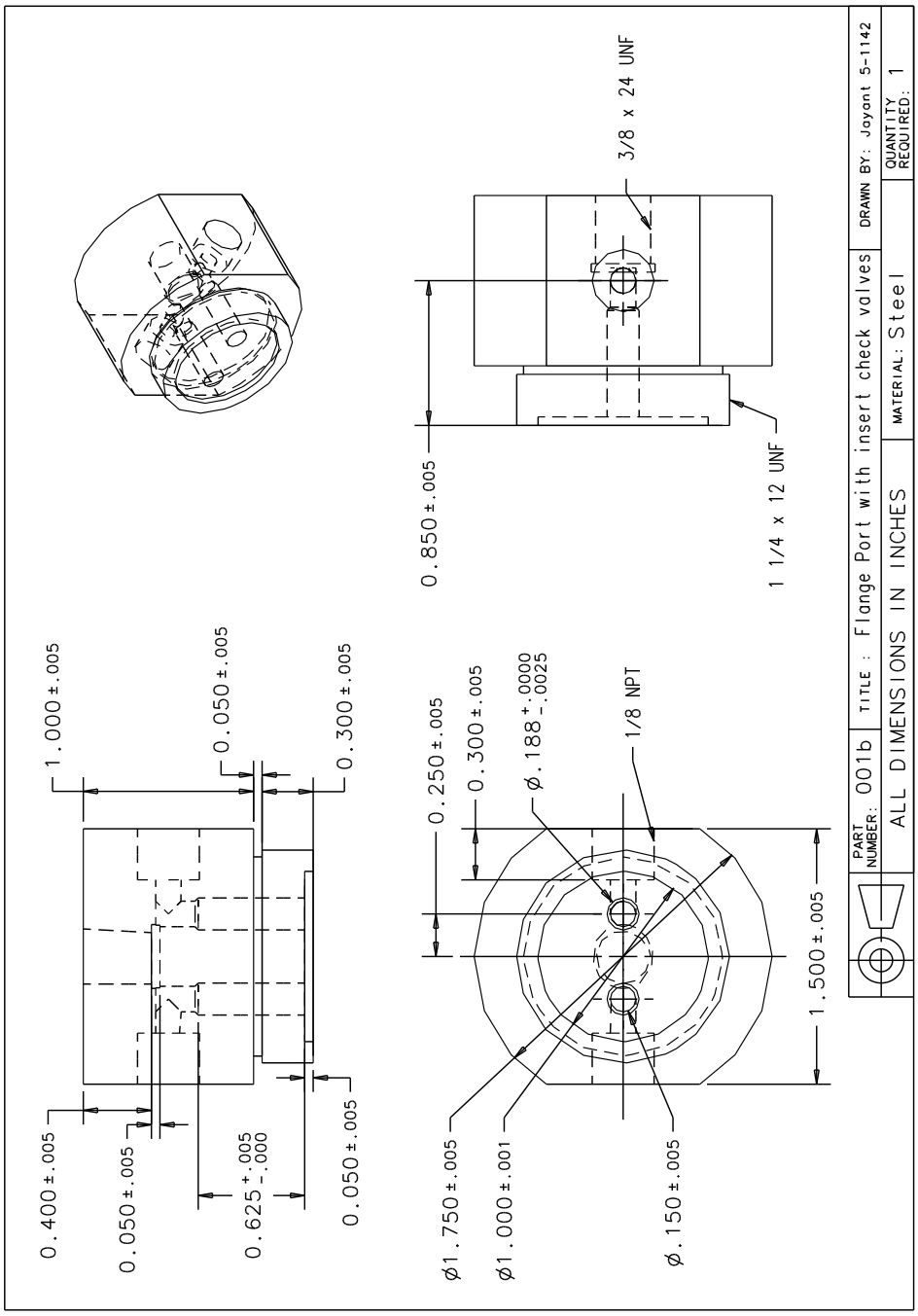

Figure A.2 Pumping head: Type I check valves

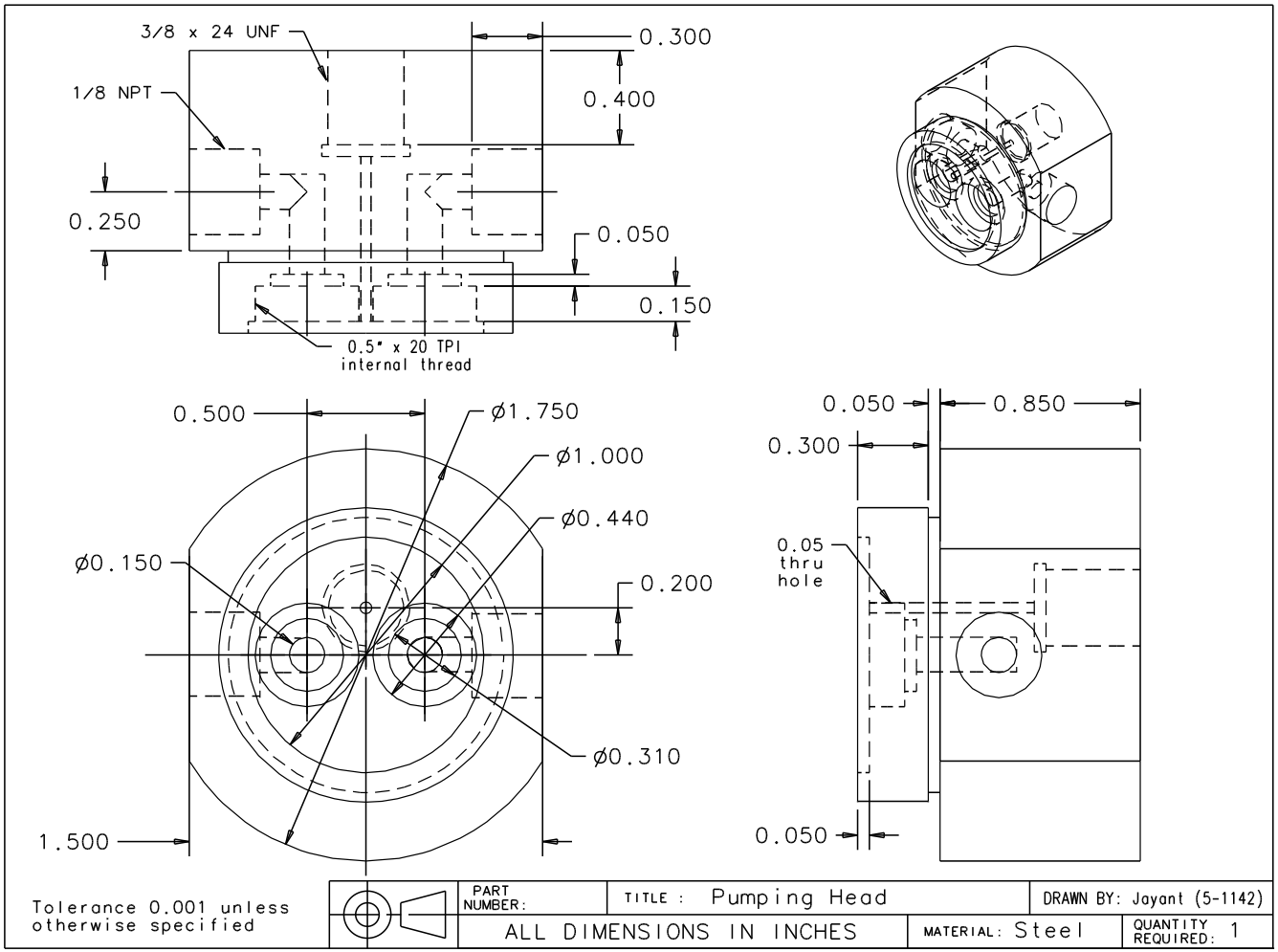

Figure A.3 Pumping head: Type II check valves

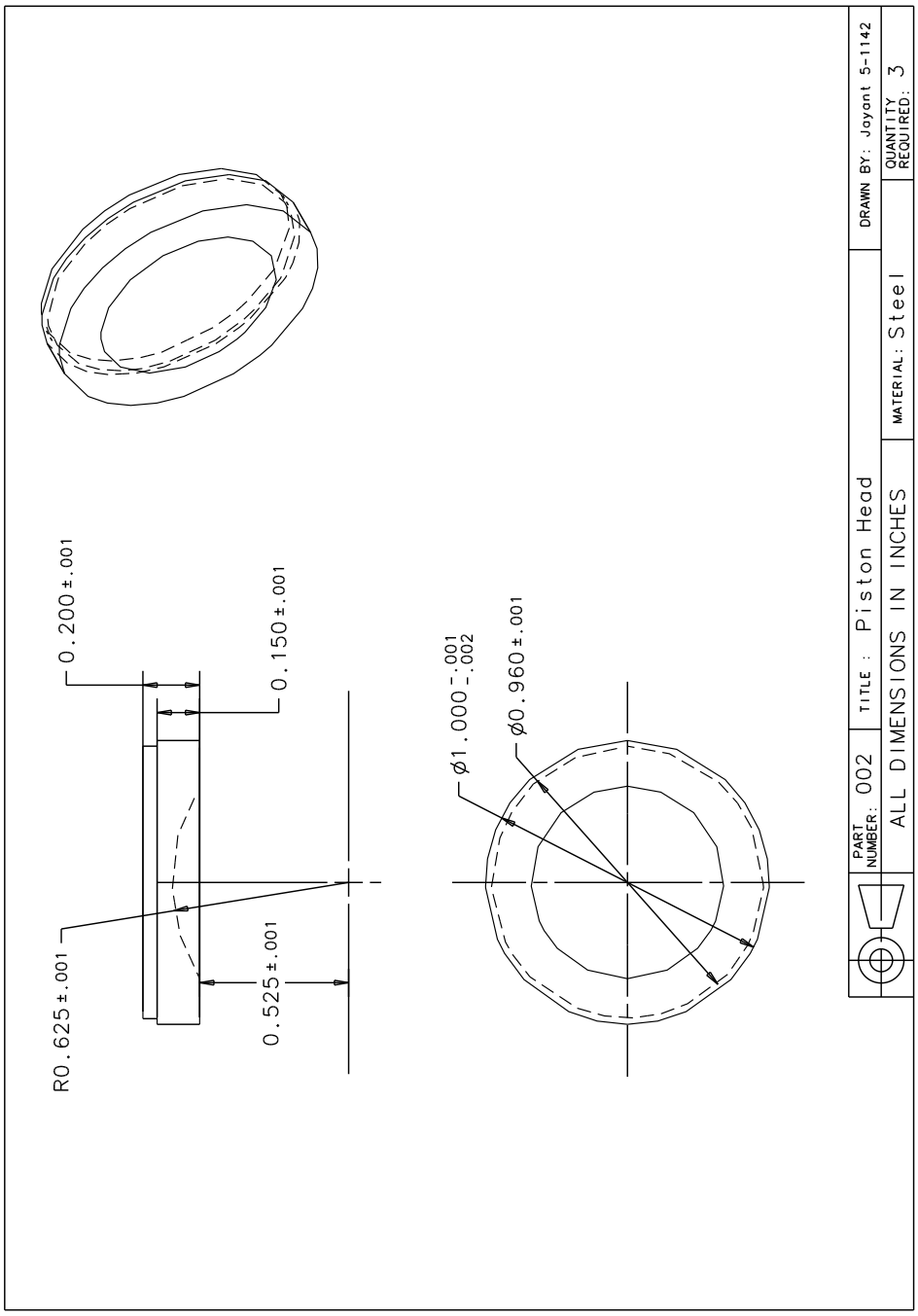

Figure A.4 Pumping piston

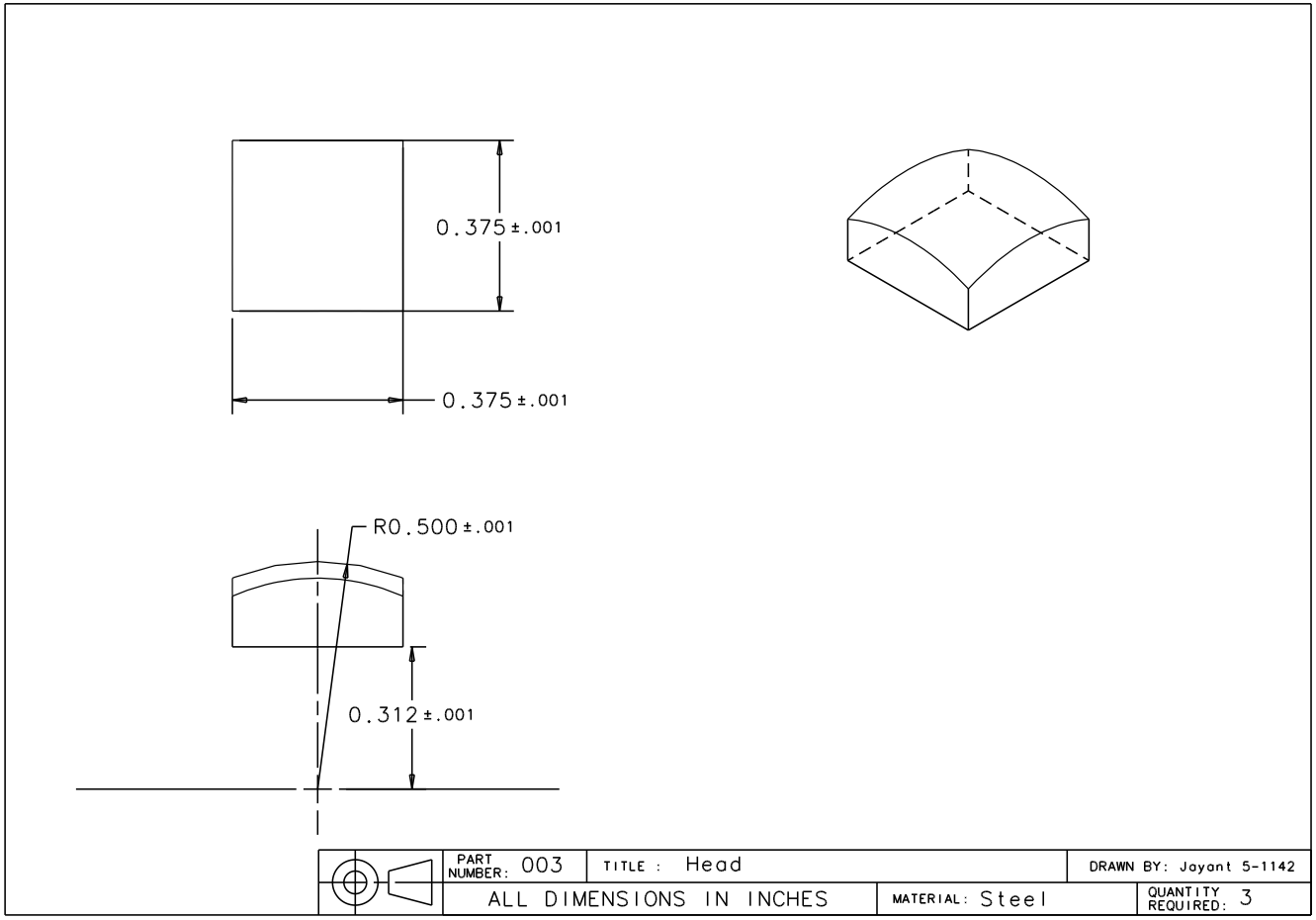

Figure A.5 Piezostack assembly spherical end cap

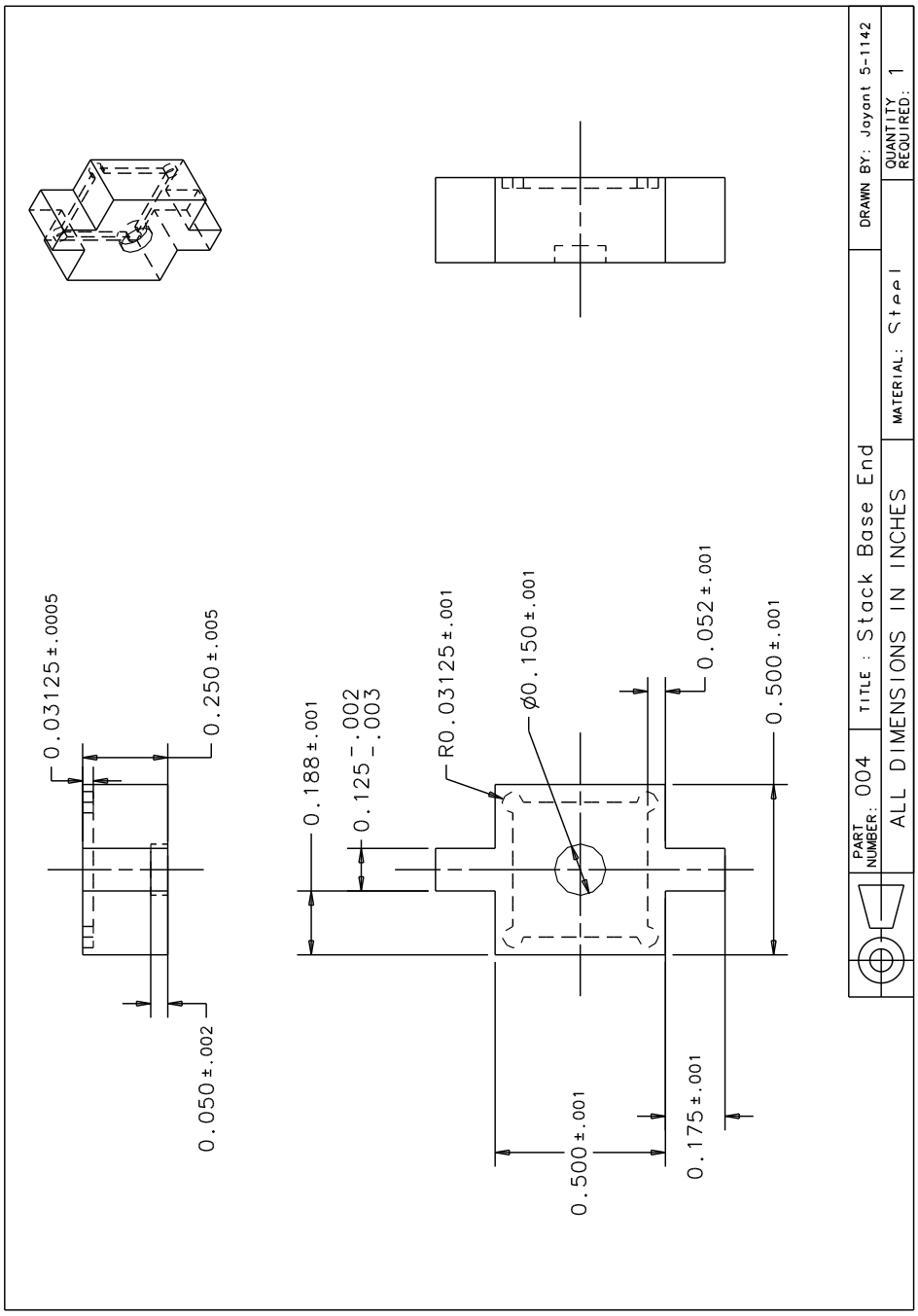

Figure A.6 Piezostack assembly base

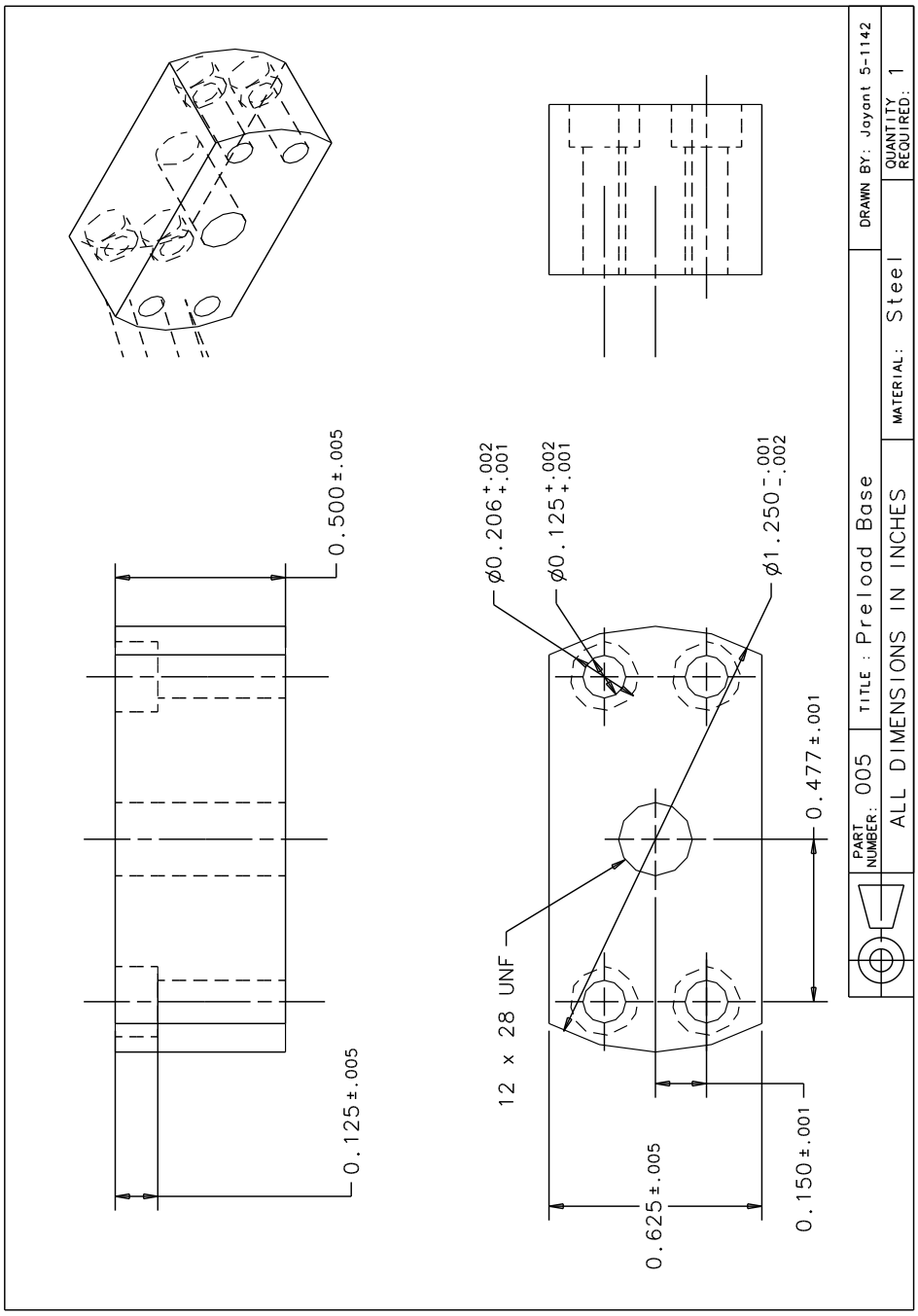

Figure A.7 Preload base fixture

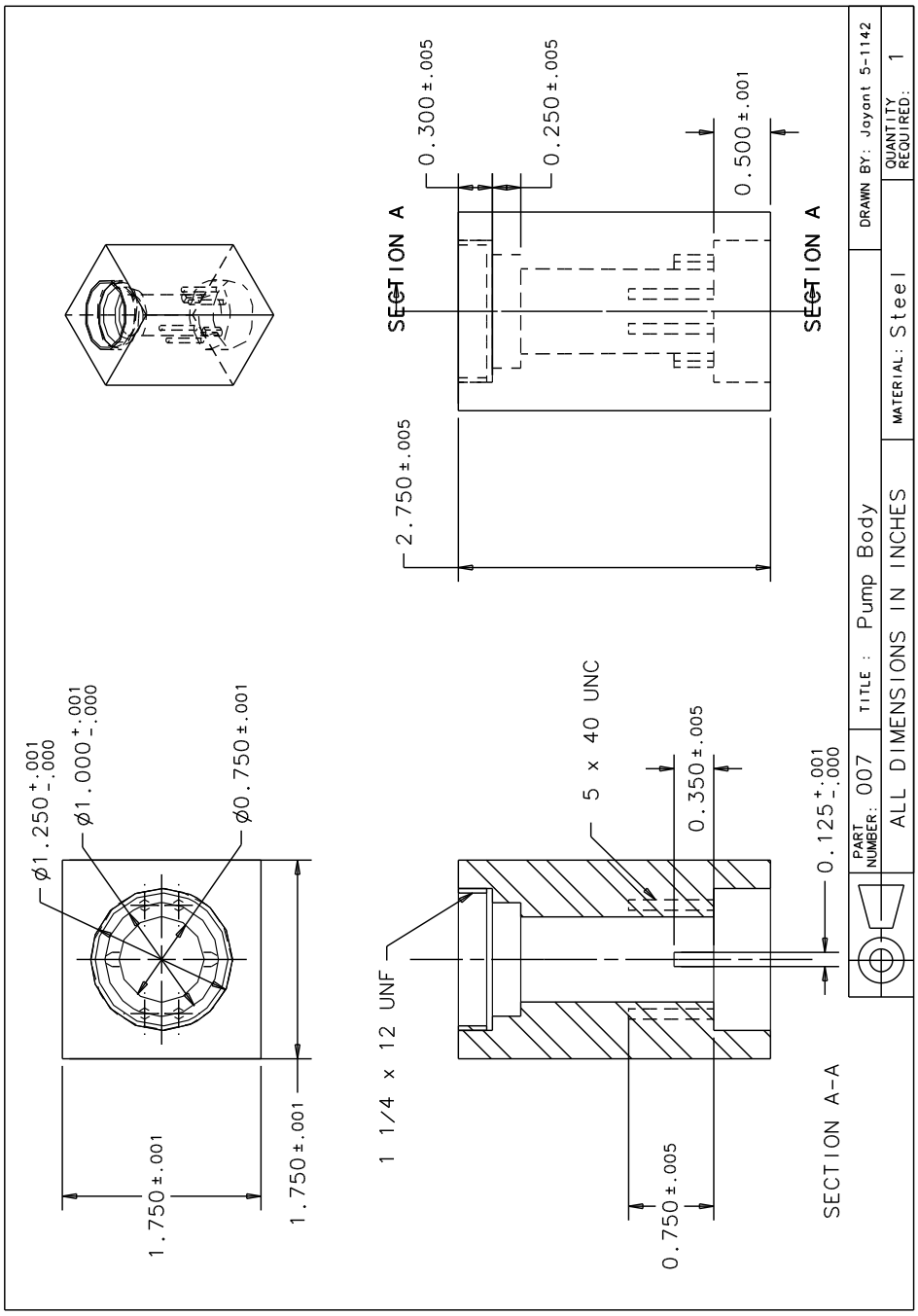

Figure A.8 Pump body

Appendix B

State-Space Analysis of the Device

The MATLAB program based on the state-space analysis described in Chapter 6, used to calculate the response of the device is reproduced below.

```
% actuator theory
% models the piezo-pump directly driving a hydraulic actuator
% uses a lumped parameter, state space model
% sweeps through a frequency range and plots cylinder velocities
%

close all
clear all

%------------------------ input data ---------------------------------------
in = 0.0254;                % m/in   inch to meter conversion
psi = 6895;                 % Pa/psi psi to Pa conversion
cst = 1e-6;                 % m^2/s  centistokes
% fluid
beta = 0.11e9;              % Pa     measured fluid bulk modulus
rho = 859;                  % kg/m^3 fluid density
nu = 36*cst;                % m^2/s  fluid kinematic viscosity
% tubing
```

```
Eal = 70e9;                    % Pa     tubing, aluminum Youngs Modulus
Est = 210e9;                   % Pa     tubing, steel, Youngs Modulus
di = 3.175e-3;                 % m      tubing inner dia
do = 4.7625e-3;                % m      tubing outer dia
lin = 15e-2;                   % m      'in' side tubing length
lout = 15e-2;                  % m      'out' side tubing length
% pumping chamber
gap = 0.05*in;                 % m      pumping chamber gap
dp = 1*in;                     % m      pumping chamber dia
ap = pi*dp^2/4;                % m^2    pumping chamber area
% output actuator
bore = 0.5*in;                 % m      output actuator bore
shaft = 0.25*in;               % m      output actuator shaft dia
lact = 1.5*in;                 % m      output actuator travel
mact = 50e-3;                  % kg     output actuator piston mass
aout = pi*(bore^2-shaft^2)/4;% m^2    output actuator area
Bout = 2e2;                    % Ns/m   damping, output actuator
fr = 1.8*9.81;                 % N      static friction
% External load
mdead = 0.0;                   % kg     deadweight 0, 2.8, 5.0
Mout = mdead + mact;           % kg     mass, output
Kout = 0.0;                    % N/m    spring, output
% piezostack
fb = 5000;                     % N      blocked force
lambda = 25.4e-6*0.9;          % m      free displacement
kp = fb/lambda;                % N/m    piezostack stiffness
cv = fb/100;                   % N/V    effective force-voltage coefficient
mpiezo = 2*16e-3;              % kg     mass of two piezos
mpiston = 17e-3;               % kg     mass of the piston
bp = 2e3;                      % Ns/m   damping of piston, puft
mp = mpiezo/3 + mpiston;       % kg     effective mass of piezos and piston
```

```
% derived parameters
rcv = 50e6*rho;                 % Pa s/m3  check valve resistance, puft
r3 = 128*nu*lin/pi/di^4*rho;    % Pa s/m3 'in' side resistance
r4 = 128*nu*lout/pi/di^4*rho;   % Pa s/m3 'out' side resistance
cc = ap*gap/beta;               % m3/Pa fluid capacitance, pumping chamber
% system
Vo = 100;                      % V      peak - peak excitation voltage
fpumpvec = [25:50:600];        % Hz   piezostack pumping frequency
%fpumpvec = 100;
pbias = 50*psi;                % Pa   system bias pressure
pcrack = 5*psi;                % Pa   check valve cracking pressure
ncyc = 10;                     %      number of pumping cycles to look at
nptsper = 50;                  %      number of points per cycle
ltipts = 10;                   %      number of points the system is
                               %      assumed to be LTI
%-------------------------------------------------------------------------
warning off
% start freq loop ************************************************************
h = waitbar(0,'Calculating cylinder velocities ...');
for fstep = 1:length(fpumpvec),
   fpump = fpumpvec(fstep);
   waitbar(fstep/length(fpumpvec),h);
   % start time loop ********************************************************
   tmax = ncyc/fpump;
   tvec = linspace(0,tmax,nptsper*ncyc-1);    %% for ncyc cycles, nptsper cycle
   dt = tvec(2) - tvec(1);
   exvec =  Vo/2*sin(2*pi*fpump*tvec);  %% excitation voltage
   x0 = [ 0 0 pbias pbias pbias 0 0 ]';  %% initialize state vector
   %% [ xp xout p2 p1 pc xpdot xoutdot ]' actual states

   yout(1) = x0(2);
```

```
xs = x0;
for timestep = 2:length(tvec),
   x0 = xs;                    %% initial value is final value of last step
   x1 = xs(1);
   x2 = xs(2);
   p3 = xs(3);
   p4 = xs(4);
   pc = xs(5);
   x3 = xs(6);
   x4 = xs(7);
   %-- evaluate check valve states
   if p4 > pc+pcrack,
      rcvin = rcv;
   else
      rcvin = rcv*1e6;
   end
   if pc > p3+pcrack;
      rcvout = rcv;
   else
      rcvout = rcv*1e6;
   end
   rout(timestep) = rcvout;
   rin(timestep) = rcvin;
   l3 = x2 + lact/2;              % m, length of 'out' cylinder side
   l4 = lact/2 - x2;              % m, length of 'in' cylinder side
   c3 = aout*l3/beta;             % m3/Pa    fluid capacitance, cylinder
   c4 = aout*l4/beta;             % m3/Pa    fluid capacitance, cylinder
   %-- assemble state space matrices
   a1 = kp/mp;
   a2 = bp/mp;
   a3 = ap/mp;
```

```
a4 = cv/mp;
a5 = ap/cc;
a7 = 1/cc*(1/(rcvout+r3));
a8 = 1/cc*(1/(rcvin+r4));
a6 = a7+a8;
a9 = 1/c3*(1/(rcvout+r3));
a10 = aout/c3;
a11 = 1/c4*(1/(rcvin+r4));
a12 = aout/c4;
a13 = aout/Mout;
a14 = Kout/Mout;
a15 = Bout/Mout;

A = zeros(7);

A(1,:) = [  0    0    0    0    0    1    0 ];
A(2,:) = [  0    0    0    0    0    0    1 ];
A(3,:) = [  0    0  -a9    0   a9    0 -a10 ];
A(4,:) = [  0    0    0 -a11  a11    0  a12 ];
A(5,:) = [  0    0   a7   a8  -a6   a5    0 ];
A(6,:) = [-a1    0    0    0  -a3  -a2    0 ];
A(7,:) = [  0 -a14  a13 -a13    0    0 -a15 ];

B = [ 0 0 0 0 0 a4 0 ]';
const = [ 0 0 0 0 0 0 -fr/Mout-9.81]';
B = [B const];
C = [ 0 1 0 0 0 0 0 ];
D = [0 0];
% solve the system
sys = ss(A,B,C,D);
exvect = linspace(exvec(timestep-1),exvec(timestep),ltipts)';
```

```
      const_exec = ones(length(exvect),1);
      invect = [exvect const_exec];
      txvect = linspace(tvec(timestep-1),tvec(timestep),ltipts);
      [ys,ts,xs] = lsim(sys,invect,txvect,x0);
      yout(timestep) = ys(ltipts);
      xs = xs(ltipts,:)';
   end
   % end time loop ************************************************************

   %figure(2)
   %plot(tvec,yout/in)
   %xlabel('Time, seconds');
   %ylabel('Cylinder displacement, in');

   plin = polyfit(tvec(length(tvec)/2:length(tvec)),yout(length(tvec)/2: ...
          length(tvec)),1);
   cyl_vel(fstep) = plin(1)/in;              % cylinder velocity, in/sec
end
close(h)
% end freq loop ***************************************************************
figure(1)
plot(fpumpvec,cyl_vel,'ro-');
xlabel('Pumping frequency, Hz');
```

BIBLIOGRAPHY

[1] R.W. Prouty. *Helicopter performance, stability and performance*. Robert E. Kriege Publishing Company, Inc., Malabar, FL, 1990.

[2] J.R. Olson. Reducing helicopter costs. *Vertiflite*, 39(1):10–16, January/February 1993.

[3] E.A. Fradenburgh. The first 50 years were fine ... but what should we do for an encore? *Journal of the American Helicopter Society*, 40(1):3–19, January 1995. The 1994 Alexander A. Nikolsky Lecture.

[4] Inderjit Chopra. Status of application of smart structures technology to rotorcraft systems. *Journal of the American Helicopter Society*, 45(4):228–252, October 2000.

[5] G. Reichert. Helicopter vibration control - a survey. *Vertica*, 5(1):1–20, 1981.

[6] R.G. Loewy. Helicopter vibrations, a technological perspective. *Journal of the American Helicopter Society*, 29(4):3–20, October 1984.

[7] Wayne Johnson. *Helicopter theory*. Dover Publications, Inc., New York, NY, 1980.

[8] Alfred Gessow and Garry C. Myers, Jr. *Aerodynamics of the helicopter*. College Park Press, College Park, MD, 1985.

[9] Andreas Paul Friedrich Bernhard. *Smart Helicopter Rotor with Active Blade Tips*. PhD thesis, University of Maryland, College Park, MD 20742 USA, February 2000.

[10] C. W. Ellis and R. Jones. Application of an absorber to reduce helicopter vibration levels. *Journal of the American Helicopter Society*, 8(3):30–38, July 1963.

[11] E. P. Schuett. Application of passive helicopter rotor isolation for alleviation of rotor induced vibration. *Journal of the American Helicopter Society*, 14(2):34–48, April 1969.

[12] K. B. Amer and J. R. Neff. Vertical-plane pendulum absorbers for minimizing helicopter vibratory loads. *Journal of the American Helicopter Society*, 19(4):44–48, October 1974.

[13] A.E. Staple. An evaluation of active control of structural response as a means of reducing helicopter vibration. In *15th European Rotorcraft Forum*, pages 51.1–51.18, Amsterdam, The Netherlands, September 1989.

[14] A.E. Staple and D.M. Wells. Development and testing of an active control of structural response system for the EH101 helicopter. In *16th European Rotorcraft Forum*, Glasgow, Scotland, September 1990.

[15] W.A. Welsh, P.C. von Hardenberg, P.W. von Hardenberg, and A.E. Staple. Test and evaluation of fuselage vibration utilizing active control of structural response (acsr) optimized to ads-27. In *46th American Helicopter Society Forum*, pages 21–37, Washington, DC, May 1990.

[16] Mitsuhiro Aso and Shun-ichi Bandoh. The development of the total vibration reduction (TVR) system. In *55th American Helicopter Society Forum*, pages 202–208, Montreal, Canada, May 1999.

[17] T. Millott and W. Welsch. Helicopter active noise and vibration reduction. In *25th European Rotorcraft Forum*, Rome, Italy, September 1999. Paper G-23.

[18] P.R. Payne. Higher harmonic rotor control. *Aircraft Engineering*, 30(354):222–226, August 1958.

[19] I. Chopra and J. C. McCloud III. A numerical simulation study of open-loop, closed loop and adaptive multicyclic control systems. *Journal of the American Helicopter Society*, 28(1):311–325, October 1983.

[20] K. Nguyen and I. Chopra. Application of higher harmonic control to rotors operating at high speed and thrust. *Journal of the American Helicopter Society*, 35(3):78–89, July 1990.

[21] K. Nguyen and I. Chopra. Application of higher harmonic control (HHC) to hingeless rotors. *Vertica*, 14(4):545–556, October 1990.

[22] K. Nguyen and I. Chopra. Effects of higher harmonic control on rotor performance and control loads. *Journal of Aircraft*, 29(3), May/June 1992.

[23] C.E. Hammond. Wind tunnel results showing rotor vibratory loads reduction using higher harmonic blade pitch. *Journal of the American Helicopter Society*, 28(1):10–15, January 1983.

[24] E.R. Wood, R.W. Powers, C.H. Cline, and C.E. Hammond. On developing and flight testing a higher harmonic flight control system. *Journal of the American Helicopter Society*, 30(1):3–20, January 1985.

[25] W. Miao, S.B.R. Kottapali, and H.M Frye. Flight demonstration of higher harmonic control (HHC) on the S-76. In *42nd American Helicopter Society Forum*, Washington DC, June 1986.

[26] M. Polychroniadis and M. Achache. Higher harmonic control: flight tests of an experimental system on an sa 349 research gazelle. In *42nd American Helicopter Society Forum*, Washington DC, June 1986.

[27] J. Shaw, N. Albion, E.J. Hanker, and R.S Teal. Higher harmonic control: wind tunnel demonstration of fully effective vibratory hub forces suppression. *Journal of the American Helicopter Society*, 34(1):14–25, January 1989.

[28] M. Kretz. Relaxation of rotor limitations by feedback control. *Proceedings of the 33rd Annual Forum of the American Helicopter Society*, 1977.

[29] K.F. Guinn. Individual blade control independent of a swashplate. *Journal of the American Helicopter Society*, 27(3):25–32, July 1982.

[30] N. D. Ham. A simple system for helicopter individual-blade-control using modal decomposition. *Vertica*, 4(1/2):23–28, 1980.

[31] N. D. Ham. Helicopter individual blade control and its applications. In *39th American Helicopter Society Forum*, St. Louis, MO, May 1983.

[32] N. D. Ham. Helicopter-individual blade control research at mit 1977-1985. *Vertica*, 11(1/2):109–122, 1987.

[33] D. Teves, V. Klöppel, and P. Richter. Development of active control technology in the rotating system, flight testing and theoretical investigations. In *18th European Rotorcraft Forum*, September 1992.

[34] P. Richter and A. Blaas. Full scale wind tunnel investigation of an individual blade control system for the bo-105 hingeless rotor. In *19th European Rotorcraft Forum*, Cernobbio, Italy, 1993 September.

[35] S.A. Jacklin, A. Blaas, D. Teves, and R. Kube. Reduction in helicopter BVI noise, vibration and power consumption through individual blade control. In *51st Annual Forum of the American Helicopter Society*, Fort Worth, TX, May 1995.

[36] P. Lorber, C. Park, D. Polak, J. O'Neill, and W. A. Welsh. Active rotor experiments at Mach scale using root pitch IBC. *Presented at the American Helicopter Society 57th Annual Forum, Washington DC*, May 9-11 2001.

[37] N. D. Ham. Helicopter gust alleviation, attitude stabilization and vibration reduction using individual blade control through a conventional swashplate. In *11th European Rotorcraft Forum*, London, UK, September 1985.

[38] T.R. Quackenbush. Testing of a stall flutter suppression system for helicopter rotors using individual blade control. *Journal of the American Helicopter Society*, 29(3):38–4, 1984.

[39] D. Morbitzer, U.T.P. Arnold, and M. Müller. Vibration and noise reduction through individual blade control, experimental and theoretical results. In *24th European Rotorcraft Forum*, Marseilles, France, September 1998. Paper TE-10.

[40] M. Müller, U.T.P. Arnold, and D. Morbitzer. On the importance and efficiency of 2/rev ibc for noise, vibration and pitch link load reduction. In *25th European Rotorcraft Forum*, Rome, Italy, September 1999. Paper G-4.

[41] Judah H. Milgram. *A comprehensive aeroelastic analysis of helicopter main rotors with trailing edge flaps for vibration reduction*. PhD thesis, University of Maryland, Aerospace Department, College Park, MD, January 1997.

[42] Friedrich K. Straub. A feasibility study of using smart materials for rotor control. *Smart Materials and Structures*, 5(1):1–10, February 1996.

[43] T.A. Millott and P.P. Friedmann. Vibration reduction in rotorcraft using active control: a comparison of various approaches. *Journal of Guidance, Control and Dynamics*, 18(4):664–673, August 1995.

[44] J.L. McCloud, III. An analytical study of a multicyclic controllable twist rotor. In *31st American Helicopter Society Forum*, Washington, DC, May 1975.

[45] A. Z. Lemnios and F. K. Dunn. Theoretical study of multicyclic control of a controllable twist rotor. Technical Reports NASA-CR-151959, NASA, April 1976.

[46] J.L. McCloud, III and A.L. Weisbrich. Wind tunnel test results of a full-scale multicyclic controllable twist rotor. In *34th American Helicopter Society Forum*, Washington, DC, May 1978.

[47] Inderjit Chopra and John. L McCloud, III. A numerical simulation study of open-loop, closed-loop and adaptive multicyclic control systems. *Journal of the American Helicopter Society*, 28(1):311–325, January 1983.

[48] S. Dawson and F. K. Straub. Design, validation and testing of a model rotor with tip mounted active flaps. *Proceedings of the 50th Annual Forum of the American Helicopter Society, Washington DC*, May 1994.

[49] F. K. Straub. Active flap control for vibration reduction and performance improvement. *Proceedings of the 51st Annual Forum of the American Helicopter Society, Fort Worth, TX*, May 1995.

[50] S. Dawson, A. Hassan, and Friedrich K. Straub. Wind tunnel test of an active flap rotor: BVI noise and vibration reduction. In *51st American Helicopter Society Forum*, pages 631–648, Fort Worth, TX, May 1995.

[51] A. P. F. Bernhard, J. O'Neill, F. Kohlhepp, W. Welsh, and P. Lorber. Active Rotor Control (ARC) of a mach-scale trailing edge flap rotor. *Presented at the American Helicopter Society 57th Annual Forum, Washington DC*, May 9-11 2001.

[52] T.A. Millott and P.P. Friedmann. Vibration reduction in helicopter rotors using an actively controlled partial span trailing edge flap located on the blade. Technical Report NASA-CR-4611, NASA, June 1994.

[53] T.A. Millott and P.P. Friedmann. Vibration reduction in rotorcraft using the actively controlled trailing edge flap and issues related to practical implementation. In *54th American Helicopter Society Forum*, Washington, DC, May 1998.

[54] Judah Milgram and Inderjit Chopra. A parametric design study for actively controlled flaps. *Journal of the American Helicopter Society*, 43(2):110–119, April 1998.

[55] Robert Ormiston. Aeroelastic considerations for rotorcraft primary control with on-blade elevons. *Presented at the American Helicopter Society 57th Annual Forum, Washington DC*, May 9-11 2001.

[56] Matthew Tarascio, Marc Gervais, Tim Gowen, Jun Ma, Kiran Singh, Gaurav Gopalan, Kristi Kleinhesselink, Yong sheng Zhao, and Inderjit Chopra. Raven SAR Rotorcaft. Technical report, Alfred Gessow Rotorcraft Center, University of Maryland, College Park, MD 20742, 2001. In response to the 2001 Annual AHS International Student Design Competition - Graduate Category.

[57] I. Chopra. Review of current status of smart structures and integrated systems. *SPIE Smart Structures and Integrated Systems*, 2717:20–62, 1996.

[58] I. Chopra. Status of application of smart structures technology to rotorcraft systems. *Presented at the Innovations in Rotorcraft Technology, Royal Aeronautical Society, London*, 2717:20–62, June 1997.

[59] Daniel J. Jendritza and Hartmut Jonocha, editors. *Adaptronics and Smart Structures*. Springer Verlag GmbH, 1999.

[60] B.K. Wada, J.L. Fanson, and E.F. Crawley. Adaptive structures. *Journal of Intelligent Material Systems and Structures*, 1(2):157–174, April 1990.

[61] Patricia W. Stevens and Edward C. Smith. Active interrogation of helicopter rotor faults using trailing edge flap actuation. *Presented at the American Helicopter Society 57th Annual Forum, Washington DC*, May 9-11 2001.

[62] E.F. Crawley. Intelligent structures for aerospace: a technology overview and assessment. *AIAA Journal*, 32(8):1689–1699, August 1994.

[63] QuickPack actuators. Active Control eXperts, ACX.

[64] Shoko Yoshikawa, Michael Farrell, David Warkentin, Robert Jacques, and Erik Saarmaa. Monolithic piezoelectric actuators and vibration dampers with interdigitated electrodes. In *SPIE symposium on smart structures and materials, conference on smart structures and integrated systems*, pages 578–585, Newport Beach, CA, March 1999.

[65] Andrew J. Moskalik and Diann Brei. Force-deflection behavior of piezoelectric c-block actuator arrays. *Smart Materials and Structures*, 8(5):531–543, October 1999.

[66] M.W. Hooker. Properties and performance of RAINBOW piezoelectric actuator stacks. In *SPIE symposium on smart structures and materials, conference on industrial and commercial applications of smart structures technologies*, pages 413–420, San Diego, CA, March 1997.

[67] Thunder actuators. Face International Corporation, http://www.faceinternational.com, Norfolk, VA, 1999.

[68] K.M. Mossi and R.P. Bishop. Characterization of different types of high-performance THUNDER actuators. In *SPIE symposium on smart structures and materials, conference on smart materials technologies*, pages 43–52, Newport Beach, CA, March 1999.

[69] Craig D. Near. Piezoelectric actuator technology. In *SPIE symposium on smart structures and materials, conference on smart structures and integrated systems*, pages 246–258, San Diego, CA, February 1996.

[70] K. Uchino. *Piezoelectric Actuators and Ultrasonic Motors*. Kluwer Academic Publishers, Boston, 1997.

[71] B. Jaffe, W. R. Cook Jr., and H. Jaffe. *Piezoelectric Ceramics*. Academic Press Ltd, 1971.

[72] Jeanette Epps and Inderjit Chopra. Shape memory alloy actuators for in-flight tracking of helicopter rotor blades. *Smart Materials and Structures*, 10(1):104–111, 2001.

[73] Jeanette J. Epps. *In-Flight Tracking of Helicopter Rotor Blades with Tabs Using Shape Memory Alloys*. PhD thesis, University of Maryland, College Park, MD 20742 USA, 2000.

[74] Harsha Prahlad and Inderjit Chopra. Design of a variable twist tilt-rotor blade using shape memory alloy (SMA) actuators. In *Proceedings of SPIEs Annual Symposium on Smart Structures and Materials, Newport Beach, CA*, volume 4327, pages 46–59, 2001.

[75] Jayanth N. Kudva, Brian P. Sanders, Jennifer L. Pinkerton-Florance, and Ephrahim Garcia. Overview of the DARPA/AFRL/NASA Smart Wing Phase II program. *Proceedings of the 8th SPIE Conference on Smart Structures and Materials: Industrial and Commercial Applications of Smart Structures Technologies, Newport Beach, CA*, 4332:383–389, March 2001.

[76] Jayanth N. Kudva, Christopher A. Martin, Lewis B. Scherer, Peter A. Jardine, Anna-Maria Rivas McGowan, Renee C. Lake, George P. Sendeckyi, and Brian P. Sanders. Overview of the DARPA/AFRL/NASA Smart Wing program. *Proceedings of the 6th SPIE Conference on Smart Structures and Materials: Industrial and Commercial Applications of Smart Structures Technologies, Newport Beach, CA*, 3674:230–236, March 1999.

[77] Product catalog. http://www.adaptamat.com/, Adaptamat Limited, Yrityspiha 5, FIN-00390 Helsinki, Finland, 2001.

[78] Peter Che-Hung Chen. *Development of a smart rotor with induced-strain actuation of blade twist*. PhD thesis, University of Maryland, Aerospace Department, College Park, MD, 1996.

[79] Peter C. Chen and Inderjit Chopra. Hover test of a smart rotor with induced strain actuation of blade twist. *AIAA Journal*, 35(1):6–16, January 1997.

[80] Peter C. Chen and Inderjit Chopra. Wind tunnel test of a smart rotor model with individual blade twist control. *Journal of Intelligent Material Systems and Structures*, 8(5):414–425, May 1997.

[81] Aaron A. Bent and Nesbitt W. Hagood. Anisotropic actuation with piezoelectric fiber composites. *Journal of Intelligent Material Systems and Structures*, 6(3):338–349, 1995.

[82] John P. Rodgers and Nesbitt W. Hagood. Manufacture of adaptive composite plates incorporating piezoelectric fiber composite plies. In *36th AIAA/ASME/ASCE/AHS/ASC Structures, Structural Dynamics and Materials Conference and AIAA/ASME Adaptive Structures Forum*, pages 2824–2835, New Orleans, LA, April 1995.

[83] John P. Rodgers, Aaron A. Bent, and Nesbitt W. Hagood. Characterization of interdigitated electrode piezoelectric fiber composites under high electrical and mechanical loading. In *SPIE symposium on smart structures and materials, conference on smart structures and integrated systems*, pages 642–659, San Diego, CA, March 1996.

[84] John P. Rodgers. *Development of an integral twist-actuated rotor blade for individual blade control*. PhD thesis, Massachusetts Institute of Technology, Department of Aeronautics and Astronautics, Cambridge, MA, October 1998.

[85] H.B. Strock, M.R. Pascucci, M.V. Parish, and A.A. Bent. Active pzt fibers: a commercial production process. In *SPIE symposium on smart structures and materials, conference on smart materials technologies*, pages 22–31, Newport Beach, CA, March 1999.

[86] W. Keats Wilkie, Matthew L. Wilbur, Paul H. Mirick, Carlos E.S. Cesnik, and SangJoon Shin. Aeroelastic analysis of the NASA/ARMY/MIT active twist rotor. In *55th American Helicopter Society Forum*, Montreal, Canada, May 1999.

[87] Carlos E.S. Cesnik, SangJoon Shin, W. Keats Wilkie, Matthew L. Wilbur, and Paul H. Mirick. Modeling, design and testing of the NASA/ARMY/MIT active twist rotor prototype blade. In *55th American Helicopter Society Forum*, Montreal, Canada, May 1999.

[88] Matthew L. Wilbur, W. Keats Wilkie, William T. Yeager, Renee C. Lake, Chester Langston, Carlos E.S. Cesnik, and SangJoon Shin. Hover testing of the NASA/ARL/MIT active twist rotor. In *8th Army Research Office (ARO) workshop on the aeroelasticity of rotorcraft systems*, State College, PA, October 1999.

[89] Robert Derham, Douglas Weems, M. Bobby Mathew, and Richard Bussom. The design evolution of an active materials rotor. *Presented at the American Helicopter Society 57th Annual Forum, Washington DC*, May 9-11 2001.

[90] Curtis Walz and Inderjit Chopra. Design and testing of a helicopter rotor model with smart trailing edge flaps. In *35th AIAA/ASME/ASCE/AHS/ASC structures, structural dynamics and materials conference and AIAA/ASME/AHS adaptive structures forum*, Hilton Head, SC, April 1994.

[91] Oren Ben-Zeev and Inderjit Chopra. Advances in the development of an intelligent helicopter rotor employing smart trailing edge flaps. *Smart Materials and Structures*, 5(1):11–25, February 1996.

[92] Nikhil A. Koratkar and Inderjit Chopra. Analysis and testing of a Froude scaled rotor with piezoelectric bender actuated trailing-edge flaps. *Journal of Intelligent Material Systems and Structures*, 8(7):555–70, July 1997.

[93] Nikhil A. Koratkar and Inderjit Chopra. Analysis and testing of a Mach scaled helicopter rotor in hover with piezoelectric bender actuated trailing-edge flaps. In *SPIE symposium on smart structures and materials, conference on smart structures and integrated systems*, pages 266–290, San Diego, CA, March 1998.

[94] Nikhil A. Koratkar and Inderjit Chopra. Analysis and testing of a Mach scaled rotor model with piezoelectric bender actuated trailing-edge flaps. In *40th AIAA/ASME/ASCE/AHS/ASC structures, structural dynamics and materials conference and AIAA/ASME/AHS adaptive structures forum*, pages 2380–2402, St. Louis, MO, April 1999.

[95] Nikhil A. Koratkar and Inderjit Chopra. Design, fabrication and testing of a Mach scaled-rotor model with trailing edge flaps. In *55th American Helicopter Society Forum*, pages 558–578, Montreal, Canada, May 1999.

[96] Nikhil A. Koratkar and Inderjit Chopra. Hover testing of a Mach-scaled rotor with trailing-edge flaps. In *SPIE symposium on smart structures and materials, conference on smart structures and integrated systems*, Newport Beach, CA, March 2000.

[97] Nikhil A. Koratkar and Inderjit Chopra. Windtunnel testing of a Mach-scaled rotor with trailing-edge flaps. In *56th American Helicopter Society Forum*, Virginia Beach, VA, May 2000.

[98] Nikhil Ashok Koratkar. *Smart Helicopter Rotor with Piezoelectric Bender Actuated Trailing-Edge Flaps*. PhD thesis, University of Maryland, College Park, MD 20742 USA, 2000.

[99] M.V. Fulton and Robert .A. Ormiston. Hover testing of a small-scale rotor with on-blade elevons. In *53rd American Helicopter Society Forum*, pages 249–273, Virginia Beach, VA, May 1997.

[100] M.V. Fulton and Robert .A. Ormiston. Small-scale rotor experiments with on-blade elevons to reduce blade vibratory loads in forward flight. In *54th American Helicopter Society Forum*, Washington, DC, May 1998.

[101] M.V. Fulton. Analysis of an active rotor and comparison with small scale experimental data. In *8th Army Research Office (ARO) workshop on the aeroelasticity of rotorcraft systems*, State College, PA, October 1999.

[102] Andreas P.F. Bernhard and Inderjit Chopra. Development of a smart moving blade tip activated by a piezo-induced bending-torsion coupled beam. In *SPIE symposium on smart structures and materials, conference on smart structures and integrated systems*, pages 63–79, San Diego, CA, February 1996.

[103] Andreas P.F. Bernhard and Inderjit Chopra. Hover testing of an active rotor blade tip and structural analysis of the actuator beam. In *39th AIAA/ASME/ASCE/AHS/ASC structures, structural dynamics and materials conference and AIAA/ASME/AHS Adaptive structures forum*, pages 3299–3325, Longbeach, CA, April 1998.

[104] Andreas P.F. Bernhard and Inderjit Chopra. Hover testing of active rotor blade-tips using a piezo-induced bending-torsion coupled beam. *Journal of Intelligent Material Systems and Structures*, 9(12):963–974, December 1998.

[105] Michael G. Spencer, Robert M. Sanner, and Inderjit Chopra. An adaptive neurocontroller for vibration suppression and shape control of a flexible beam. *Journal of Intelligent Material Systems and Structures*, 9(3):160, 1998.

[106] Michael G. Spencer, Robert M. Sanner, and Inderjit Chopra. Neurocontrol of simulated full scale rotor vibrations using trailing edge flaps. In *40th AIAA/ASME/ASCE/AHS/ASC structures, structural dynamics and materials conference and AIAA/ASME/AHS adaptive structures forum*, pages 2744–2752, St. Louis, MS, April 1999.

[107] Michael G. Spencer. *Development of a real time adaptive neural network controller for active rotorcraft vibration reduction*. PhD thesis, University of Maryland, Aerospace Department, College Park, MD, March 2000.

[108] Nikhil Koratkar. Wind tunnel testing of a smart rotor with trailing edge flaps. In *The 12th International Conference on Adaptive Structures Technology*, University of Maryland, College Park, MD, October 2001.

[109] C.M. Bothwell, Ramesh Chandra, and Inderjit Chopra. Torsional actuation with extension-torsional composite coupling and magnetostrictive actuators. *AIAA Journal*, 33(4):723–729, April 1995.

[110] Joseph W. Clement, Diann Brei, Andrew J. Moskalik, and Ron Barrett. Bench-top characterization of an active rotor blade flap system incorporating c-block actuators. In *39th AIAA/ASME/ASCE/AHS/ASC structures, structural dynamics and materials conference and AIAA/ASME/AHS adaptive structures forum*, pages 2857–2869, Longbeach, CA, April 1998.

[111] Joseph W. Clement, Diann Brei, and Ron Barrett. Wind tunnel testing of a high authority, airspeed insensitive, rotor blade flap. In *40th AIAA/ASME/ASCE/AHS/ASC structures, structural dynamics and materials conference and AIAA/ASME/AHS adaptive structures forum*, pages 2414–2424, St. Louis, MO, April 1999.

[112] Eric F. Prechtl and Steven R. Hall. An x-frame actuator servo-flap actuation system for rotor control. In *SPIE symposium on smart structures and materials, conference on smart structures and integrated systems*, pages 309–320, San Diego, CA, March 1998.

[113] Eric F. Prechtl and Steven R. Hall. Design of a high efficiency, large stroke, electromechanical actuator. *Smart Materials and Structures*, 8(1):13–30, February 1999.

[114] Eric F. Prechtl and Steven R. Hall. Preliminary testing of a Mach-scaled active rotor blade with trailing-edge servo flap. In *SPIE symposium on smart structures and materials, conference on smart structures and integrated systems*, pages 14–21, Newport Beach, CA, March 1999.

[115] Eric F. Prechtl and Steven R. Hall. Hover testing of a Mach-scaled rotor with an active trailing edge flap. In *8th Army Research Office (ARO) workshop on the aeroelasticity of rotorcraft systems*, State College, PA, October 1999.

[116] Eric F. Prechtl. *Design and Implementation of a Piezoelectric Servo-Flap Actuation System for Helicopter Rotor Individual Blade Control*. PhD thesis, Massachusetts Institute of Technology, Department of Aeronautics and Astronautics, Cambridge, MA, February 2000.

[117] Friedrich K. Straub and R.J. King. Application of smart materials to helicopter rotor active control. In *SPIE symposium on smart structures and materials, conference on industrial and commercial applications of smart structures technologies*, pages 66–77, San Diego, CA, March 1996.

[118] Friedrich K. Straub, M.A. Ealey, and M.L. Schetky. Application of smart materials to helicopter rotor active control. In *SPIE symposium on smart structures and materials, conference on industrial and commercial applications of smart structures technologies*, pages 99–113, February, CA, March 1997.

[119] Friedrich K. Straub, Hieu T. Ngo, V. Anand, and D.B. Domzalski. Development of a piezoelectric actuator for trailing-edge flap control of rotor blades. In *SPIE symposium on smart structures and materials, conference on smart structures and integrated systems*, pages 2–13, Newport Beach, CA, March 1999.

[120] Friedrich K. Straub and Bruce D. Charles. Comprehensive modeling of rotors with trailing edge flaps. In *55th American Helicopter Society Forum*, Montreal, Canada, May 1999.

[121] Friedrich K. Straub. Development of a full scale smart rotor system. In *8th Army Research Office (ARO) workshop on the aeroelasticity of rotorcraft systems*, State College, PA, October 1999.

[122] Friedrich K. Straub. Smart rotor technology developments - challenges and payoffs. In *The 12th International Conference on Adaptive Structures Technology*, University of Maryland, College Park, MD, October 2001.

[123] D. Schimke, Peter Jänker, A. Blaas, R. Kube, G. Schewe, and Ch. Keßler. Individual blade control by servo-flap and blade root control, a collaborative research and development programme. In *23rd European Rotorcraft Forum*, pages 46.1–46.16, Dresden, Germany, September 1997.

[124] D. Schimke, Peter Jänker, V. Wendt, and B. Junker. Wind tunnel evaluation of a full scale piezoelectric flap control unit. In *24th European Rotorcraft Forum*, Marseilles, France, September 1998. Paper TE-02.

[125] P. Jänker, V. Klöppel, F. Hermle, T. Lorkowski, S. Storm, M. Christmann, and M. Wettemann. Development and evaluation of a hybrid piezoelectric actuator for advanced flap control technology. In *25th European Rotorcraft Forum*, Rome, Italy, September 1999. Paper G-21.

[126] B.G. van der Wall R. Kube, A. Büter, U. Ehlert, W. Geissler, M. Raffel, and G. Schewe. A multi concept approach for development of adaptive rotor systems. In *8th Army Research Office (ARO) workshop on the aeroelasticity of rotorcraft systems*, State College, PA, October 1999.

[127] T. Lorkowski, P. Jänker, F. Hermle, , S. Storm, M. Christmann, and M. Wettemann. Development of a piezoelectrically actuated leading edge flap for dynamic stall delay. In *25th European Rotorcraft Forum*, Rome, Italy, September 1999. Paper G-20.

[128] Francois Toulmay, Valentin Kloppel, Francois Lorin, Bernhard Enenki, and Jacques Gaffiero. Active blade flaps - the needs and current capabilites. *Presented at the American Helicopter Society 57th Annual Forum, Washington DC*, May 9-11 2001.

[129] Taeoh Lee and Inderjit Chopra. Design and static testing of a trailing-edge flap actuator with piezostacks for a rotor blade. In *SPIE symposium on smart structures and materials, conference on smart structures and integrated systems*, pages 321–332, San Diego, CA, March 1998.

[130] Taeoh Lee and Inderjit Chopra. Development and validation of a refined piezostack-actuated trailing-edge flap actuator for a helicopter rotor. In *SPIE symposium on smart structures and materials, conference on smart structures and integrated systems*, Newport Beach, CA, March 1999.

[131] Taeoh Lee. *Design of a High Displacement Smart Trailing-Edge Flap Actuator Incorporating Dual-Stage Mechanical Stroke Amplifier for Rotors*. PhD thesis, University of Maryland, College Park, MD 20742, USA, 2000.

[132] D. A. Fink, T. J. Hawkey, M. Gaudreau, B. Wellman, and R. A. Ormiston. An electromagnetic actuator for individual blade control. *Presented at the American Helicopter Society 57th Annual Forum, Virginia Beach, Virginia*, May 2000.

[133] D. A. Fink, T. J. Hawkey, M. Gaudreau, B. Wellman, and R. A. Ormiston. An electromagnetic actuator for individual blade control. *AHS National Specialists' Meeting "Improving Rotorcraft Acceptance Through Active Controls Technology, Bridgeport, Connecticut*, October 2000.

[134] Louis R. Centolanza and Edward C. Smith. Design and experimental testing of an induced-shear piezoelectric actuator for rotor blade trailing edge flaps. In *41th AIAA/ASME/ASCE/AHS/ASC structures, structural dynamics and materials conference and AIAA/ASME/AHS adaptive structures forum*, Atlanta, GA, April 2000. Paper AIAA-2000-1713.

[135] A.E. Glazounov, Q.M. Zhang, and C. Kim. New torsional actuator based on shear piezoelectric response. In *SPIE symposium on smart structures and materials, conference on smart materials technologies*, pages 82–93, San Diego, CA, March 1998.

[136] Marc Duvernier, Livier Reithler, Jean Yves Guerrero, and Rinaldo Rossi. Active control system for a rotor blade trailing-edge flap. *Smart Structures and Materials 2000: Smart Structures and Integrated Systems*, 3985:52–61, March 2000.

[137] Physik Instrumente (PI). *Products for Micropositioning, US-edition*, 1997.

[138] S. Ueha and Y. Tomikawa. *Ultrasonic Motors: Theory and Application*. Clarendon Press, Oxford, 1993.

[139] T. Sashida and T. Kenjo. *An Introduction to Ultrasonic Motors*. Clarendon Press, Oxford, 1993.

[140] S. Li, W. Cao, and L. E. Cross. The extrinsic nature of nonlinear behavior observed in lead zirconate titanate ferroelectric ceramic. *Journal of Applied Physics*, 69(10):7219–7224, 1991.

[141] ANSI/IEEE. *IEEE Standard on Piezoelectricity*, 1987. Std. 176.

[142] Morgan Matroc, Inc. (Electro Ceramics Division). Guide to modern piezoceramic ceramics. Bedford, Ohio, 1997.

[143] Irwin Vigness. Dilatations in rochelle salt. *Physical Review*, 48:198–202, 1935.

[144] R. F. Brown. Effect of two-dimensional mechanical stress on the dielectric properties of poled ceramic barium titanate and lead zirconate titanate. *Canadian Journal of Physics*, 39:741–753, 1961.

[145] H. H. A. Kreuger and D. Berlincourt. Effects of high static stress on the piezoelectric properties of transducer materials. *Journal of the Acoustical Society of America*, 33(10):1339–1344, 1961.

[146] H. H. A. Kreuger. Stress sensitivity of piezoelectric ceramics, part 1: Sensitivity to compressive stress parallel to the polar axis. *Journal of the Acoustical Society of America*, 42(3):636–645, 1967.

[147] H. H. A. Kreuger. Stress sensitivity of piezoelectric ceramics, part 3: Sensitivity to compressive stress perpendicular to the polar axis. *Journal of the Acoustical Society of America*, 43(3):583–591, 1968.

[148] P. C. Chen and I. Chopra. Hover testing of smart rotor with induced-strain actuation of blade twist. *AIAA Journal*, 35(1), January 1997.

[149] R. Gerson, S. R. Burlage, and D. Berlincourt. Dynamic tensile stress of a ferroelectric ceramic. *Journal of the Acoustical Society of America*, 33(11):1483–1485, 1961.

[150] Q. M. Zhang, J. Zhao, K. Uchino, and J. Zheng. Change of the weak-field properties of $Pb(Zr,Ti)O_3$ piezoceramics with compressive uniaxial stresses and its links to the effect of dopants on the stability of the polarizations in the materials. *Journal of Materials Research*, 12(1), January 1997.

[151] D. J. Inman, Jeffrey J. Dosch, and Ephrahim Garcia. A self-sensing piezoelectric actuator for collocated control. *Journal of Intelligent Materials and Smart Structures*, 3:166–185, Jan 1992.

[152] J. Qui and J. Tani. Vibration control of a cylindrical shell using distributed piezoelectric sensors and acuators. *Journal of Intelligent Material Systems and Structures*, 6(4):474–481, April 1 1995.

[153] P. Samuel and D. Pines. Health monitoring/damage detection of a rotorcraft planetary geartrain using piezoelectric sensors. *Proceedings of SPIE's 4th Annual Symposium on Smart Structures and Materials, San Diego, CA*, 3041:44–53, March 2-6 1997.

[154] S. Hanagud, M. W. Obal, and A. J. Calise. Optimal vibration control by the use of piezoelectric sensors and actuators. *Journal of Guidance, Control and Dynamics*, 15(5):1199–1206, 1992.

[155] E. H. Anderson and N. W. Hagood. Simultaneous piezoelectric sensing/actuation: Analysis and application to controlled structures. *Journal of Sound and Vibration*, 174(5):617–639, 1994.

[156] C. K. Lee and T.C. O'Sullivan. Piezoelectric strain rate gages. *Journal of the Acoustical Society of America*, 90(2):945–953, August 1991.

[157] C. K. Lee, T. C. O'Sullivan, and W. W. Chiang. Piezoelectric strain rate sensor and actuator designs for active vibration control. *Proceedings of the 32nd AIAA/ASME/ASCE/AHS/ASC Structures, Structural Dynamics and Materials Conference*, (4):2197–2207, April 8-10 1991.

[158] James W. Dally, William F. Riley, and Kenneth G. McConnell. *Instrumentation for Engineering Measurements*. John Wiley and Sons, Inc., 1993.

[159] David F. Stout. *Handbook of Operational Amplifier Circuit Design*. McGraw Hill Book Company, 1976.

[160] Edward F. Crawley and Javier de Luis. Use of piezoelectric actuators as elements of intelligent structures. *AIAA Journal*, 25(10):1373–1385, 1987.

[161] J. Esteban, F. Lalande, and C. A. Rogers. Parametric study on the sensing region of a collocated pzt actuator-sensor. *Proceedings, 1996 SEM VIII International Congress on Experimental Mechanics*, June 1996.

[162] M. W. Lin and C. A. Rogers. modeling of the actuation mechanism in a beam structure with induced strain actuators. AIAA-93-1715-CP, 1993.

[163] M. W. Lin and C. A. Rogers. bonding layer effects on the actuation mechanism of an induced strain actuator/substructure system. *SPIE*, 2190:658–670, 1994.

[164] Measurements group, inc. http://www.measurementsgroup.com, email: email@measurementsgroup.com, Raleigh, NC, 2000.

[165] O. E. Mattiat. *Ultrasonic Transducer Materials*. Plenum Press, New York, 1971.

[166] Leander W. Matsch. *Capacitors, Magnetic Circuits and Transformers*. Prentice-Hall Inc., 1964.

[167] Ralph S. Woollett and Charles L. LeBlanc. Ferroelectric non-linearities in transducer ceramics. *IEEE Transactions on Sonics and Ultrasonics*, SU-20(1):24–31, 1973.

[168] C. Liang, F. Sun, and C. A. Rogers. Coupled electro-mechanical analysis of piezoelectric ceramic actuator driven systems - determination of the actuator power consumption and system energy transfer. *Proceedings of the SPIE Smart Structures and Intelligent Systems Symposium*, 1917:286–298, 1993.

[169] Dan J. Clingman and M. Gamble. High-voltage switching piezo drive amplifier. *Proceedings of the SPIE Smart Structures and Materials Symposium*, 3326:472–478, March 1998.

[170] G. A. Zvonar, A.J. Luan, F. C. Lee, D. K. Lindner, S. Kelly, D. Sable, and T. Schelling. High-frequency switching amplifiers for electrostrictive actuators. *Proceedings of the SPIE Smart Structures and Materials Symposium*, 2721:465–475, 1996.

[171] David Newton, John Main, Ephrahim Garcia, and Lloyd Massengill. Piezoelectric actuation systems: Optimization of driving electronics. *Proceedings of the SPIE Smart Structures and Materials Symposium*, 2717:259–266, February 1996.

[172] C. Niezrecki and H. H. Cudney. Power factor correction methods applied to piezoelectric actuators. *Proceedings of the 34th AIAA/ASME/ASCE/AHS/ASC Structures, Structural Dynamics and Materials Conference*, (AIAA-93-1688-CP):3261–3268, April 1993.

[173] C. Niezrecki and H. H. Cudney. Improving the power consumption characteristics of piezoelectric actuators. *Journal of Intelligent Material Systems and Structures*, 5(4):522–529, 1994.

[174] Chul H. Park and Daniel J. Inman. A uniform model for series r-l and parallel r-l shunt circuits and power consumption. *Proceedings of the SPIE Smart Structures and Materials Symposium*, 3668:797–804, March 1999.

[175] Del Toro. *Principles of Electrical Engineering*. Prentice-Hall Inc., 1972.

[176] Dale F. Berndt and Suhash C. DuttaRoy. Inductor simulation using a single unity gain amplifier. *IEEE Journal of Solid State Circuits*, SC-4:161–162, June 1969.

[177] Suhash C. DuttaRoy and V. Nagarajan. On inductor simulation using a unity gain amplifier. *IEEE Journal of Solid State Circuits*, SC-5:95–98, June 1970.

[178] A. J. Prescott. Loss compensated active gyrator using differential-input operational amplifiers. *Electronic Letters*, 2:283–284, July 1966.

[179] J. S. Paine and Z. Chaudhry. The impact of amplification on efficiency and energy density of induced strain actuators. *Proceedings of the ASME Aerospace Division*, AD-52:511–516, 1996.

[180] Lisa D. Mauck and Christopher S. Lynch. Piezoelectric hydraulic pump development. *Journal of Intelligent Material Systems and Structures*, 11:758–764, October 2000.

[181] J. Wallaschek. Piezoelectric ultrasonic motors. *Journal of Intelligent Material Systems and Structures*, 6:71–83, 1995.

[182] U. Schaaf. Pushy motors. *IEE Review*, pages 105–108, 1995.

[183] Jeremy E. Frank, Gary H. Koopmann, Weicheng Chen, and George A. Lesieutre. Design and performance of a high force piezoelectric inchworm motor. *Proceedings of the 6th SPIE Smart Structures and Materials Symposium: Smart Structures and Integrated Systems, Newport Beach, CA*, 3668:717–723, March 1999.

[184] Timothy P. Galante, Jeremy E. Frank, Julien Bernard, Weicheng Chen, George A. Lesieutre, and Gary H. Koopmann. Design, modeling and performance of a high force piezoelectric inchworm motor. *Proceedings of the 5th SPIE Smart Structures and Materials Symposium: Smart Structures and Integrated Systems, San Diego, CA*, 3329:756–767, March 1998.

[185] Khanh Duong and Ephrahim Garcia. Design and performance of a rotary motor driven by piezoelectric stack actuators. *Japanese Journal of Applied Physics, Part 1*, 35(12A):6334–6341, December 1996.

[186] Eric M. Mockensturm, Jeremy E. Frank, Gary H. Koopmann, and George A. Lesieutre. Modeling and simulation of a resonant bimorph actuator drive. *Proceedings of the 8th SPIE Smart Structures and Materials Symposium: Smart Structures and Integrated Systems, Newport Beach, CA*, 4327:472–480, March 2001.

[187] George A. Lesieutre, Gary H. Koopmann, Eric M. Mockensturm, Jeremy E. Frank, and Weicheng Chen. Resonant bimorph-driven high-torque piezoelectric rotary motor. *Proceedings of the 8th SPIE Smart Structures and Materials Symposium: Industrial and Commercial Applications of Smart Structures Technologies, Newport Beach, CA*, 4332:357–363, March 2001.

[188] Jeremy E. Frank, Gary H. Koopmann, Weicheng Chen, Eric M. Mockensturm, and George A. Lesieutre. Design and performance of a resonant roller wedge actuator. *Proceedings of the 7th SPIE Smart Structures and Materials Symposium: Smart Structures and Integrated Systems, Newport Beach, CA*, 3985:198–206, March 2000.

[189] Micro Pulse Systems, Inc., 3950 Carol Ave., Santa Barbara, CA 93110. *Product Catalog*.

[190] Shuchi Shoji and Masayoshi Esashi. Microflow devices and systems. *Journal of Micromechanics and Microengineering*, 4:157–171, 1994.

[191] D. Accoto, O. T. Nedelcu, M. C. Carrozza, and P. Dario. Theoretical analysis and experimental testing of a miniature piezoelectric pump. *IEEE International Symposium on Micromechatronics and Human Science*, pages 261–268, 1998.

[192] Nesbitt W. Hagood, David C. Roberts, Laxminarayana Saggere, Kenneth S. Breuer, Kuo-Shen Chen, Jorge A. Carretero, Hanqing Li, Richard Mlcak, Seward W. Pulitzer, Martin A. Schmidt, Mark S. Spearing, and Yu-Hsuan Su. Microhydraulic transducer technology for actuation and power generation. *Proceedings of the 7th SPIE Smart Structures and Materials Symposium: Smart Structures and Integrated Systems, Newport Beach, CA*, 3985:680–688, March 2000.

[193] Amos Ullmann. The piezoelectric valve-less pump - performance enhancement analysis. *Sensors and Actuators*, A(69):97–105, 1998.

[194] Amos Ullmann, Ilan Fono, and Yehuda Taitel. A piezoelectric valve-less pump - dynamic model. *Transactions of the ASME*, 123:92–98, March 2001.

[195] T. Gerlach, M. Schuenemann, and H. Wurmus. A new micropump principle of the reciprocating type using pyramidic micro flow channels as passive valves. *Journal of Micromechanics and Microengineering*, 6:199–201, 1995.

[196] J. Smits. Piezoelectric micropump with three valves working peristalically. *Sensors and Actuators*, A(21-23):203–206, 1990.

[197] Jung-Ho Park, Kazuhiro Yoshida, and Shinichi Yokota. Resonantly driven piezoelectric micropump - fabrication of a micropump having high power density. *Mechatronics: Mechanics, Electronics, Control*, 9(7):687–702, October 1999.

[198] Jinhyeong Yoo, Jayant Sirohi, and Norman M. Wereley. Design of an MR hydraulic power actuation system. *Proceedings of the 8th SPIE Conference on Smart Structures and Integrated Systems, Newport Beach, CA*, 4327:148–158, March 2001.

[199] F. K. Straub. A feasibility study of using smart materials for rotor control. *Smart Materials and Structures*, 5(1):1–10, February 1996.

[200] J. Garcia-Bonito, M. J. Brennan, S. J. Elliott, A. David, and R. J. Pinnington. A novel high-displacement piezoelectric actuator for active vibration control. *Smart Materials and Structures*, 7(1):31–42, 1998.

[201] P. Tang, A. Palazzolo, A. Kascak, G. Montague, and W. Li. Combined piezoelectric-hydraulic actuator based active vibration control for a rotordynamic system. *Journal of Vibration and Acoustics*, 117:285–293, July 1995.

[202] Lisa D. Mauck and Christopher S. Lynch. Piezoelectric hydraulic pump. *Proceedings of the 6th SPIE Conference on Smart Structures and Integrated Systems, Newport Beach, CA*, 3668:844–852, March 1999.

[203] Lisa D. Mauck and Christopher Lynch. Piezoelectric hydraulic pump optimization. *Proceedings of the 11th International Conference on Adaptive Structures Technology*, pages 100–107, 1999.

[204] Lisa D. Mauck, Jacqueline Menchaca, and Christopher S. Lynch. Piezoelectric hydraulic pump development. *Proceedings of the 7th SPIE Conference on Smart Structures and Integrated Systems, Newport Beach, CA*, 3985:729–739, March 2000.

[205] Lisa D. Mauck, William Sumner Oates, and Christopher S. Lynch. Piezoelectric hydraulic pump performance. *Proceedings of the 8th SPIE Conference on Smart Structures and Materials: Industrial and Commercial Applications of Smart Structures Technologies, Newport Beach, CA*, 4332:246–253, March 2001.

[206] William Sumner Oates. Piezoelectric pump design and system dynamic model. Master's thesis, Georgia Institute of Technology, Atlanta, GA 30332, USA, April 2001.

[207] Khalil Nasser, Donald J. Leo, and Harley H. Cudney. Compact piezohydraulic actuation system. *Proceedings of the 7th SPIE Conference on Smart Structures and Integrated Systems, Newport Beach, CA*, 3991:312–322, March 2000.

[208] Khalil M. Nasser. Development and analysis of the lumped parameter model of a piezohydraulic actuator. Master's thesis, Virginia Polytechnic Institute and State University, Blacksburg, VA 24061, USA, November 2000.

[209] Khalil Nasser and Donald J. Leo. Efficiency of frequency-rectified piezohydraulic and piezopneumatic actuation. *Journal of Intelligent Material Systems and Structures*, 11:798–810, October 2000.

[210] M. J. Gerver, J. H. Goldie, J. R. Swenbeck, R. Shea, P. Jones, R. T. Ilmonen, D. M. Dozor, S. Armstrong, R. Roderick, F. E. Nimblett, and R. Iovanni. Magnetostrictive water pump. *Proceedings of the 6th SPIE Conference on Smart Structures and Integrated Systems, Newport Beach, CA*, 3329:694–705, March 1998.

[211] Katsunobu Konishi, Toshio Yoshimura, Kyoji Hashimoto, and Nobuhiko Yamamoto. Hydraulic actuators driven by piezoelectric elements(1st report, trial piezoelectric pump and its maximum power). *Journal of Japanese Society of Mechanical Engineering (C)*, 59(564):213–220, 1993.

[212] Katsunobu Konishi, Toshio Yoshimura, Kyoji Hashimoto, Takahiko Hamada, and Taro Tamura. Hydraulic actuators driven by piezoelectric elements(2nd report, enlargement of piezoelectric pumps output power using hydraulic resonance). *Journal of Japanese Society of Mechanical Engineering (C)*, 60(571):228–235, 1994.

[213] Katsunobu Konishi, Kyoji Hashimoto, Teruhisa Miyamoto, and Taro Tamura. Hydraulic actuators driven by piezoelectric elements(3rd report, position control using piezoelectric pump and hydraulic cylinder. *Journal of Japanese Society of Mechanical Engineering (C)*, 61(591):134–141, 1995.

[214] Katsunobu Konishi, Hiroyuki Ukida, and Takahiro Kotani. Hydraulic actuators driven by piezoelectric elements(4th report, construction of mathematical models for simulation. *Journal of Japanese Society of Mechanical Engineering (C)*, 63(605):158–165, 1997.

[215] John Watton. *Fluid Power Systems*. Prentice-Hall, 1989.

[216] D.McCloy and H.R. Martin. *Control of Fluid Power: Analysis and Design*. Ellis Horwood Limited, Chichester, England, second(revised) edition, 1980.

[217] Miko Elwenspoek and Remco Wiegerink. *Mechanical Microsensors*. Springer-Verlag, 2001.

[218] The Lee Company. *Technical Hydraulic Handbook*, 1997.

[219] John A. Main, David V. Newton, LLoyd Massengill, and Ephrahim Garcia. Efficient power amplifiers for piezoelectric applications. *Smart Materials and Structures*, 5(6):766–775, 1996.

[220] HERO precision power amplifier, model PA9810. ROHRER Meß und Systemtechnik, email: rohrer@t-online.de, Munich, Germany, 1999. Technical manual.

[221] The pressure, strain and force handbook. OMEGA Engineering Inc., One Omega Drive, P.O. Box 4047, Stamford CT 06907-0047,http://www.measurementsgroup.com, 2000.

[222] Hydraulic R-DDV servovalves. HR Textron, 25200 W. Rye Canyon Road, Santa Clarita, CA 91355, http://www.hrtextron.com, October 2000.

[223] Frank M. White. *Fluid Mechanics*. McGraw-Hill Inc., New York, second edition, 1986.

[224] Matlab users manual- version 5.3. Mathworks, Inc., 3 Apple Hill Drive, Natick, MA 01760-2098, http://www.mathworks.com, 2001.

[225] C. Dorny. *Understanding Dynamic Systems: Approaches to Modeling, Analysis and Design*. Prentice-Hall, New Jersey, 1993.

[226] E. Doebelin. *System Dynamics Modeling and Response*. Charles E. Merrill Publishing Company, Columbus, Ohio, 1972.

[227] E. Doebelin. *System Modeling and Response, Theoretical and Experimental Approaches*. John Wiley & Sons, New York, 1980.

[228] Tarik Bourouina and Jean-Paul Grandchamp. Modeling micropumps with electrical equivalent networks. *Journal of Micromechanics and Microengineering*, (6):398–404, 1996.

[229] J. L. Shearer, A.J. Murphy, and H.H. Richardson. *Introduction to System Dynamics*. Addison Wesley, 1967.

[230] S. Timoshenko. *Strength of Materials, Part-II*. D. Van Nostrand.

[231] George A. Lesieutre, Lei Fang, Gary H. Koopmann, Suresh P. Pai, and Shoko Yoshikawa. Heat generation of a piezoceramic induced strain actuator embedded in a glass/epoxy composite panel. *Proceedings of the 3rd SPIE Conference on Smart Structures and Materials, San Diego, CA*, 2717:267–275, 1996.

[232] Joon Park, Milan Mitrovic, Gregory P. Carman, and H. T. Hahn. Design and testing of a mesoscale actuator device (MAD). *Smart Structures and Materials 2000: Smart Structures and Integrated Systems*, Proceedings of the SPIE Vol. 3985:717–728, March 2000.

[233] S. Yarlagadda, M. H. W. Chan, H. Lee, G. A. Lesieutre, and D. W. Jensen. Low temperature thermal conductivity, heat capacity and heat generation of pzt. *Journal of Intelligent Material Systems and Structures*, 6:757–764, Nov-Dec 1995.

[234] A. Ochi, S. Takahashi, and S. Tagami. Temperature characteristics for multilayer piezoelectric ceramic actuator. *Japanese Journal of Applied Physics*, 24:209–212, 1984. Suppl. 24-3.

[235] S. Takahashi, S. Hirose, and K. Uchino. Stability of PZT piezoelectric ceramics under vibration level change. *Journal of the American Ceramic Society*, 77:2429–2432, 1994.

[236] Eric M. Flint, Chen Liang, and Craig A. Rogers. Self induced temperature rise of stack actuators due to dynamic excitation. *Proceedings of the 2nd SPIE Conference on Smart Structures and Integrated Systems, San Diego CA*, 2443:422–433, March 1995.

[237] Frank P. Incropera and David P. DeWitt. *Fundamentals of Heat and Mass Transfer*. John Wiley and Sons, third edition, 1990.

[238] Thermal management products catalog. Chomerics North America, Parker Hannifin Corporation, 77 Dragon court, Woburn MA 01888-4014, http://www.chomerics.com, 2001.

[239] Technical reference for ferrotec thermoelectric cooling modules. Ferrotec America Corporation, 40 Simon street, Nashua NH 03060, http://www.ferrotec-america.com, 2001.

[240] Material selector guide. Cytek Engineered Materials, Inc., Havre de Grace, MD, 1995.

[241] Bing Zhang and Christopher Cadou. Performance modeling of a piezo-hydraulic actuator. *Proceedings of the 12th International Conference on Adaptive Structures Technology, College Park MD 20742 USA*, October 2001.